DIAGNOSTIC ULTRASOUND

Imaging and Blood Flow Measurements

DIAGNOSTIC ULTRASOUND

Imaging and Blood Flow Measurements

K. Kirk Shung

Taylor & Francis
Taylor & Francis Group
Boca Raton London New York

A CRC title, part of the Taylor & Francis imprint, a member of the Taylor & Francis Group, the academic division of T&F Informa plc.

Published in 2006 by
CRC Press
Taylor & Francis Group
6000 Broken Sound Parkway NW, Suite 300
Boca Raton, FL 33487-2742

Printed in the United States of America on acid-free paper
10 9 8 7 6 5 4 3 2 1

International Standard Book Number-10: 0-8247-4096-3 (Hardcover)
International Standard Book Number-13: 978-0-8247-4096-2 (Hardcover)
Library of Congress Card Number 2005048513

Library of Congress Cataloging-in-Publication Data

Shung, K. Kirk.
Diagnostic Ultrasound : imaging and blood flow measurements / by K. Kirk Shung.
p. cm.
Includes bibliographical references and index.
ISBN 0-8247-4096-3
Diagnosis, Ultrasonic. 2. Blood flow – Measurement. 3. Laser Doppler blood flowmetry. I. Title.

RC78.7.U4S53 2005
616.07'543–dc22 2005048513

T&F informa
Taylor & Francis Group
is the Academic Division of T&F Informa plc.

Visit the Taylor & Francis Web site at
http://www.taylorandfrancis.com

and the CRC Press Web site at
http://www.crcpress.com

This book is dedicated to my wife, Linda, and three children: Albert, Simon, and May

Preface

The field of medical imaging is advancing at a rapid pace. Imaging modalities like x-ray radiography, x-ray computed tomography (CT), ultrasound, nuclear imaging, magnetic resonance imaging (MRI), and optical imaging have been used in biology and medicine to visualize anatomical structures as large as the lung and liver and as small as molecules. Ultrasound is considered the most cost-effective among them. It is used routinely in hospitals and clinics for diagnosing a variety of diseases. It is the tool of choice in obstetrics and cardiology because it is safe and capable of providing images in real time. New applications in small-animal imaging and cellular imaging are being explored.

Although many clinical books on ultrasound have been published, very few technical books are available. This has been a major problem for the author in teaching graduate courses in ultrasonic imaging at the Department of Bioengineering, Pennsylvania State University, and Department of Biomedical Engineering, University of Southern California, over the past 25 years. It is for this purpose that this book was written. The book is intended as a textbook for a senior or first-year graduate-level course in ultrasonic imaging in a biomedical engineering, electrical engineering, medical physics, or radiological sciences curriculum. An attempt has been made to minimize mathematical derivation and to place more emphasis on physical concepts.

Chapter 1 gives an overview of the field of ultrasonic imaging and its role in diagnostic medicine relative to other imaging modalities. Chapter 2 and Chapter 3 are relatively longer and describe the fundamental physics involved and a crucial device in ultrasound, ultrasonic transducers. Conventional imaging approaches and Doppler measurements are discussed in Chapter 4 and Chapter 5. More recent developments, including contrast imaging and four-dimensional imaging, are described in Chapter 6 through Chapter 9. In Chapter 10, current status and standards on ultrasound bioeffects are reviewed. Chapter 11 discusses methods that have been used to measure ultrasonic properties of tissues. This chapter is optional and may be eliminated at the discretion of the instructor. A list of relevant references is found at the end of each chapter and some of the chapters suggest further reading materials. Material contained in the book should be more than sufficient for a one-semester graduate senior-level course.

The book should also be of interest to radiologists with some technical background and practicing engineers and physicists working in the imaging industry.

K. Kirk Shung

Acknowledgment

The author gratefully acknowledges the financial support provided by NIH Grant No. P41-EB2182 during the period when this book was written.

The Author

K. Kirk Shung, Ph. D., obtained a B.S. in electrical engineering from Cheng-Kung University in Taiwan in 1968, an M.S. in electrical engineering from the University of Missouri, Columbia, in 1970, and a Ph.D. in electrical engineering from the University of Washington, Seattle, in 1975. He did postdoctoral research at Providence Medical Center in Seattle, Washington, for 1 year before being appointed a research bioengineer holding a joint appointment in the Institute of Applied Physiology and Medicine. He became an assistant professor in the bioengineering program, Pennsylvania State University, University Park in 1979 and was promoted to professor in 1989. He was a Distinguished Professor of Bioengineering at Penn State until September 1, 2002, when he joined the department of biomedical engineering, University of Southern California, Los Angeles, as a professor. He has been the director of NIH Resource on Medical Ultrasonic Transducer Technology since 1997.

Dr. Shung is a fellow of the IEEE, the Acoustical Society of America, and the American Institute of Ultrasound in Medicine. He is a founding fellow of the American Institute of Medical and Biological Engineering. He served two terms as a member of the NIH Diagnostic Radiology Study Section. He received the IEEE Engineering in Medicine and Biology Society Early Career Award in 1985 and coauthored a best paper published in *IEEE Transactions* on Ultrasonics, Ferroelectrices, and Frequency Control in 2000. He was the distinguished lecturer for the IEEE UFFC Society from 2002 through 2003 and was elected an outstanding alumnus of Cheng-Kung University in Taiwan in 2001.

Dr. Shung has published more than 200 papers and book chapters. He is the author of a textbook, *Principles of Medical Imaging*, published by Academic Press in 1992, and coedited a book, *Ultrasonic Scattering by Biological Tissues*, published by CRC Press in 1993. Dr. Shung's research interests are ultrasonic transducers, high-frequency ultrasonic imaging, and ultrasonic scattering in tissues.

Contents

1 Introduction

1.1 HISTORY

The potential of ultrasound as an imaging modality was realized as early as the late 1940s when, utilizing sonar and radar technology developed during World War II, several groups of investigators around the world started exploring diagnostic capabilities of ultrasound (Goldberg and Kimmelman, 1988). In the early 1950s, John Wild and John Reid in Minnesota developed a prototype B-mode ultrasonic imaging instrument and were able to demonstrate the capability of ultrasound for imaging and characterization of cancerous tissues at frequencies as high as 15 MHz. John Wild's pioneering effort and accomplishment were recognized with the Japan Prize in 1991. At the same time, apparently unaware of the effort by Wild and Reid, Douglas Howry and Joseph Holms at the University of Colorado at Denver also built an ultrasonic imaging device with which they produced cross-sectional images of the arm and leg.

Starting in the late 1940s, medical applications of ultrasound in Japan were explored by Kenji Tanaka and Toshio Wagai. Two Japanese investigators, Shigeo Satomura and Yasuhara Nimura, were credited with the earliest development of ultrasonic Doppler devices for monitoring tissue motion and blood flow in 1955. Virtually simultaneously with the work going on in Japan and in the U.S., Inge Edler and Hellmuth Hertz at the University of Lund in Sweden worked on echocardiography, an ultrasound imaging technique for imaging cardiac structures and monitoring cardiac functions. In parallel with these developments on the diagnostic front, William Fry and his colleagues at the University of Illinois at Urbana worked on using high-intensity ultrasound beams to treat neurological disorders in the brain.

The primary form of ultrasonic imaging to date has been that of a pulse–echo mode. The principle is very similar to that of sonar and radar. In essence, following an ultrasonic pulse transmission, echoes from the medium being interrogated are detected and used to form an image. Much of the terminology used in ultrasound was imported from the field of sonar and radar. Although pulse–echo ultrasound had been used to diagnose a variety of medical problems since the 1950s, it did not become a widely accepted diagnostic tool until the early 1970s when gray-scale ultrasound with nonlinear echo amplitude to gray level mapping was introduced. Continuous wave (CW) and pulsed wave Doppler (PW) ultrasound devices for measuring blood flow also became available during that time. Duplex ultrasound scanners that combined both functions, thus allowing the imaging of anatomy and the measurement of blood flow with one single instrument, soon followed. Today, ultrasound is the second most utilized diagnostic imaging modality in medicine, second only to conventional x-ray, and is a critically important diagnostic tool of any medical facility.

Although ultrasound has been in existence for more than 40 years and is considered a mature technology by many, the field is by no means in a stagnant state. Technical advances are still being made. The introduction of contrast agents, harmonic imaging, flow and tissue displacement imaging, multidimensional imaging, and high-frequency imaging are just a few examples. In this book, these new developments, along with fundamental physics, instrumentation, system architecture, biological effects of ultrasound, and clinical applications, will be discussed in detail.

1.2 ROLE OF ULTRASOUND IN MEDICAL IMAGING

Ultrasound not only complements the more traditional approaches such as x-ray, but also possesses unique characteristics that are advantageous in comparison to other competing modalities such as x-ray computed tomography (CT), radionuclide emission tomography, and magnetic resonance imaging (MRI). More specifically:

- Ultrasound is a form of nonionizing radiation and is considered safe to the best of present knowledge.
- It is less expensive than imaging modalities of similar capabilities.
- It produces images in real time, unattainable at the present time by any other methods.
- It has a resolution in the millimeter range for the frequencies being clinically used today, which may be improved if the frequency is increased.
- It can yield blood flow information by applying the Doppler principle.
- It is portable and thus can be easily transported to the bedside of a patient.

Ultrasound also has several drawbacks. Chief among them are:

- Organs containing gases and bony structures cannot be adequately imaged without introducing specialized procedures.
- Only a limited window is available for ultrasonic examination of certain organs, such as heart and neonatal brain.
- It depends on operator skill.
- It is sometimes impossible to obtain good images from certain types of patients, including obese patients.

The many advantages that ultrasound can offer have enabled it to become a valuable diagnostic tool in such medical disciplines as cardiology, obstetrics, gynecology, surgery, pediatrics, radiology, and neurology, to name just a few. The relationship among ultrasound and other imaging modalities is a dynamic one. Ultrasound is the tool of choice in obstetrics primarily because of its noninvasive nature, its cost-effectiveness, and its real-time imaging capability. This role will not change in the foreseeable future. Ultrasound also enjoys similar success in cardiology, demonstrated by the fact that echocardiography is a training that every cardiologist must have. The future of ultrasound in cardiology, however, is not as rosy as in obstetrics because, as ultrasound progresses at a rapid rate, other competing imaging

modalities such as multislice spiral CT and MR are also making great strides in improving the image acquisition rate and image quality.

Ultrasound may lose ground in certain areas but it may gain in other areas. Ultrasound mammography is an example of gradually gaining importance in breast cancer imaging. Nevertheless, at the time of heightened public concern with health care costs, the cost-effectiveness of an imaging tool is a crucial factor in planning diagnostic strategies. Diagnostic ultrasound is particularly attractive in this respect and has been anticipated by many clinicians and manufacturers to be a major modality of the future.

Although the pace of development in therapeutic ultrasound has not been as striking as in diagnostic ultrasound, significant progress has also been made in the past decades. These efforts have been primarily focused on developing better devices for hyperthermia, frequently in combination with chemotherapy or radiotherapy, for the treatment of tumors and for high-intensity focused tissue ablation.

1.3 PURPOSE OF THE BOOK

This book is based upon the notes for a graduate course on ultrasound imaging that the author has been teaching at the Department of Bioengineering, Pennsylvania State University, and the Department of Biomedical Engineering, University of Southern California, since 1985. It is intended to be a textbook for a senior- to graduate-level course in ultrasonic imaging. When the author was teaching the course, he realized that not a single book in ultrasound imaging on the market today contained sufficient technical material suitable for adoption as a textbook at the college or graduate-school level, although many excellent books for clinicians and technologists were in print. This book should also be useful as a reference for physicists, engineers, clinicians, and sonographers who are interested in learning more about the technical side of diagnostic ultrasound.

REFERENCE

Goldberg, B.B. and Kimmelman, B.A. *Medical Diagnostic Ultrasound: A Retrospective on Its 40th Anniversary.* Laurel, MD: AIUM, 1988.

FURTHER READING

Cho, Z.H., Jones, J.P., and Singh, M. *Foundations of Medical Imaging*. New York: John Wiley & Sons, 1993.

Christensen, D.A. *Ultrasonic Bioinstrumentation*. New York: John Wiley & Sons, 1988.

Evans, D.E., McDicken, W.N., Skidmore, R., and Woodcock, J.P. *Doppler Ultrasound: Physics, Instrumentation, and Clinical Applications*. New York: John Wiley & Sons, 1989.

Jensen, J.A. *Estimation of Blood Velocities Using Ultrasound*. Cambridge: Cambridge University Press, 1996.

Kino, G.S. *Acoustic Waves: Devices, Imaging, and Analog Signal Processing*. Englewood Cliffs, NJ: Prentice Hall, 1987.

Krestel, E. *Imaging Systems for Medical Diagnosis*. Aktiengesellschaft: Siemens, 1990.
McDicken, W.N. *Diagnostic Ultrasonics: Principles and Use of Instruments*. Edinburgh: Churchill Livingstone, 1991.
Suetens, P. *Fundamentals of Medical Imaging*. Cambridge: Cambridge University Press, 2002.
Shung, K.K., Smith, M.B., and Tsui, B.W.N. *Principles of Medical Imaging*, San Diego: Academic Press, 1992.
Webb, A. *Introduction to Biomedical Imaging*. New York: Wiley, 2003.
Webb, S. *The Physics of Medical Imaging*. Bristol: Adam Hilger, 1990.
Well, P.N.T. *Biomedical Ultrasonics*. London: Academic Press, 1977.
Zagzebski, J.A. *Essentials of Ultrasound Physics*. St. Louis: Mosby, 1996.

2 Fundamentals of Acoustic Propagation

Ultrasound is a sound wave characterized by such parameters as pressure, particle (or medium) velocity, particle displacement, density, and temperature. It differs from a sound wave in that its frequency is higher than 20×10^3 cycles per second or 20 kHz (kilohertz). The audible range of human ear is from 20 Hz to 20 kHz. Because ultrasound is a wave, it transmits energy just like an electromagnetic wave or radiation. Unlike an electromagnetic wave, however, sound requires a medium in which to travel and thus cannot propagate in a vacuum.

To better visualize how the sound propagates through a homogeneous medium, the medium can be modeled as a three-dimensional matrix of elements, which may represent molecules, atoms, or elemental particles, separated by perfect elastic springs representing interelement forces. To simplify the matter even more, only a two-dimensional lattice is shown in Figure 2.1, in which the elements are represented by spheres. When a particle is pushed to a distance from its neutral position, the disturbance or force is transmitted to the adjacent particle by the spring. This creates a chain reaction. If the driving force is oscillating back and forth or sinusoidally, the particles respond by oscillating in the same way. The distance, U, traveled by the particle in the acoustic propagation is called particle or medium displacement, usually in the order of a few tenths of a nanometer in water. The velocity of the particle oscillating back and forth is called particle or medium velocity, u, and is in the order of a few centimeters per second in water. It must be noted that this velocity is different from the rate at which the energy is propagating through the medium.

The velocity at which the ultrasound energy propagates through the medium is defined as the phase velocity or the sound propagation velocity, c. In water, c = 1500 m/s. This is illustrated in Figure 2.1, which shows that the sound velocity is much faster than the particle velocity. Although the particle has only moved a short distance, the perturbation has already been transmitted to other particles over a much longer distance, U'. As a sinusoidal disturbance is propagated into a liquid medium, regions of medium compression and rarefaction will be produced, as shown in Figure 2.2. The displacement of the particles, U, is in the same direction as the direction of wave propagation, X. This type of wave is called a longitudinal or compressional wave.

The particle displacement in the rarefaction region is the largest and it is the smallest in the compression. If the displacement of the particles vs. distance or the displacement of a particle vs. time is plotted, it can be seen that the particle moves in a sinusoidal format as shown in Figure 2.3. The wavelength of a sound wave, λ, is defined as the distance between two points of the same phase in space. For example,

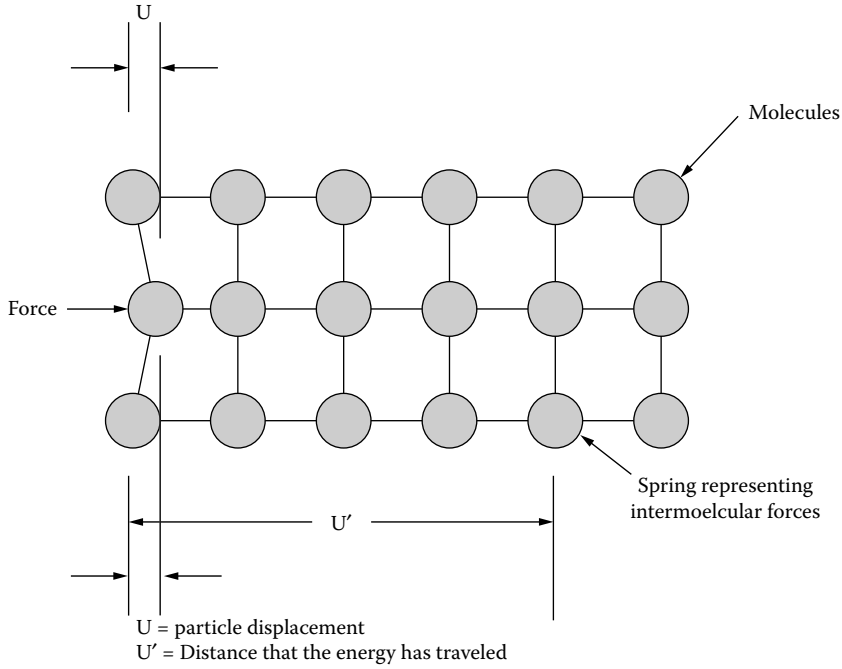

FIGURE 2.1 A two-dimensional matrix of molecules perturbed by an external force. The actual physical displacement of the lattices, *U*, is much smaller than the distance that the energy has traveled, represented by *U′*.

two peaks, or the distance for one cycle of wave to occur at a fixed time and the period, *T*, is defined as the time lapse between two points in time of the same phase, that is, two peaks or the time that it takes for one cycle of wave to occur at a fixed point in space. It follows from these definitions that

$$Tc = \lambda \tag{2.1}$$

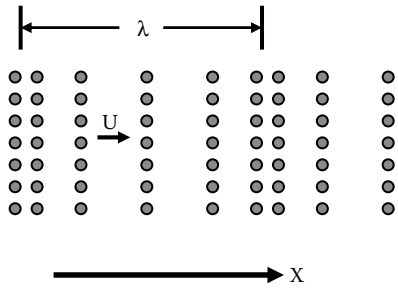

FIGURE 2.2 Regions of compression and rarefaction are formed in a medium during a sinusoidal wave propagation.

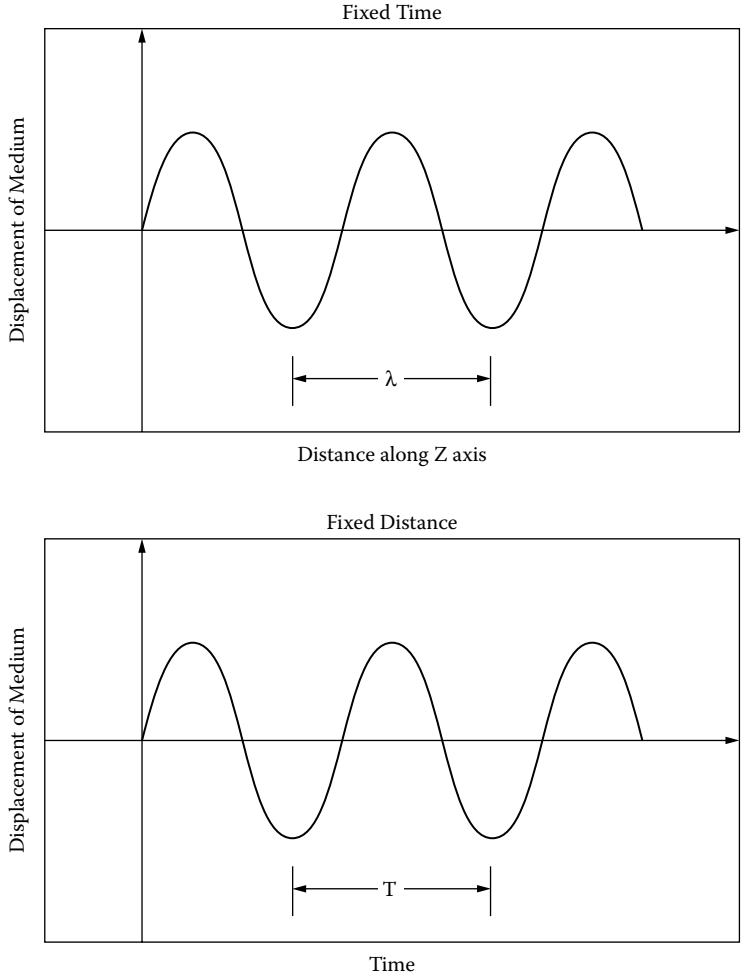

FIGURE 2.3 At a fixed time, the distance between two troughs or two peaks is defined as the wavelength, whereas, at a fixed distance, the time lapse between two troughs is called the period.

Because frequency, f, is defined as $f = 1/T$, Equation (2.1) can be rewritten as

$$f\lambda = c \tag{2.2}$$

For an ultrasonic wave at 5 MHz, the wavelength is about 300 μm. It will be shown later that the spatial resolution of an ultrasonic imaging system, that is, its capability to resolve an object spatially, is primarily determined by the wavelength. The ultimate resolution that a 5-MHz ultrasonic imaging system can achieve is 300 μm. To improve the resolution, one option is to increase the frequency. In contrast, the wavelengths

involved in x-ray or optical imaging are much shorter. Thus, for these modalities, the frequency in general is not as critical when spatial resolution is concerned.

2.1 STRESS AND STRAIN RELATIONSHIPS

Acoustic propagation involves the propagation of a mechanical disturbance whose behavior can be derived from the fundamental concepts of strain and stress. An incremental cube of material within a body with external forces applied to it is shown in Figure 2.4. The stress is defined as the tensile force exerted on the incremental cube by other parts of the body per unit area. On a unit surface perpendicular to the *Z*-axis or *Z*-plane, the stress can be separated into three components:

κ_{zz} = longitudinal stress in the *Z*-direction
κ_{yz} = shear stress in the *Y*-direction
κ_{xz} = shear stress in the *X*-direction

Similarly, κ_{zy}, κ_{yy}, κ_{xy} and κ_{zx}, κ_{yx}, κ_{xx} denote the stresses acting on the *Y*- and *X*-planes. The deformation of the cube caused by an external force is described by the parameter, strain, defined as the displacement per unit distance. The longitudinal strain in the *Z*-direction by the *Z*-plane is

$$\varepsilon_{zz} = \frac{\partial W}{\partial z}$$

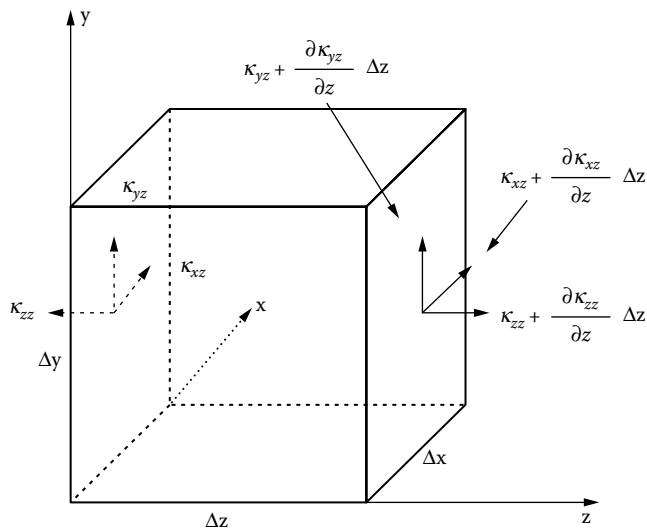

FIGURE 2.4 A stress applied to a unit cube.

and the shear strain in the *X*-direction by the *Z*-plane along the *Z*-axis is

$$\varepsilon_{xz} = \frac{\partial U}{\partial z}$$

where *U*, *V*, and *W* denote the displacements in the *X*-, *Y*-, and *Z*-directions, respectively. They are functions of (*x*,*y*,*z*). The longitudinal and shear strains are graphically illustrated in Figure 2.5.

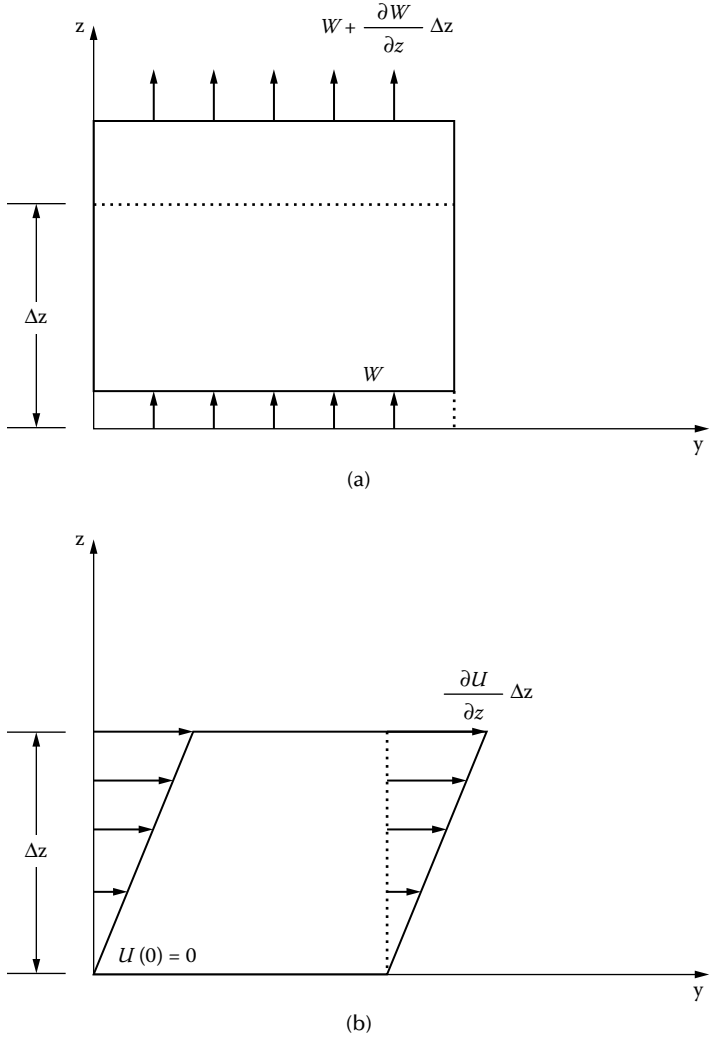

FIGURE 2.5 (a) Longitudinal strain of a *Z*-plane in the *Z*-direction. (b) Shear strain of a *Z*-plane in the *Y*-direction.

Under the condition of small displacements, the stress-strain relationships are linear (Malecki, 1969):

$$\kappa_{zz} = (\nu + 2\mu)\frac{\partial W}{\partial z} = (\nu + 2\mu)\varepsilon_{zz} \tag{2.3}$$

$$\kappa_{yz} = \mu\frac{\partial V}{\partial z} = \mu\varepsilon_{yz} \tag{2.4}$$

$$\kappa_{xz} = \mu\frac{\partial U}{\partial z} = \mu\varepsilon_{xz} \tag{2.5}$$

where ν and μ are Lamé constants and μ is also called the shear modulus because it relates the shear strain to shear stress. The Lamé constants are related to the more conventional material constants, such as Young's modulus (E), bulk modulus (B), and Poisson's ratio (ξ), by the following equations:

$$E = \frac{\mu(3\nu + 2\mu)}{\nu + \mu}$$

$$B = \nu + \frac{2\mu}{3}$$

$$\xi = \frac{\nu}{2(\nu + \mu)}$$

The definitions of these conventional elastic constants can be better understood by examining Figure 2.6, which shows a square bar under tensile stress. The Young's modulus is defined as the ratio of stress/strain or $\kappa_{zz}/\varepsilon_{zz}$ and the Poisson ratio is

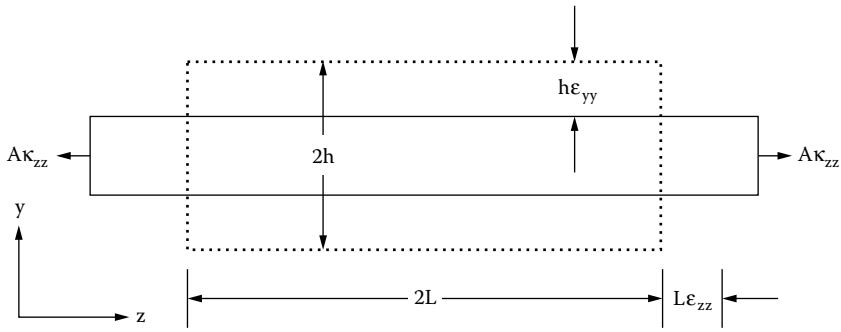

FIGURE 2.6 A bar of square cross-section under tensile stress. 2L and A are the length and the cross-sectional area of the bar, respectively; 2h is the height.

defined as the negative of the ratio of strain in the transverse direction to the strain in the longitudinal direction, or $-\varepsilon_{yy}/\varepsilon_{zz}$.

The bulk modulus is the inverse of the compressibility of the medium. The compressibility (G) of a medium is defined as the negative of the change in volume per unit volume per unit change in pressure:

$$G = -\frac{1}{V}\frac{\partial V}{\partial p}$$

where V denotes the volume of a medium and p the pressure. Pressure is the normal compressional force applied on a surface per unit area of the surface and is expressed in pascals or newtons/m^2. Therefore, the pressure applied on a surface equals the negative of the stress applied on that surface. For a surface perpendicular to the Z-axis, $p = -\kappa_{zz}$. In a fluid in which μ approaches 0, $B \sim \nu$ and $E \sim 0$.

2.2 ACOUSTIC WAVE EQUATION

The equation of motion in the Z-direction for an incremental cube as shown in Figure 2.4 can be readily obtained by applying Newton's second law, that is, summing the net force applied on the cube in the Z-direction:

$$\frac{\partial \kappa_{zz}}{\partial z} + \frac{\partial \kappa_{zy}}{\partial y} + \frac{\partial \kappa_{zx}}{\partial x} = \rho \frac{\partial^2 W}{\partial t^2} \tag{2.6}$$

where ρ is the mass density of the cube and t is time. The left-hand side of the equation is the total force acting on the cube in the Z-direction and the right-hand side is simply the product of the mass and the acceleration produced by the force.

2.2.1 Compressional Wave

For the case in which no shear stresses are present, κ_{zy} and $\kappa_{zx} = 0$ and Equation (2.6) can be reduced to:

$$\frac{\partial \kappa_{zz}}{\partial z} = \rho \frac{\partial^2 W}{\partial t^2} \tag{2.7}$$

Substituting Equation (2.3) into Equation (2.7),

$$\frac{\partial^2 W}{\partial z^2} = \frac{\rho}{\nu + 2\mu}\frac{\partial^2 W}{\partial t^2} \tag{2.8}$$

This second-order differential equation is called the wave equation. The solutions for this equation have the form of $f(z \pm ct)$, where the negative sign indicates a wave

traveling in the +*Z*-direction and the positive sign indicates a wave traveling in the –*Z*-direction. The displacement, *W*, is in the same direction as the wave propagation direction, *Z*. This type of wave is called a compressional or longitudinal wave. The sinusoidal solution for this equation is:

$$W^{\mp}(z,t) = W_0 e^{j(\omega t \pm kz)} \tag{2.9}$$

where

W^- and W^+ denote displacements for positive- and negative-treveling waves, respectively
ω = angular frequency = $2\pi f$
$k = \omega/c$ is the wave number

Sound velocity c is given by

$$c = \sqrt{\frac{\nu + 2\mu}{\rho}} \tag{2.10}$$

For a fluid, $\mu = 0$,

$$c = \sqrt{\frac{B}{\rho}} = \sqrt{\frac{1}{G\rho}} \tag{2.11}$$

It is worth noting from this equation that the sound velocity in a medium is determined by the density and the compressibility of a medium. Sound velocity in air is much smaller than that in water. This is because, although air has a small density, its compressibility is quite large and thus offsets the smaller density.

2.2.2 Shear Wave

For a case in which $\kappa_{zz} = \kappa_{zy} = 0$, a new type of wave in which the displacement, *W*, is perpendicular to the direction of propagation, *X*, is characterized by:

$$\frac{\partial \kappa_{zx}}{\partial x} = \rho \frac{\partial^2 W}{\partial t^2}$$

By substituting $\kappa_{zx} = \mu(\partial W/\partial x)$ into the preceding equation,

$$\frac{\partial^2 W}{\partial x^2} = \frac{\rho}{\mu} \frac{\partial^2 W}{\partial t^2} \tag{2.12}$$

This equation describes a wave traveling in the *X*-direction with a displacement in the *Z*-direction. The sinusoidal solution to Equation (2.12) is

$$W^{\mp}(x,t) = W_0 e^{j(\omega t \pm k_t x)} \tag{2.13}$$

This type of wave expressed by Equation (2.13) is called a shear or transverse wave. The wave number for the shear wave is given by $k_t = \omega/c_t$, where c_t is the shear wave propagation velocity given by

$$c_t = \sqrt{\frac{\mu}{\rho}} \tag{2.14}$$

It is obvious from Equation (2.14) that a shear wave can only exist in a medium with nonzero shear modulus, that is, fluid cannot support the propagation of a shear wave.

As apparent from Equation (2.11) and Equation (2.14), the longitudinal and shear velocities are affected by the mechanical properties of a tissue. Pathological processes that alternate these properties can cause the sound velocity to change. Therefore, if the velocity can be accurately measured, the result can be used to infer or diagnose the pathology. A few ultrasonic devices in the market today for diagnosing osteoporosis are based upon this principle because osteoporosis causes a loss of bone mass.

2.3 CHARACTERISTIC IMPEDANCE

For sinusoidal excitation, the medium velocity or particle velocity in the *Z*-direction, u_z, can be found from the particle displacement, *W*, by differentiating *W* with respect to *t*:

$$u_z = \frac{\partial W}{\partial t} = j\omega W$$

It can be seen that the particle velocity is always 90° out of phase relative to the displacement. Pressure is related to the stress by the following equation:

$$p = -\kappa_{zz}$$

Thus, it follows from Equation (2.3) that

$$p = -(\nu + 2\mu)\frac{\partial W}{\partial z} \tag{2.15}$$

For a longitudinal wave, the displacement *W* is given by Equation (2.9). Substituting Equation (2.9) into Equation (2.15),

$$p^{\pm} = \pm jk(\nu + 2\mu)W^{\pm} = \pm j\omega\rho c W^{\pm}$$

Replacing $j\omega W$ by u_z,

$$p^{\pm} = \pm\rho c u_z^{\pm} \tag{2.16}$$

TABLE 2.1
Acoustic Properties of Biological Tissues and Relevant Materials

Material	Speed (m/s) at 20 to 25°C	Acoustic Impedance (Mrayl)	Attenuation Coefficient (np/cm at 1 MHz)	Backscattering Coefficient ($cm^{-1}sr^{-1}$ at 5 MHz)
Air	343	0.0004	1.38	—
Water	1480	1.48	0.00025	—
Fat	1450	1.38	0.06	—
Myocardium (perpendicular to fibers)	1550	1.62	0.35	8×10^{-4}
Blood	1550	1.61	0.02	2×10^{-5}
Liver	1570	1.65	0.11	5×10^{-3}
Skull bone	3360	6.00	1.30	—
Aluminum	6420	17.00	0.0021	—

Note that the pressure, like the velocity, is 90° out of phase relative to the displacement. Equation (2.16) also indicates that the pressure and velocity are in phase for the positive-traveling wave, and 180° out of phase for the negative-traveling wave.

The specific acoustic impedance of a medium is defined as:

$$Z^{\pm} = \frac{p^{\pm}}{u_z^{\pm}} = \pm \rho c \tag{2.17}$$

where the product, ρc, is also called the characteristic acoustic impedance of the medium. The acoustic impedance has a unit of kg/m^2-sec, or rayl, to commemorate Lord Rayleigh, the father of modern acoustics. The positive and negative signs are for the positive- and negative-traveling waves, respectively.

The acoustic velocity and impedance for a few common materials and biological tissues are listed in Table 2.1. The acoustic velocity in a medium is a sensitive function of the temperature but its dependence on frequency is minimal over the frequency range from 1 to 15 MHz. As will be seen later, the acoustic impedance is a very important parameter in ultrasonic imaging because it determines the amplitude of the echoes reflected or scattered by tissue components. These echoes are acquired by an imaging device to form an image.

2.4 INTENSITY

The intensity of an ultrasonic wave is the average energy carried by a wave per unit area normal to the direction of propagation over time. It is well known that energy consumed by a force, F, which has moved an object by a distance, L, is equal to FL. The power is defined as energy per unit time. Ultrasound is a pressure

wave; thus, one may intuitively deduce from the preceding relationship that the power, P, carried by an ultrasonic wave is given by

P = (force exerted by the pressure wave · medium displacement)/time
= force · medium velocity

Now, because intensity, $i(t)$, is the power carried by the wave per unit area, it follows that

$$i(t) = dP/dA = p(t)u(t)$$

For the case of sinusoidal propagation, the average intensity, I, can be found by averaging $i(t)$ over a cycle:

$$I = p_0 u_0 \cdot \frac{1}{T}\int_0^T \sin^2 \omega t = \frac{1}{2} p_0 u_0 \tag{2.18}$$

where p_0 and u_0 denote peak values of pressure and medium velocity, respectively, and T is the period. Because $Z = p/u = \rho c$, substituting $p = \rho c u$ into Equation (2.18),

$$I = \frac{1}{2}\rho c u_0^2$$

Here it is appropriate to define a few terms related to ultrasound intensity that have been used frequently in medical ultrasound as indicators of exposure level. These definitions are necessary because a majority of the current ultrasonic imaging devices are of the pulse-echo type in which very short pulses of ultrasound consisting of a few cycles of the oscillation are transmitted. This is illustrated in Figure 2.7.

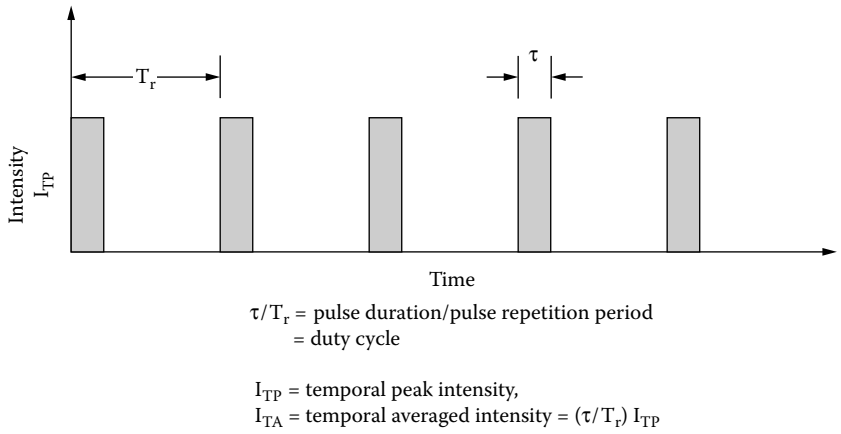

FIGURE 2.7 An ultrasonic pulse train in time with a temporal peak intensity I_{TP}, pulse duration τ, and pulse repetition period T.

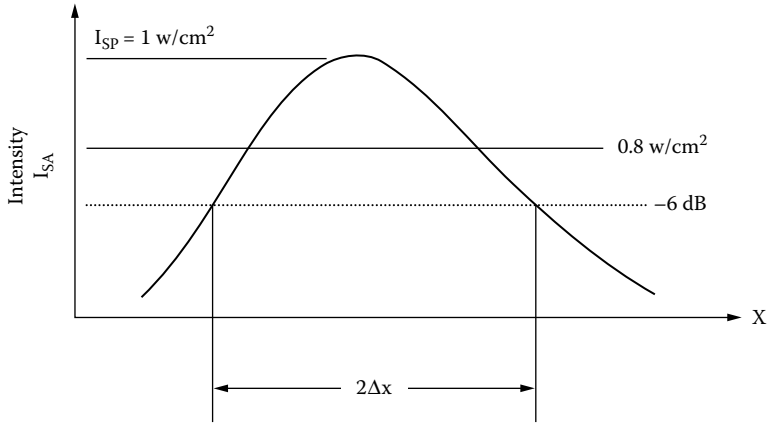

FIGURE 2.8 The ultrasonic lateral beam profile in the *X*-direction with the propagation direction in the *Z*-direction.

Therefore, the temporal averaged intensity differs from that given by Equation (2.18). Moreover, the intensity within an ultrasound beam in general is not spatially uniform. The typical profile of an ultrasonic beam is shown in Figure 2.8. The spatial averaged intensity, I_{SA}, is defined as the average intensity over the ultrasound beam:

$$I_{SA} = \frac{1}{2\Delta x}\int_{-\Delta x}^{\Delta x} I(x)\,dx$$

where $2\Delta x$ is the beam width, which is often defined as the spatial extent between the two −3 or −6 dB points. In Figure 2.8, it can be seen the spatial peak intensity in the beam is 1 W/cm^2 and the spatial average intensity is only 0.8 W/cm^2.

Temporal average intensity is defined as the average intensity over a pulse repetition period, T_r, and is given by the product of duty factor and temporal peak intensity where the duty factor is defined as

$$\text{Duty factor} = \text{pulsed duration } (\tau)/\text{pulsed repetition period } (T_r)$$

In Figure 2.7, it can be seen that the duty factor is 0.1. Whenever biological effects of ultrasound are considered, it is absolutely crucial to state or understand which definition of intensity is being used (AIUM, 1984). In general, spatial average temporal average intensity, I_{SATA}, and spatial peak temporal average intensity, I_{SPTA}, are preferred. The U.S. Food and Drug Administration (FDA) also requires reporting a few other numbers when submitting an ultrasonic device for approval, including I_{SPPA}, spatial peak pulse averaged intensity, and the total power emitted by a probe.

The spatial peak pulse averaged intensity is defined as the spatial peak intensity averaged over the pulse duration. As an example, a probe at 5 MHz emitting a total power of 1.1 mW at a pulse repetition frequency of 3 kHz may have an I_{SPTA} of

1.1 mW/cm^2, I_{SPPA} of 25 W/cm^2, and spatial peak and temporal peak pressure of 0.66 MPa at the focal point. These numbers indicate that the time-averaged intensity may be low, but the instantaneous peak pressure and intensity, which is a concern for mechanical bioeffects, can be very high. The potential bioeffects of ultrasound will be discussed in Chapter 10.

2.5 RADIATION FORCE

An acoustic wave exerts a force on any interface across which ultrasonic intensity decreases in the direction of wave propagation. For a plane wave of intensity, I, propagating in a medium with a sound velocity, c, the radiation force per unit area or radiation pressure, f_r, is given by

$$f_r = a\ (I/c) \tag{2.19}$$

where a is a constant depending upon the acoustic properties of the target and its geometry (Kossoff, 1972).

If a target is made of a material of large acoustic impedance, such as steel, and reflects almost completely the ultrasound beam propagating in water, $a = 2$. If the target is a perfect absorber, $a = 1$. This can be understood by simply considering the momentum transfer that occurs at the boundary, i.e.,

$$f_r\,\Delta t = \Delta(\rho u)$$

where ρ is the mass and u is the particle velocity of a medium at the interface between the medium and a target.

Because the momentum transfer that occurs at the interface for a perfect reflector is twice as large as that for an absorber, f_r acting on a perfect reflector should be twice as large. A more complete treatment can be found in Westervelt (1951).

The radiation force is a very useful parameter for determining power of an ultrasonic beam. A device that has often been used for measuring the intensity of an ultrasonic beam called "radiation force balance" is shown in Figure 2.9. A target with the surface covered by an absorbing or a reflective material is suspended in water. The ultrasonic radiator should be positioned so that the beam is normally incident upon the target. The weight determined by the balance would yield the radiation pressure from which the intensity can be calculated using Equation (2.19).

The radiation force has been used as a means to perturb an object remotely so that, from the displacement of the object, which can be measured via ultrasonic imaging, an assessment of the elastic properties of the medium surrounding the object may be made (Nightingale et al., 1999).

2.6 REFLECTION AND REFRACTION

As a plane ultrasonic wave encounters an interface between two media, I and II, of different acoustic impedance, it will be reflected and refracted. Part of the energy carried by the incident wave is reflected and travels at the same velocity as the

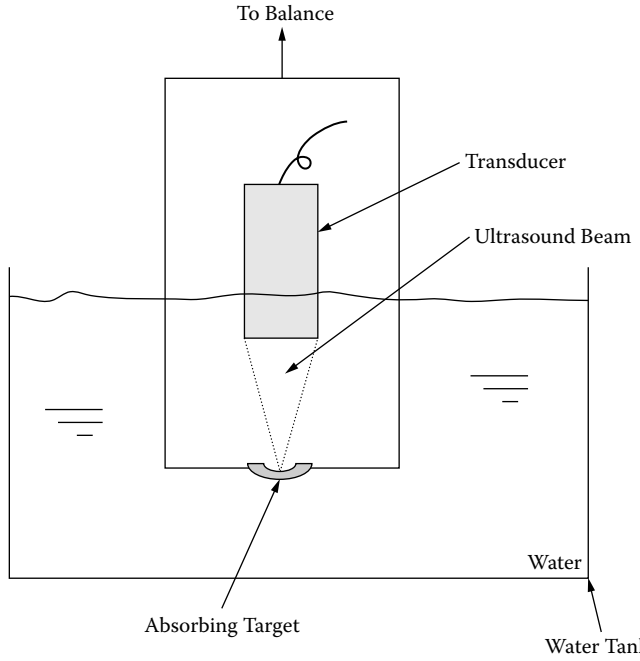

FIGURE 2.9 A radiation balance with an absorbing target.

incident wave. The transmitted or refracted wave in the second medium travels at a different velocity. The directions of the reflected and refracted waves are governed, just as in optics, by Snell's law. This is illustrated in Figure 2.10, in which the subscripts *i*, *r*, and *t* refer to incident, reflected, and transmitted or refracted waves, respectively. As in optics,

$$\theta_i = \theta_r \quad \text{and} \quad \sin\theta_i/\sin\theta_t = c_1/c_2 \tag{2.20}$$

When $\theta_t = \pi/2$, $\sin\theta_t = 1$, and $\theta_{ic} = \sin^{-1}, c_1/c_2$ if $c_2 > c_1$. For any incident angle greater than θ_{ic}, there is no transmission, that is, total reflection occurs. Therefore, θ_{ic} is called the critical angle.

The pressure reflection and transmission coefficients, *R* and *T*, can be easily found by using the boundary conditions that the pressure and particle velocity should be continuous across the boundary.

$$R = \frac{p_r}{p_i} = \frac{Z_2\cos\theta_i - Z_1\cos\theta_t}{Z_2\cos\theta_i + Z_1\cos\theta_t} \tag{2.21}$$

$$T = \frac{p_t}{p_i} = \frac{2Z_2\cos\theta_t}{Z_2\cos\theta_i + Z_1\cos\theta_t} \tag{2.22}$$

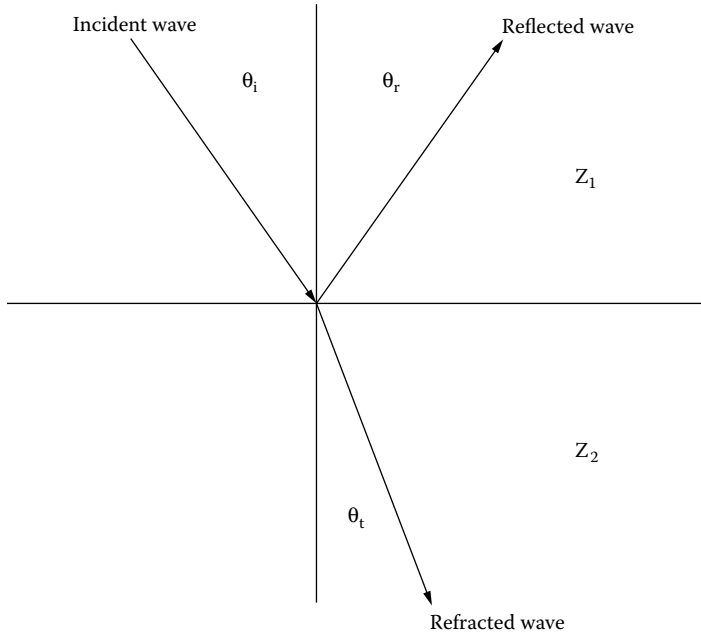

FIGURE 2.10 A plane ultrasonic wave reflected and refracted by a flat interface between two media.

For normal incidence, $\theta_i = \theta_t = 0$ and Equation (2.21) and Equation (2.22) become

$$R = p_r/p_i = (Z_2 - Z_1)/(Z_2 + Z_1) \tag{2.23}$$

$$T = p_t/p_i = 2Z_2/(Z_2 + Z_1) \tag{2.24}$$

Because $p = Zu$, $I = p_o^2/2Z$, from Equation (2.21) and Equation (2.22), it can be shown that

$$\frac{I_r}{I_i} = \left(\frac{Z_2 \cos\theta_i - Z_1 \cos\theta_t}{Z_2 \cos\theta_i + Z_1 \cos\theta_t} \right)^2 \tag{2.25}$$

$$\frac{I_t}{I_i} = \frac{4Z_2 Z_1 \cos\theta_i}{(Z_2 \cos\theta_i + Z_1 \cos\theta_t)^2} \tag{2.26}$$

The quantities (I_r/I_i) and (I_t/I_i) are intensity reflection and transmission coefficients, respectively, at the interface. For normal incidence, $\theta_i = \theta_t = 0$, Equation (2.25) and Equation (2.26) become

$$I_r/I_i = [(Z_2 - Z_1)/(Z_2 + Z_1)]^2 \tag{2.27}$$

$$I_t/I_i = 4Z_2Z_1/(Z_2 + Z_1)^2 \tag{2.28}$$

As an acoustic wave propagates through an inhomogeneous medium such as biological tissues, part of its energy will be lost due to absorption and scattering (to be discussed later) and part of its energy will be lost due to specular reflection at the boundary of two adjacent layers of tissues. The ultrasonic images are formed from the specularly reflected echoes due to planar interfaces as well as the diffusely scattered echoes due to small inhomogeneities in tissue parenchyma. Therefore, any change in the elastic properties of the tissues as a result of a disease may be detectable from the ultrasonic image. This has been the principal rationale behind the conventional pulse-echo ultrasonic imaging methods.

Because scattering and reflection depend on the elastic properties of the tissues, which determine the acoustic impedance of the tissue, intuitively one may postulate that echographic visualizability of tissues is determined mostly by their connective tissue content (Fields and Dunn, 1973). The acoustic impedance of connective tissues and tissues containing high concentrations of connective tissues has been found to be much higher than other types of tissue components, such as fat and protein and tissues containing less connective tissues. The velocity in collagen has been found to be approximately $1.7 \cdot 10^5$ cm/sec (Goss and O'Brien, 1979).

The acoustic impedance of blood vessels, which are composed mainly of connective tissues, should be and was found to be higher than that of most other tissues (Geleskie and Shung, 1982). Because of their higher impedance than surrounding tissues, tissues that contain more connective tissues should be more echogenic that those that contain less. However, it must be noted that the attenuation of ultrasound in connective tissues is also much higher (Greenleaf, 1986). Very little energy can transmit through a mass such as a solid tumor composed of mainly connective tissues. Thus, an acoustic shadow may be created behind such a mass. This has been used as one of the criteria for diagnosing tumors.

The origin of the ultrasonic echoes observed in an ultrasonic image for most of the soft tissues has not yet been determined. However, experimental evidence suggests that, at least in muscle and myocardium, the collagen fibers surrounding the muscle fibers affect the echogenicity of these tissues to a great extent (Hete and Shung, 1993). Although the postulation that tissue echogenicity is largely determined by its connective tissue content may appear to be true, other factors, such as cellular dimension and tissue complexity, should also play an important role and cannot be ignored (Shung and Thieme, 1993). There has been a long-standing interest in correlating the acoustic parameters, such as scattering, attenuation, and acoustic impedance, to the biological composition of the tissues or ultrasonic characterization of biological tissues (Greenleaf, 1986; Shung and Thieme, 1993).

2.7 ATTENUATION, ABSORPTION, AND SCATTERING

When an ultrasonic wave propagates through a heterogeneous medium, its energy is reduced or attenuated as a function of distance. The energy may be diverted by reflection or scattering or absorbed by the medium and converted to heat. The reflection and scattering of a wave by an object actually are referring to the same phenomenon: the redistribution of the energy from the primary incident direction into other directions. This redistribution of energy is termed ''reflection'' when the wavelength and wavefront

of the wave are much smaller than the object and "scattering" if the wavelength and the wavefront are greater than or comparable to the dimension of the object.

2.7.1 Attenuation

The pressure of a plane monochromatic wave propagating in the *Z*-direction decreases exponentially as a function of z:

$$p(z) = p(z = 0)e^{-\alpha z} \tag{2.29}$$

where $p(z = 0)$ is the pressure at $z = 0$ and α is the pressure attenuation coefficient.

Therefore,

$$\alpha = \frac{1}{z}\ln\left[\frac{p(z = 0)}{p(z)}\right]$$

The attenuation coefficient has a unit of nepers per centimeter and is sometimes expressed in units of decibels per centimeter or

$$\alpha(\text{dB/cm}) = 20(\log_{10}e)\alpha(\text{np/cm}) = 8.686\alpha(\text{np/cm})$$

To convert alpha in nepers per centimeter to decibels per centimeter, simply multiply alpha in nepers per centimeter by 8.686. If a tissue has an attenuation coefficient of 0.1 np/cm, then in decibels per centimeter, $\alpha = 8.686 \times 0.1$ dB/cm = 0.8686 dB/cm. Typical values of the attenuation coefficient for some materials are given in Table 2.1.

The relative importance of absorption and scattering to attenuation of ultrasound in biological tissues is a matter that is continuously debated. Investigations to date have shown that scattering contributes little to attenuation—at most, a few percentage points—in most soft tissues (Shung and Thieme, 1993). Therefore, it is safe to say that absorption is the dominant mechanism for ultrasonic attenuation in biological tissues.

2.7.2 Absorption

As was discussed earlier, part of the ultrasound energy propagating in an inhomogeneous medium is lost due to the redistribution of the energy, such as scattering and reflection, and part of the energy is absorbed by the medium. The energy absorbed by the medium is converted to heat. The absorption mechanisms in biological tissues are quite complex and have been assumed to arise from (1) classical absorption due to viscosity; and (2) a relaxation phenomenon. Both mechanisms depend upon the frequency of the wave. In earlier developments, an ideal fluid with $\mu \sim 0$ has been assumed; this means that the absorption due to the classical viscous loss is ignored. However, in reality, this is seldom the case. Recall the definition of shear strain in the *X*-direction along the *Z*-axis:

$$\varepsilon_{xz} = \frac{\partial U}{\partial z}$$

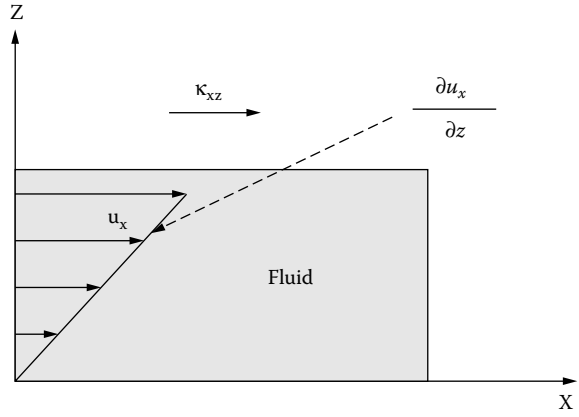

FIGURE 2.11 Shear stress in the *X*-direction on a the *Z*-plane produces a velocity gradient along the *Z*-direction.

In fluids, the rate of strain (which is of more interest than the strain) is given by

$$\frac{\partial \varepsilon_{xz}}{\partial t} = \frac{\partial}{\partial t}\frac{\partial U}{\partial z} = \frac{\partial u_x}{\partial z} \tag{2.30}$$

where u_x is the particle velocity in the *X*-direction and $\partial u_x/\partial z$ is the velocity gradient along the *Z*-axis.

When a fluid with finite viscosity is subject to shear stress, κ_{xz}, as shown in Figure 2.11, it exhibits a velocity gradient, $\partial u_x/\partial z$. The coefficient of viscosity, denoted as η with a unit poises, is defined as the ratio of shear stress to the resultant velocity gradient:

$$\eta = \frac{\kappa_{xz}}{\partial u_x/\partial z} \tag{2.31}$$

It has been shown that, for a homogeneous medium like water, the absorption coefficient for an ultrasonic wave of frequency ω is related to viscosity and frequency by the following expression:

$$\alpha = \frac{2\omega^2\eta}{3\rho c}$$

where $\eta = \mu/j\omega$ from Equation (2.5) and Equation (2.31).

Note here that the absorption coefficient is proportional to ω^2. In many homogeneous materials, such as air and water, in which the elemental particles of the medium are much smaller than the wavelength, this (frequency)^2 dependence of

absorption is seen; however, in most biological materials, this is not the case. Experimental results on attenuation coefficient of ultrasound in biological tissues indicate an approximately linear dependence on frequency below 15 MHz and an alternative theory is needed to explain this behavior. It has been theorized that ultrasonic absorption in biological tissues is dominated by a relaxation process.

When an elemental particle in a medium such as a molecule is pushed to a new position by a force and then released, a finite time is required for the particle to return to its neutral position. This time is called the relaxation time of the particle. For a medium composed of the same types of particles, the relaxation time is also the relaxation time of the medium. If the relaxation time is short compared to the period of the wave, its effect on the wave should be small. However, if the relaxation time is comparable to the period of the wave, the particle may not be able to return to its neutral state completely before a second wave arrives. When this occurs, the wave is moving in one direction and the molecules are moving in the other direction. More energy is thus required to reverse the direction of the particle motion.

If the frequency is increased high enough that the molecules simply cannot follow the wave motion, the relaxation effect again becomes negligible. Maximum absorption occurs when the relaxation motion of the particles is completely out of synchronization with the wave motion. Therefore, the relaxation process is characterized by a relaxation frequency in which the absorption is maximal and is negligibly small for low-frequency and high-frequency regions, as illustrated in Figure 2.12. Mathematically, the relaxation process can be represented by the following equation:

$$\alpha_r = \frac{Bf^2}{1+(f/f_R)^2}$$

where

α_r is a component of the absorption coefficient due to the relaxation process
f_R is the relaxation frequency = $1/T_R$ (T_R = relaxation time)
B is a constant

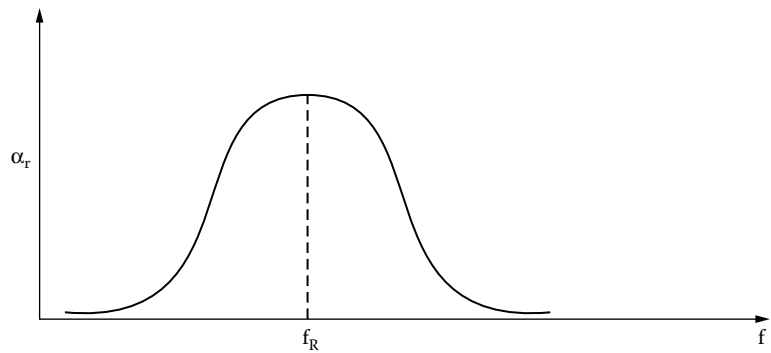

FIGURE 2.12 Ultrasonic absorption caused by a relaxation process characterized by relaxation frequency f_R.

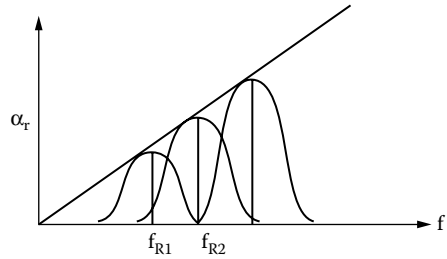

FIGURE 2.13 Ultrasonic absorption caused by multiple relaxation processes characterized by relaxation frequency f_{R1}, f_{R2} ····.

Many components, giving rise to many relaxation frequencies, are in biological tissue. The absorption coefficient in a tissue can be expressed as

$$\alpha_a / f^2 = A + \sum_i \frac{B_i}{1 + (f/f_{Ri})^2} \tag{2.32}$$

where A is a constant associated with classical absorption and B_i and f_{Ri} are the relaxation constants and frequencies, respectively, associated with different tissue components (Dunn and Goss, 1986).

Figure 2.13 illustrates a possible scenario for this equation, in which many relaxation processes may overlap, resulting in a linear increase in the diagnostic ultrasound frequency range or a constant $\alpha\lambda$. Figure 2.14 shows the absorption of ultrasound in various biological tissues as a function of frequency. As can be seen, the absorption is more or less linearly proportional to frequency ($\alpha\lambda$ is constant) in

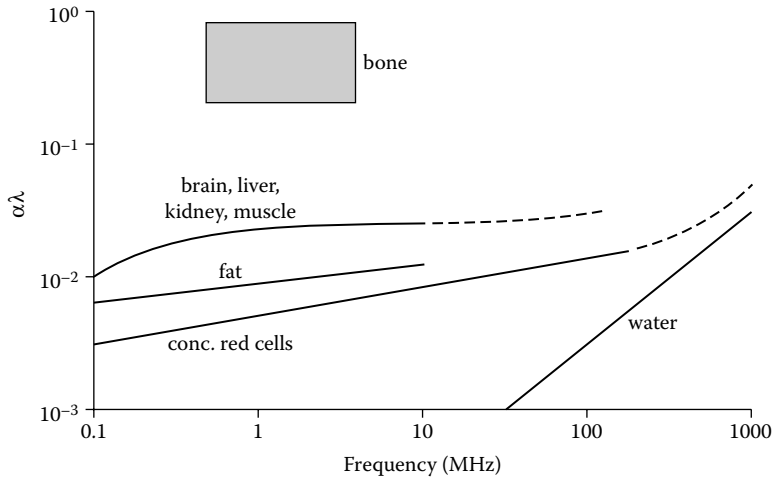

FIGURE 2.14 Ultrasonic absorption in biological tissues as a function of frequency.

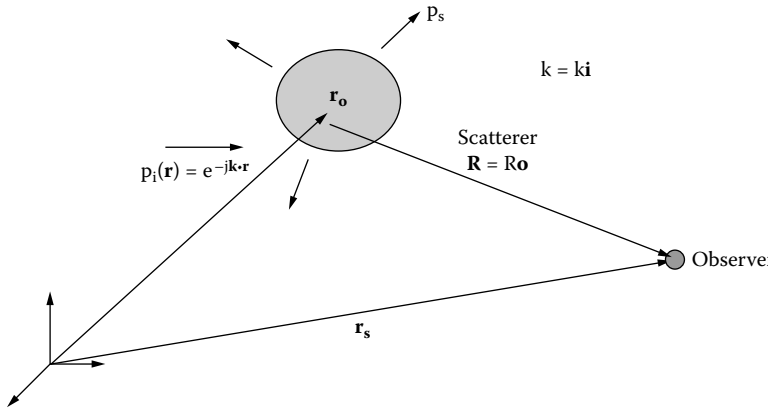

FIGURE 2.15 A plane wave incident upon a scatterer.

diagnostic ultrasound frequency range. This figure also shows that the absorption of ultrasound in water is proportional to f^2.

2.7.3 Scattering

As a wave is incident on an object as shown in Figure 2.15, part of the wave will be scattered and part of it will be absorbed by the object. The scattering characteristics are most conveniently expressed by a term called scattering cross-section.

Assume that the incident pressure is a plane monochromatic wave $p_i(r) = e^{-j\mathbf{k}\cdot\mathbf{r}}$ where $\mathbf{k} = k\mathbf{i}$ (where $\mathbf{i}$ denotes a unit vector in the incident direction) and $\mathbf{r}$ are vectors representing the wave number and the position. The scattered wave at $\mathbf{r_s}$ due to a scatterer at $\mathbf{r_o}$ is given by

$$p_s(\mathbf{r_s}) = \frac{e^{-jkR}}{R} p_i(\mathbf{r_o})\, f(\mathbf{o},\mathbf{i}) \tag{2.33}$$

where $\mathbf{o}$ is a unit vector in the direction of observation, provided that the observation point is in the far field of the scatterer and $R = |\mathbf{r_s} - \mathbf{r_0}|$ if $kR \gg 1$.

The term $f(\mathbf{o},\mathbf{i})$ in Equation (2.33) is called the scattering amplitude function; this describes the scattering properties of the object and depends upon the directions of incidence and observation. The incident intensity in a medium of acoustic impedance Z is given by

$$I_i = \frac{1}{2}\frac{|p_i|^2}{Z} \tag{2.34}$$

and the scattered intensity is given by

$$I_s = \frac{1}{2}\frac{|p_s|^2}{Z} \tag{2.35}$$

Substituting Equation (2.33) and Equation (2.34) into Equation (2.35) and rearranging the equation,

$$I_s = \frac{|f(\mathbf{o},\mathbf{i})|^2}{R^2} I_i \tag{2.36}$$

Rearranging (2.36),

$$\sigma_d(\mathbf{o},\mathbf{i}) = |f(\mathbf{o},\mathbf{i})|^2 = \frac{I_s R^2}{I_i} \tag{2.37}$$

where the term $\sigma_d(\mathbf{o},\mathbf{i}) = |f|^2$ is defined as the differential scattering cross-section, which is the power scattered in the **o** direction with the incident direction **i** in one solid angle per unit incident intensity. When $\mathbf{o} = -\mathbf{i}$, $\sigma_d(\mathbf{i},-\mathbf{i})$ is called the backscattering cross-section.

Figure 2.16 gives a graphical illustration of a differential scattering cross-section. By integrating σ_d over the 4π solid angle, the scattering cross-section, σ_s, which is

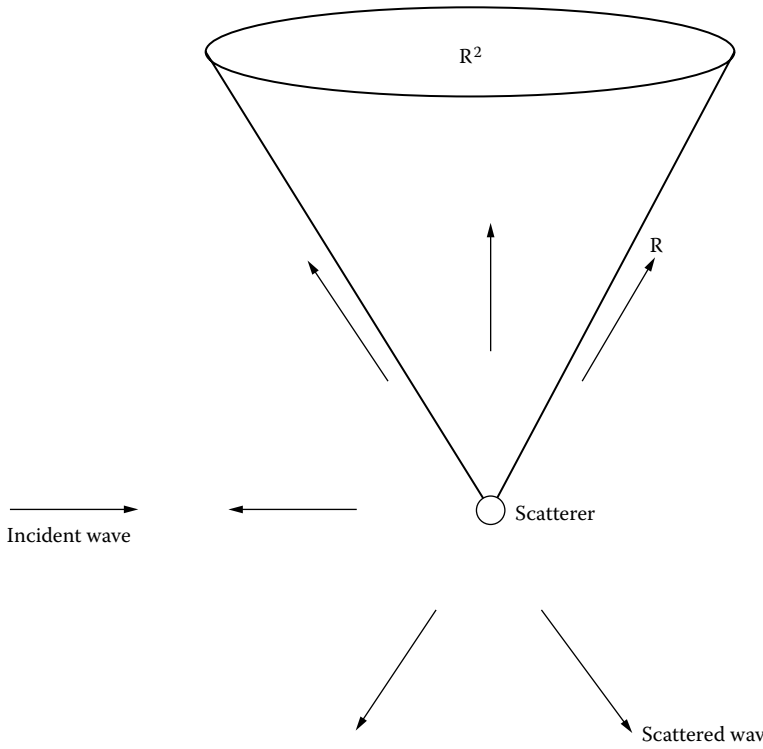

FIGURE 2.16 The differential scattering cross-section of a scatterer represents the power scattered by the scatterer into one solid angle or steradian that encompasses an area of R^2.

defined as the power scattered by the object per unit incident intensity, can be found:

$$\sigma_s = \int_{4\pi} \sigma_d \, d\Omega = \int_{4\pi} |f(\mathbf{o},\mathbf{i})|^2 \, d\Omega$$

where $d\Omega$ is the differential solid angle.

Similarly, an absorption cross-section, σ_a, can be defined as the total power absorbed by the object. Thus, the attenuation in wave intensity due to the presence of the object is simply

$$2\alpha = \sigma_a + \sigma_s$$

where 2α is the intensity attenuation coefficient. If a number of objects are present, the intensity attenuation coefficient should be:

$$2\alpha = n(\sigma_a + \sigma_s)$$

where n is the object concentration per unit volume.

This relation is valid only if n is small or volume concentration given by $n \cdot$(object volume) < 1%. As n increases, multiple scattering occurs; particle-particle interactions may take place (Twersky, 1978) and this relation no longer holds.

To solve analytically for the scattering cross-section of an object of arbitrary shape is impossible, although computer-based methods such as finite element analysis may be used. However, a number of approximations exist that can simplify the problem considerably. One of these is the Born approximation, which assumes that the wave inside the object is the same as the incident wave (Morse and Ingard, 1968). This is a valid assumption if the size of the object is much smaller than the wavelength or the acoustic properties of the scatterer are similar to those of the surrounding medium. By applying this approximation and using the wave equation, the scattering cross-section of an object can be found. The scattering cross-section for a sphere whose radius is much smaller than the wavelength is given by (Morse and Ingard, 1968):

$$\sigma_s = \frac{4\pi k^4 a^6}{9}\left(\left|\frac{G_e - G}{G}\right|^2 + \frac{1}{3}\left|\frac{3\rho_e - 3\rho}{2\rho_e + \rho}\right|^2\right) \tag{2.38}$$

where

k is the wave number
a is the radius of the sphere
G_e and G are the adiabatic compressibilities of the particle and the surrounding medium
ρ_e and ρ are the corresponding mass densities

Equation (2.38) can be applied to calculate the ultrasonic scattering properties of the red blood cells because the size of a red blood cell is much smaller than the wavelength of ultrasound in the frequency range from 1 to 15 MHz. Assume that the human blood can be approximated as a fluid sphere of 3-μm radius. Using:

G_e (compressibility for red blood cell) = $34.1 \cdot 10^{-12}$ cm²/dyne
ρ_e (density for the red blood cell) = 1.092 gm/cm³
G (compressibility for plasma) = $40.9 \cdot 10^{-12}$ cm²/dyne
ρ (density for plasma) = 1.021 gm/cm³

the scattering cross-section for a red blood cell is found to be $\sigma_s = 1.1 \cdot 10^{-12}$ cm² at 10 MHz, which is quite small. For an incident intensity of 1 W/cm², only $\sigma_s \cdot I_i = 1.1 \cdot 10^{-12}$ W of power is scattered by the red cell.

In a dense distribution of scatterers like biological tissues, for instance, human blood consisting of $5 \cdot 10^9$ red blood cells in 1 cm³, scatterer-to-scatterer interaction cannot be ignored. To take this into consideration, a parameter called backscattering coefficient in a unit of centimeter-steradians^{-1} is often used. It is also sometimes called the volumetric backscattering cross-section and is defined as the power backscattered by a unit volume of scatterers in one solid angle per unit incident intensity.

The physical meaning of the backscattering coefficient can be easily understood simply by replacing the scatterer in Figure 2.16 by a unit scattering volume. Because the tissues are fairly inhomogeneous, the scattered signals acquired may vary greatly at any single frequency and over a band of frequencies. A parameter frequently used to describe scattering behavior of a tissue is the integrated backscatter. The integrated backscatter (IB) is defined as the frequency average of the backscatter over the band width of the signal, which can be expressed mathematically as

$$IB = \frac{1}{2\Delta\omega} \int_{\omega_0 - \Delta\omega}^{\omega_0 + \Delta\omega} e(\omega)\, d\omega$$

where
$2\Delta\omega$ is the band width
ω_0 is the center frequency of the spectrum
$e(\omega)$ is the backscattered signal at angular frequency ω

However, to eliminate the dependence of the backscattered signal from tissues on the electrical and acoustic characteristics of the experimental system, the IB is usually expressed in decibels by comparing the backscattered signal to a reference signal, e.g., the echo from a flat reflector. Therefore,

$$IB(dB) = 20 \log \left\{ \frac{1}{2\Delta\omega} \left[\int_{\omega_o - \Delta\omega}^{\omega_o + \Delta\omega} e(\omega) d\omega \Big/ \int_{\omega_o - \Delta\omega}^{\omega_o + \Delta\omega} e_r(\omega) d\omega \right] \right\}$$

where $e_r(\omega)$ is the reflected signal from the flat reflector at angular frequency ω. The backscattering coefficients for several tissues are listed in Table 2.1.

The fact that the acoustic scattering characteristics of an object including angular scattering pattern depend upon the shape, size, and acoustic properties of the scatterer has been known for many years. Ideally, the structure and acoustic properties of the scatterers can be deduced from measuring their scattering properties. This problem is of interest to many scientists in such diverse fields as geophysics, oceanography, and communication. It is generally termed remote sensing or detection. Although the potential of characterizing a tissue structure from its scattering properties was realized in the biomedical ultrasound community almost three decades ago, this field still remains in its infancy, primarily due to the complex nature of biological tissues.

Preliminary experimental investigations *in vitro* thus far have shown that different tissues exhibit different angular scattering pattern and frequency dependence (Shung and Thieme, 1993). The backscattering coefficient defined as backscattering cross-section per unit volume of scatterers for five different types of bovine tissues as a function of frequency is shown in Figure 2.17 (Fei and Shung, 1985). Experimental results on scattering by red blood cells (Yuan and Shung, 1988) are in good

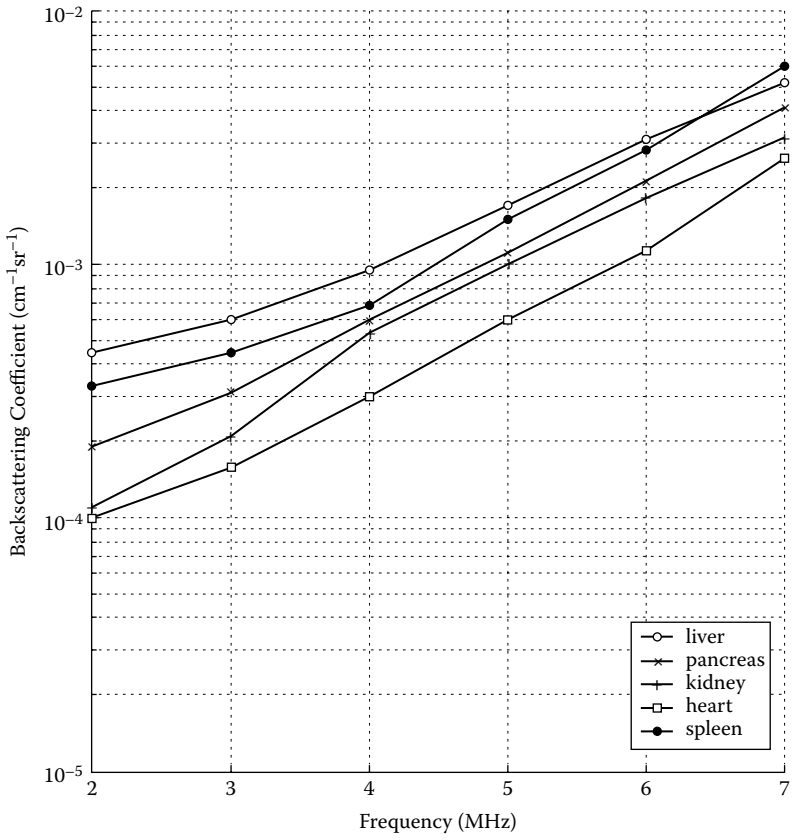

FIGURE 2.17 Ultrasonic backscatter coefficient for several bovine soft tissues as a function of frequency.

agreement with Equation (2.38). Scattering from myocardium has been shown to have a third-power dependence on frequency (Shung and Thieme, 1993).

Based on this evidence and more recent results indicating that ultrasonic scattering increases as the muscle is stretched, it was suggested that the scattering from muscle may be attributed to the collagen fibers in the muscle because the scattering from cylinders whose radius is much smaller than the wavelength is proportional to f^3. Experimental results on scattering from tissues thus far have been very scanty and inconclusive. The precise origin of ultrasonic scattering from many tissues is still unknown, although efforts to shed more light on this subject are under way (Shung and Thieme, 1993).

Because pathological processes in tissues involve anatomical variations, it is likely that they will result in corresponding changes in ultrasonic backscatter. This has been demonstrated by several recent investigations. Figure 2.18 shows that the

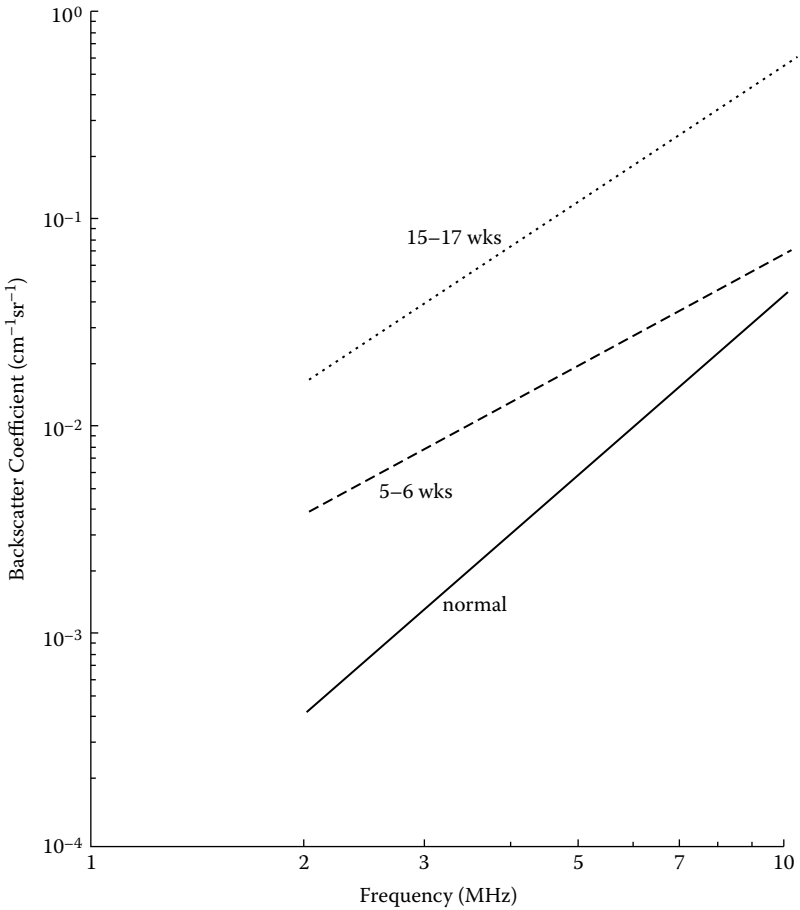

FIGURE 2.18 Ultrasonic backscatter coefficient for canine myocardium as a function of frequency. Solid, dashed, and dotted lines represent data for normal myocardium, myocardium 5 to 6 weeks following infarction, and myocardium 15 to 17 weeks following infarction, respectively.

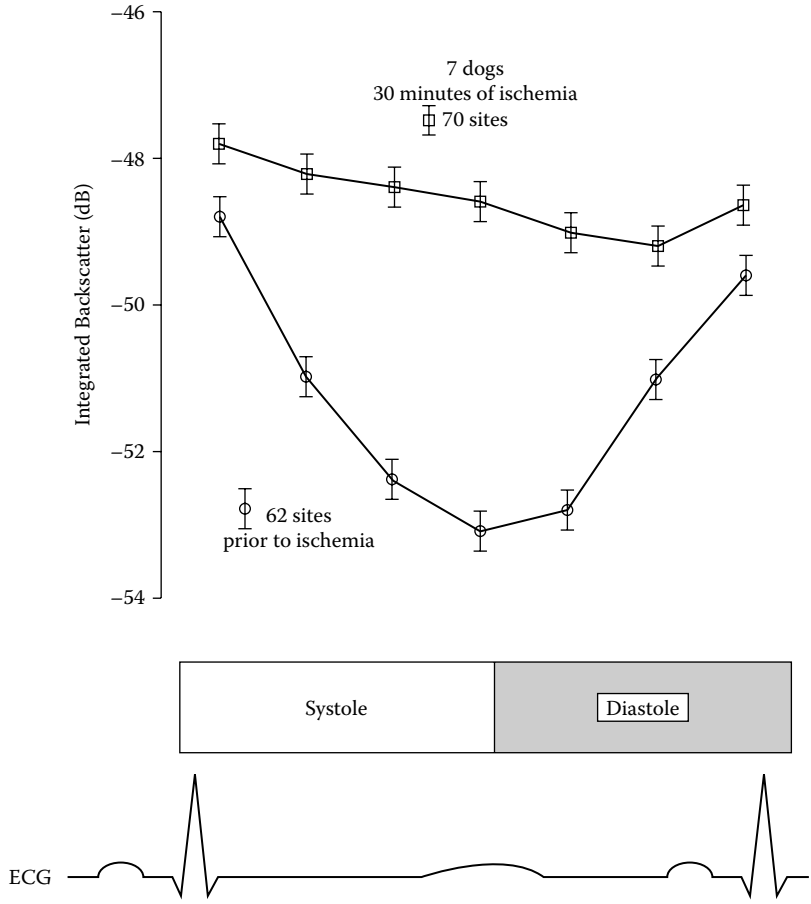

FIGURE 2.19 Integrated backscatter from canine myocardium as a function of the cardiac cycle.

backscattering coefficient for regions of infarcted myocardium is substantially higher than that for normal myocardium (Wickline et al., 1993). In addition, myocardial ultrasonic backscatter is shown to be related to the contractional state of the tissue (Figure 2.19). The myocardial backscatter was found to be the highest at the end diastole and lowest at the end systole during a cardiac cycle; this cyclic behavior was blunted in ischemic heart (Wickline et al., 1993).

In summary, the attenuation of ultrasound in biological tissues can be attributed to two mechanisms: (1) scattering and (2) absorption. The question remains, however, as to the relative importance of these mechanisms, although absorption is believed to be the dominant mechanism. Attenuation in general is not desirable because it limits the depth of ultrasound penetration into the body. However, it may yield useful information for diagnostic purposes because it carries information about the properties of the tissues if it can be accurately estimated. Extensive work has

also been carried out to demonstrate that tissue pathology can affect the attenuation coefficient of tissues to a great extent. Infarcted myocardium and malignant tumors in liver and breast were all shown to have an increased attenuation. Unfortunately, measuring attenuation *in vivo* has been proven to be quite a difficult task. Various schemes have been developed with little success.

2.8 NONLINEARITY PARAMETER B/A

The spatial peak temporal peak intensity I_{SPTP} of modern ultrasonic diagnostic instrument can sometimes reach the level of more than 100 W/cm^2; thus, nonlinear acoustic phenomena may not be ignored in treating ultrasonic propagation in tissues (Hamilton and Blackstock, 1998). Although finite amplitude acoustics has been in existence for a long time, it has not been given much attention in diagnostic ultrasound until recently, when harmonic imaging became popular (Tranquart et al., 1999). In fact, it has been shown that, in many instances, harmonic imaging that utilizes the harmonics generated due to the nonlinear propagation yields better images than conventional ultrasonic imaging. Other reasons for studying the nonlinear properties are: (1) new tissue parameters may be derived for tissue characterization; and (2) nonlinearity can influence, to a significant extent, how the ultrasound energy is absorbed by the tissue.

The nonlinear behavior of a fluid medium can be expressed by a second-order parameter B/A. For an adiabatic process in which the entropy is constant or there is no energy flow, the relation between pressure and density can be expressed as a Taylor series expansion of pressure, p, about the point of equilibrium density, ρ_o, and entropy, s_o,

$$p = p(s_0, \rho_0) + A\left(\frac{\rho - \rho_0}{\rho_0}\right) + \frac{1}{2}B\left(\frac{\rho - \rho_0}{\rho_0}\right)^2 + \cdots$$

where

$$A = \rho_0\left[\frac{\partial p(s_0, \rho_0)}{\partial \rho}\right]$$

and

$$B = \rho_0^2\left[\frac{\partial^2 p(s_0, \rho_0)}{\partial \rho^2}\right]$$

From these two equations and the definition of sound speed (Morse and Ingard, 1968),

$$c^2 = \frac{\partial p(s_0, \rho_0)}{\partial \rho}$$

we can show that B/A is given by

$$B/A = 2\rho_0 c_0 \left[\frac{\partial c(s_0, \rho_0)}{\partial p} \right] \tag{2.39}$$

Equation (2.39) can be converted to parameters that are easier to measure using thermodynamic relationships:

$$B/A = 2\rho_0 c_0 \left[\frac{\partial c(s,T)}{\partial p} \right] + 2\frac{c_0 T \beta_v}{C_p} \left[\frac{\partial c(s,p)}{\partial T} \right] \tag{2.40}$$

where

T is temperature
C_p is the heat capacity per unit mass at constant pressure
β_v is the volume coefficient of thermal expansion

The first term represents change in sound speed per unit change in pressure at constant temperature and entropy. The second term represents the change in sound speed per unit change in temperature at constant pressure and entropy. Therefore, the B/A parameter can be estimated from these quantities, which are known or measurable. This approach is called the thermodynamic method. It can also be estimated by a finite amplitude method in which the second pressure harmonic is measured and extrapolated back to the source to eliminate the effect of absorption. The preliminary findings are that B/A

- Is linearly proportional to solute concentration in aqueous solutions of proteins
- Is insensitive to the molecular weight of the solute at fixed concentrations
- Ranges from 6 to 11 for soft tissues
- May depend upon tissue structure

The B/A values for a few tissues and relevant materials are given in Table 2.2.

TABLE 2.2
***B/A* Values for Various Materials**

Material	*B/A*
Water	5.0 at 20°C
Bovine serum albumin (20 g/100 ml)	6.2 at 25°C
Beef liver	7.8 at 23°C
Human breast fat	9.2 at 22°C
Porcine muscle	6.5 at 25°C
Porcine whole blood	6.2 at 30°C

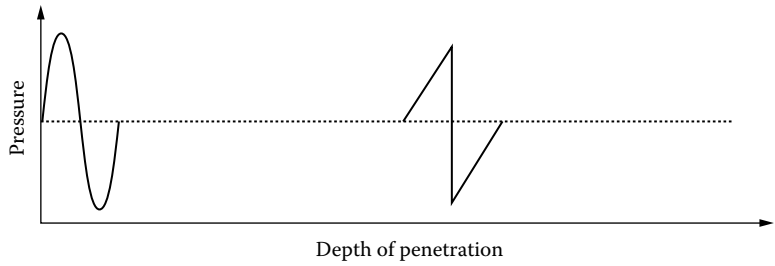

FIGURE 2.20 Wave distortion resulting from the nonlinear interaction between ultrasound and the medium.

The nonlinearity of ultrasonic wave propagation can cause the distortion of waveforms, as illustrated in Figure 2.20, which shows that a sinusoidal waveform becomes a sawtooth waveform as a result of the generation of higher harmonics after propagating in a medium. This is plausible in that the velocity in a denser region of the medium should be greater. The harmonic amplitudes relative to that at the fundamental or first harmonic frequency as a function of the normalized propagation distance z/z_1 are shown in Figure 2.21, where $z_1 = \rho c^2/[(1 + 0.5B/A)kp_0]$ (Pierce, 1986). Here, k is

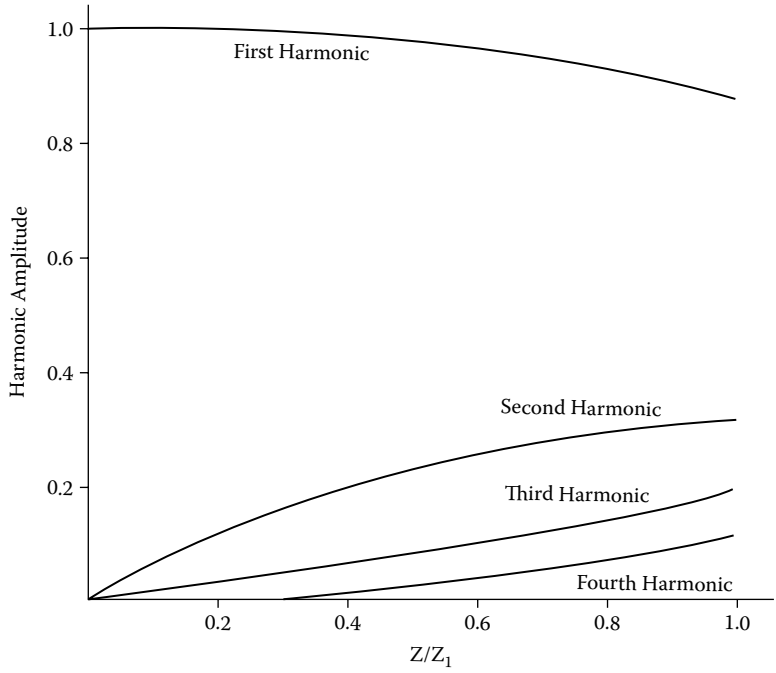

FIGURE 2.21 Harmonic amplitude as a function of the normalized depth of penetration as a plane acoustic wave propagates into a liquid medium.

the wave number and p_0 is the peak pressure. It is clear that the amplitude of the fundamental frequency drops and the amplitudes of higher harmonics increase as the propagation distance increases.

2.9 DOPPLER EFFECT

The Doppler effect describes a phenomenon in which a change in the frequency of sound emitted from a source is perceived by an observer when the source or the observer is moving or both are moving. The reason for the perceived frequency change for a moving source and a stationary observer is illustrated in Figure 2.22. In diagram (a), the sound source, S_p, is stationary and producing a uniform spherical spreading of the wave and the frequency of the sound perceived by an observer is $f = c/\lambda$, where c is the velocity of sound in the medium and λ is the wavelength shown as the distance between two crests in Figure 2.22(a).

In diagram (b), the sound source is moving to the right at a velocity v. The source motion changes the distance between the crests, increasing frequency and decreasing the wavelength to the right and decreasing the frequency and increasing the wavelength to the left. The frequency perceived by an observer on the right is

$$f' = \frac{c}{\lambda'} = \frac{c}{\lambda - vT} = \frac{c}{(c-v)T} = \frac{c}{c-v} f$$

and the frequency seen by an observer on the left is

$$f' = \frac{c}{c+v} f$$

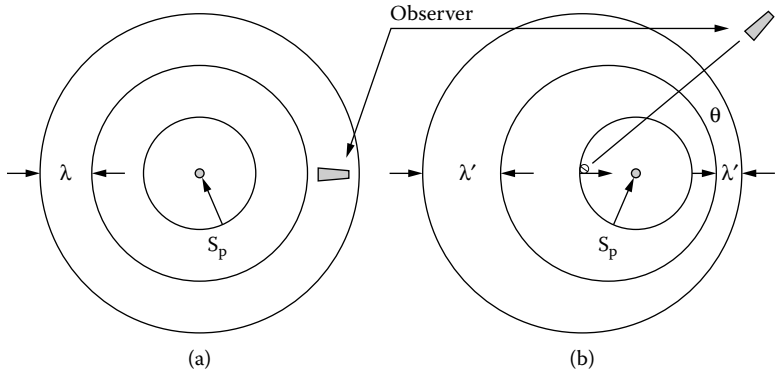

FIGURE 2.22 A stationary observer perceives a change in frequency of a wave emitted by a moving source toward the observer resulting from a change in wavelength. (a) The source is stationary. (b) The source is moving at a velocity v.

The difference between the actual frequency of the source, f, and the perceived frequency, f', is called the Doppler frequency, f_d. A similar relationship can also be obtained for a moving observer. When combining these relationships, for a source moving with a velocity v and an observer with velocity v', the Doppler frequency can be found to be given by:

$$f_d = f' - f = \left(\frac{c + v'}{c - v} - 1 \right) f \tag{2.41}$$

If the source and the observer are moving at the same velocity, v, assuming that $c >> v$, then Equation (2.41) can be reduced to:

$$f_d = \frac{2vf}{c} \tag{2.42}$$

For the situation in which the velocity is making an angle of θ relative to the direction of sound propagation, as shown in Figure 2.22(b), v in Equation (2.42) should be replaced by $v(\cos\theta)$:

$$f_d = \frac{2v(\cos\theta)f}{c} \tag{2.43}$$

The Doppler effect is used in ultrasonic Doppler devices for the measurement and imaging of blood flow transcutaneously, i.e., without penetrating the skin in any manner. In these devices, ultrasonic waves are launched into a blood vessel by an ultrasonic transducer and the scattered radiation from the moving red cells is detected by the same transducer or a separate transducer. Appropriate instrumentation is incorporated to extract the Doppler frequency, which is proportional to the red cell velocity.

REFERENCES

American Institute of Ultrasound in Medicine. *Safety Considerations for Diagnostic Ultrasound*. Laurel, MD: AIUM, 1984.

Dunn, F. and Goss, S.A. Definitions of terms and measurements of acoustical quantities. In Greenleaf, J.F., Ed. *Tissue Characterization with Ultrasound*, Boca Raton, FL: CRC Press, 1986, 1–14.

Fei, D.Y. and Shung, K.K. Ultrasonic backscatter from mammalian tissues. *J. Acoust. Soc. Am.* 1985, 78:871–877.

Fields, S. and Dunn, F. Correlation of echographic visualization of tissue with biological composition and physiological state. *J. Acoust. Soc. Am.* 1972, 54:809–811.

Geleskie, J.V. and Shung, K.K. Further studies on the acoustic impedance of major bovine blood vessel walls. *J. Acoust. Soc. Am.* 1982, 71:467–470.

Goss, S.A. and O'Brien, W.D., Jr. Direct ultrasonic velocity measurements of mammalian collagen treads. *J. Acoust. Soc. Am.* 1979, 65:507–511.

Greenleaf, J.A. *Tissue Characterization with Ultrasound*. Boca Raton, FL: CRC Press, 1986.
Hamilton, M.F. and Blackstock, D.T. *Nonlinear Acoustics*. San Diego: Academic Press, 1998.
Hete, B. and Shung, K.K. Scattering of ultrasound from skeletal muscle tissue. *IEEE Trans. Ultrasonics, Ferroelectrics, Frequency Control*. 1993, 40:354–365.
Kossoff, G. Rradiation force. In: Reid, J.M. and Sikov, M.R., Eds. *Interaction of Ultrasound and Biological Tissues*. Rockville, MD: FDA, 1972:159–161.
Malecki, I. *Physical Foundations of Technical Acoustics*. New York: Pergamon Press, 1969.
Morse, P.M. and Ingard, K.U. *Theoretical Acoustics*. New York: McGraw-Hill, 1968.
Nightingale, K.R., Nightingale, R.W., Palmeri, M.L., and Trahey, G.E. Finite element analysis of radiation force induced tissue motion with experimental validation. In Schneider, S.C., Levy, M., and McVoy, B.R., Eds. *Proc. 1999 IEEE Ultrasonics Symp*. New York: IEEE, 1999:1319–1323.
Pierce, A. *Acoustics: an Introduction to Physical Principles and Applications*. New York: McGraw-Hill, 1986.
Shung, K.K. and Thieme, G.A. *Ultrasonic Scattering by Biological Tissues*. Boca Raton, FL: CRC Press, 1993.
Tranquart, F., Grenier, N., Eder, V., and Pourcelot, L. Clinical use of ultrasound tissue harmonic imaging. *Ultrasound Med. Biol*. 1999, 25:889–894.
Twersky, V. Acoustic bulk parameters in distributions of pair-correlated scatterers. *J. Acoust. Soc. Am*. 1978, 64:1710–1719.
Westervelt, P.J. The theory of steady forces caused by sound waves. *J. Acoust. Soc. Am*. 1951, 23:312–315.
Wickline, S.A., Perez, J.E., and Miller, J.G. Cardiovascular tissue characterization *in vivo*. In Shung, K.K. and Thieme, G.A., Eds. *Ultrasonic Scattering in Biological Tissues*. Boca Raton, FL: CRC Press, 1993, 313–345.
Yuan, Y.W. and Shung, K.K. Ultrasonic backscatter from flowing whole blood. I. Dependence on shear rate and hematocrit. *J. Acoust. Soc. Am*. 1988, 84:52–58.

3 Ultrasonic Transducers and Arrays

All ultrasonic imaging systems require a device called an ultrasonic transducer to convert electrical energy into ultrasonic or acoustic energy and vice versa. Ultrasonic transducers come in a variety of forms and sizes ranging from single-element transducers for mechanical scanning and linear arrays, to multidimensional arrays for electronic scanning. Although performance of an ultrasonic scanner is critically dependent upon transducers/arrays, array/transducer performance has been one of the bottlenecks that prevent current ultrasonic imagers from reaching their theoretical resolution limit.

The primary reason for this is that medical ultrasonic array/transducer design and fabrication are processes of a broad interdisciplinary nature. They require knowledge from a variety of disciplines, such as acoustics and vibration, electrical engineering, material sciences and engineering, medical imaging, and anatomy and physiology. It is little wonder that, to date, the design of transducers is still mostly empirical, generally involving a trial-and-error approach. Many manufacturers regard their expertise in designing and manufacturing transducers as a trade secret of the highest order. The most critical component of an ultrasonic transducer is a piezoelectric element.

3.1 PIEZOELECTRIC EFFECT

The piezoelectric (pressure-electric) effect is a phenomenon in which a material, upon the application of an electrical field, changes its physical dimensions and vice versa (Cady, 1964; Kino, 1987). The piezoelectric effect was discovered by French physicists Pierre and Jacques Curie in 1880. The direct and reverse piezoelectric effects are illustrated in Figure 3.1(a) and (b), respectively. The direct effect refers to the phenomenon in which the application of a stress causes a net charge to appear across the electrodes and the inverse effect concerns the production of a strain upon the application of a potential difference across the electrodes. Certain naturally occurring crystals such as quartz and tourmaline are piezoelectric.

The physical reason that the piezoelectric phenomenon occurs can be idealistically explained by considering that a piezoelectric material consists of innumerable electric dipoles. When undisturbed, these dipoles are randomly distributed, resulting in a neutral state or no net charge. An electrical potential difference applied across a slab of piezoelectric material realigns the dipoles in the material in a preferential direction and results in a deformation or a change in the thickness of the slab. Conversely, a stress that causes a deformation of the material and reorientation of the dipoles induces a net charge across the electrodes.

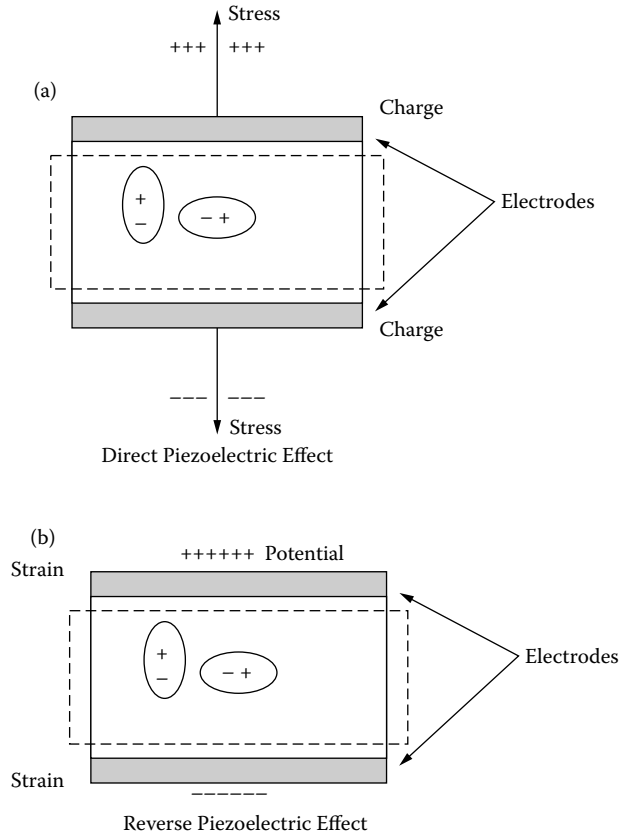

FIGURE 3.1 (a) Direct piezoelectric effect in which a stress induces a charge separation. (b) Reverse piezoelectric effect in which a potential difference across the electrodes induces a strain.

Naturally occurring piezoelectric crystals are seldom used today as transducer materials in diagnostic ultrasonic imaging because of their weak piezoelectric properties. The most popular material is a polycrystalline ferroelectric ceramic material, lead zirconate titanate, $Pb(Zr, Ti)O_3$ or PZT, which possesses very strong piezoelectric properties following polarization. Polarization of a ferroelectric material is carried out by heating it to a temperature just above the Curie temperature of the material and then allowing it to cool slowly in the presence of a strong electric field; this is typically in the order of 20 kV/cm applied in the direction in which the piezoelectric effect is required. The electrical field is usually applied to the material by means of two electrodes. This process aligns the dipoles along the direction of polarization.

A great variety of ferroelectric materials exists. Barium titanate ($BaTiO_3$) was among the first developed. Lead metaniobate ($PbNb_2O_6$) and lithium niobate ($LiNbO_3$) have also been used. Certain piezoelectric properties of PZT can be enhanced by doping. As a result, many types of PZT are commercially available. In order to define

and better understand the physical meaning of the piezoelectric properties of a material, the constitutive equations that govern the piezoelectric effect must be examined.

3.2 PIEZOELECTRIC CONSTITUTIVE EQUATION

Because the piezoelectric effect involves the interaction between electric fields and the mechanical deformation, the constitutive equations relate the electric properties to mechanical properties of the material.

With no electric field, the stress and the strain relationship described in Chapter 2 is given by Equation (2.3), Equation (2.4), and Equation (2.5). Because most materials are anisotropic, written in tensor form, the stress-strain relationship is given by

$$[\boldsymbol{\kappa}] = [\mathbf{C}]\,[\boldsymbol{\varepsilon}] \tag{3.1}$$

where $[\boldsymbol{\kappa}]$, $[\mathbf{C}]$, and $[\boldsymbol{\varepsilon}]$ are the stress, the elastic constant, and the strain tensor, respectively.

Upon the application of an electric field, Equation (3.1) needs to be modified to include the effect of the electric field. Taking the electric field $[\mathbf{E}]$ and the strain $[\boldsymbol{\varepsilon}]$ as independent variables and the electric displacement $[\mathbf{D}]$ and stress $[\boldsymbol{\kappa}]$ as dependent variables, the piezoelectric constitutive equations are given by

$$[\boldsymbol{\kappa}] = [\mathbf{C}^{\mathbf{E}}][\boldsymbol{\varepsilon}] - [\mathbf{e}][\mathbf{E}] \tag{3.2}$$

$$[\mathbf{D}] = [\mathbf{K}^{\boldsymbol{\varepsilon}}][\mathbf{E}] + [\mathbf{e}][\boldsymbol{\varepsilon}] \tag{3.3}$$

where $[\mathbf{e}]$, $[\mathbf{C}^{\mathbf{E}}]$, and $[\mathbf{K}^{\boldsymbol{\varepsilon}}]$ are the piezoelectric stress constant tensor, elastic constant tensor when the electric field $[\mathbf{E}] = 0$, and dielectric constant tensor when strain $[\boldsymbol{\varepsilon}] = 0$ or clamped dielectric constant tensor, respectively. The physical meaning of $[\mathbf{C}^{\mathbf{E}}]$ and $[\mathbf{K}^{\boldsymbol{\varepsilon}}]$ can be readily understood by setting $\mathbf{E}$ and $[\boldsymbol{\varepsilon}] = 0$, respectively, in Equation (3.2) and Equation (3.3). Letting $[\boldsymbol{\varepsilon}] = 0$ in Equation (3.2),

$$[\mathbf{e}] = -[\boldsymbol{\kappa}]/[\mathbf{E}] \tag{3.4}$$

where $[\mathbf{e}]$, the piezoelectric stress constant, is the resultant stress change per unit change in electric field without strain or while being clamped. It has the unit of newtons per volt-meter or coulombs per square meter.

The constitutive equation can be written in another form when $[\boldsymbol{\kappa}]$ and $[\mathbf{E}]$ are treated as independent variables:

$$[\boldsymbol{\varepsilon}] = [\mathbf{d}][\mathbf{E}] + [\boldsymbol{\gamma}^{\mathbf{E}}][\boldsymbol{\kappa}] \tag{3.5}$$

$$[\mathbf{D}] = [\mathbf{K}^{\boldsymbol{\kappa}}][\mathbf{E}] + [\mathbf{d}][\boldsymbol{\kappa}] \tag{3.6}$$

where $[\mathbf{K}^{\boldsymbol{\kappa}}]$ is the free dielectric constant, which is the dielectric constant when no stress is present and $[\mathbf{d}] = [\boldsymbol{\varepsilon}]/[\mathbf{E}]$ is transmission or piezoelectric strain constant representing the resulting change in strain per unit change in electric field with a

unit of coulombs per newton when no stress is present. $[\boldsymbol{\gamma}^{\mathbf{E}}] = [\boldsymbol{\varepsilon}]/[\boldsymbol{\kappa}]$ from Equation (3.5) is the compliance of the material for $[\mathbf{E}] = 0$ and $[\boldsymbol{\gamma}^{\mathbf{E}}] = 1/[\mathbf{C}^{\mathbf{E}}]$. The relationship between $[\mathbf{e}]$ and $[\mathbf{d}]$ can be found from Equation (3.2) by setting $[\boldsymbol{\kappa}] = 0$,

$$[\mathbf{C}^{\mathbf{E}}]\,[\boldsymbol{\varepsilon}] - [\mathbf{e}][\mathbf{E}] = 0$$

Therefore,

$$[\mathbf{e}] = [\mathbf{C}^{\mathbf{E}}]\,[\boldsymbol{\varepsilon}]/[\mathbf{E}] = [\mathbf{C}^{\mathbf{E}}]\,[\mathbf{d}].$$

If $[\mathbf{D}]$ and $[\boldsymbol{\kappa}]$ are treated as the independent variables, the constitutive equations are given by

$$[\mathbf{E}] = [\boldsymbol{\alpha}^{\boldsymbol{\kappa}}][\mathbf{D}] - [\mathbf{g}][\boldsymbol{\kappa}] \tag{3.7}$$

$$[\boldsymbol{\varepsilon}] = [\mathbf{g}][\mathbf{D}] + [\boldsymbol{\gamma}^{\mathbf{D}}][\boldsymbol{\kappa}] \tag{3.8}$$

where $[\mathbf{g}] = -[\mathbf{E}]/[\boldsymbol{\kappa}]$ is the receiving constant with a unit of volt-meter per newton representing the change in electric field per unit change in applied stress when $[\mathbf{D}] = 0$, that is, no current or under open circuit conditions. $[\boldsymbol{\gamma}^{\mathbf{D}}]$ is the compliance when $[\mathbf{D}] = 0$ and $[\boldsymbol{\alpha}^{\boldsymbol{\kappa}}] = 1/[\mathbf{K}^{\boldsymbol{\kappa}}]$ when $[\boldsymbol{\kappa}] = 0$.

The dielectric constant $[\mathbf{K}]$ of a piezoelectric material depends on the extent of freedom of the material. Two values are often quoted in the literature. If the material is clamped so that it cannot move in response to an applied field or the strain is zero, the dielectric constant measured is designated as the clamped dielectric constant $[\mathbf{K}^{\mathbf{e}}]$. If the material is free to move without restriction, the dielectric constant measured is denoted as $[\mathbf{K}^{\boldsymbol{\kappa}}]$, the free dielectric constant. The transmitting constant and the receiving constant are related by the following relationship (Kino, 1987):

$$[\mathbf{d}] = [\mathbf{g}]\,[\mathbf{K}^{\boldsymbol{\kappa}}] \tag{3.9}$$

As was mentioned, these equations are in tensor form because most piezoelectric materials or crystals are anisotropic. To describe the piezoelectric properties of a material completely, 18 piezoelectric stress constants and 18 receiving constants are required. Fortunately, because these materials usually are symmetric, a smaller number of constants are actually needed. For instance, quartz has only five constants. Depending on the symmetry of the crystal, the principal axis is defined as the direction in which a stress produces a charge polarization parallel to the strain (Cady, 1964). A plate cut with its surface perpendicular to the x-axis is called an x-cut, and so forth. The x-, y-, and z-directions are indicated by numbers 1, 2, and 3, respectively, For polarized ceramics, the 3-direction is usually used to denote the polarization direction.

A piezoelectric strain constant, d_{33}, represents the strain produced in the 3-direction by applying an electric field in the 3-direction; d_{13} is the strain in the 1-direction produced by an electric field in the 3-direction when no external stress is present. Here it is important to note that the piezoelectric properties of a material depend upon boundary conditions and therefore upon the shape of the

TABLE 3.1
Properties of Important Piezoelectric Materials

Property	PVDF	Quartz (*x*-cut)	PZT-5H	Lead Niobate
d_{33} (10^{-12} c/n)	15	2.31	583	100
g_{33} (10^{-2} v-m/n)	14	5.78	1.91	4.3
k_t	0.11	0.14	0.55	0.34
K^{κ} (10^{-11} F/m)	9.7	3.98	3010	3054
c (m/sec)	2070	5740	3970	3100
ρ (kg/m^3)	1760	2650	7450	5900
Curie temp (°C)	100	573	190	500

Note: ρ and c denote density and sound speed, respectively.

material. For example, the piezoelectric constant of a material in the plate form is different from that in the rod form.

The ability of a material to convert one form of energy into another is measured by its electromechanical coupling coefficient, defined as stored mechanical energy/total stored energy. The total stored energy includes mechanical and electrical energy. It should be noted that this quantity is not the efficiency of the transducer. If the transducer is lossless, its efficiency is 100%. However, the electromechanical coupling coefficient is not necessarily 100% because although some of the energy is stored as mechanical energy, the rest may be stored dielectrically in the form of electrical potential energy. Because only the stored mechanical energy is useful, the electromechanical coupling coefficient is a measure of the performance of a material as a transducer. The piezoelectric constants for a few important piezoelectric materials are listed in Table 3.1.

A few important material geometries are frequently used in ultrasonic imaging. These are shown in Figure 3.2, using the effect of geometry on electromechanical coupling coefficient as an example. For a disc of PZT-5H with the diameter much larger than the thickness (Figure 3.2c), the thickness mode electromechanical coupling coefficient, k_t, is used. For a long, tall element with the sides of the square cross-section much smaller than the thickness (Figure 3.2a) and a tall element with rectangular cross-section (Figure 3.2b), the electromechanical coupling coefficients are denoted respectively as k_{33} and k_{33}'. The geometry shown in Figure 3.2(b) is the most important because it is often used in linear arrays. It is interesting to note that the electromechanical coupling coefficient is highest in the bar mode shown in (Figure 3.2a) because more energy is irradiated in the long axis direction because the bar is surrounded by air, which has a much lower acoustic impedance than PZT. The effect of material shape on other measured piezoelectric properties can be found in Table 3.2.

In addition to PZT, piezoelectric polymers have been found to be useful in a number of applications (Brown, 1992). One of these polymers is polyvinylidence difluoride (PVDF), which is semicrystalline. After processes like polymerization, stretching, and poling, a thin sheet of PVDF with a thickness in the order of 6 to 50 μm can be used as a transducer material. The advantages of this material are that

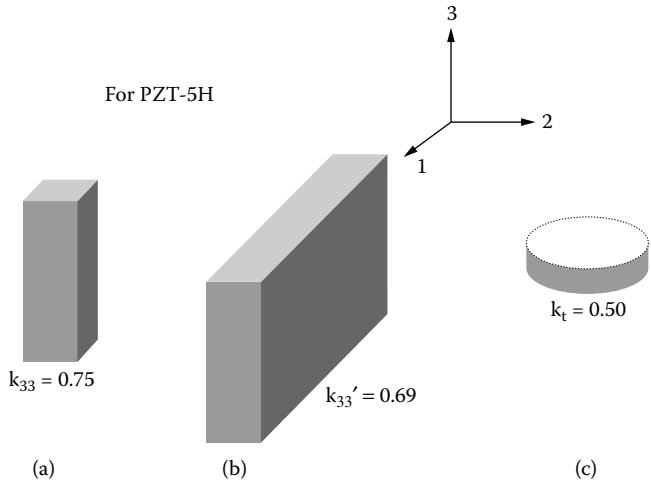

FIGURE 3.2 The geometry of a piezoelectric material influences its piezoelectric properties. This is illustrated by way of the electrical mechanical coupling coefficient: (a) a tall element of square cross-section frequently seen in composite materials; (b) a tall element frequently seen in linear arrays; (c) a circular disc frequently seen in single-element transducers.

it is wideband, flexible, and inexpensive. The disadvantages are that it has a very low transmitting constant, its dielectric loss is large, and the dielectric constant is low. Although PVDF is not an ideal transmitting material, it does possess a fairly high receiving constant. Miniature PVDF hydrophones are commercially available. P(VDF–TrFE) copolymers have been shown to have a higher electromechanical coupling coefficient.

One of the most promising frontiers in transducer technology is the development of piezoelectric composite materials (Smith, 1989). Innovation in fabrication technology has allowed the preparation of PZT polymer 1–3 composites for applications in the 1- to 7.5-MHz range. These 1–3 composites consist of small PZT rods embedded in a low-density polymer and are illustrated in Figure 3.3(a). In this figure, the dark and light regions indicate the piezoelectric ceramic phase and the polymer

TABLE 3.2
Material Properties of PZT-5H of Different Geometry

Property	Bar Mode	Plate Mode	Element Mode
Velocity (m/s)	3850	4580	4000
Acoustic impedance (Mrayl)	28.9	34.3	30.0
Electromechanical coupling coefficient	0.75	0.51	0.73

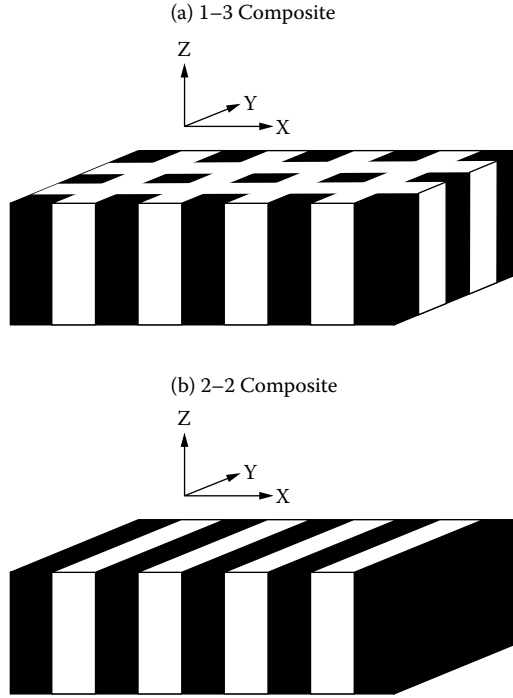

FIGURE 3.3 Two different configurations of piezoceramic composites: (a) 1–3 composite; (b) 2–2 composite.

phase, respectively. These composites have been used for low-frequency underwater applications for many years.

The notation 1–3, 2–2, etc. was coined by Newnham et al. (1978). A notation of 1–3 means that one phase of the composite is connected only in one direction whereas the second phase is connected in all three directions. A notation of 2–2 means that both phases are connected in two directions as illustrated in Figure 3.3(b). These composites, typically in volume concentration of 20 to 70% PZT, have a lower acoustic impedance (4 to 25 Mrayls) than conventional PZT (34 Mrayls), which better matches the acoustic impedance of human skin. The composite material can be made flexible with a free dielectric constant, K^{κ}, from $44 \cdot 10^{-11}$ to $2213 \cdot 10^{-11}$ F/m and with a k_t higher than that of PZT. The higher coupling coefficient and better impedance matching can lead to higher transducer sensitivity and improved image resolution. An electron micrograph of a 2–2 composite is shown in Figure 3.4 with 28 μm PZT–5H piezoelectric ceramics and 5-μm polymer filler.

One of the problems associated with composite materials is the higher fabrication cost. Typical procedures involve first dicing PZT and subsequently filling the gaps with a polymer and injection molding. The performances of composite annular and linear arrays with frequencies from 3 to 7.5 MHz have been found to be superior to similar PZT devices. A substantial number of commercial high-performance arrays are made from composites.

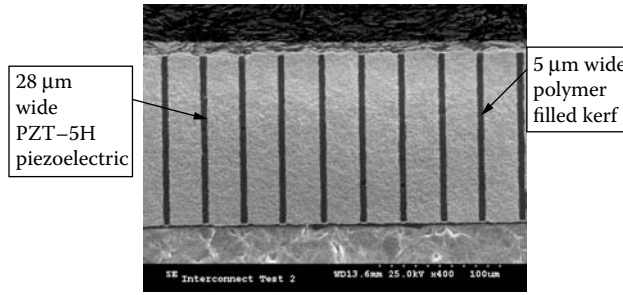

FIGURE 3.4 An electron micrograph of a 2–2 composite consisting of PZT 5H piezoceramics separated by polymer.

Conventional PZT has grain size on the order of 3 to 5 µm, which is not particularly suited for high-frequency applications. Fine-grain PZT and single-crystal ferroelectric materials like $Pb(Zn_{1/3}Nb_{2/3})O_3$–$PbTiO_3$ (PZN–PT) and $Pb(Mg_{1/3}Nb_{2/3})O_3$–$PbTiO_3$ (PMN–PT), which have been shown to have a higher dielectric constant and electromechanical coupling coefficient than conventional PZT, are potentially promising piezoelectric materials for high-frequency applications (Shrout et al., 1990; Zipparo et al., 1997).

3.3 ULTRASONIC TRANSDUCERS

The simplest ultrasonic transducer is a single-element piston transducer as shown in Figure 3.5; Figure 3.5(a) and Figure 3.5(b) show a photo and the internal construction of a single-element ultrasonic transducer, respectively. The most important component of such a device is the piezoelectric element. A number of factors are involved in choosing a proper piezoelectric material for transmitting and/or receiving the ultrasonic wave. They include stability, piezoelectric properties, and the strength of the material. The surfaces of the element are electroded with fired-on silver or sputtered chrome–gold. The outside electrode is usually grounded to protect patients from electrical shock. The housing is metallic or plastic. An acoustic isolating material is placed between the piezoelectric element and the housing to prevent ringing of the housing that follows the vibration of the piezoelectric element.

By considering the two surfaces of the piezoelectric element as two independent vibrators (as illustrated in Figure 3.6), one can easily see that the resonant frequencies for such a transducer are given by

$$f_o = \frac{nc_p}{2L} \tag{3.10}$$

with the lowest resonant frequency being $n = 1$,

where

c_p is the acoustic wave velocity in the transducer material
L is the thickness of the piezoelectric material
n is an odd integer

(a)

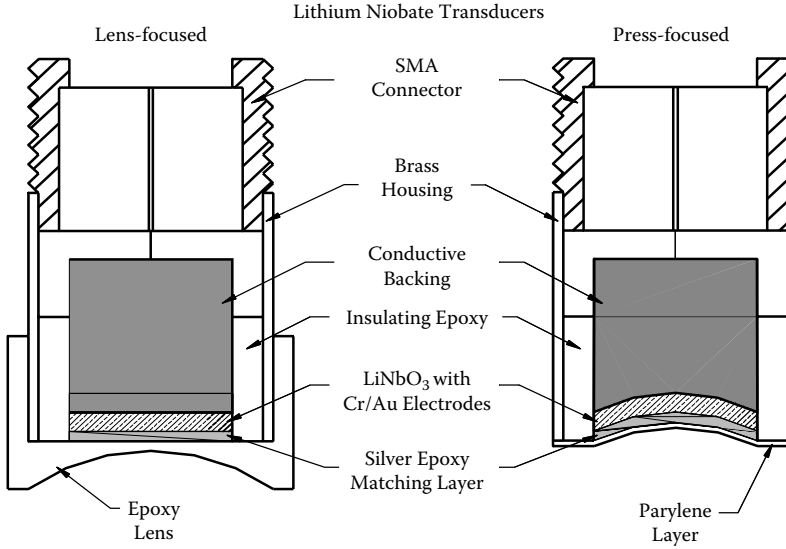

(b)

FIGURE 3.5 (a) Photo and (b) detailed construction of two single-element ultrasonic transducers with one or two matching layers and the backing material. The transducer on the left has a lens, whereas the one on the right is self-focused.

In other words, resonance occurs when L is equal to odd multiples of one-half wavelength or

$$L = n\frac{\lambda_p}{2} \tag{3.11}$$

where λ_p is the wavelength in the piezoelectric material.

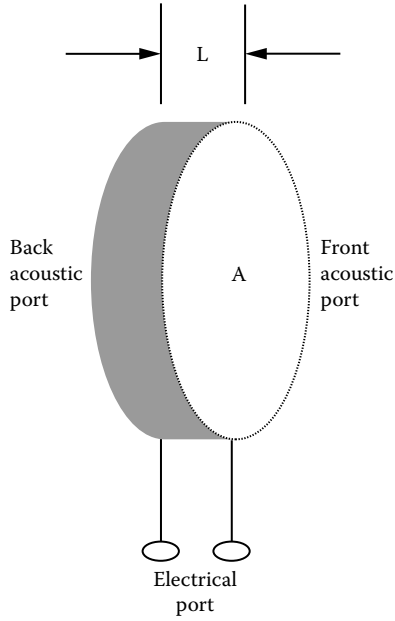

FIGURE 3.6 A piezoceramic disc can be treated as a electromechanical device with two acoustic ports representing the front and rear interfaces between the ceramic and the surrounding media and an electrical port.

The transducer can be treated as a three-port network as shown in Figure 3.6: two mechanical ports represent the front and back surfaces of the piezoelectric crystal and one electrical port represents the electrical connection of the piezoelectric material to the electrical generator (Kino, 1987). Various sophisticated one-dimensional circuit models exist to model the behavior of the transducer. The best known are the Mason model, the Redwood model, and the KLM model (Krimholtz, Leadom, and Mettaei, 1970) Commercial software based on these models is available.

The Mason model can be derived by considering the three-port configuration shown in Figure 3.7 for a circular disc with area, A, and thickness, L, where I, V, F, and u denote current, voltage, force, and medium velocity, respectively.

Using the transmission line theory, the constitutive equations relating mechanical properties to electrical properties, and boundary conditions that u and F must be continuous across interfaces, the following simultaneous equations can be obtained:

$$\begin{bmatrix} F_1 \\ F_2 \\ V_3 \end{bmatrix} = -j \begin{bmatrix} Z_c \cot k_p L & Z_c \operatorname{cosec} k_p L & \dfrac{e}{\omega K^{\varepsilon}} \\ Z_c \operatorname{cosec} k_p L & Z_c \cot k_p L & \dfrac{e}{\omega K^{\varepsilon}} \\ \dfrac{e}{\omega K^{\varepsilon}} & \dfrac{e}{\omega K^{\varepsilon}} & \dfrac{1}{\omega C_0} \end{bmatrix} \begin{bmatrix} u_1 \\ u_2 \\ I_3 \end{bmatrix} \tag{3.12}$$

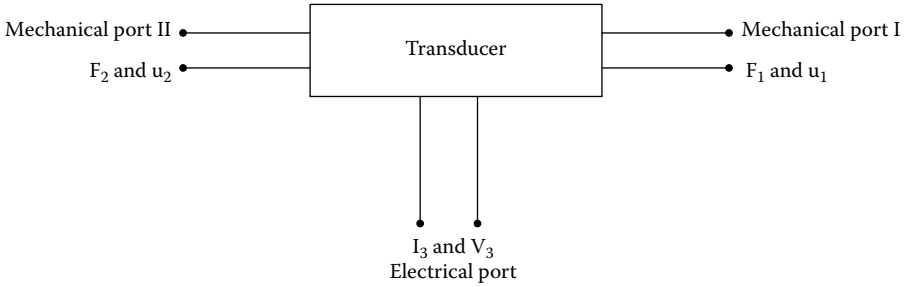

FIGURE 3.7 A system model for a single-element transducer.

where $Z_c = Z_0 A$ is the radiation impedance and Z_0 is the acoustic impedance of the piezoelectric element, e, the piezoelectric stress constant, k_p, the wave number in the piezoelectric material, and $C_0 = K^{\varepsilon}(A/L)$, the clamped capacitance. These simultaneous equations can be represented by an electrical equivalent network, shown in Figure 3.8, where $Z_{11} = -jZ_c\cot(k_pL)$, $Z_{12} = -jZ_c\mathrm{cosec}(k_pL)$, $Z_{11} - Z_{12} = jZ_c\tan(k_pL/2)$, and $n = e(A/L)$.

Assuming that the loading media have acoustic impedances Z_1, and Z_2 at ports I and II, respectively, the input electrical impedance, Z_3, of the transducer at the electrical port can be readily calculated using this equivalent network.

$$Z_3 = \frac{V_3}{I_3} = \frac{1}{j\omega C_0}\left\{1 + k_t^2 \frac{j(Z_1 + Z_2)Z_c \sin k_p L - 2Z_c^2(1 - \cos k_p L)}{\left[\left(Z_c^2 + Z_1 Z_2\right)\sin k_p L - j(Z_1 + Z_2)Z_c \cos k_p L\right] k_p L}\right\} \tag{3.13}$$

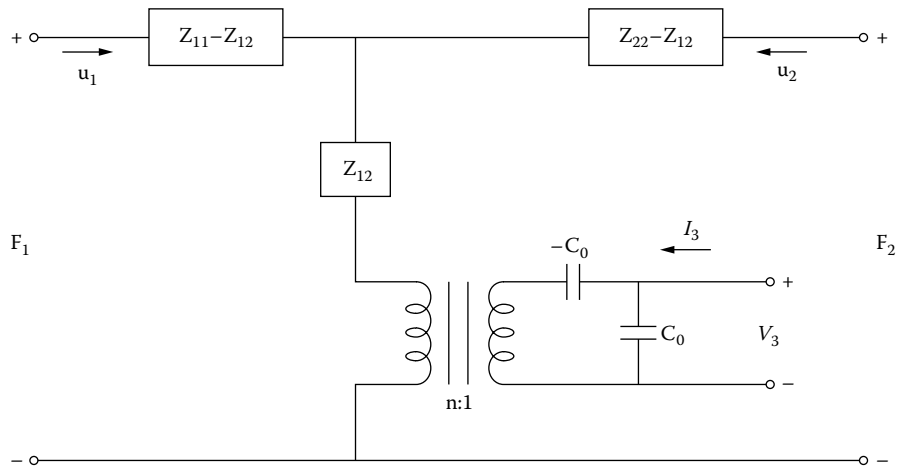

FIGURE 3.8 The Mason model or equivalent circuit for a single-element transducer.

The special case where Z_1 and $Z_2 = 0$ means a disc loaded by air on both sides. Z_3 becomes

$$Z_3 = \frac{1}{j\omega C_0} + Z_a \tag{3.14}$$

where Z_a is given by

$$Z_a = -\frac{k_t^2}{j\omega C_0}\frac{\tan(k_p L/2)}{k_p L/2} \tag{3.15}$$

Equation (3.14) can be represented by an equivalent network consisting of an impedance, Z_a, in series with a capacitor, C_0. It can be shown easily that $Z_a \rightarrow -k_t^2/(j\omega C_0)$ when $\omega \rightarrow 0$. Therefore, at low frequencies, a circular disc resonating in air basically behaves like a free capacitor, $C_0^{\kappa} = Z_a + C_0 = K^{\kappa}(A/L)$. As $\omega \rightarrow \infty$, Equation (3.14) yields that $Z_3 \rightarrow 1/(j\omega C_0)$. It behaves like a clamped capacitor, $C_0 = K^{\varepsilon}(A/L)$. This phenomenon has been used as a method for measuring K^{ε} and K^{κ} of a piezoelectric material.

A more careful examination of Equation (3.13) would show that the input impedance has a minimum and maximum as a function of frequency for a transducer irradiating into a medium with acoustic impedance, Z_1, with a backing medium of acoustic impedance, Z_2. These frequencies are called the series and parallel resonant frequencies, respectively. At these frequencies, the transducer can be represented by two-port networks consisting of a capacitor and a resistor. At series resonance, or simply resonance, $\omega = \omega_r$, Z_3 is minimal, and the phase angle changes from –90 to 90°. At parallel or antiresonance, $\omega = \omega_a$, Z_3 is maximal and the phase angle changes from 90 to –90°. These two networks are shown in Figure 3.9(a) and (b), where R_a and R_r are the radiation resistances at parallel and series resonance, respectively, and are given by

$$R_a = \frac{4k_t^2 Z_c}{\omega_a C_0(Z_1 + Z_2)} \tag{3.16}$$

$$R_r = \frac{\pi(Z_1 + Z_2)}{4k_t^2 \omega_r C_0 Z_c} \tag{3.17}$$

A plot of the magnitude and phase of a circular disc resonating in air as a function of frequency is shown in Figure 3.9(c), where the resonance and antiresonance frequencies and the change in phase near these frequencies are clearly seen.

A more popular one-dimensional transducer mode is the KLM model shown in Figure 3.10. This model divides a piezoelectric element into two halves, each represented by a transmission line. It is more physically intuitive. The effects of matching layers and backing material can be readily included.

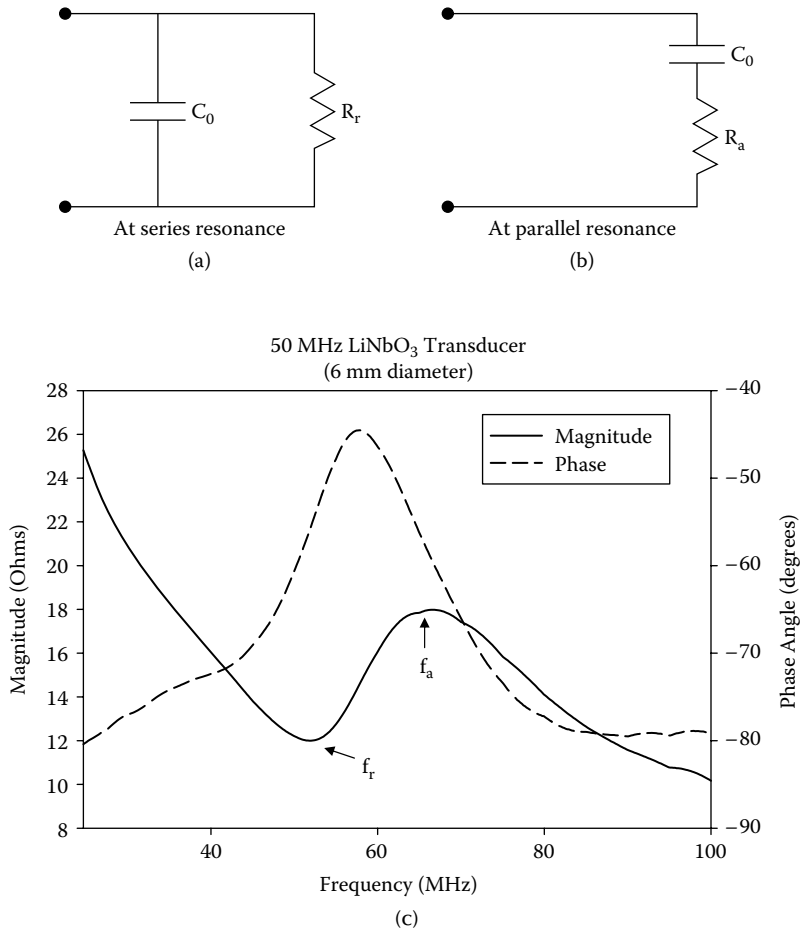

FIGURE 3.9 Equivalent electrical network for a single-element transducer near resonance (a) at series resonance and (b) at parallel resonance. (c) The magnitude and phase of a circular disc resonating in air as a function of frequency; this shows the magnitude and phase of the input electrical impedance of a circular piston transducer irradiating into air and backed by air.

A typical response for a PZT 5A single-element transducer of 1-cm diameter, 5.5-MHz resonant frequency, loaded by water and air-backed that is obtained with the KLM model is given in Figure 3.11. The pulse–echo waveform and the echo spectrum are shown. The vertical scale is the ratio of output voltage/input voltage in millivolts per volt. A Q-factor can be defined for the transducer as

$$Q = f_o/(f_2 - f_1) \tag{3.18}$$

where f_o is the resonant frequency and f_2 and f_1 are the frequencies at which the amplitude drops to –3 or –6 dB relative to the maximum. The difference, $f_2 - f_1$, is referred to as the bandwidth of the transducer.

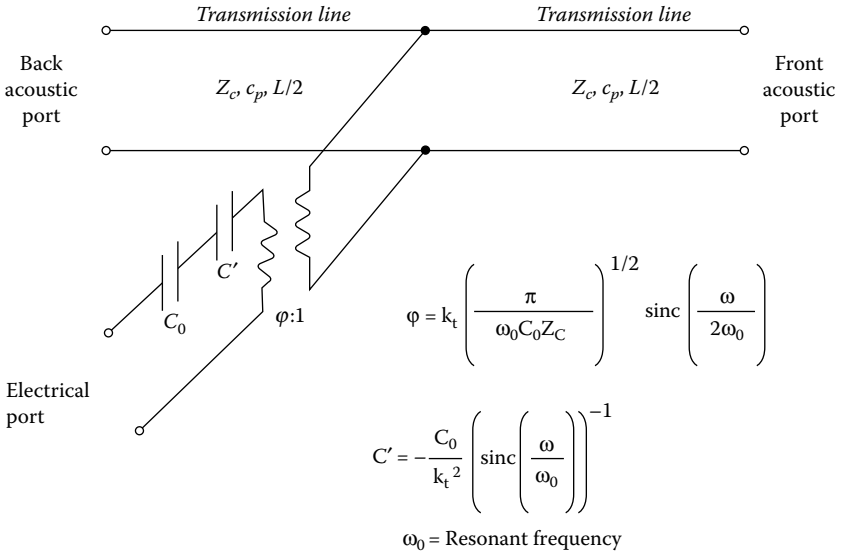

FIGURE 3.10 The KLM model for a single-element transducer.

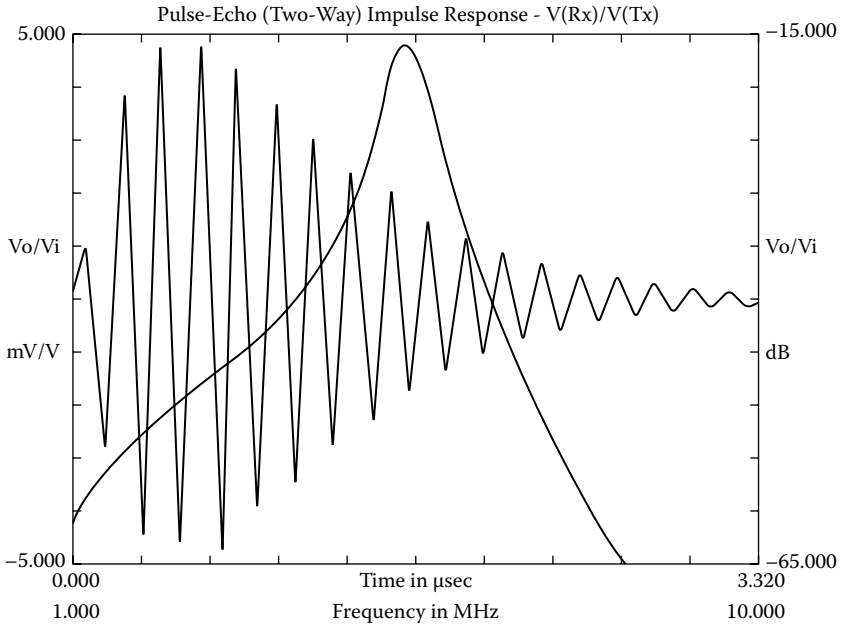

FIGURE 3.11 The pulse–echo waveform and its spectrum of a single-element transducer with no matching and backing obtained by the KLM model.

Two Q-factors, electrical Q and mechanical Q, have been used to describe ultrasonic transducers because, after all, they are electromechanical devices. In applications in which maximal output is needed and bandwidth requirement is not crucial, as in a continuous-wave ultrasonic Doppler flow meter, the Q of the transducer should be large; however, in pulse–echo imaging devices, the Q should be small, on the order of 1 to 2. Electrical matching, which optimizes electrical Q, or mechanical matching, which optimizes mechanical Q, can be used to adjust the Q or bandwidth of a transducer.

3.4 MECHANICAL MATCHING

When a transducer is excited by an electrical source, it rings at its natural resonant frequency. For continuous-wave application, the transducers are air backed, allowing as much energy irradiated into the forward direction as possible. Due to the mismatch in acoustic impedance between the air and the piezoelectric material, acoustic energy at this interface is reflected into the forward direction. Thus, very little energy is lost out of the back port. The drawback is that this mismatch, which produces the so-called ringing effect for pulse–echo applications, is very undesirable because it lengthens the pulse duration. As will be discussed later, the pulse duration affects the capability of an imaging system for resolving small objects.

Absorptive backing materials with an acoustic impedance similar to that of the piezoelectric material can be used to damp out the ringing or to increase bandwidth. The backing material should not only absorb part of the energy from the vibration of the back face but also minimize the mismatch in acoustic impedance. It absorbs as much as possible of the energy that enters it. It must be noted that suppression of ringing or shortening of pulse duration is achieved by sacrificing sensitivity because a large portion of the energy is absorbed by the backing material. Various types of backing materials, including tungsten-loaded epoxy and silver-loaded epoxy, have been used with good success. Several backing materials are listed in Table 3.3.

The performance of a transducer can also be improved by using acoustic matching layers in the front. It can be easily shown that, for a monochromatic plane wave, 100% transmission occurs for a layer of material of $\lambda_m/4$ thickness and acoustic impedance Z_m, where λ_m is the wavelength in the matching layer material (Kinsler et al., 1982) and

$$Z_m = (Z_p Z_l)^{1/2} \tag{3.19}$$

In Equation (3.19), Z_p and Z_l are the acoustic impedances of the piezoelectric element and the loading medium, respectively. For wideband transducers, however, Desilets et al. (1978) showed that, for a single matching layer, Equation (3.19) should be modified to

$$Z_m = \left(Z_p Z_l^2\right)^{1/3} \tag{3.20}$$

TABLE 3.3
Acoustic Properties of Transducer Materials

Matching Layers	Acoustic Impedance (MRayl)	Sound Velocity (mm/ms)	Ref.
Ceramic-loaded epoxy	2.8 to 11.3	1.5 to 3.9	Selfridge 1985
Glass	10.1 to 16.0	4.5 to 5.66	Selfridge 1985
Parylene	2.83 (Parylene C)	2.20	Thiagarajan 1991
Si/RTV composite	Tapered from 1.5 to 12 through thickness (experimental)	1.0 to 8.0 (theoretical)	Sayers 1984
Backing Material			
Tungsten-loaded epoxy	6 to 36	1.5 to 3.5	Kino 1987
Brass (70% Cu, 30% Zn)	40.6	4.70	Selfridge 1985
Carbon, pyrolytic	7.31	3.31	Selfridge 1985
Air	0.00043	0.334	Selfridge 1985
Lens Material			
RTV rubber	0.99 to 1.46	0.96 to 1.16	Selfridge 1985
Polyurethane	1.38 to 2.36	1.33 to 2.09	Selfridge 1985
Silicone rubber (Sylgard)	1.03	1.05	Kino 1987
Composite Fillers			
RTV	0.99 to 1.46	0.96 to 1.16	Kino 1987
Epoxy	2.8 to 6.0	2.7	Gururaja 1985
Polyurethane (Tetrad)	1.26	2.43	Gururaja1985
Polyurethane (MSI solid 80)	1.14	2.27	Gururaja1985
Polymer/microballoon	0.5	2.02	Shung 1996

For two matching layers, the acoustic impedances of the two layers should be, respectively,

$$Z_{m1} = \left(Z_p^4 Z_l^3\right)^{1/3} \tag{3.21}$$

$$Z_{m2} = \left(Z_p Z_l^6\right)^{1/7} \tag{3.22}$$

State-of-the-art transducers and arrays that use composites can achieve a bandwidth better than 70%, merely with front matching and light backing, without losing much sensitivity. The reason for this is that optimal matching allows energy to be transmitted into the forward direction and reduces ringing resulting from reverberation of pulses, thus widening the bandwidth. Some of the materials that have been used for matching layers and filler materials in composites are tabulated in Table 3.3.

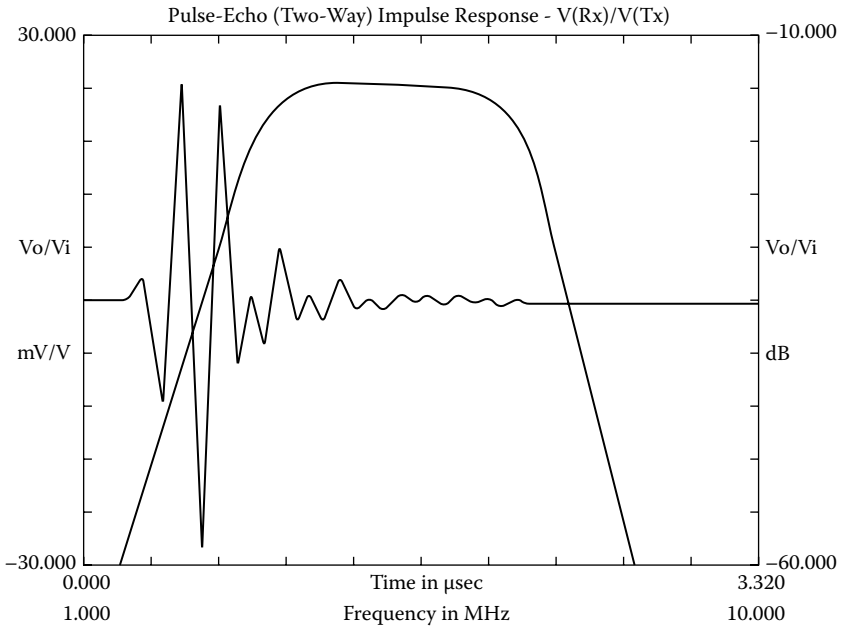

FIGURE 3.12 The performance of the transducer is improved by matching and backing.

3.5 ELECTRICAL MATCHING

Maximizing energy transmission and/or bandwidth can also be achieved by matching the electrical characteristics of the transducer to the electrical source and amplifier. Circuit components may be placed between the transducer and external electrical devices (Desilets et al., 1978; Goldberg and Smith, 1994). Consider the equivalent circuit for a transducer at series resonance shown in Figure 3.9(a). For maximal power transmission, the transducer input impedance should be real and the input resistance should match that of the source. To tune out the clamped capacitance, a shunt inductor of the value, $1/(\omega_r^2 C_0)$, may be used. A shunt inductor of the value, $1/(\omega_a^2\, C_0) + R_a^2\, C_0$, can be used for the circuit at parallel resonance shown in Figure 3.9(b). A transformer may be used to match the resistance.

The substantial improvement in transducer performance by including acoustic matching, backing, and electrical tuning in the design of a 5.1-MHz PZT-5A transducer is demonstrated in Figure 3.12; a 72% bandwidth and much improved sensitivity are seen.

3.6 TRANSDUCER BEAM CHARACTERISTICS

The beam characteristics produced by an ultrasonic transducer are far from ideal. It deviates significantly in many ways from an ideal parallel beam with a uniform intensity profile. It is possible to calculate the beam profile utilizing Huygens'

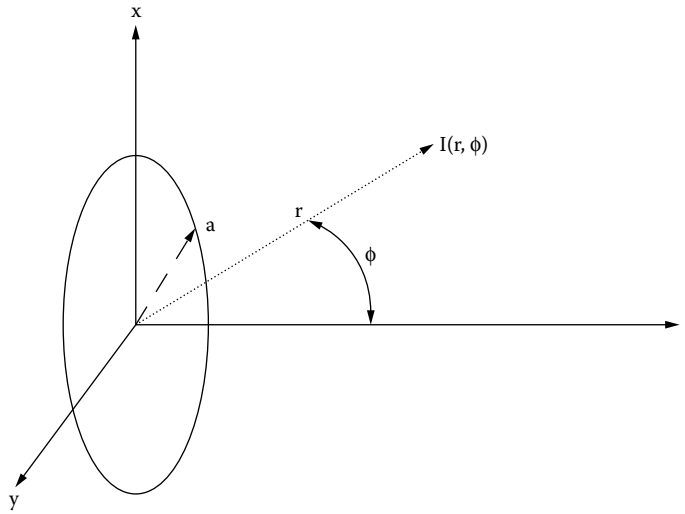

FIGURE 3.13 Coordinate system for depicting the pressure or intensity distribution of a disc piston transducer.

principle (Kinsler et al., 1982), which says that the resultant wavefront generated by a source of finite aperture can be obtained by considering the source to be composed of an infinite number of point sources. To calculate the beam profile of an ultrasonic transducer, the transducer surface is considered to consist of an infinite number of point sources, each emitting a spherical wave. The summation of the spherical wavelets generated by all point sources on the transducer surface at a certain point yields the field at that point. Referring to Figure 3.13, the axial intensity, $I(z)$, at a point z from a circular piston transducer is shown to be (Kinsler et al., 1982; Kino, 1987):

$$I(\mathrm{z}) = I_0 \sin^2\left[\frac{k}{2}\left(\sqrt{\mathrm{z}^2 + a^2} - z\right)\right] \tag{3.23}$$

where

I_0 is the maximal axial intensity
a is the radius of the disk
k is the wave number in the loading medium

$I(z) = I_0$ when

$$\frac{k}{2}\left(\sqrt{z^2 + a^2} - z\right) = n\frac{\pi}{2}$$

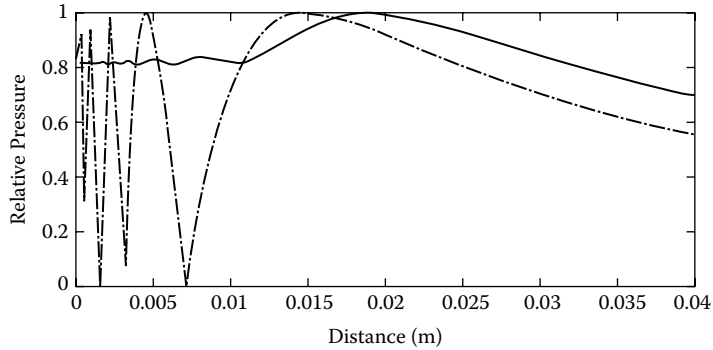

FIGURE 3.14 Axial pressure profile as a function of distance (z) for a 2.5-MHz piston transducer of 3 mm diameter for continuous wave (CW) (dashed line) and pulsed excitation (solid line).

Where n is an integer. For $n = 1$, it can be easily shown that, for $z >> a$,

$$z_o = \frac{a^2}{\lambda} \tag{3.24}$$

This is the distance between the transducer and the last maximum of the axial pressure or intensity.

3.6.1 Beam Profiles

Figure 3.14 shows the typical axial pressure profile of a circular piston transducer driven by a sinusoidal source. It is a plot of the ultrasonic peak pressure as a function of the axial distance from the center of the transducer in the medium where the wave is being propagated. The region where axial pressure oscillates, $z < z_0$, is called the near-field, or Fresnel zone, and the region where the axial pressure decreases approximately according to $1/z$ is called the far-field, or Fraunhofer zone. Obviously, z_0 is the transition point from near-field zone to far-field zone. Beyond z_0, the intensity and the pressure decrease as a function of $1/z^2$ and $1/z$, respectively.

In the far field of the transducer, $r >> a$, the angular radiation pattern is found to be (Kinsler et al., 1982; Kino, 1987):

$$I(\phi) = I(\phi = 0)\left[\frac{2J_1(ka\ \sin\phi)}{ka\ \sin\phi}\right]^2 = I(\phi = 0)\, H^2(\phi) \tag{3.25}$$

where J_1 is the Bessel function of first kind of order 1 and $H(\phi)$ is the directivity function of the aperture. The first zero for this function occurs at $ka \cdot \sin\phi = 3.83$, which means

$$\sin\phi = 0.61\frac{\lambda}{a} \tag{3.26}$$

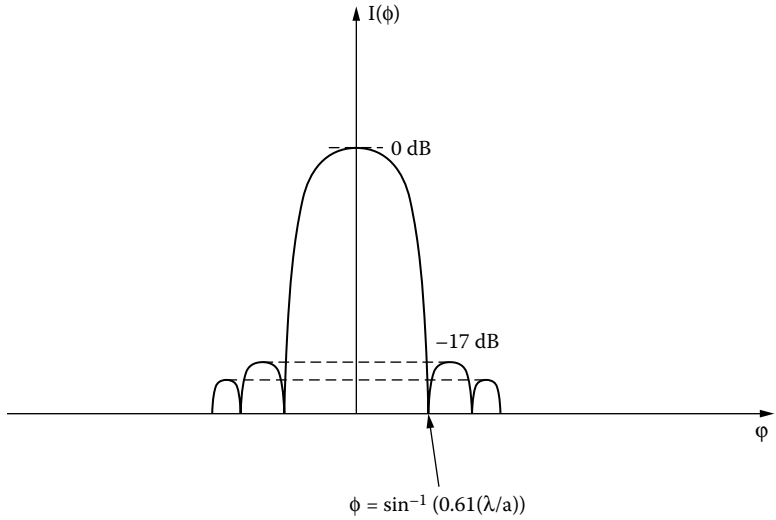

FIGURE 3.15 Angular radiation pattern of a disc piston transducer.

Figure 3.15 shows the transverse intensity profile of a transducer in the far-field zone where, in general, the distance between two points at which the pressure drops to –3 or –6 dB of the maximal value is defined as beam width. The transverse profile in the near field is extremely complex and not well defined. As z becomes greater than z_o, the beam starts to diverge (illustrated in Figure 3.16), which is an idealistic representation of the beam behavior of a circular piston transducer. In the near field, it behaves like a parallel beam and starts to diverge at z_o at an angle of ϕ. In the very far field, the transducer behaves like a point source irradiating energy into a cone confined to an angle defined by 2ϕ.

Figure 3.15 shows the angular intensity radiation pattern in the far field of an ultrasonic transducer consisting of a main lobe and several side lobes. The number of

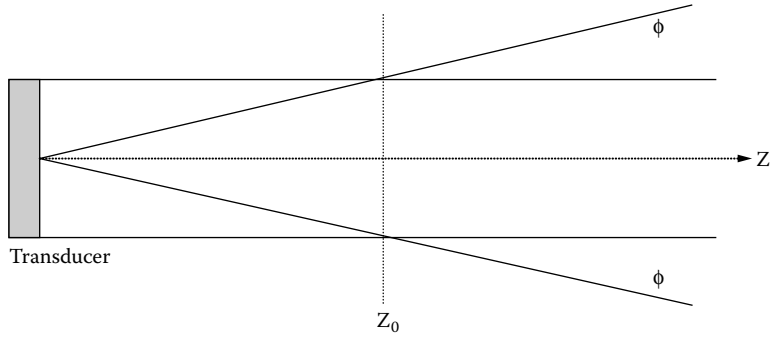

FIGURE 3.16 Idealistic representation of the beam behavior of a single-element piston transducer.

side lobes and their magnitude relative to that of the main lobe depend on the ratio of transducer aperture size to wavelength and the shape of the piezoelectric element. For a circular disc, the first side lobe level is –17 dB down from the main lobe. The relative ratio of the magnitude of the main lobe to that of a side lobe can be modified by shading or tapering the element or weighting the driving signal to the piezoelectric element.

Shading the element and weighting the input signal amplitude are termed aperture and amplitude apodization, respectively. As the ratio of the aperture size to wavelength becomes larger, ϕ decreases or the beam becomes sharper, accompanied by an increase in the number of side lobes. Side lobes are very undesirable in ultrasonic imaging because they produce spurious signals, resulting in artifacts in the image and a reduction in contrast resolution. Therefore, to have a sharper beam by increasing the ratio of transducer aperture size to wavelength, more side lobes are introduced and z_o is shifted farther away from the transducer.

Consequently, for a particular application, a compromise must be reached or a lens may be used to shift the focal point closer to the transducer. A gray-scale representation of the acoustic field produced by a circular piston transducer of 0.5-cm radius at 5 MHz is shown in Figure 3.17, where $z_o = 8.1$ cm. Here, the brightness is proportional to pressure amplitude.

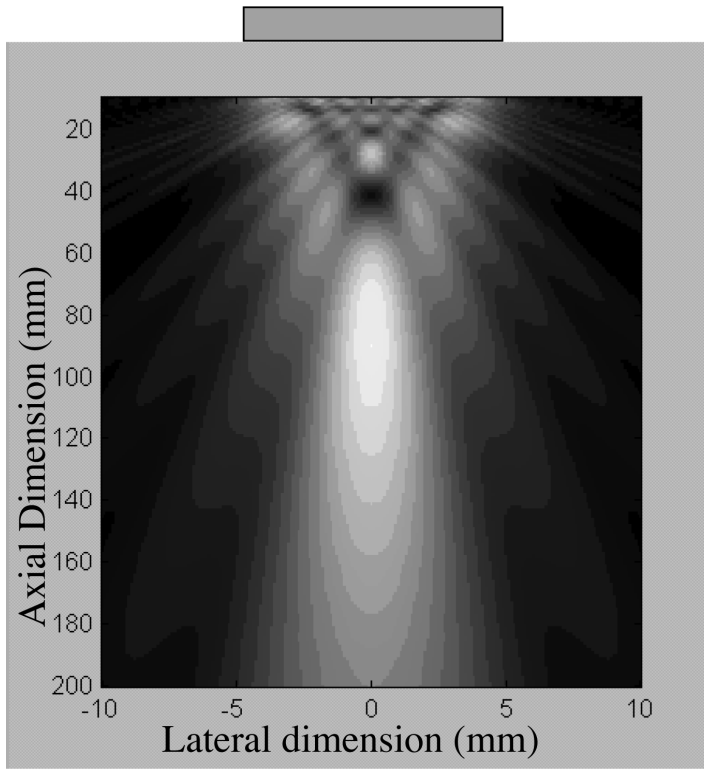

FIGURE 3.17 The pressure amplitude distribution of a single-element transducer with CW excitation.

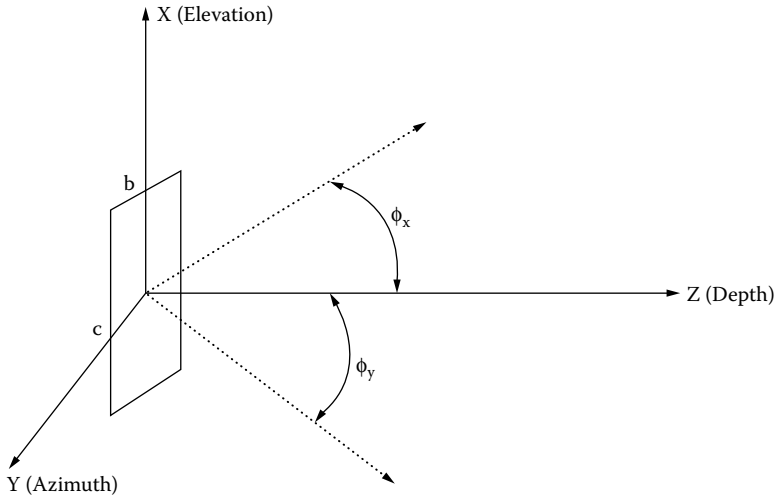

FIGURE 3.18 Coordinate system and nomenclature frequently used in ultrasonic transducer literature.

For a rectangular element, which is the basic unit of an array with dimension c in the x-direction and b in the y-direction, shown in Figure 3.18, the directivity function is given by

$$H(\phi_x,\phi_y)=\frac{\sin[(kc\sin\phi_x)/2]}{(kc\sin\phi_x)/2}\cdot\frac{\sin[(kb\sin\phi_y)/2]}{(kb\sin\phi_y)/2} \tag{3.27}$$

where ϕ_x and ϕ_y are angles in the x–z- and y–z-planes, respectively. The directions of x and y are frequently referred to as the elevation and azimuthal directions in the literature. The ratio $(\sin x)/x$ is the sinc function, which is zero when $x = n\pi$, where n is an integer. Therefore, the first zeros for $H(\phi_x,\phi_y)$ are at

$$\phi_x=\sin^{-1}\frac{\lambda}{c},\phi_y=\sin^{-1}\frac{\lambda}{b} \tag{3.28}$$

For rectangular elements, the ratio of the magnitude of the main lobe to that of the first side lobe is –13 dB. Again, this can be controlled by tapering, shading, or apodization. If the shape of the element is modified to have parabolic profile or tapering, this ratio drops to –22 dB.

It is worth noting here that the radiation pattern of a radiator depends upon the boundary conditions. If the surrounding structure is rigid (technically called a rigid baffle), Equation (3.25) and Equation (3.27) are valid. These expressions must be modified if the surrounding structure is soft like air (technically called a soft baffle). Selfridge et al. (1980) showed that, for a rectangular element supported by air or a soft polymer, Equation (3.27) should be revised. For instance, in the y-direction the

radiation pattern is

$$H_y(\phi_y) = \frac{\sin[(kb\sin\phi_y)/2]}{(kb\sin\phi_y)/2}\cos\phi_y \tag{3.29}$$

There is an additional cosine term.

3.6.2 Pulsed Ultrasonic Field

The preceding discussion pertains only to continuous-wave propagation. Most applications of ultrasound in medicine, however, involve pulsed ultrasound. By using the Fourier transform and the principle of superposition, the field characteristics of a transducer transmitting pulses can be calculated. When a transducer is pulsed, the radiation pattern and the field characteristics become much smoother. Figure 3.19 shows the radiation pattern of a 5-MHz, 0.5-cm radius, circular piston excited by a three-cycle pulse.

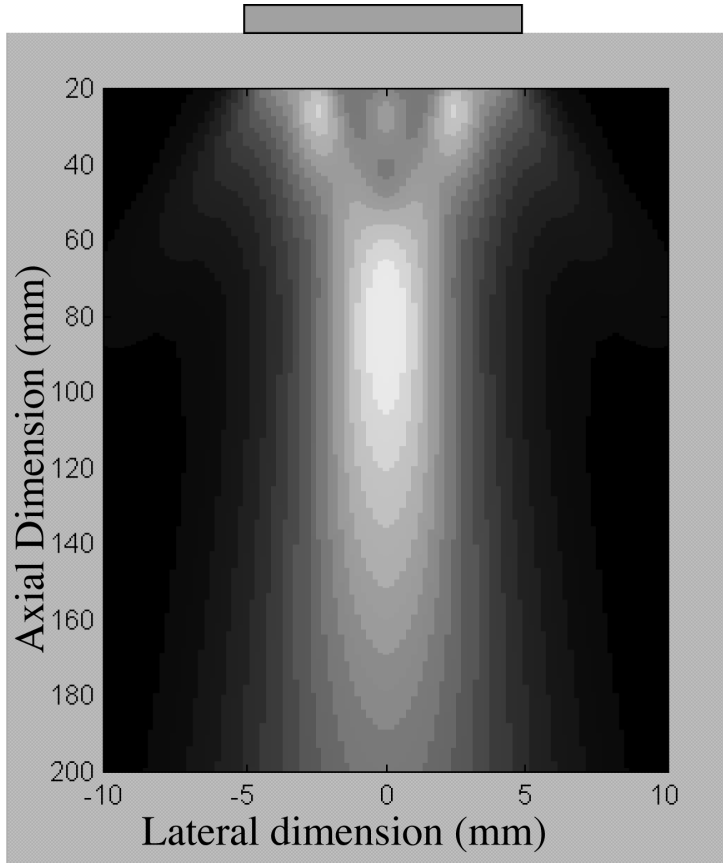

FIGURE 3.19 The pressure amplitude distribution of a single-element transducer with pulsed excitation.

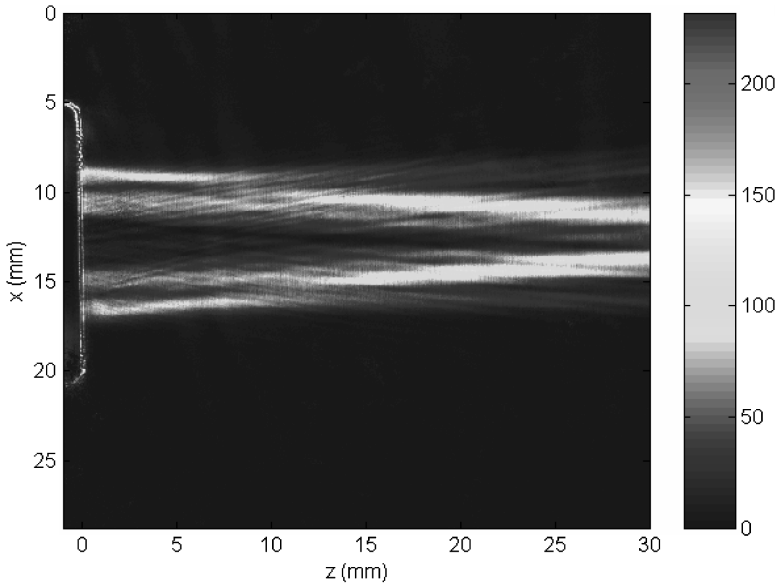

FIGURE 3.20 (See color figure following page 80.) A Schlieren image of a 10-MHz piston transducer of 1-cm diameter. The transducer is on the left of the image. The diffraction pattern near the transducer is clearly seen. The color bar indicates the acoustic intensity.

3.6.3 Visualization and Mapping of the Ultrasonic Field

A Schlieren system is an optical system that has been used frequently to visualize the ultrasonic field (Zinskin and Lewin, 1993). This method depends on the diffraction of a parallel beam of light when it traverses through a medium in which a refractive index gradient is normal to the light beam. An ultrasonic beam produces such a gradient because the propagation of an ultrasonic wave is associated with changes in the density of the medium. If the primary nondiffracted light beam is blocked, the diffracted light, which contains an image of the ultrasound beam, can be observed directly on a screen, photographed, or captured by a CCD camera and displayed on a monitor. Figure 3.20 is a Schlieren image in the near field of a 10-MHz transducer of 1-cm diameter obtained by a Schlieren system (Hanafy and Zanelli, 1991).

Although a qualitative interpretation of the Schlieren image is fairly straightforward, a quantitative analysis of the optical image is difficult (Schneider and Shung, 1996). Alternatively, a more time-consuming but well-established method, in which a nondirectional microprobe or hydrophone is used to scan the field, may be employed (Zinskin and Lewin, 1993). In addition to nondirectional, the probe should possess nonselective frequency characteristics or a very broad frequency bandwidth. It should be small in size to avoid the establishment of standing waves and minimize the effect of acoustic field averaging over the transducer face. However, in practice, it is almost impossible to satisfy all these requirements. Different types of hydrophones are commercially available, including the needle

type in which the piezoelectric element is housed in a hypodermic needle of less than 1-mm diameter and the PVDF membrane type, in which only the center of a tightly stretched membrane is poled and piezoelectrically active. The diameter of the poled spot for a membrane hydrophone can be made as small as 0.2 mm. A small target such as a small sphere or wire has also often been used to map the field.

3.6.4 Axial and Lateral Resolution

The axial and lateral resolutions of a transducer are determined by the emitted pulse duration and the beam width of the transducer (–3 or –6 dB beam width), respectively, because whether the echoes from two targets in the axial or in the lateral direction can be separated or resolved is directly related to these parameters. This is graphically illustrated in Figure 3.21(a), where it can be seen that the echoes from two targets can be clearly resolved if they are far apart. As the targets are moved increasingly closer (as shown in Figure 3.21b–d), they become increasingly difficult to resolve. Figure 3.21(d) shows what happens when the two targets coincide.

The distance in this figure represents the axial or lateral distance. The beam width at the focal point of a transducer, W_b, is linearly proportional to the wavelength.

$$W_b \approx f_{\#}\lambda \tag{3.30}$$

where $f_{\#}$ is the f number defined as the ratio of focal distance to aperture dimension. For a circular transducer of diameter 2a and a focal distance of 4a, the transducer has $f_{\#}$ of 2. The depth of focus, D_f—i.e., within this region, the intensity of the beam within –1.5 or –3 dB of the maximal intensity at the focus—is also linearly related to the wavelength.

$$D_f \approx f_{\#}^2\lambda \tag{3.31}$$

From these relationships, it is clear that an increase in frequency that decreases wavelength improves lateral and axial resolutions by reducing the beam width and the pulse duration if the number of cycles in a pulse is fixed. Unfortunately, these improvements are achieved at a cost of a shorter depth of focus.

The axial and lateral resolution of a transducer can be improved from an increase in the bandwidth by using backing and/or matching and focusing. The spectrum of an ultrasonic pulse varies as it penetrates into tissue because the attenuation of the tissues is frequency dependent. It is known that the center frequency and bandwidth of an ultrasonic pulse decrease as the ultrasound pulse penetrates deeper. In other words, the axial resolution of the beam worsens as the beam penetrates more deeply into the tissue. In commercial scanners, pulse shape and duration are maintained by time–gain–compensation and some form of signal processing.

3.6.5 Focusing

Better lateral resolution at a certain axial range can be achieved by acoustic focusing. However, an improvement in the lateral resolution or focusing at a certain range is

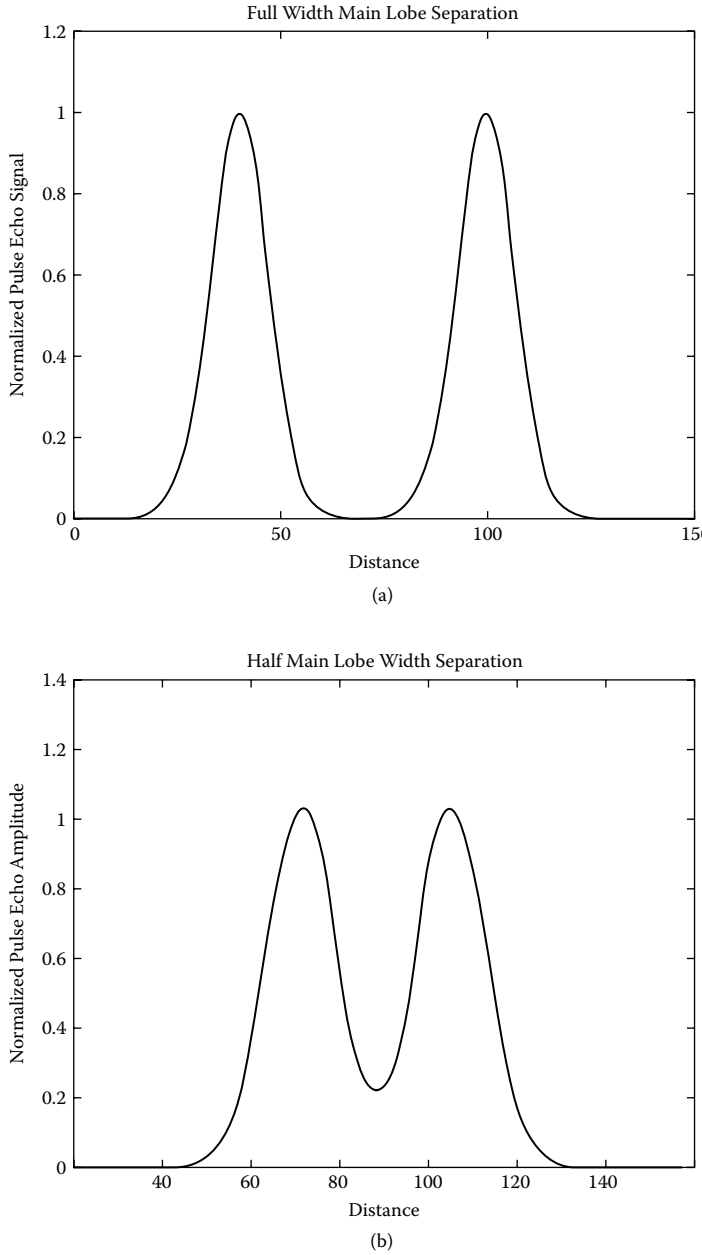

FIGURE 3.21 The spatial resolutions of an ultrasonic transducer in the axial and lateral directions are determined by the pulse duration and beam width.

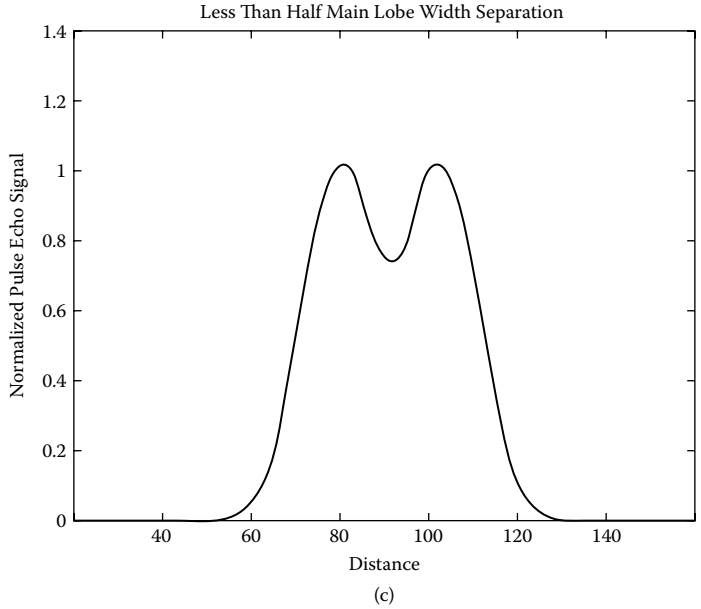

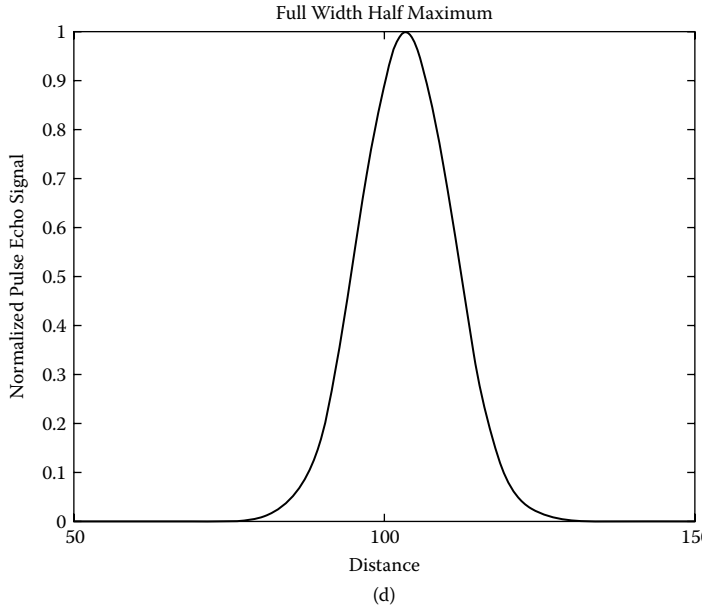

FIGURE 3.21 (Continued).

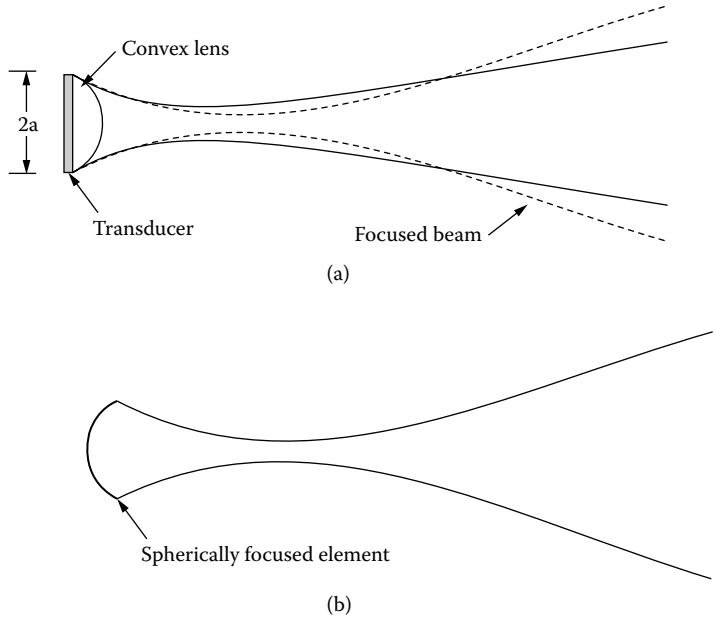

FIGURE 3.22 Two modes of focusing that have been used to focus ultrasonic beams: (a) focusing with a lens and (b) self-focusing.

always accompanied by a loss of resolution in the region beyond the focal zone, as illustrated in Figure 3.22(a).

The general principles of focusing are identical to those in optics. Two schemes that are often used, a lens and a spherical or bowl type transducer, are illustrated in Figure 3.22(a) and (b). The acoustic lens shown in Figure 3.22(a) is a convex lens, which means that the sound velocity in the lens material is less than the medium into which the beam is launched. The convex lens is preferred in biomedical ultrasonic imaging because it conforms better to the shape of the body curvature. Some of the lens materials frequently used in medical applications can be found in Table 3.3. Concave lenses made of Plexiglas or polystyrene have also been used. The focal length, z_f, of a lens is given by

$$z_f = \frac{R_c}{1 - 1/n} \tag{3.32}$$

where

R_c is the radius of curvature and $n = c_1/c_2$
c_1 is the velocity in the lens
c_2 is velocity in the medium

The focal region formed by an acoustic lens is generally ellipsoidal. Its dimension depends on the relationship between wavelength and the diameter of the lens.

Generally, the bigger the diameter is, the smaller the focal point is. Ultrasonic imaging is diffraction limited because the beam cannot be properly focused in the region very close to the transducer and beyond the near-field and far-field transition point. For a circular piston transducer of radius a, $z_0 = a^2/\lambda$. The $f_\#$ is $a/(2\lambda)$, which is determined by the ratio of radius to wavelength. For a ratio of radius to wavelength = 10, $f_\# = 5$. This means that the beam cannot be focused beyond an $f_\#$ of 5. The only way to obtain focusing at a distance greater than this is to increase the aperture size or decrease the wavelength.

A single-element transducer can be translated or steered mechanically to form an image. Linear translators do not allow movements, permitting generation of images at a rate higher than a few frames per second, although some devices allow steering the transducer within a limited angle at a rate of 30 frames per second. Early real-time ultrasonic imaging devices almost exclusively used these types of transducers, which are called mechanical sector probes. A typical mechanical sector probe is shown in Figure 3.23. The transducer is housed in a dome bathed in some form of oil to facilitate the transmission of the ultrasonic energy from the transducer to the housing. Mechanical sector probes, which suffer from poor near-field image quality because of reverberations between the transducer and the housing and fixed focusing capability, have now been largely replaced by linear arrays.

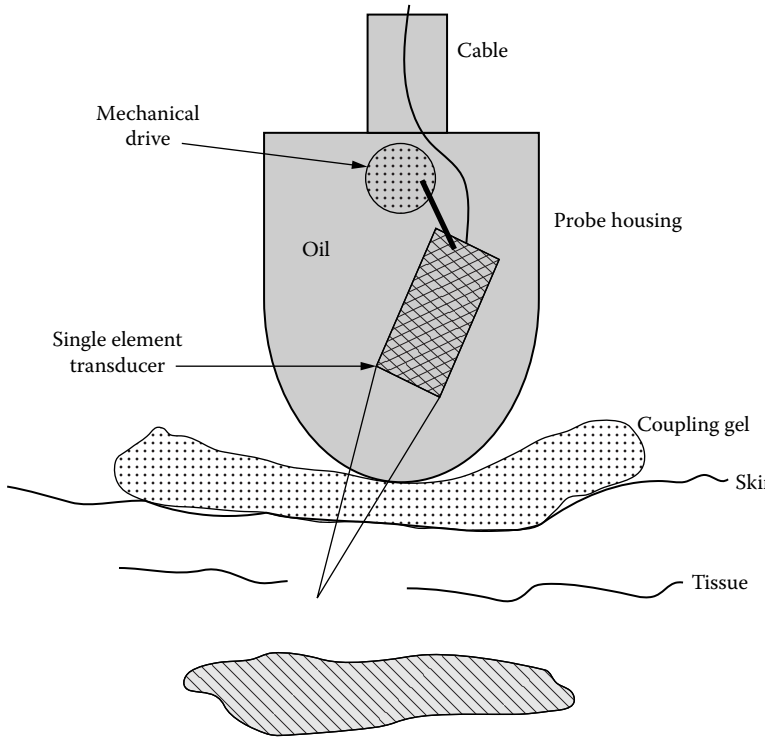

FIGURE 3.23 Detail construction of a mechanical sector probe.

3.7 ARRAYS

Arrays are transducer assemblies with more than one element. These elements may be rectangular in shape and arranged in a line (called linear or one-dimensional array and shown in Figure 3.24a); square in shape and arranged in rows and columns (called two-dimensional array and shown in Figure 3.24b); or ring shaped and arranged concentrically (called annular array and shown in Figure 3.24c).

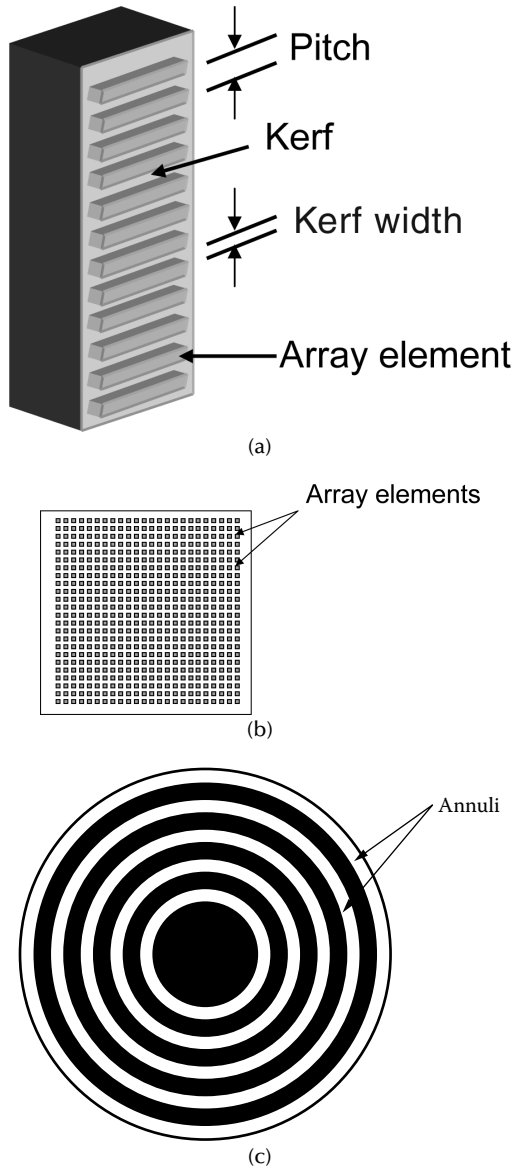

FIGURE 3.24 (a) Linear array; (b) two-dimensional array; and (c) annular array.

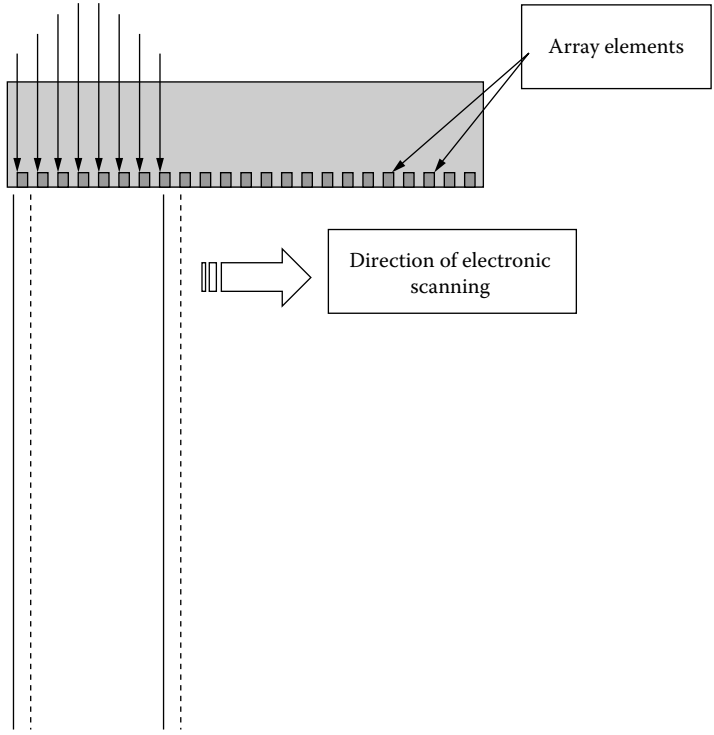

FIGURE 3.25 A linear array forms an image by electronically sweeping the beam. A group of elements is fired simultaneously to form one beam.

A linear switched array (sometimes called a linear sequenced or simply a linear array) is operated by applying voltage pulses to groups of elements in succession as shown in Figure 3.25; here, the solid line and the dashed line indicate the first and second beams, respectively. In this way, the sound beam is moved across the face of the transducer and electronically produces a picture similar to that obtained by scanning a single-element transducer manually. The amplitude of the voltage pulses can be uniform or varied across the aperture as shown in the figure by arrows of varying length. Amplitude apodization or varying the input pulse amplitude across the aperture is sometimes used to suppress side lobes at the expense of worsening the lateral resolution. If the electronic sequencing or scanning is repeated fast enough (30 frames per second), a real-time image can be generated.

Linear arrays are usually 1 cm wide and 10 to 15 cm long and have 128 to 256 elements. Typically, 32 or more elements are fired as a group. As was explained earlier, for the sake of achieving as good a lateral resolution as possible, the irradiating aperture size must be made as large as possible. The aperture size is in turn limited by the requirement of maintaining a large number of scan lines. This point will become clearer in Chapter 4. Figure 3.26 shows the detailed construction of a linear array consisting of a backing material, a layer of piezoelectric material sandwiched between two

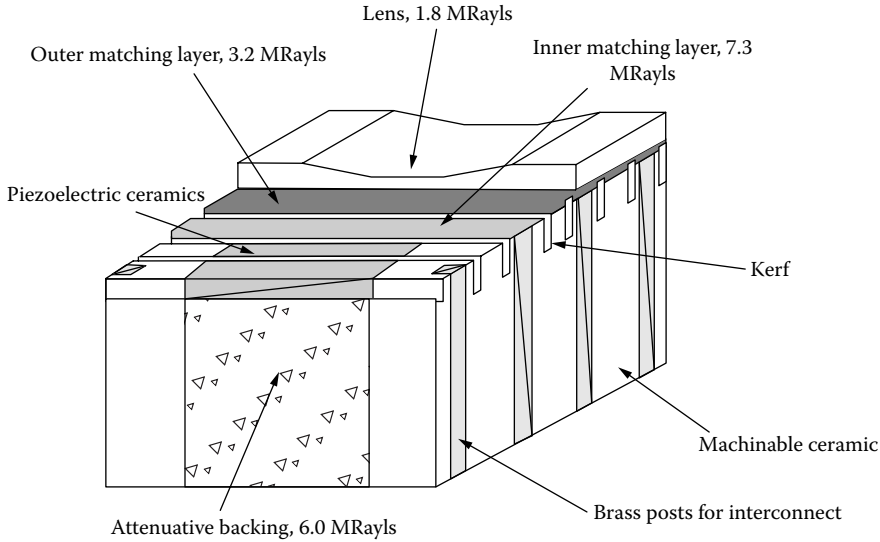

FIGURE 3.26 Detail construction of a linear array with two matching layers, a lens, and light backing.

electrodes, and two matching layers. Here, a concave lens is used to focus the imaging plane in the elevation direction or to control the slice thickness of the imaging plane.

This is a problem of crucial importance in two-dimensional imaging with one-dimensional arrays because the slice thickness cannot be controlled throughout the depth of view. The slice thickness is the smallest only at the focal point of the lens and becomes worse closer to the array or beyond the focal point. A large slice thickness can cause serious image artifacts, (including a reduction in contrast). Referring also to Figure 3.24(a), the space between two elements is called a "kerf" and the distance between the centers of two elements is called a "pitch." The kerfs may be filled with acoustic isolating material or simply air to minimize acoustic cross-talk. The kerfs are often cut into the lens and backing to minimize acoustic cross-talk between adjacent elements through the backing, the lens, and matching layers. The size of a pitch in a linear array ranges from $\lambda/2$ to $3\lambda/2$, where λ is the wavelength in the medium into which ultrasound in launched and is not as critical as in a phased array (Steinberg, 1976; Shung and Zipparo, 1996).

The linear phased array, while similar in construction, is quite different in operation. A phased array is smaller (1 cm wide and 1 to 3 cm long) and usually contains fewer elements (96 to 256). Referring to Figure 3.27, if the difference in path length between the center element and element number, n, is $\Delta r_n = r - r_n$, at a point $P(r,\phi_x)$, the time difference is then

$$\Delta t_n = \frac{\Delta r_n}{c} = \frac{x_n \sin \phi_x}{c} + \frac{x_n^2}{2cr} \tag{3.33}$$

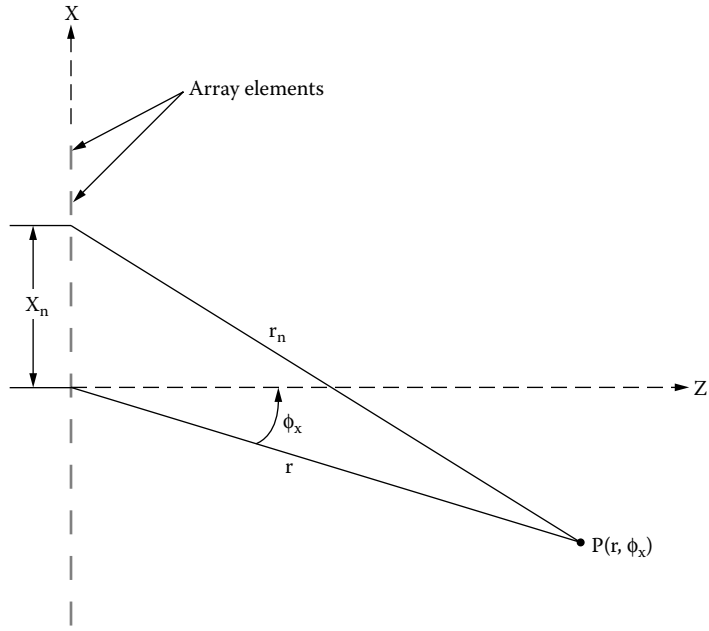

FIGURE 3.27 A two-dimensional coordinate system depicting the difference in path length between the center element of a linear array and the *n*th element.

where the first and the second terms on the right-hand side of the equation indicate the time differences due to steering and focusing, respectively.

Therefore, the pulse exciting the center element should be delayed by a time period of Δt_n relative to the pulse exciting the element n if the ultrasonic pulses are to arrive at point P simultaneously. The ultrasonic beam generated by a phased array can be focused and steered by properly delaying the signals going to the elements for transmission or arriving at the elements for receiving, as illustrated in Figure 3.28, according to Equation (3.33). The radiation pattern in the far field of a linear phased array of length L_a consisting of N elements, i.e., $z > L_a^2/4\lambda$, is given by

$$H(u) = \text{sinc}\left(\frac{bu}{\lambda}\right) \cdot \sum_{m=1}^{N} \delta\left(u - m\frac{\lambda}{g}\right) * \text{sinc}\left(\frac{L_a u}{\lambda}\right) \tag{3.34}$$

where

$u = \sin \phi_x$

$H(u)$ is the directivity function at an angle of ϕ_x

b is the width of the element

g is the pitch

The symbol * indicates the operation of convolution, δ represents the delta function, and sinc denotes the sinc function = $\sin x/x$. For arrays with regularly spaced

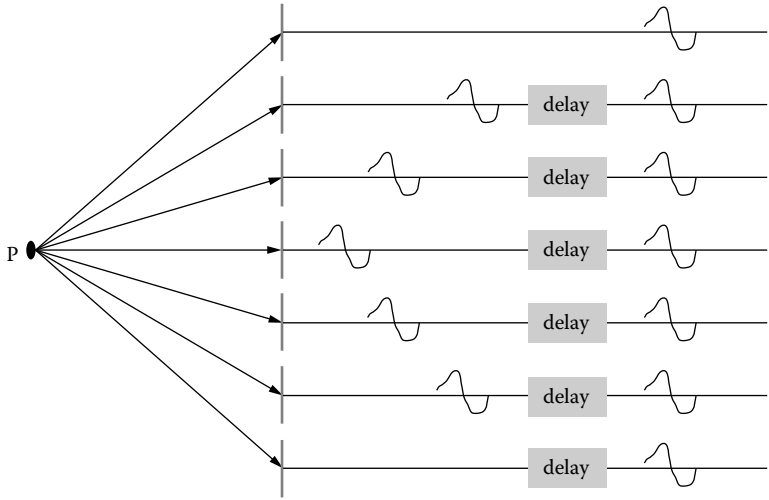

FIGURE 3.28 The echoes returned from a point scatterer at point *P* can be made to arrive at the same time by appropriately delaying the echoes detected at the elements of a linear array.

elements, high side lobes called grating lobes occur at certain angles because of constructive interference, which is related to the wavelength and the pitch by the following equation:

$$\phi_g = \sin^{-1}\left(\frac{n\lambda}{g}\right) \tag{3.35}$$

where n is an integer = ±1, ±2,….

For the grating lobes to occur at angles greater than 90°, g must be smaller than $\lambda/2$. When this condition is satisfied, the array is said to be fully sampled. The effect of pitch on the radiation pattern of a 20-element array is illustrated in Figure 3.29 where Figure 3.29(a) and Figure 3.29(b) are for 1.5 and 0.75 λ pitch, respectively. As can be seen, the grating lobes move further away from the main lobe as the pitch is reduced. Equation (3.34) also shows that the magnitude of grating lobe relative to the main lobe is determined by the width of the element, b. The smaller the value for b is, the larger is the magnitude of grating lobes relative to the main lobe. The width of the main lobe in turn is determined by L_a, the width of the array. The greater the L_a is, the smaller the main lobe is. There are ways, although not perfect, to suppress the grating lobes. These include randomizing the spacings between elements, which spreads the grating lobe energy in all directions, resulting in a "pedestal" side lobe (Turnbull and Foster, 1992) and subdicing the elements.

There are a few simple design rules for linear arrays and linear phased arrays. For linear arrays, the pitch, g, should be between 0.75 and 2λ; the ratio of the width of the array element to the thickness of the element, $b/L < 0.6$; to avoid spurious resonant modes, $b > \lambda/2$; and the cross-talk between adjacent elements < –30 dB. For phased arrays, the pitch g should be smaller than 0.5 λ, $b/L < 0.6$, and $b \sim \lambda/2$

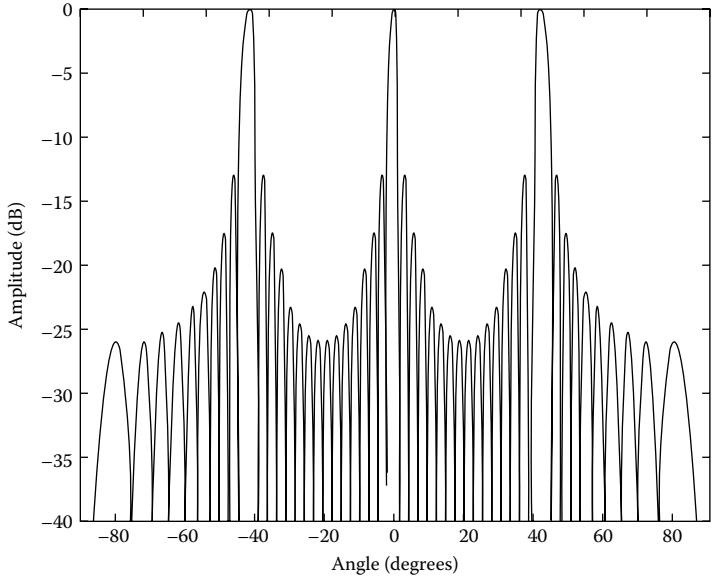

(a)

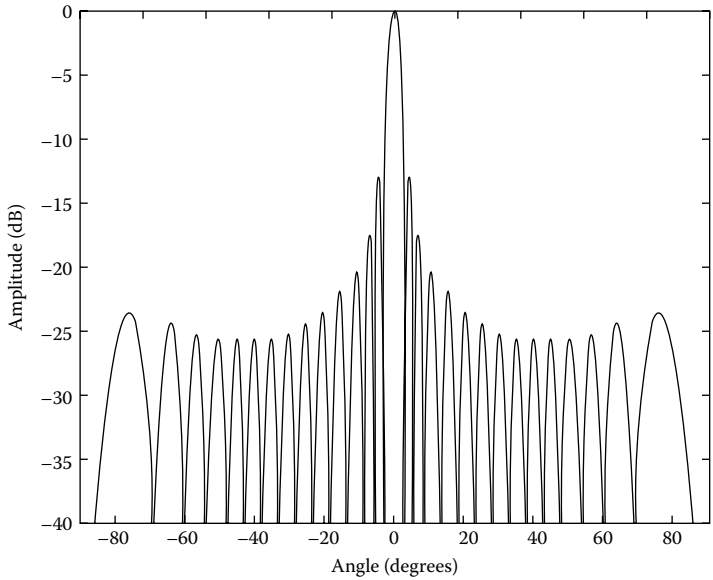

(b)

FIGURE 3.29 (a) Large grating lobes are produced at 40 and –40° by a linear array with an undesirable pitch. (b) Grating lobes are moved away when the pitch is reduced to smaller than a wavelength.

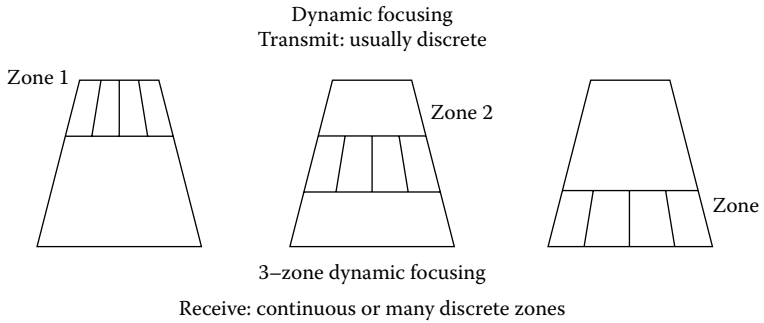

FIGURE 3.30 Discrete zone dynamic focusing is used for transmission, whereas almost continuous dynamic focusing may be used in reception.

to ensure a broad beam because the beam is steered, and the cross-talk < –35 dB because cross-talk can result in an increase in the apparent aperture size.

Phased arrays allow dynamic focusing and beam steering. Dynamic focusing can be achieved in transmission and in reception. However, multiple transmissions of pulses are needed for dynamic focusing during transmission, slowing down the frame rate. Transmission dynamic focusing is usually done in discrete zones, whereas receiving dynamic focusing can be done in many more zones or almost continuously, as illustrated in Figure 3.30.

After all data are acquired, a composite image is formed, taking only the data from the zones where the beam is focused. To maintain the beam width throughout the depth of view, state-of-the-art scanners also use the dynamic aperture apodization described earlier and shown in Figure 3.31. The aperture size is varied as a

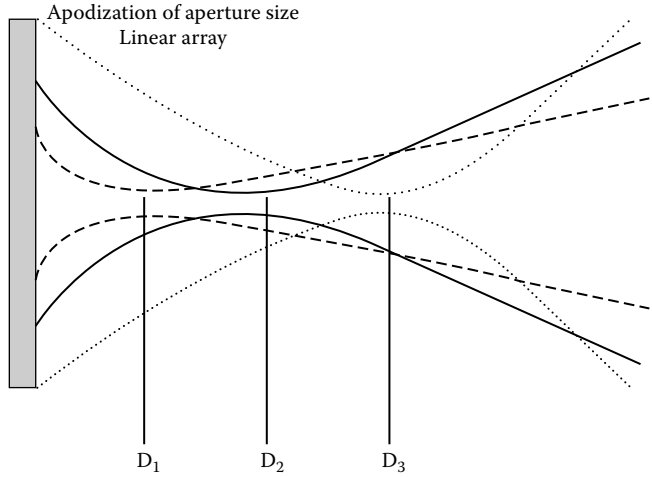

FIGURE 3.31 Aperture size apodization can be used to maintain the beam width throughout the depth of view.

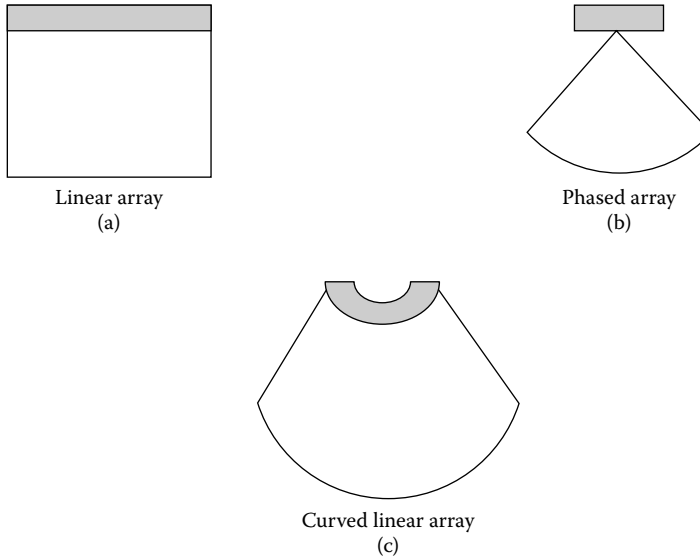

FIGURE 3.32 The shapes produced by various types of arrays: (a) linear; (b) phased; and (c) curved linear.

function of time to allow proper focus of the beam at distances D_1, D_2, and D_3. The reduction of aperture size is especially crucial in the near field, where the beam cannot be focused for a transducer of a given size. A variation of the linear array is the curved array shown in Figure 3.32(c) that allows the formation of a pie-shaped image without resorting to phased array technology, which is more complicated and expensive. In contrast, Figure 3.32(a) and Figure 3.32(b) show the shapes of images obtained by a linear array and a phased array, respectively.

Linear arrays can be focused and steered only in one plane, the azimuthal plane. Focusing in the elevation plane perpendicular to the imaging plane, which determines the slice thickness of the imaging plane, is achieved with a lens. This problem may be alleviated by using multidimensional arrays or 1.5-dimensional or two-dimensional arrays (Daft et al., 1994; Smith et al., 1995; Shung and Zipparo, 1996). A 1.5-dimensional design used to provide limited focusing capability in the elevation plane and to reduce slice thickness is shown in Figure 3.33. It is an alternative to two-dimensional, arrays which are still under intensive investigation and are not yet widely commercially available (Smith et al., 1995). In 1.5-dimensional arrays, the additional elements in the elevation direction increase the number of electronic channels and complexity in array fabrication. Two concerns associated with 1.5-dimensional arrays that do not exist in one-dimensional arrays are grating lobes in the elevation plane as a result of the small number of elements and increased footprint or aperture size.

Two-dimensional arrays shown in Figure 3.24(b) have been investigated to perform high-speed three-dimensional ultrasonic imaging for cardiac applications (Smith et al., 1995; Greenstein et al., 1997). The current two-dimensional arrays

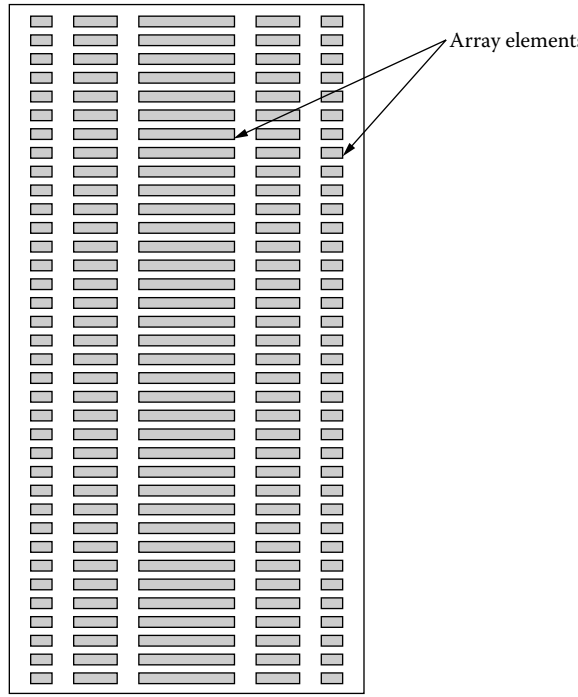

FIGURE 3.33 A 1.5-dimensional array with five rows.

may consist of more than $40 \times 40 = 1600$ elements at 2.5 to 3.5 MHz, with fewer than a few hundred elements actually wired. The square aperture has a size of 1.5×1.5 cm with each element smaller than 250×250 μm. It suffers from a severe difficulty in electrical interconnection due to the large number of elements and channels, low signal-to-noise ratio due to electrical impedance mismatching, and small element size. Fiber optics and multilayer architecture are possible solutions to the interconnection problem and array stack design.

It has been reported that Philips' recently introduced four-dimensional scanner capable of displaying three-dimensional images in real time incorporates a two-dimensional array of 60×60 elements. A novel multiplexing scheme is used to reduce the total number of electronic channels to a manageable level (Savord and Soloman, 2003). An alternative to solving the complexity and cost in electronics and interconnection would be to use sparse array technology that reduces the element and channel count at the price of poorer signal-to-noise ratio and array performance (Lockwood et al., 1996).

The annular arrays shown in Figure 3.24(c) can also achieve biplane focusing. By using appropriate externally controllable delay lines or dynamic focusing, focusing throughout the field of view can be attained. A major disadvantage of annular arrays is that mechanical steering must be used to generate two-dimensional images. The width of each annulus may be adjusted to maintain the beam intensity over the dynamically focused zones.

REFERENCES

Brown, L.F. Ferroelectric polymers: current and future ultrasound applications. *1992 IEEE Ultrason. Symp. Proc.* 1992, 539–550.

Cady, W.G. *Piezoelectricity.* New York: Dover, 1964.

Daft, C.M.W., Wildes, D.G., Thomas, L.J., and Smith, L.S. A 1.5-D transducer for medical ultrasound. *1994 IEEE Ultrason. Symp. Proc*. 1994, 1491–1495.

Desilets, C.S., Fraser, J.D., and Kino, G.S. The design of efficient broad-band piezoelectric transducers. *IEEE Trans. Sonics Ultrason.* 1978, 25:115–125.

Goldberg, R.L. and Smith, S.W. Transducers. In: Bronzino, J., Ed. *The Biomedical Engineering Handbook*, Boca Raton, FL: CRC Press, 1994:1077–1092.

Greenstein, M., Lum, P., Yoshida, H., and Seyed–Bolorforosh, M.S. A 2.5 MHz array with *Z*-axis electrically conductive backing. *IEEE Trans. Ultrason. Ferro. Freq. Contr.* 1997, 44:970–982.

Gururaja, T.R., Schulze, W.A., Cross, L.E., Newnham, R.E., Auld, B.A., and Wang, Y.J. Piezoelectric composite materials for ultrasonic transducer applications. Part I: resonant modes of vibration of PZT rod-polymer composites. *IEEE Trans. Sonics Ultrason.* 1985, 32:481–498.

Hanafy, A. and Zanelli, C.I. Quantitative real-time pulsed Schlieren imaging of ultrasonic waves. *1991 IEEE Ultrason. Symp. Proc.* 1991, 1223–1227.

Kino, G.S. *Acoustic Waves*. Englewood Cliffs, NJ: Prentice Hall, 1987.

Kinsler, L.E., Frey, A.R., Coppens, A.B., and Sanders, J.V. *Fundamentals of Acoustics*, 3rd ed. New York: John Wiley & Sons, 1982.

Krimholtz, R., Leedom, D., and Matthaei, G. New equivalent circuits for elementary piezoelectric transducers. *Electron. Lett*. 1970, 6:398–399.

Lockwood, G.R. and Foster, F.S. Optimizing the radiation pattern of sparse periodic linear arrays. *IEEE Trans. Ultrason. Ferroelect. Freq. Contr.* 1996, 43:7–14.

Newnham, R.E., Skinner, D.P., and Cross, L.E. Connectivity and piezoelectric–pyroelectric composites. *Mater. Res. Bull*. 1978, 13:525–536.

Savord, B. and Soloman, R. Fully sampled matrix transducers for real-time 3D ultrasonic imaging. *2003 IEEE Ultrason. Symp. Proc*. 2003, 945–953.

Sayers, C.M. and Tait, C.E. Ultrasonic properties of transducer backings. *Ultrasonics* 1984, 22:57–63.

Schneider, B. and Shung, K.K. Quantitative analysis of pulsed ultrasonic beam patterns using a Schlieren system. *IEEE Trans. Ultrasound Ferroelect. Freq. Contr.* 1996, 43:1181–1186.

Selfridge, A.R., Kino, G.S., and Khuri–Yakub, B.T. A theory for the radiation pattern of a rectangular narrow-strip acoustic trnasducer. *J. Appl. Phys*. 1980, 37:35–36.

Selfridge, A.R. Approximate material properties in isotropic materials. *IEEE Trans. Sonics Ultrason.* 1985, 32:381–394.

Shrout, T.R. and Fielding, J., Jr. Relaxor ferroelectric materials. *1990 IEEE Ultrason. Symp. Proc*. 1990, 711–720.

Shung, K.K. and Zipparo, M. Ultrasonic transducers and arrays. *IEEE Eng. Med. Biol. Mag*. 1996, 15:20–30.

Smith, S.W., Davidson, R.E., and Emery, C.D. Update on 2-D array transducers for medical ultrasound. *1995 IEEE Ultrason. Symp. Proc*. 1995, 1273–1278.

Smith, W.A. The role of piezocomposites in ultrasonic transducers. *1992 IEEE Ultrason. Symp. Proc*. 1989, 755–766.

Steinberg, B.D. *Principles of Aperture and Array System Design*. New York: John Wiley & Sons, 1976.

Thiagarajan, S., Jayawyrdena, I., and Martin, R.W. Design of 20-MHz wideband piezoelectric transducers for close-proximity imaging. *Biomed. Sci. Instru*. 1991, 27:57–60.

Turnbull, D.H. and Foster, F.S. Simulation of B-scan images from two-dimensional arrays. *Ultrasound Imag*. 1992, 14:323–331.

Zinskin, M.C. and Lewin, P.A. *Ultrasonic Exposimetry.* Boca Raton, FL: CRC Press, 1993.

Zipparo, M.J., Shung, K.K., and Shrout, T.R. Piezoelectric properties of fine grain PZT materials. *IEEE Trans. Ultrason. Ferroelect. Freq. Contr.* 1997, 44:1038–1048.

4 Gray-Scale Ultrasonic Imaging

The transducers/arrays described in Chapter 3 are used to generate and receive ultrasound signals required to form an image. In this chapter, other crucial components of an imaging system that generates, processes, and displays the ultrasound signal into an image are discussed. Typically, the image is displayed in gray scale. It can also be represented by such formats as rainbow or heated object scale depending upon the preference of the manufacturer and the clinical need. It must be stressed that these images yield mostly information about the anatomy of the imaged object. Various modes of ultrasound imaging have been used over the years.

4.1 A (AMPLITUDE)-MODE AND B (BRIGHTNESS)-MODE IMAGING

A-mode is the simplest and earliest mode of ultrasonic imaging. A block diagram for A-mode instruments is shown in Figure 4.1. A signal generator that produces high-intensity short pulses or a pulser is used to excite a single-element transducer. The returned echoes from the tissues are detected by the same transducer, amplified, and processed for display. A coupling medium in the form of an aqueous gel or oil is used to couple the transducer to the body because of the mismatch in acoustic impedance between the body and the transducer. Without the gel, very little energy can be transmitted into the body.

The echoes returned from various structures due to large interfaces between organs or small inhomogeneities in the organ, such as cells, small blood vessels, ducts, etc. (Shung and Thieme 1993), are first amplified by a preamplifier. The preamplifier that provides the initial state of signal amplification with a gain of a few decibels is an amplifier with high input electrical impedance and low noise. A second-stage amplification is provided by the time–gain–compensation (TGC) amplifier that may have a gain greater than 40 dB. TGC is needed because ultrasound energy is attenuated by tissues as it penetrates deeper into the body. Energy loss is affected not only by tissue attenuation that is exponentially related to the depth of penetration (as previously discussed) but also by beam diffraction. Therefore it is quite difficult to compensate for the energy loss accurately. A variety of TGC curves, shown in Figure 4.2, have been used and are usually available in an ultrasonic scanner for the operator to select.

The amplified signal is then demodulated, involving envelope detection and filtering, and logarithmically compressed. Logarithmic compression is needed because the dynamic range of the received echoes, which is defined as the ratio of the largest echo to the smallest echo above noise level detected by the transducer, is very large—on the order of 100 to 120 dB. Typical display units or cathode ray

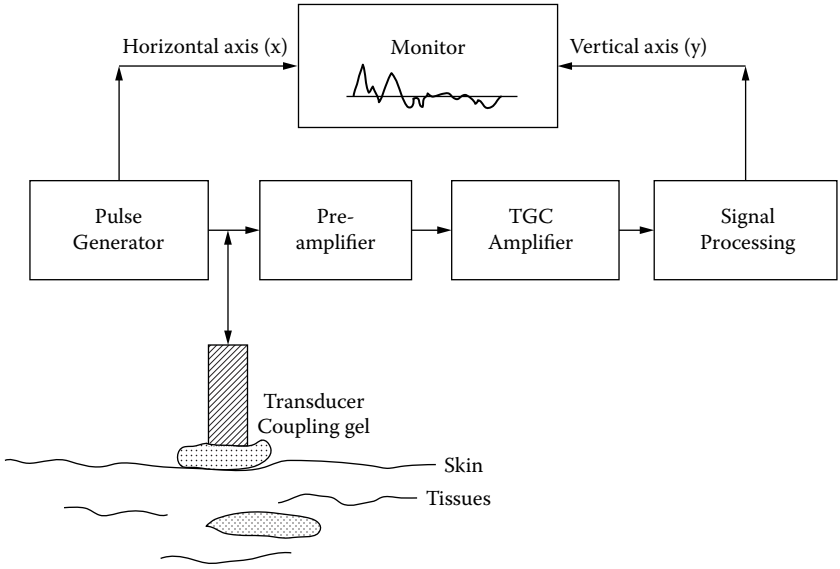

FIGURE 4.1 Block diagram of an A-mode scanner.

tube (CRT) monitors can only display signals with a dynamic range up to 40 dB at best. The horizontal axis of the CRT monitor is synchronized or triggered by pulses generated by the pulser; the vertical axis or vertical deflection of the electron beam is driven by the output of the signal processing unit, which is the demodulated and log-compressed echo amplitude or simply the video signal.

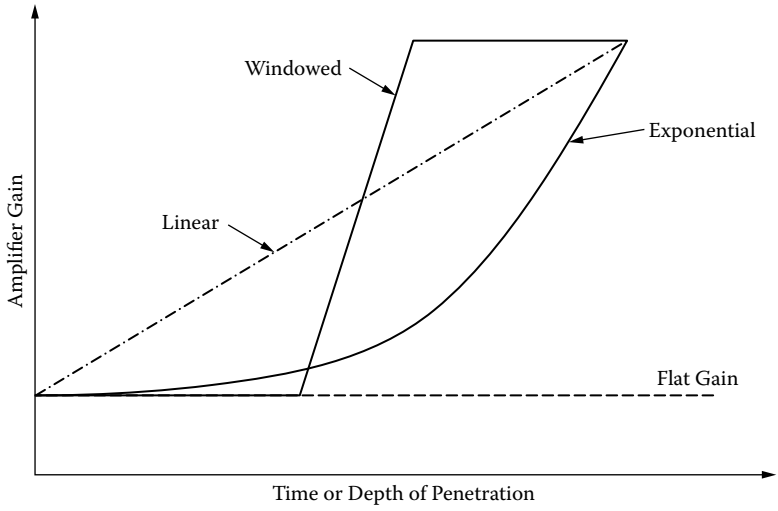

FIGURE 4.2 Time–gain–compensation curves frequently used in ultrasonic imaging.

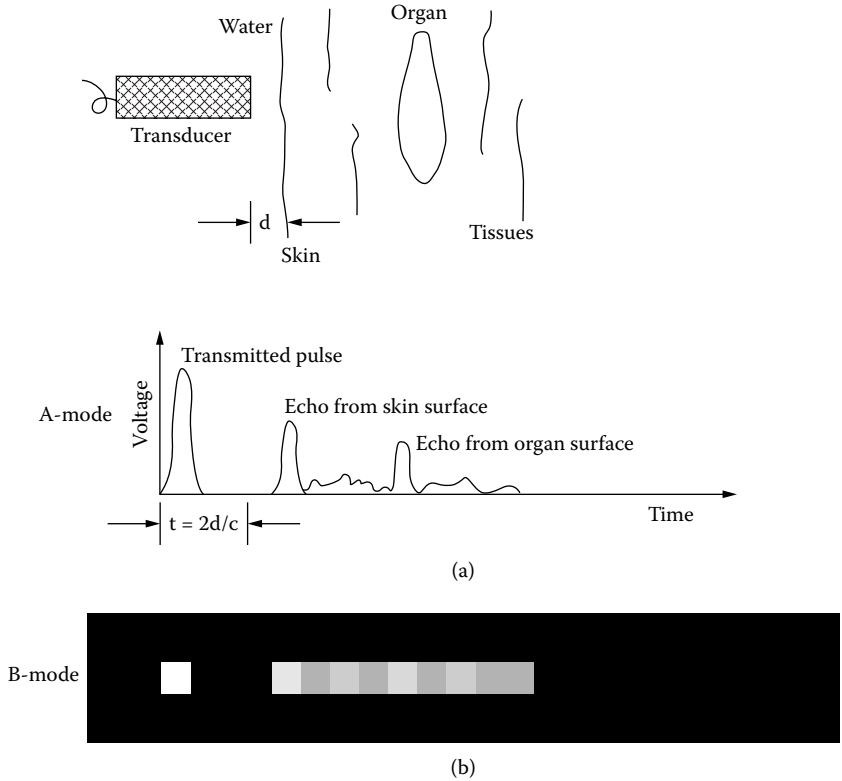

FIGURE 4.3 (a) A-mode display of returned echoes as function of time of flight for the arrangement shown on the top of the figure that depicts a transducer sending out a short pulse into the human body and receiving the returned echoes. (b) B-mode display of (a) in which the echo amplitude in each pixel is represented by gray level. Brighter pixels represent echoes with higher amplitude. Each square in (b) denotes a pixel of the display.

The type of information obtained by an A-mode instrument, called an A-line and depicted in Figure 4.3(a), can be displayed in an alternative format. In a B-mode display, the echo amplitude is used to modulate the intensity of the electronic beam of the CRT monitor. Therefore, the echo amplitude is represented by the brightness or gray level of the display. Figure 4.3(b) shows a B-mode display of the A-line shown in Figure 4.3(a). Each square in Figure 4.3(b) depicts a pixel of the monitor display where the brightness is proportional to echo amplitude. It is not necessary to display the echo information in this manner.

The echo amplitude or video signal vs. gray level mapping can be made adjustable, as illustrated in Figure 4.4, depending upon the clinical application. For example, windowed gray-scale mapping may be used to enhance the image contrast of tissues in regions where there are no strong reflectors or strong echoes need to be suppressed. This is an option available in commercial scanners. An A-line or single line of the B-mode display yields information about the position of the echo, given by $d = ct/2$

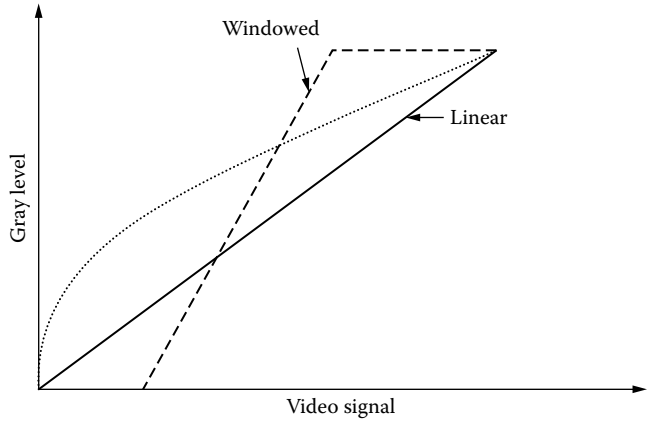

FIGURE 4.4 Various forms of gray-scale to echo-amplitude mapping.

where d is the distance from the transducer to the target; t is the time of flight or the time needed for the pulse to travel from the transducer to the target and return to the transducer; and c is the sound velocity in the tissues, which is assumed to be a constant of 1540 m/s in commercial scanners, and information about the acoustic properties of the tissues (e.g., size and acoustic impedance). Sound velocity can be assumed to be a constant because, in tissues, it does not vary significantly—typically, less than 5%, as previously discussed. This assumption sometimes may cause errors in distance, area, or volume measurements and image distortion.

A majority of commercial scanners on the market today are two-dimensional B-mode scanners in which the beam position is also monitored. Figure 4.5 shows a static B-scanner in which the position of the transducer in the x–y-plane is encoded. The positional information of the beam, plus the video signal representing echoes returned from the z-direction, is converted into a format compatible with a CRT

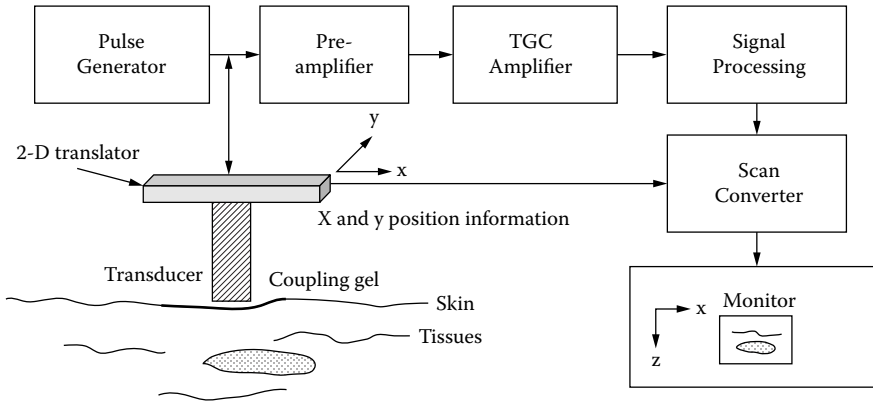

FIGURE 4.5 Block diagram of a static B-mode scanner.

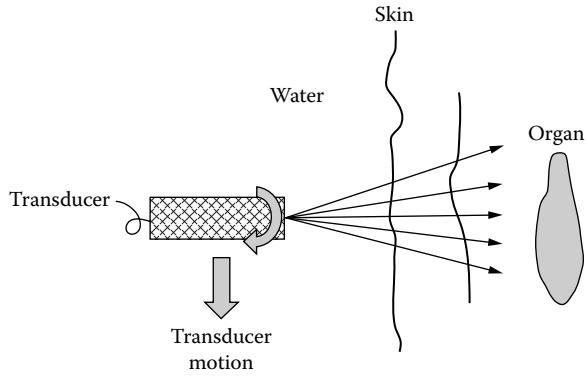

FIGURE 4.6 Compound scan is performed by combining two different modes of motion of the transducer in forming one image. In this case, the motions are linear translation and sweeping within a sector angle of the transducer.

monitor in a device, called a scan-converter, and is almost invariably digital today. If the transducer is scanned in the x-direction, the image formed represents an image of structures in the x–z-plane.

Images can also be formed by superposition of multiple images after translating and rotating the transducer at a fixed x-position within a sector angle, as illustrated in Figure 4.6. This is called compound B-scan. The advantages of doing this are to make the image look smoother or suppress the speckle pattern (which will be discussed later) and to average out the specular echoes due to flat interfaces. The disadvantage is that it slows down the image acquisition rate. Static B-scanners are no longer used today because of poor image quality due to the lack of dynamic focusing and low image acquisition rate except for high-frequency (higher than 20 MHz) applications. Modern B-mode scanners can acquire images faster than 30 frames per second to allow monitoring of organ motion.

Depending upon the mechanisms used to drive a transducer, the real-time scanners are classified into mechanical-sector and electronic-array scanners. Because electronic array systems generally produce images of better quality, modern ultrasonic scanners are almost exclusively array-based systems. Figure 4.7(a), Figure 4.7(b), and Figure 4.7(c) show a photograph of a modern ultrasonic scanner, an image produced by a linear curved array, and an image produced by a linear phased array, respectively.

The block diagram of an earlier analog B-mode imaging system is shown in Figure 4.8. A pulser is switched on to a group of elements with or without delays. The returned echoes detected by the array elements are processed by the front-end analog beam former, consisting of a matrix of delay lines, transmit/receive (T/R) switches, and amplifiers. Several components in a B-mode scanner perform the same functions as those in the A-mode system. These include the TGC amplifier and signal processing units for signal compression, demodulation, and filtering. Various forms of TGC from which the operator can choose are available on the console. The timing

(a)

(b)

FIGURE 4.7 (a) A photo of a modern ultrasonic scanner. (b) An image of a fetus *in utero* obtained by a linear curved array. The head and a limb of the fetus can be clearly seen. (c) A four-chamber view of the heart obtained from the apex of the heart with a phased array. (Courtesy of Philips Ultrasound.)

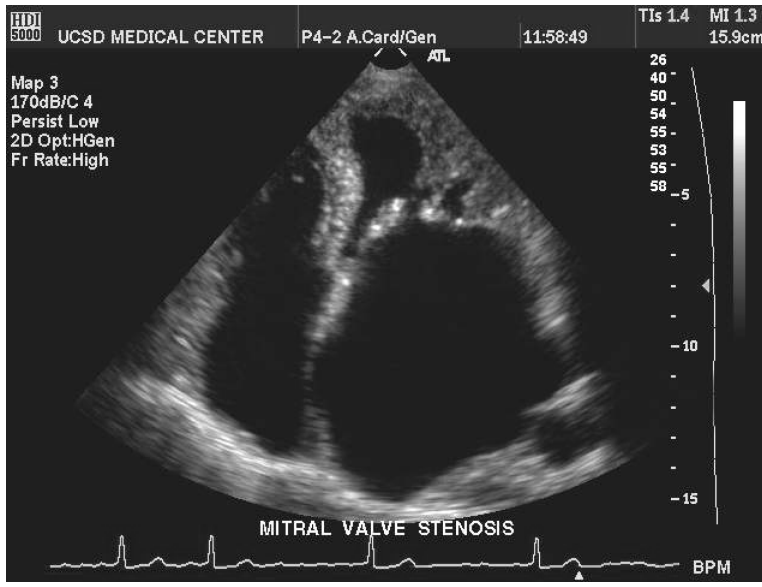

(c)

FIGURE 4.7 (Continued).

and control signals are all generated by a central unit. The image is displayed on a storage monitor.

In later systems, shown in Figure 4.9, after signal processing, the signal is digitized by an analog to digital (A/D) converter. In high-end systems, a digital beam former (Figure 4.10) is used. The A/D conversion following preamplification is accomplished in the beam former. This makes the system much more expensive

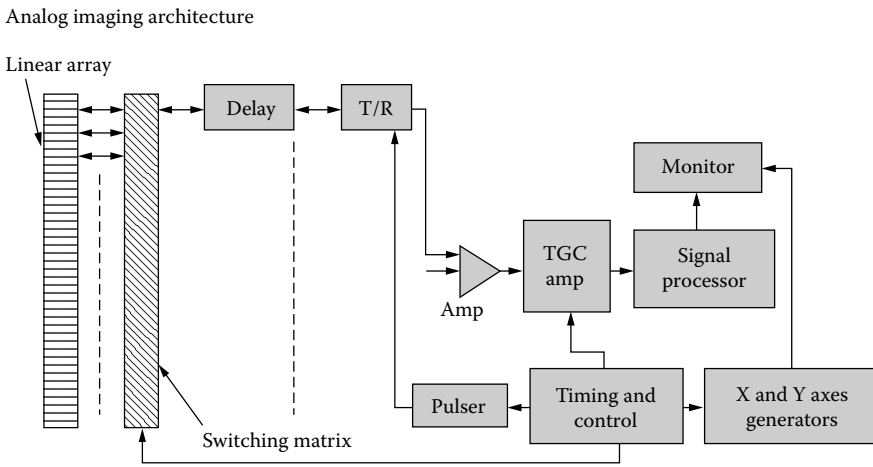

FIGURE 4.8 Block diagram of an analog ultrasonic imaging system developed in the 1970s.

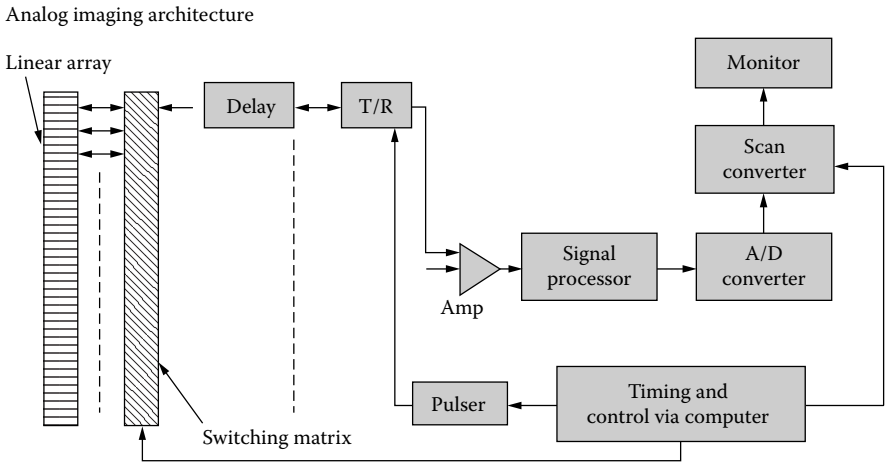

FIGURE 4.9 Block diagram of an ultrasonic imaging system that utilizes an analog beam former.

because many more A/D converters of a higher sampling rate are required. The accuracy of the A/D conversion is determined by the number of bits of the A/D converter. An 8-b A/D converter digitizes the signal into $2^8 = 256$ gray levels. For better contrast resolution, more bits are needed. High-end machines display more than 256 gray levels. The scan converter is a digital memory device that stores the data converted from the format in which they were collected into a format that can be displayed by a monitor. Before display, the video data may be processed again via band pass filtering, high pass filtering, low pass filtering, gray-scale mapping, etc.

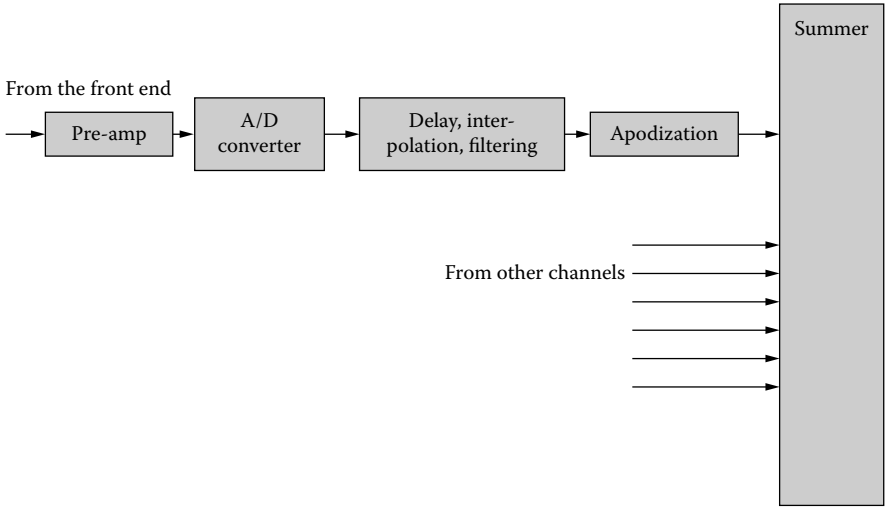

FIGURE 4.10 Block diagram of a digital beam former.

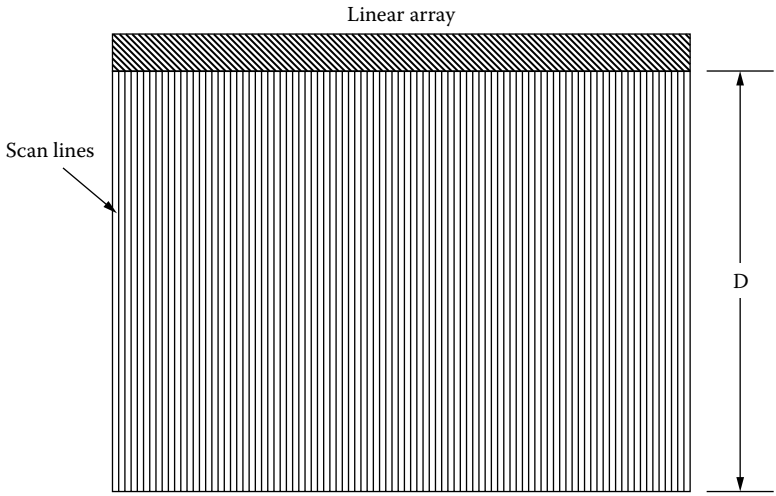

FIGURE 4.11 Image format obtained by a linear array.

Signal processing performed before and after the scan converter are called pre- and postprocessing, respectively.

For most of the B-mode scanners, only one ultrasound pulse is transmitted at any one instant of time. As seen from Figure 4.11, the time needed to form one frame of image, t_f, can be readily calculated from the following equation:

$$t_f = \frac{2DN}{c} \tag{4.1}$$

where

D is the depth of penetration determined by the pulse repetition frequency of the pulser
N is the number of scan lines in the image
c is the sound speed in tissue

Rearranging this equation,

$$FDN = \frac{c}{2} \tag{4.2}$$

where $F = 1/t_f$ is the frame rate.

The depth of penetration, D, is specified by the pulse repetition period of the scanner, which should be long enough to allow all the echoes of interest to be detected. Range ambiguity can result if the pulse repetition period is too short. For instance, range ambiguity (i.e., it is not clear which pulse causes the echo from the object) can occur if the time of flight from an object of interest is longer than the pulse repetition period.

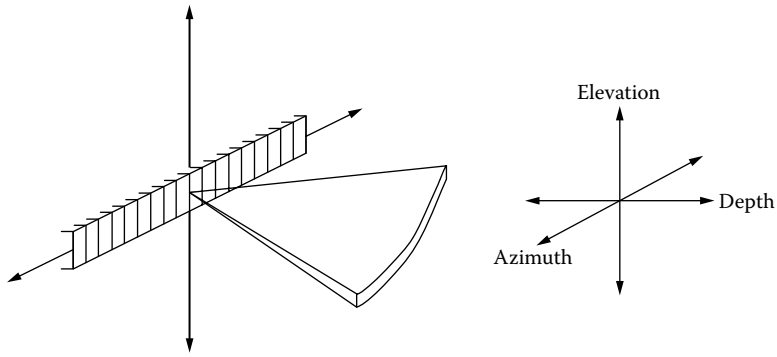

FIGURE 4.12 Image format obtained by a phased array.

Looking at Equation (4.2), it is readily apparent that, to change any one of the *F*, *D*, and *N* parameters, the rest will be affected because sound velocity in tissues is assumed to be a constant. One example is that, if the depth of penetration is increased, the frame rate or the number of scan lines must be reduced.

4.1.1 Resolution of B-Mode Ultrasonic Imaging Systems

The resolution of a B-mode imaging system in the imaging or the azimuthal plane is determined by the duration of the pulse in the depth direction (i.e., in the direction of the beam) and the width of the ultrasonic beam in the lateral direction (i.e., in the direction perpendicular to the beam), as previously discussed. The slice thickness of the imaging plane or the beam width in the elevation plane is fixed and determined by the lens properties. Figure 4.12 shows the image format obtained by a phased array.

4.1.2 Beam Forming

In real-time imaging with linear arrays, the ultrasonic beam can be dynamically focused and steered by applying appropriate time delays to the transmitted pulses or/and received echoes utilizing Equation (3.33), as illustrated in Figure 3.27, which shows the top view of several elements of a linear array. Equation (3.33) can be obtained by considering that the difference in path length between the *n*th element and the center element is $\Delta r = r_n - r$, where from the cosine law, r_n given by

$$r_n = \left[r^2 + x_n^2 - 2rx_n \cos(90^0 + \phi_x) \right]^{1/2}$$

$$= \left[r^2 + x_n^2 + 2rx_n \sin(90^0 + \phi_x) \right]^{1/2}$$

$$\therefore \Delta r_n = r \left[\frac{\left(r^2 + x_n^2 + 2rx_n \sin\phi_x \right)^{1/2}}{r} - 1 \right]$$

By making the assumption that $r >> x_n$—that is, the point P is in the far field of the array—and using the approximation $(1 + x)^{1/2} \sim 1 + (1/2)x$ for $x \sim 0$, this equation can be simplified to

$$\therefore \Delta r_n \approx x_n \sin\varphi_x + \frac{x_n^2}{2r}$$

The timing needs to be adjusted to make the transmitted pulse emitted by each element relative to other elements to arrive at the point P at the same time. The time delay of the transmitted pulse to the center element relative to the nth element is therefore given by Equation (3.33), which is

$$\Delta t_n = \Delta r_n / c \approx \frac{x_n \sin\varphi_x}{c} + \frac{x_n^2}{2cr}$$

where the first and second terms represent the time delays needed for achieving beam steering and focusing, respectively.

The same criteria can be applied to the receiving beam or the echo returned from point P. A delay of Δt_n to the echo received by the center element is needed to make the echo and the echo received by the nth element being summed at the same time, illustrated in Figure 3.28.

This time delay function is one of the functions provided by the beam former of the ultrasonic imaging system. Other functions of the beam former are weighting and apodization of the transmitted and received signals. In earlier days, beam forming was predominantly accomplished with analog devices or by analog beam formers. The problems with these devices are bulky delay lines, incapability of finer delays, electrical impedance mismatch, limited bandwidth, switching transients, and insertion loss.

Digital beam formers are used today in most high-end systems. A digital beam former is primarily a sampling–delay–sum–detection process as opposed to the delay–sum–detection–sampling process in analog systems. As was discussed, a drawback of the digital beam formers is their cost, which increases with the number of array elements and electronic channel counts. Currently, digital beam formers in commercial scanners sampled the data at 20 to 40 MHz to 8 to 12 b.

Mathematically, the beam-forming function can be summarized by the following equation (Thomenius, 1996):

$$e(t) = \sum_{i=1}^{N} A_{ri} \sum_{j=1}^{N} A_{tj} V\left[t - \Delta t_{ri} - \Delta t_{tj} + \frac{2r(t)}{c}\right] \tag{4.3}$$

where

$e(t)$ is the summed echo waveform at the summing amplifier
$V(t)$ is the transmitted waveform

N is the number of array elements
$r(t)$ is the focal distance at a particular time
A_{ri} and A_{tj} are the weighting functions for reception at channel i and transmission at channel j
Δt_{tj} and Δt_{ri} are the time delays applied during transmission and reception to elements j and i, respectively

For uniform excitation and receive weighting, $A_{tj} = 1$ and $A_{ri} = 1$. For systems that use fixed transmission focusing, this equation is reduced to

$$e(t) = \sum_{i=1}^{N} A_{ri} V\left[t - \Delta t_{ri} + \frac{2r(t)}{c}\right] \tag{4.4}$$

4.1.3 Speckle

The B-mode ultrasonic images exhibit a granular appearance, called speckle pattern, which is caused by the constructive and destructive interferences of the wavelets scattered by the tissue components as they arrive at the transducer surface (Wagner et al., 1983; Shung and Thieme 1993). This speckle appearance very much resembles the speckle pattern that results from laser scattering by a rough surface. If the incident ultrasound beam is totally coherent like the laser beam, the speckle carries no information about the microstructure of the tissues. Fortunately, ultrasonic scanners use partially coherent incident waves, i.e., pulses. Thus, the speckle patterns exhibited by tissues contain useful information about the structures of the tissues that can be used clinically for tissue differentiation.

The resemblance between laser and ultrasound speckles has been extensively analyzed (Wagner et al., 1983). The histogram of the video signals or echo amplitude returned from tissues or the number of occurrences plotted as a function of the amplitude of these echoes, V, follows a Rician distribution (shown in Figure 4.13) similar to the distribution of the magnitude of a phasor $V = X + jY$ with a uniform phase. The symbol σ^2 denotes the variance of the real component, X, or imaginary component, Y. This means that the signal contains random and ordered components. If there are no ordered components, the histogram should follow a Rayleigh distribution given by

$$P(V) = \frac{V}{2\pi\sigma_V^2} e^{-\frac{V^2}{2\sigma_V^2}} \quad \text{for } V \geq 0$$

where $V^2 = X^2 + Y^2$, and σ_V^2 , the variance of the magnitude of a phasor V, $= (2 - \pi/2)$ $\sigma^2 = 0.42\ \sigma^2$. Here, $\sigma^2 = \langle X^2\rangle - \langle X\rangle^2$. $\langle X\rangle$ denotes the mean of X. It can be easily found that $\langle V\rangle = 1.91\ \sigma_V$. This means that the signal-to-noise ratio for a Rayleigh distributed signal would be a constant at 1.91.

The question of whether the speckle is a friend or foe has been debated for many years. On the one hand, speckles provide diagnostic information for clinicians to make a diagnosis. A clear example is that different organs exhibit different speckle

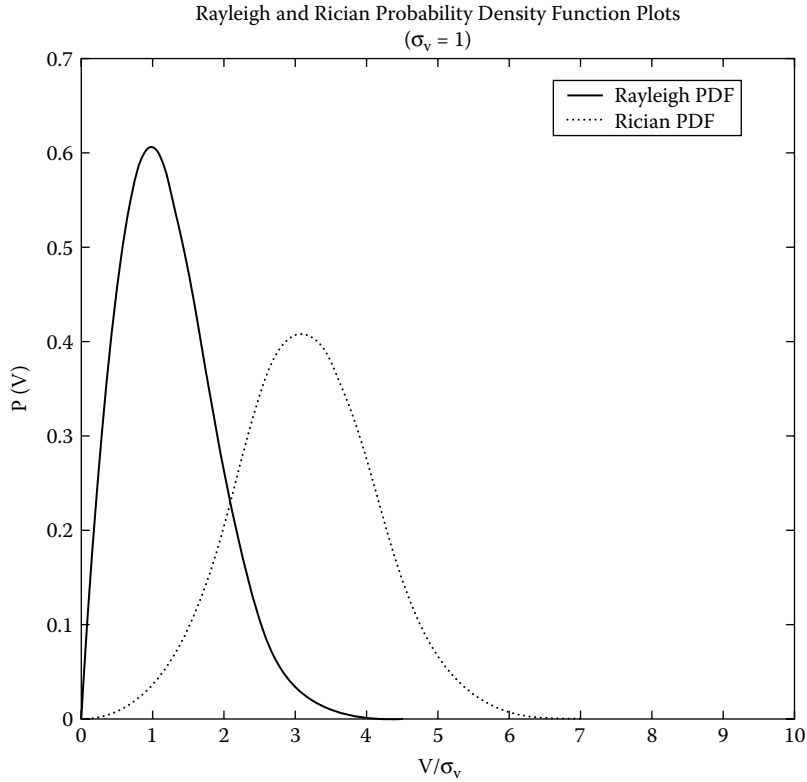

FIGURE 4.13 Histograms or probability density function (PDF) of echo amplitude from biological tissues follow a Rician distribution (dashed line), a special form of which is the Rayleigh distribution (solid line). $P(V)$ is the probability density at an amplitude, V, and σ_v is the variance of V.

or textural patterns and tumors frequently exhibit different speckle patterns from normal tissues. On the other hand, speckles degrade spatial resolution of the imaging system. Smaller objects may be obscured by the speckles. The most optimal resolution appears to smooth out somewhat the speckle pattern while maintaining as much as possible the spatial resolution and the frame rate. Frame averaging via spatial compounding or frequency compounding has been studied and implemented in commercial scanners. Spatial or frequency compounding describes a signal processing method in which multiple frames are acquired at different imaging angles or spatial positions or at different frequencies and subsequently averaged to form one frame of image.

4.1.4 Image Quality

The most objective way of assessing the image quality of an ultrasound system is to use the operator receiving characteristics (ROC) curves (Shung et al., 1992), in which human involvement is included. To be meaningful statistically, many subjects

need to be studied to obtain a measurement in which inter- and intraobserver variations are considered. Although this approach is the most desirable, it is very complicated and expensive. Simpler but quantitative measures such as spatial resolution and contrast resolution are often preferred. The spatial resolution can be assessed by imaging standardized targets or phantoms consisting of point or wire targets embedded in water- or tissue-mimicking gels. The spatial resolution measured this way depends strongly upon the instrument settings. A more convenient approach is to determine the point spread function of the system.

4.1.4.1 Point Spread Function

The point spread function of an imaging system (Shung et al., 1992) is the spatial point response, which is the inverse spatial Fourier transform of the spatial transfer function of an imaging system if it can be treated as a linear system. Suppose that the point spread function and the spatial transfer function of an imaging system can be denoted as $h(\mathbf{x})$ and $H(\boldsymbol{\nu})$, respectively, where $\mathbf{x}$ and $\boldsymbol{\nu}$ are vectors representing spatial distance with a unit of centimeters and spatial frequency with a unit of cycles per centimeter. The input (the object to be imaged), S, and output (the image acquired by the imaging system), O, are related by the following equation in the spatial frequency domain:

$$O(\boldsymbol{\nu}) = H(\boldsymbol{\nu})S(\boldsymbol{\nu}) \tag{4.5}$$

In the spatial domain, their relationship is given by

$$o(\mathbf{x}) = h(\mathbf{x}) * s(\mathbf{x}) = \int_{-\infty}^{\infty} s(\mathbf{x})h(\mathbf{x}-\chi)\,d\chi \tag{4.6}$$

where * denotes convolution.

The point spread function of an ultrasound system can be assessed by imaging a small point target embedded in a homogeneous gel medium or a point target suspended in a water bath and mapping the gray level of the image. Figure 4.14 shows the gray level of such an image as a function of one dimension of the spatial vector, $\mathbf{x}$, represented by x_1. System I, which has a sharper point spread function, should have a better resolution than System II.

4.1.4.2 Contrast

Spatial resolutions of an imaging system are also affected by other parameters, including noise and the contrast of the object to be imaged. Figure 4.15 shows a spherical void with scattering property, which may be represented by η_o—the backscattering coefficient, as discussed in Chapter 2—surrounded by a background medium with backscattering coefficient η_m. The object contrast may be defined as

$$\gamma_o = \frac{\eta_o - \eta_m}{\eta_0} \tag{4.7}$$

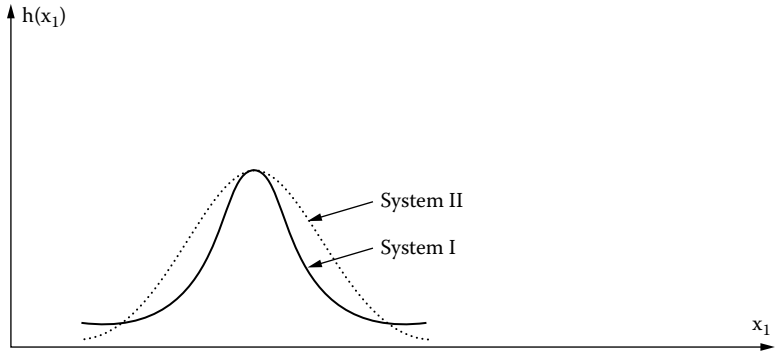

FIGURE 4.14 Point spread functions of two imaging systems represented by gray-scale distributions as a function of one spatial dimension. System I has a narrow point spread function and therefore better spatial resolution than System II.

The image contrast is defined as

$$\gamma_i = \frac{g_o - g_m}{g_0} \tag{4.8}$$

where g_o and g_m denote the video signals or gray levels of the object and background.

A good imaging system would enhance or accentuate the object contrast. The minimum contrast required for an imaging system to detect the object of a specific size in the presence of image noise is called the contrast resolution. These two parameters are interrelated. A system with superior resolution for high-contrast objects may not be capable of maintaining the same resolution as the contrast is reduced.

Side lobes and grating lobes produced by a single-element transducer or array as discussed in Chapter 3 are undesirable because they would degrade the contrast resolution of an ultrasonic imaging system. Consider the example of the spherical void phantom. The echoes resulting from the side lobes or grating lobes will contribute to the echoes generated by the main lobe or beam. For a void with no

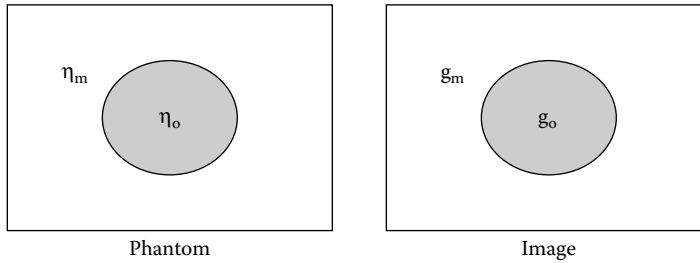

FIGURE 4.15 Diagram denoting a spherical void phantom with a scattering property different from the surrounding medium and the corresponding image.

scatterers, like a cyst, these echoes produced by the side or grating lobes will appear in the void, reducing the contrast between the void and the surrounding medium.

4.1.4.3 Noises

An ultrasonic imaging system has two sources of noises: acoustic noises produced by the transducer/array and spurious acoustic interactions and electronic noises produced by the imaging system. Acoustic noises may result from the cross-talk among elements in an array and between the active element(s) and the support structures, from spurious reflections and refractions, and from grating and side lobes. The electronic noises are generated by the cross-coupling of cables and electronic elements, and active devices. Typically, acoustic noises are larger and more troublesome than electronic noises.

4.1.5 Phase Aberration Compensation

In commercial scanners, the sound velocity in tissues is assumed to be a constant. This could cause image degradation if the sound velocity of a region of tissues deviates substantially from this assumed value. It is known that fat and skin velocities differ appreciably from 1540 m/s. The predetermined time delays calculated with the assumed velocity in the beam former may not be sufficiently accurate to achieve proper focus. Various methods have been used to compensate for this aberration caused by the phase difference of the pulses arriving at the transducers or arrays (Flax and O'Donnell, 1988; Nock and Trahey, 1989).

One method uses a region of a tissue with prominent features, e.g., a blood vessel, as a target. The arrival times of all returned echoes at each element of an array are adjusted via cross-correlation of echoes or pulses returned from the target region. Another method compensates for the velocity difference by adjusting the delays of the arriving echoes until the brightness from a region of tissues is maximized. These methods have been demonstrated to be capable of improving image quality under certain conditions. They have found very limited use because they slow the frame rate and the improvement is marginal. One reason for the limited success has been attributed to the fact that the phase difference in the elevation plane cannot be compensated. Implementation of phase aberration compensation with multidimensional arrays is under way and may yield fruitful results.

4.1.6 Clinical Applications

B-mode ultrasound has numerous applications because it is noninvasive and can display two-dimensional cross-sectional images of anatomical structures in real time. Some of the many applications of B-mode ultrasound include:

- Obstetrics for monitoring the status of the fetus
- Gynecology for diagnosing problems in the ovary
- General radiology for diagnosing liver tumors and gall bladder diseases

- Vascular surgery for detecting arterial stenosis and deep vein thrombosis and for characterizing atherosclerotic plaques
- Cardiology for diagnosing valvular diseases and monitoring the integrity of cardiac wall functions

4.2 M-MODE AND C-MODE

In M-mode display, one intensity-modulated A-line or one B-line is swept across the monitor as a function of time at a rate much slower than the pulse repetition frequency (PRF) of the A-line, as illustrated in Figure 4.16. The sweep of the electron beam in the *x*-axis is controlled by a slow ramp generator; the triggering of the *y*-axis is synchronized with the pulser. The rest of the device is similar to the A-mode device. In this format, the ultrasound beam is fixed at a certain position or angle and the displacement of a target relative to the probe along the beam direction is displayed as a function of time. The motion of a swinging pendulum at positions a, b, and c can be clearly discerned on the display. This type of display is most useful for monitoring the motion of anatomical structure—for example, valves in the heart. Figure 4.17 shows the M-mode display of a mitral valve prolapse, an abnormal displacement of the valvular leaflets.

C-mode is a form of display similar to conventional radiography if a second transducer is used to detect the pulse after traversing a medium (illustrated in Figure 4.18). The image obtained is then a two-dimensional gray-scale map of the

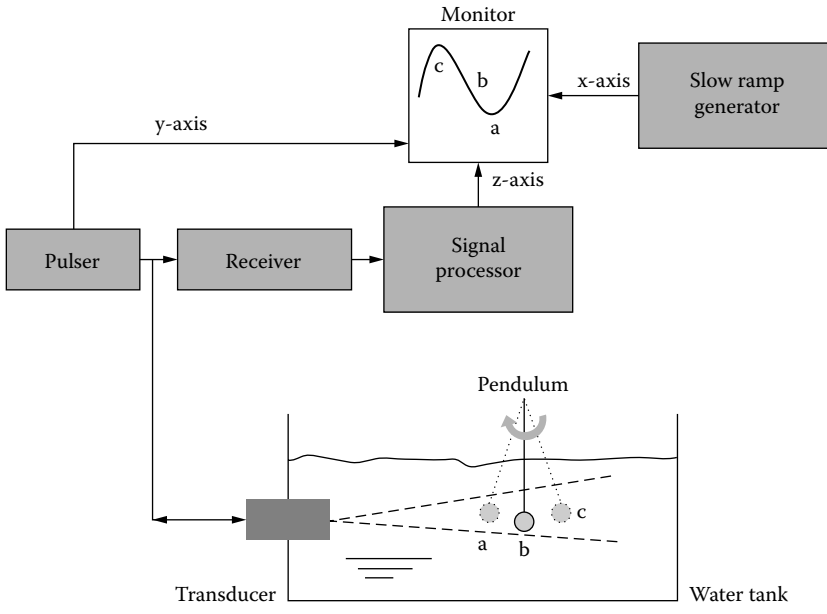

FIGURE 4.16 Block diagram of an M-mode ultrasonic imaging system.

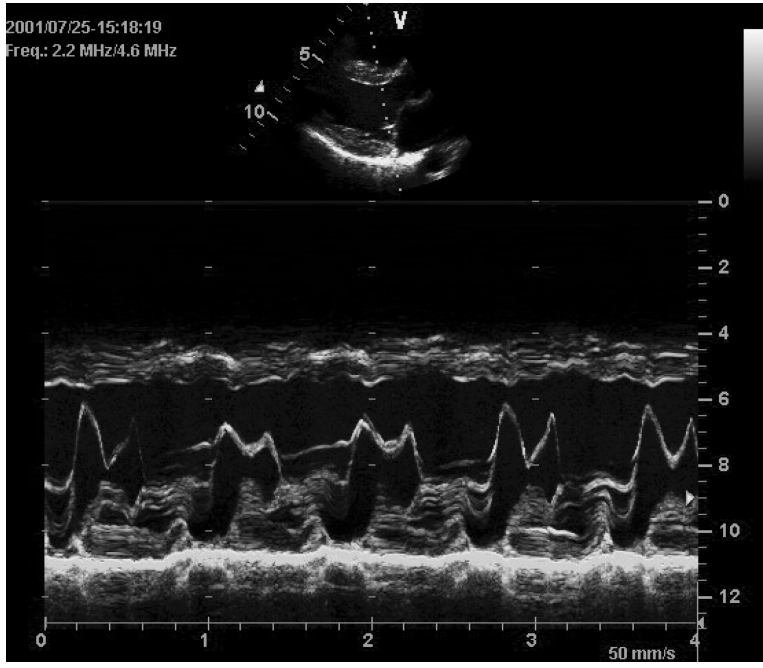

FIGURE 4.17 M-mode image of a mitral valve prolapse. The top of the figure is a B-mode display of the heart. The white line indicates the ultrasound beam direction along which the M-mode image in the bottom is acquired. (Courtesy of GE Medical Systems.)

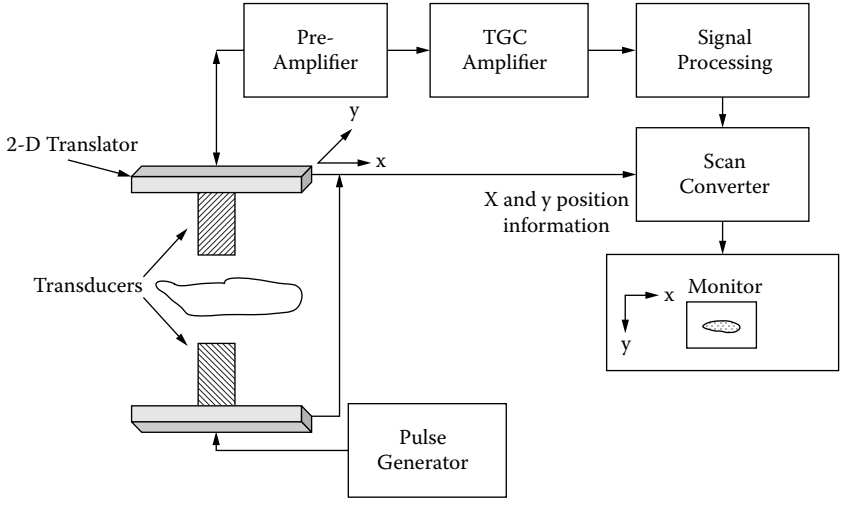

FIGURE 4.18 Block diagram of a C-mode ultrasonic imaging system.

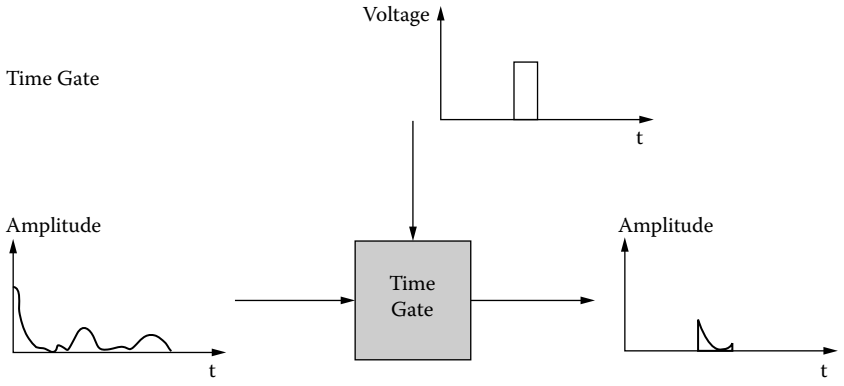

FIGURE 4.19 Time gate performs the function of turning on and off a signal in time.

ultrasonic attenuation coefficient experienced by the pulse in the object. Reflection type of C-mode ultrasonography is also possible by using time gating to select only the echoes that originate from a certain plane or at a constant depth relative to the transducer.

The concept of time gating is illustrated in Figure 4.19. The time gate is primarily a switch that is turned on by an external pulse and allows the input waveform to pass. The output signal consists of only the input waveform within the time duration when the gate is on. C-mode display is seldom used in clinical scanners but is quite popular in acoustic microscopy that can be operated in B-mode or in C-mode at frequencies ranging from 40 MHz to 3 GHz. Acoustic microscopy has many applications in nondestructive evaluation of materials such as integrated circuits, but is of only limited interest in biomedicine.

4.3 ULTRASOUND COMPUTED TOMOGRAPHY (CT)

Computed tomography has been successfully used in x-ray and magnetic resonance imaging to produce tomograms, defined as two-dimensional images of two-dimensional slices. CT principle is quite straightforward and can easily be implemented once the signals are digitized so that they can be processed with a computer (Shung et al., 1992). A two-dimensional object of interest is divided into many pixels or voxels in three dimensions. The property of the pixel can be retrieved by performing multiple measurements at different positions or angles with the imaging system. For x-ray CT, x-ray generators and detectors are used to perform such measurements to estimate the x-ray attenuation coefficients of all pixels. An image is formed from mapping the estimated attenuation coefficient to a gray scale. It is plausible that CT principle can be readily extended to ultrasound. The feasibility of ultrasound CT has been studied for many years (Greenleaf, 1983).

Two types of ultrasound CT images (attenuation CT and velocity CT) can be obtained because ultrasound propagation in a tissue is affected by attenuation and sound velocity. The difference is that, in one, the ultrasound property in a pixel to be

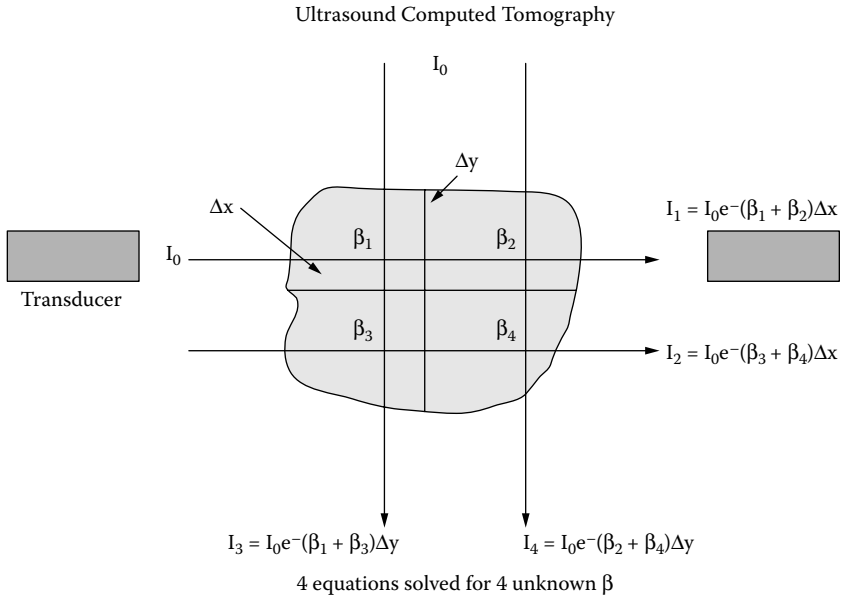

FIGURE 4.20 Graphical illustration of ultrasound CT principle.

estimated is sound velocity, whereas in the other attenuation is estimated. A graphical illustration of ultrasound attenuation CT is shown in Figure 4.20. One transducer is used as a transmitter and the other as a receiver. The object of interest is divided into four pixels, each assigned an intensity attenuation coefficient denoted by $\beta = 2\alpha$. The pixel dimensions are represented by Δx and Δy. The transmitted intensities are exponentially related to the incident intensity, as discussed in Chapter 2. The transmitter and receiver assembly is translated and then rotated to collect multiple sets of data. In Figure 4.20, only four sets of data are shown. The data sets are inverted to extract the ultrasound properties, assuming that Δx and Δy are equal (this is a valid assumption when the number of pixels is large).

Mathematical iteration, among a host of methods, has been used to accomplish the data inversion (Shung et al., 1992). Ultrasound CT has achieved limited success to date. The reason is twofold. First, the ultrasound beam cannot be approximated as a pencil beam because it is refracted as it propagates through an interface. In addition, it suffers losses not only due to attenuation but also due to reflection at tissue interfaces and beam diffraction. Second, ultrasound cannot penetrate into regions of the body that contain bones and air. Even so, ultrasound CT has been envisioned to have potential applications in imaging organs such as the breast and testicle.

4.4 CODED EXCITATION IMAGING

The instantaneous intensity of the transmitted pulse and the energy contained in the pulse are regulated by the FDA and are thus limited because of the concern with potential bioeffects. Therefore, although increasing the pulse energy will increase

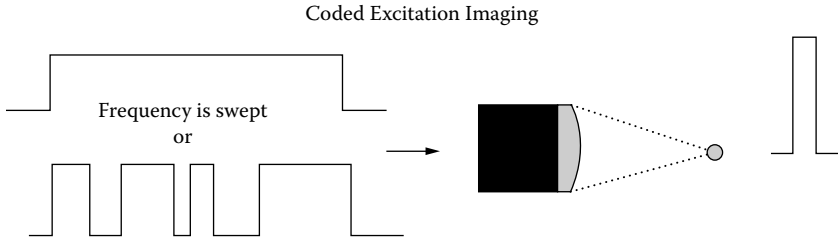

FIGURE 4.21 Excitation signals to the transducer of an ultrasonic imaging system may be encoded by frequency or pulse duration. The resultant benefit is the increased ultrasonic energy imparted into the body because of the longer exposure duration and thus the improved signal-to-noise ratio and increased depth of penetration.

the signal-to-noise ratio of the returned echoes, this simply cannot be done and is not a valid alternative in biomedical imaging. To overcome this limitation, several scanner manufacturers have adopted a novel approach in which the increased energy is spread over a longer time duration while maintaining the instantaneous intensity level. This form of imaging uses a transmitted signal consisting of chirp of coded pulses (shown in Figure 4.21) (O'Donnell, 1992). The coded pulses can be frequency modulated or pulse duration modulated. The returned echoes are matched with the excitation codes to retrieve the pulse amplitude. The benefit of coded excitation imaging is the increased depth of penetration at the cost of increased complexity, reduced frame rate, and inferior axial resolution. These problems have now been largely overcome. Coded excitation image quality is comparable to that obtained with conventional B-mode imaging.

4.5 COMPOUND IMAGING

As was discussed in previous sections, a compound scan can suppress speckle pattern, thus improving contrast and image quality at a cost of reduced scanning speed. During the time when static scanners were the work horses, this was indeed a problem. Increased speed in electronics and computer processing has allowed this to be achieved in real time with linear arrays. The beam is electronically steered into multiple directions and images superimposed. The superior image quality resulting from compounding is apparent. An image obtained with compound imaging is shown in Figure 4.22.

4.6 SYNTHETIC APERTURE IMAGING

To reduce the cost in beam forming for arrays in which hundreds of electronic channels are needed, synthetic aperture imaging can be used (Karaman and O'Donnell, 1995). This type of imaging can be accomplished in "receive" only or in "transmit and receive." Synthetic aperture imaging during "receive" is illustrated in Figure 4.23, in which four linear elements are shown. All four elements are excited simultaneously for transmission to achieve the largest aperture that is required to obtain the best lateral

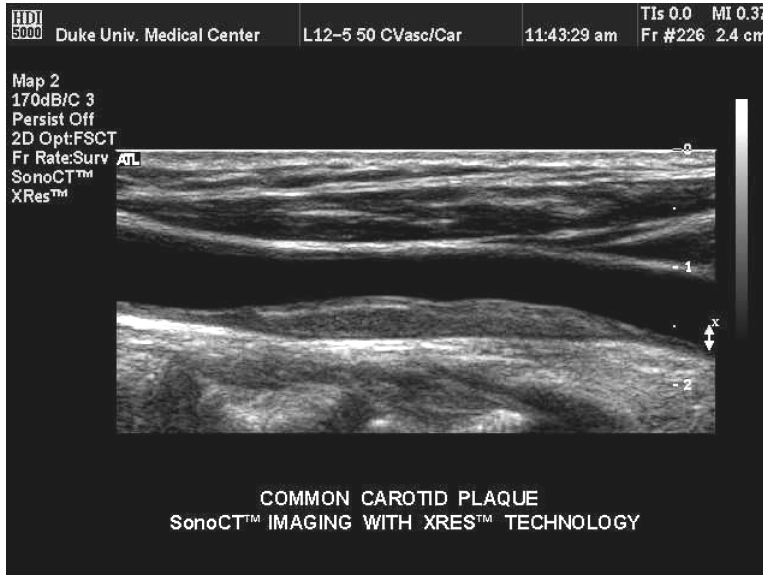

FIGURE 4.22 An image of a carotid artery containing an atherosclerotic plaque obtained by real-time compound scanning. (Courtesy of Philips Medical Systems.)

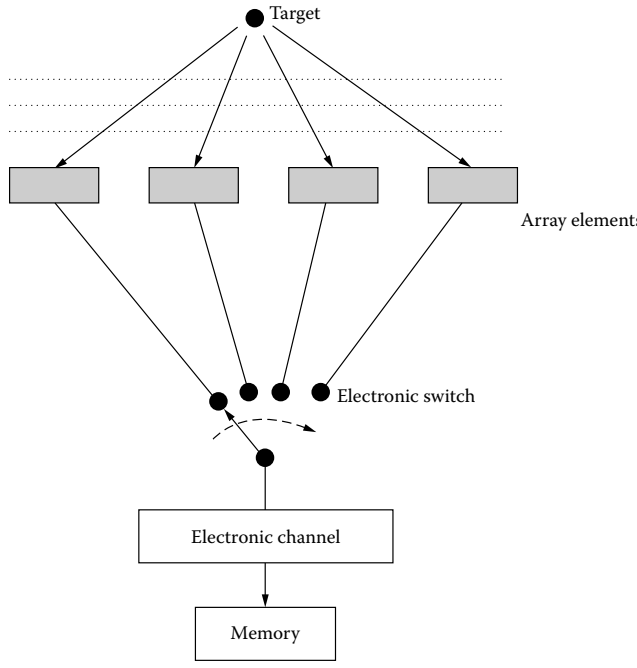

FIGURE 4.23 Synthetic aperture imaging during reception.

resolution. During reception, a switch is used to sample the waveform detected at each element so that only one channel of electronics is needed, in contrast to conventional imaging in which four channels are needed. The data from all elements can be stored in a memory for later processing; this includes applying the delays for focusing, filtering, and scan conversion. The advantages of synthetic aperture imaging are reduced cost and complexity, which are important in such cases as intravascular imaging, in which the disposable probe is so small that it is impossible to mount a large number of integrated circuits in the probe.

REFERENCES

Flax, S.W. and O'Donnell, M. Phase-aberration correction using signals from point reflectors and diffuse scatterers: basic principles. *IEEE Trans. Ultrason. Ferroelect. Freq. Contr.* 1988, 35:768–778.

Greenleaf, J.F. Computerized tomography with ultrasound. *Proc. IEEE* 1983, 71:330–337.

Karaman, M. and O'Donnell, M. Synthetic aperture imaging for small scale systems. *IEEE Trans. Ultrason. Ferroelect. Freq. Contr.* 1995, 42:429–442.

Nock, L. and Trahey, G.E. Phase aberration correction in medical ultrasound using speckle brightness as a quality factor. *J. Acoust. Soc. Am.* 1989, 85:1819–1826.

O'Donnell, M. Coded excitation system for improving the penetration of real-time phased array imaging system. *IEEE Trans. Ultrason. Ferroelect. Freq. Contr.* 1992, 39:341–351.

Shung, K.K., Smith, M.B., and Tui, B.W.N. *Principles of Medical Imaging*. San Diego: Academic Press, 1992.

Shung, K.K. and Thieme, G.A. *Ultrasonic Scattering by Biological Tissues*. Boca Raton, FL: CRC Press, 1993.

Thomenius, K.E. Evolution of ultrasound beam formers. In Levy, M., Schneider, S.C., and McVoy, B.R., Eds. *Proc. 1996 IEEE Ultrason. Symp*. New York: IEEE, 1996, 1615–1622.

Wagner, R.F., Smith, S.W., Sandrik, J.M., and Lopez, H. Statistics of speckle in ultrasound B-scans. *IEEE Trans. Sonics Ultrason*. 1983, 30:156–163.

5 Doppler Flow Measurements

As was discussed earlier in Chapter 2, the Doppler effect provides a unique capability for ultrasound to measure blood flow (Evans and McDicken, 2000, Jensen, 1996). Upon insonification by an ultrasound beam, the echoes scattered by blood carry information about the velocity of blood flow. Blood flow measurements are frequently performed in a clinical environment to assess the state of blood vessels and functions of an organ. Ultrasonic Doppler instruments allow a measurement of instantaneous blood flow velocity. Combined with pulse–echo instruments, instantaneous flow rate in a blood vessel as a function of time and cardiac output can be measured noninvasively with ultrasound. At present, very few clinical options are available to do so.

Figure 5.1 shows an ultrasound beam of frequency f insonifying a blood vessel making an angle of θ relative to the velocity, v. Here it is assumed that blood flows in a vessel with a uniform velocity v. The returned echoes are Doppler shifted. The Doppler shift frequency, f_d, is related to the ultrasound frequency, f, by Equation (2.43):

$$f_d = \frac{2v\cos\theta}{c} f$$

where c is the sound velocity in blood and may be assumed to be 1540 m/s. The Doppler-shifted frequencies happen to be in the audio range for blood flow velocities in the human body for an ultrasound frequency between 1 and 15 MHz.

Conventionally, two different approaches have been used for ultrasonic Doppler flow measurements: continuous wave (CW) and pulsed wave (PW) Doppler.

5.1 NONDIRECTIONAL CW FLOW METERS

A CW system is shown in Figure 5.2. A probe consisting of two piezoelectric elements, one for transmitting the ultrasound signal and one for receiving echoes returned from blood, is excited by an oscillator. The Doppler-shifted echoes are amplified, demodulated, and band-pass filtered to remove the carrier frequency and other spurious signals. Suppose that the ultrasound signal generated by the oscillator is given by $A\cos(\omega t)$, where A denotes signal amplitude and ω, the angular frequency, = 2πf. The demodulated signal would be

$$g_d(\omega, \omega_d) = A\cos(\omega t) B\cos[(\omega + \omega_d)t] = \frac{1}{2} AB\{\cos[(2\omega + \omega_d)t] + \cos(\omega_d t)\}$$

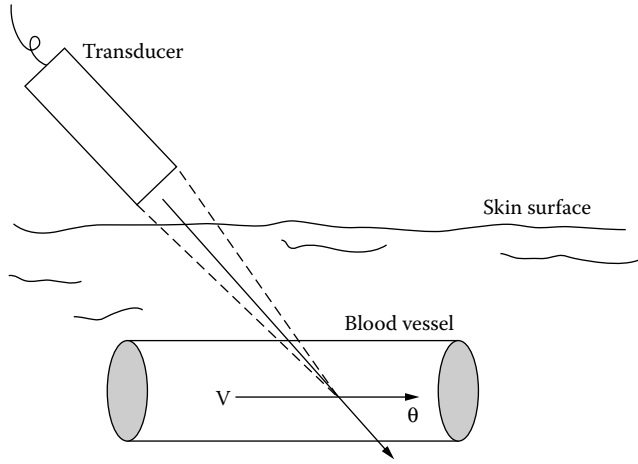

FIGURE 5.1 An ultrasound beam is incident upon a blood vessel and makes an angle of θ relative to the direction of blood flow.

where the echoes are represented by $B\cos[(\omega + \omega_d)t]$ and $\omega_d = 2\pi f_d$. The magnitude of constant B is determined by the scattering strength of blood.

Much work has been done to better understand the relationship between the Doppler power generated by blood and hematological and hemodynamic factors (Shung et al., 1992; Mo and Cobbold, 1993). Doppler power from blood has been

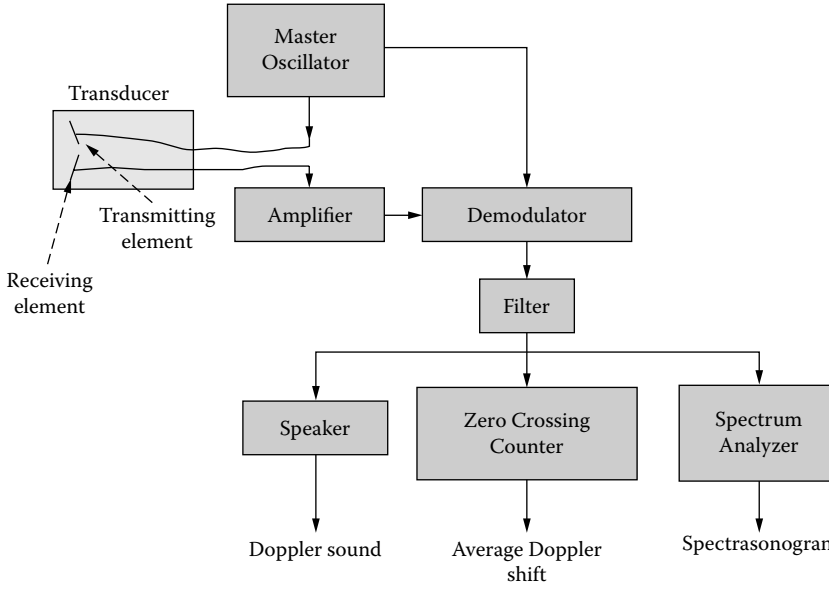

FIGURE 5.2 Block diagram of a CW Doppler flow meter.

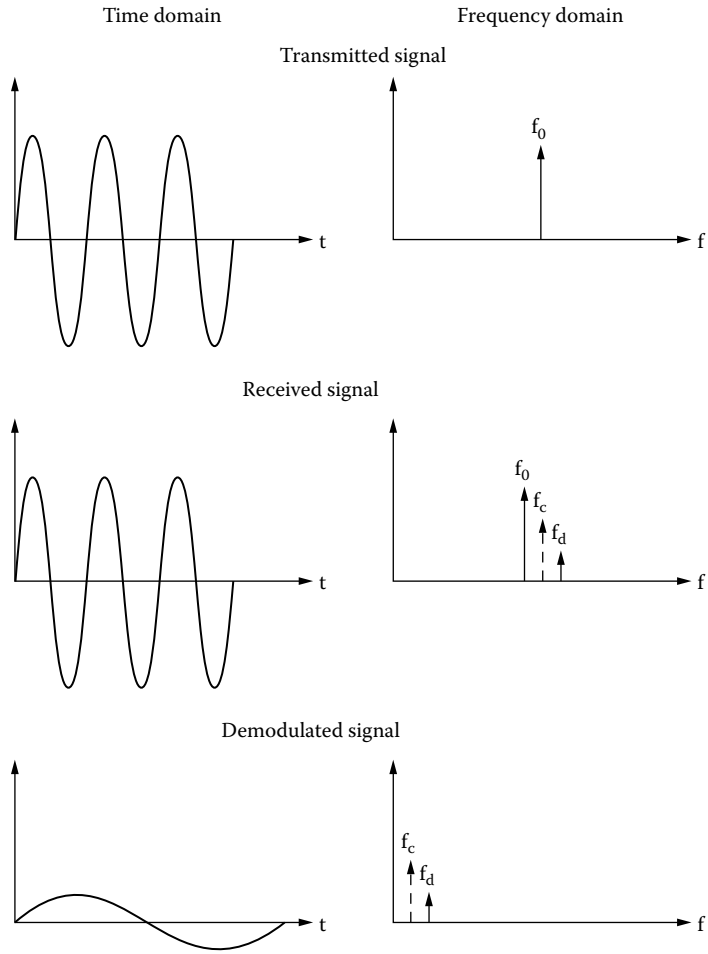

FIGURE 5.3 Doppler signals in the time and frequency domain showing the effect of demodulation.

found to be related to flow disturbance, hematocrit, and the degree of red blood aggregation; this is in turn affected by the concentration of plasma proteins such as fibrinogen and local shear rate. The output of the demodulator contains the ultrasound carrier frequency and the Doppler shift, as illustrated in Figure 5.3, where the signals in the time and frequency domains are shown on the left and right, respectively. The carrier signal can be readily removed by band-pass filtering by setting the cut-off frequency of the band-pass filter at the high end to be much lower than the carrier frequency.

A problem in ultrasonic Doppler blood flow measurement is that the blood vessels that produce large reflected echoes are slow moving as well. In Doppler terminology, these large, slow-moving echoes are called clutter signals (shown in Figure 5.3 as f_c). The cut-off frequency of the band-pass filter at the low end must

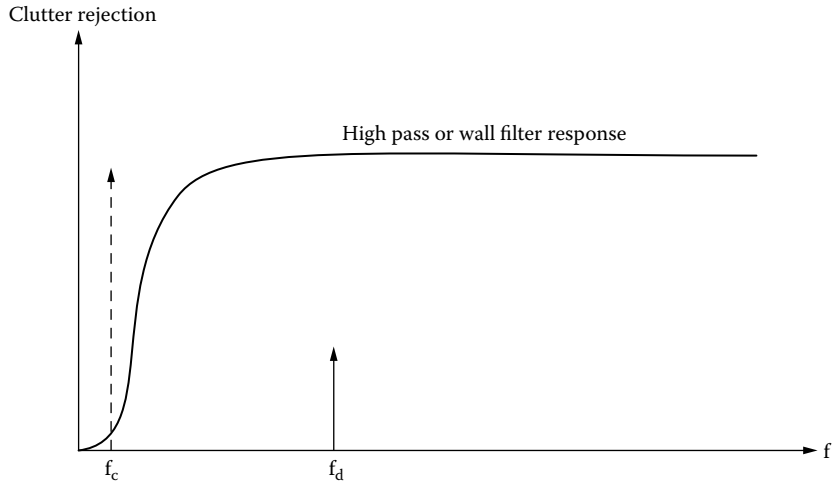

FIGURE 5.4 Clutter rejection filter or wall filter is used to suppress large echoes produced by slow moving blood vessel walls.

be designed to minimize the interference of these clutter signals. The design of this band-pass filter in the low-frequency region that performs the function of a high-pass (also called clutter rejection) filter has been problematic because the magnitude of clutter signals is several orders higher than those from blood and may mask those from slow moving blood (Figure 5.4). A filter with a very steep slope or a method that carries out some forms of echo cancellation may be used (Jensen, 1996).

The signal after band-pass filtering can be processed in different ways. It may be heard with a speaker because the Doppler shift is in the audible range. Alternatively, a zero-crossing counter can be used to estimate the mean Doppler frequency, or a spectrum analyzer can be used to display the spectrum. The zero-crossing counter estimates the number of zero-crossings of a signal. The number of zero-crossings, N, and the mean frequency, f_m, of a signal are given, respectively, by

$$N = 2\sqrt{\frac{\int_0^\infty f^2 P(f)\,df}{\int_0^\infty P(f)\,df}} \tag{5.1}$$

$$f_m = \frac{\int_0^\infty fP(f)\,df}{\int_0^\infty P(f)\,df} \tag{5.2}$$

where $P(f)$ is the probability density function at frequency f. For a pure sinusoidal signal of frequency f_m, $N = 2f_m$. Complication arises if the signal is not sinusoidal

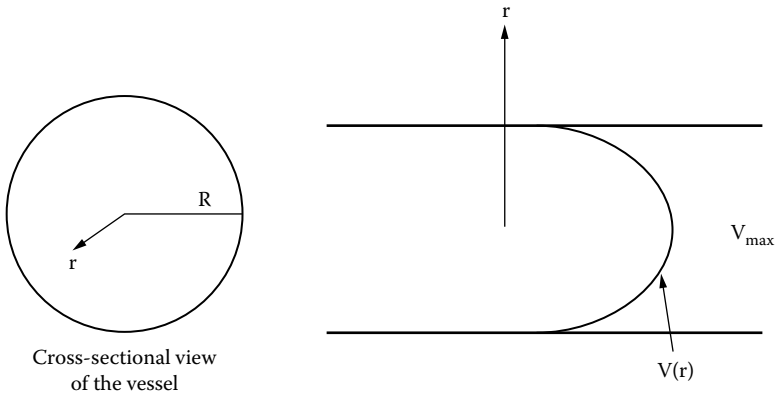

FIGURE 5.5 Laminar blood flow in an artery has a parabolic flow profile.

as in the case of Doppler flow measurements in which the blood flow is not uniform. For blood flow in a vessel, the velocity is related to radial distance, *r*, shown in Figure 5.5, by the following equation (Nichols and O'Rourke, 1990):

$$v(r) = v_{max}\left[1 - \left(\frac{r}{R}\right)^n\right] \tag{5.3}$$

where

v_{max} is the peak velocity
n is an index indicating the nature of flow
R is the radius of the blood vessel

For parabolic flow, $n = 2$ and $N = 1.15\ f_{max}$, where f_{max} is the maximal Doppler frequency.

The spectrum is usually displayed in the format shown in Figure 5.6, in which the vertical axis indicates Doppler frequency or velocity, the horizontal indicates axis time, and the gray scale indicates the intensity of the Doppler signal at that frequency or velocity. At each instant of time, the line displayed represents the Doppler spectrum calculated at that time within a 5- to 10-ms time window. From the Doppler spectrum, the mean frequency or other frequencies (e.g., median frequency) where the Doppler power spectrum is split into two equal halves and mode frequency, where the Doppler power is the highest, can be readily estimated.

Doppler flow meters have been used to assess vascular disorders noninvasively. Flow disturbances near a stenosis cause the Doppler spectrum to broaden because blood flow velocity fluctuates. However, a caveat must be recognized to avoid misdiagnoses: transit time spectral broadening. This is illustrated in Figure 5.7(a) for a single scatterer traversing an ultrasound beam at velocity *v*. A finite time is needed for the scatterer to traverse the beam. In the time domain, a finite time duration is

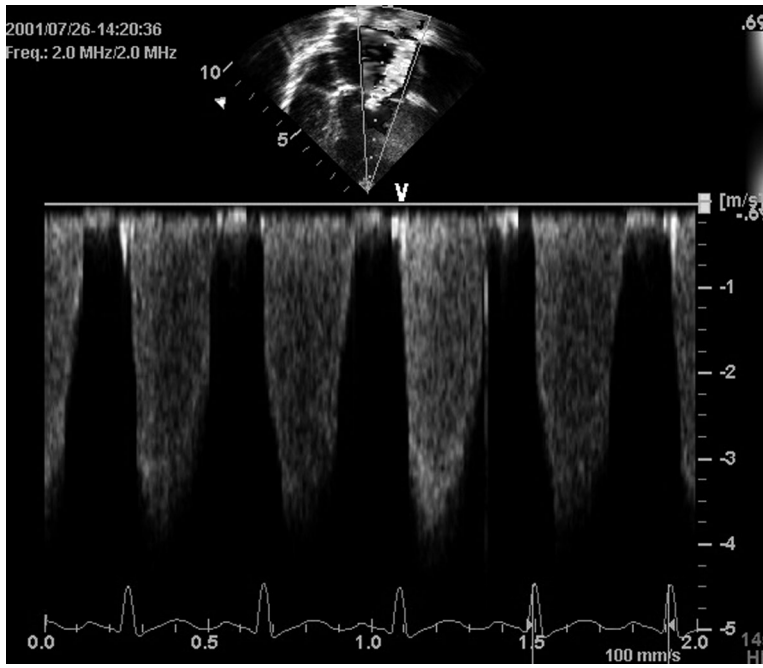

FIGURE 5.6 Spectrasonogram of CW Doppler signals produced by a mitral valve regurgitation jet. The top image is a B-mode apical four-chamber view of the heart. The dotted line indicates the direction of the Doppler beam. (Courtesy of GE Medical Systems.)

defined by Δt (–3-dB time duration from peak value) shown in Figure 5.7(b). Translated into the frequency domain, the result is a spectrum with a bandwidth, Δf, purely caused by this transit time effect, instead of a single Doppler spectral line representing velocity v. This is graphically displayed in Figure 5.7(c).

5.2 DIRECTIONAL DOPPLER FLOW METERS

Nondirectional Doppler devices cannot differentiate the direction of blood flow. A few methods have been developed to extract flow direction from the Doppler signal.

5.2.1 Single Sideband Filtering

In Figure 5.2, it is possible to divide the output from the demodulator into two paths. In one path, a high-pass filter is used to filter out signals at frequencies lower than f_o; in the other, a low-pass filter is used to filter out signals higher than f_o, as illustrated in Figure 5.8. In this figure, the portions of the spectrum above and below f_o are the forward flow and reverse flow Doppler signals, respectively. In this way, the output from one channel contains only forward flow signals and the other contains reverse flow signals. Although this approach is straightforward, the design of the filters can be difficult because the drop-off regions of these filters are very close to f_o.

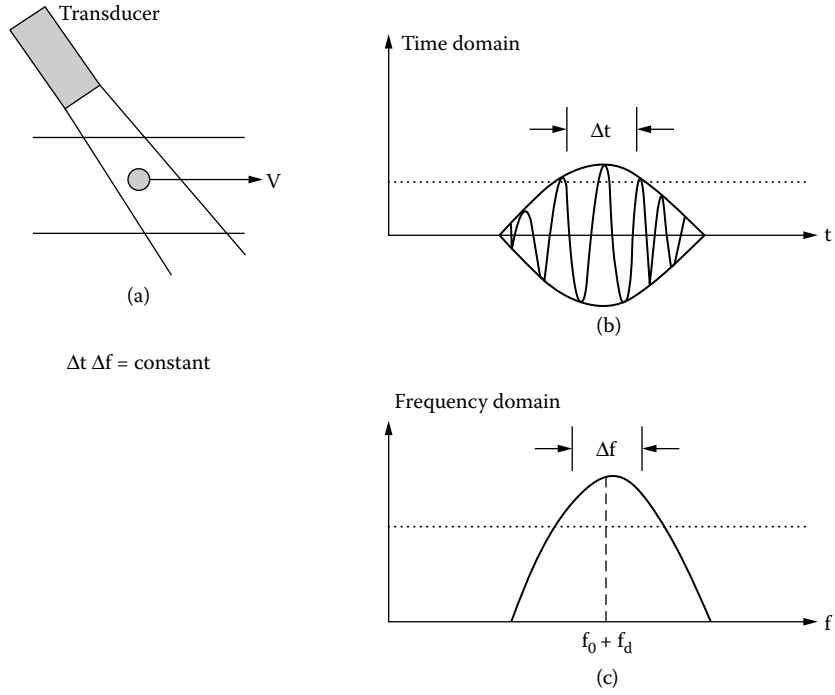

FIGURE 5.7 Transit time broadening causes an increase in the bandwidth in the frequency domain of the Doppler spectrum.

5.2.2 Heterodyne Demodulation

The block diagram of a directional Doppler device that uses heterodyne demodulation is given in Figure 5.9. A heterodyne oscillator generates a sinusoidal signal at a frequency f_h. The mixer between the oscillator and the heterodyne oscillator

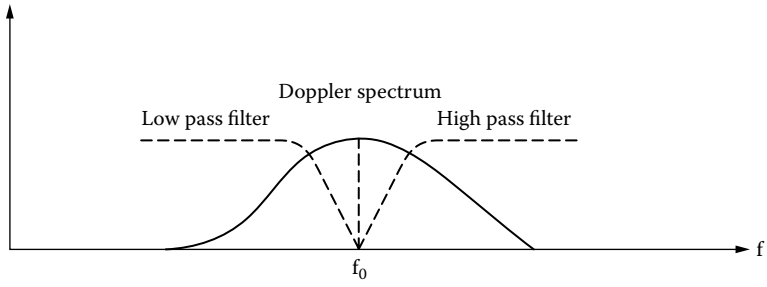

FIGURE 5.8 Two filters around the carrier frequency can be used to separate forward and reverse flow.

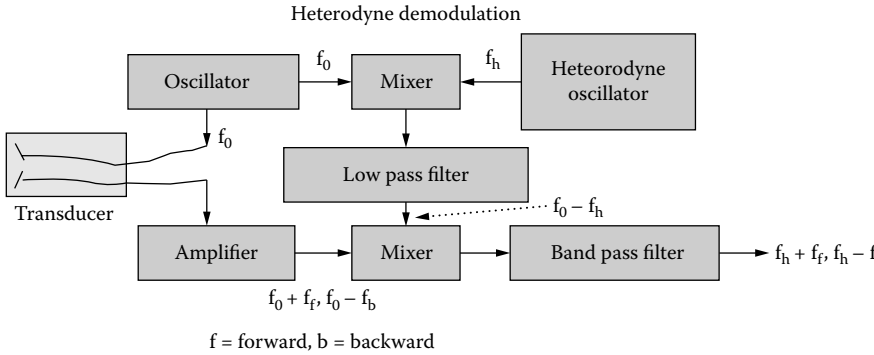

FIGURE 5.9 Block diagram for heterodyne demodulation.

performs a multiplication operation. Its output is given by

$$g_{m1}(\omega_o, \omega_h) = C\cos(\omega_o t)D\cos(\omega_h t) = \frac{1}{2}CD[\cos(\omega_o + \omega_h)t + \cos(\omega_o - \omega_h)t]$$

where C and D are the amplitudes of the signals produced by the oscillator and the heterodyne oscillator, respectively.

For the sake of simplicity, assume that $C = D = 1$ because here only the frequencies are of concern. After low-pass filtering, only the $\cos(\omega_o - \omega_h)t$ term is left. This signal is then mixed again with the signals detected by the receiving transducer element that contain the Doppler-shifted frequencies in the forward and backward directions, $f_o - f_b$ and $f_o + f_f$. The output of the second mixer is

$$\begin{aligned} g_{m2}(\omega_o, \omega_h, \omega_f, \omega_b) &= \cos(\omega_o - \omega_h)t \cdot [\cos(\omega_o + \omega_f)t + \cos(\omega_o - \omega_b)t] \\ &= \frac{1}{2}[\cos(2\omega_o - \omega_h + \omega_f)t + \cos(2\omega_o - \omega_b - \omega_h)t \\ &\quad + \cos(\omega_h + \omega_f)t + \cos(\omega_h - \omega_b)t] \end{aligned}$$

After low-pass filtering, the signal becomes

$$g_d(\omega_b, \omega_f, \omega_h) = [\cos(\omega_h + \omega_f)t + \cos(\omega_h - \omega_b)t]$$

The effect of heterodyne demodulation in comparison to conventional demodulation in the frequency domain is shown in Figure 5.10.

5.2.3 Quadrature Phase Demodulation

Figure 5.11 and Figure 5.12 show how quadrature phase demodulation can be used to obtain directional information. Here, it is assumed again that the amplitudes of

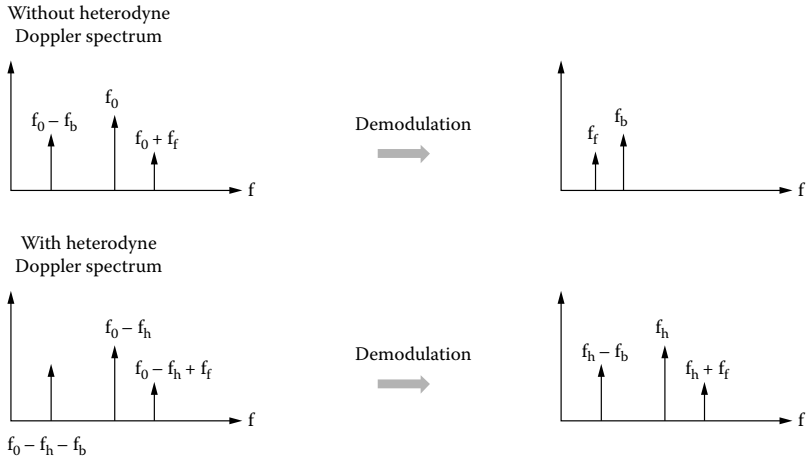

FIGURE 5.10 The effect of heterodyne demodulation in frequency domain.

signals are all equal to 1 to simplify the mathematical operation. The direct channel output is

$$\cos\omega_o t \cdot [\cos(\omega_o + \omega_f)t + \cos(\omega_o - \omega_b)t]$$

$$= \frac{1}{2}[\cos(2\omega_o + \omega_f)t + \cos(2\omega_o - \omega_b)t + \cos\omega_f t + \cos\omega_b t]$$

After low-pass filtering, the signal becomes $\cos\omega_f t + \cos\omega_b t$.

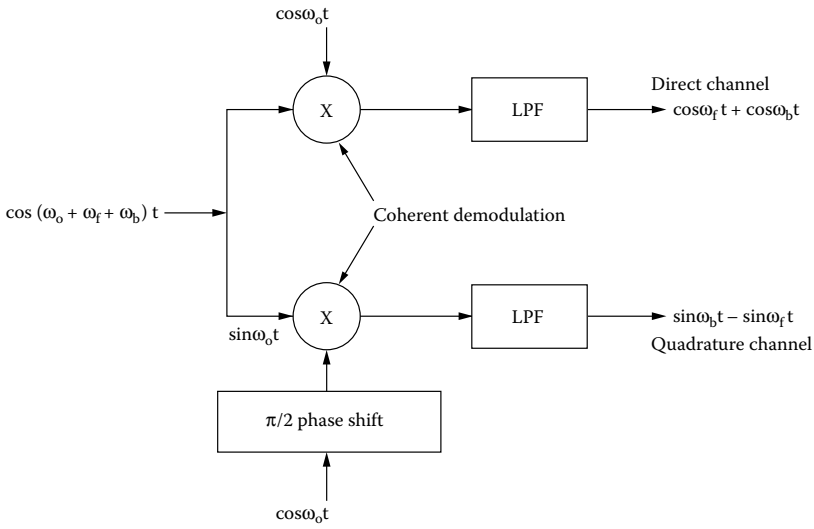

FIGURE 5.11 Quadrature demodulation.

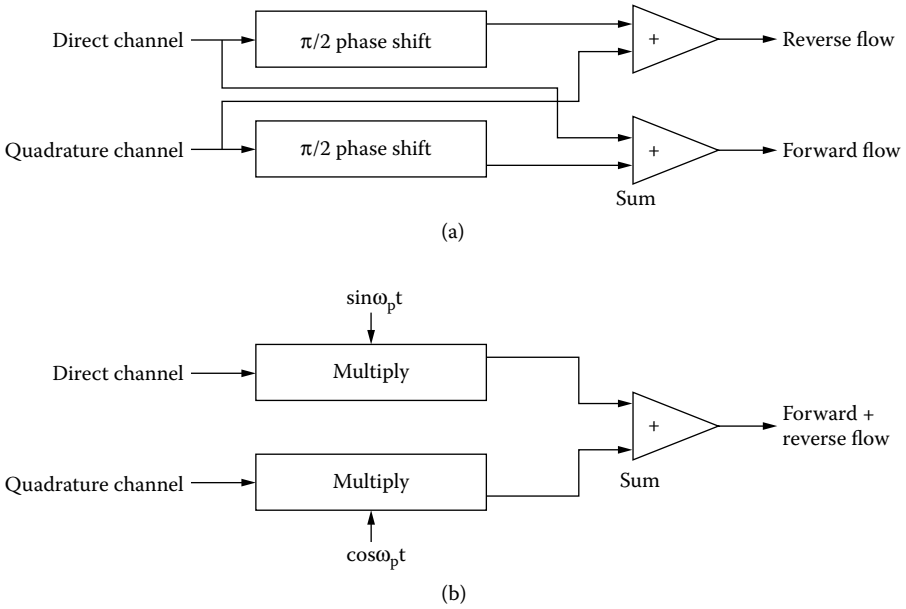

FIGURE 5.12 Separation of forward and reverse flows can be accomplished in the phase domain (a) and in the frequency domain (b).

The quadrature channel output is

$$\cos\left(\omega_o - \frac{\pi}{2}\right)t \cdot [\cos(\omega_o + \omega_f)t + \cos(\omega_o - \omega_b)t]$$

$$= \sin\omega_0 t[\cos(\omega_0 + \omega_f)t + \cos(\omega_o - \omega_b)t]$$

After low-pass filtering, the signal becomes $-\sin\omega_f t + \sin\omega_b t$.

To retrieve the directional information from these signals, a phase domain method and a frequency domain method may be used (illustrated in Figure 5.12a and Figure 5.12b, respectively). In the phase domain method, the direct channel output after $\pi/2$ phase shift is summed with the quadrature channel output to yield the reverse flow signal:

$$D(t) + Q(t + \pi/2) = \cos\omega_f t + \cos\omega_b t - \sin\left(\omega_f t - \frac{\pi}{2}\right) + \sin\left(\omega_b t - \frac{\pi}{2}\right) = 2\cos\omega_b t$$

The quadrature channel output after $\pi/2$ phase shift is summed with the direct channel output to yield the forward flow signal, $2\cos\omega_f t$.

In the frequency domain method, the direct channel signal is multiplied with a sinusoidal signal, $\sin\omega_p t$, and summed up with the quadrature channel signal multiplied by $\cos\omega_p t$:

$$D(t)\sin\omega_p t = \sin\omega_p t \cdot [\cos\omega_f t + \cos\omega_b t]$$

$$= \frac{1}{2}[\sin(\omega_p - \omega_f)t + \sin(\omega_p + \omega_f)t + \sin(\omega_p - \omega_b)t + \sin(\omega_p + \omega_b)t]$$

$$Q(t)con\omega_p t = \cos\omega_p t \cdot [-\sin\omega_f t + \sin\omega_b t]$$

$$= \frac{1}{2}[\sin(\omega_p - \omega_f)t - \sin(\omega_p + \omega_f)t - \sin(\omega_p - \omega_b)t + \sin(\omega_p + \omega_b)t]$$

Therefore,

$$D(t)\sin\omega_p t + Q(t)con\omega_p t = \sin(\omega_p - \omega_f)t + \sin(\omega_p + \omega_b)t$$

5.3 PULSED DOPPLER FLOW METERS

A problem with a CW Doppler is its inability to differentiate the origins of the Doppler signals produced within the ultrasound beam. Signals coming from blood flowing in two blood vessels in the same vicinity, e.g., an artery and a vein, may overlap. To alleviate this problem, a pulsed wave Doppler may be used. As illustrated in Figure 5.13, ultrasound bursts of relatively long duration consisting of many cycles

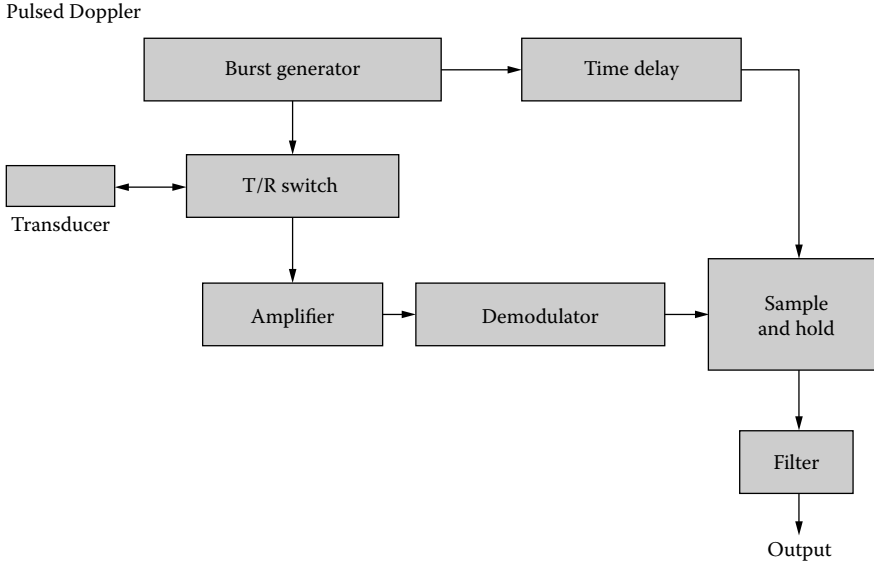

FIGURE 5.13 Block diagram of pulsed Doppler flow meter.

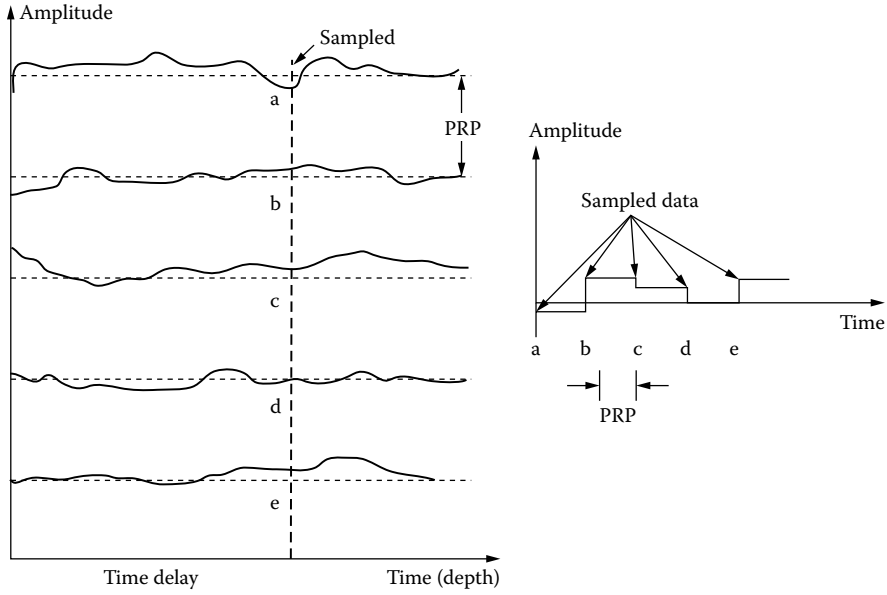

FIGURE 5.14 Principle used by pulsed Doppler to acquire Doppler signals.

are used to excite the probe. The returned echoes received by the same transducer are amplified and demodulated. The demodulated signal is then sampled and held by a sample-and-hold circuit, which is triggered by the delayed pulses. The time-delayed pulses allow the selection of the location where the Doppler shift frequency is monitored.

Figure 5.14 illustrates the principle behind pulsed Doppler flow meters. Each waveform in the left panel represents the echo waveform received by the transducer after a burst is transmitted. The waveforms are separated by the pulse repetition period (PRP). The time delay is set to allow the sampling of the waveform at points a, b, c, d, and e. The sample-and-hold circuit samples the waveforms at these points and holds the voltage at the sampled level until the next sampling time, as illustrated in the right-hand panel. Following band-pass filtering, the Doppler signal can be displayed or heard as the CW Doppler.

A drawback of the pulsed Doppler is the limit of the highest Doppler frequency or maximal velocity that it can measure. This is determined by the pulse repetition frequency (PRF) of the device, which must be at least twice as large as the maximal Doppler frequency. This may pose a problem when measuring high velocities in the body, e.g., outflow tracts of cardiac valves and stenosis in a blood vessel. To avoid aliasing, the PRF of the pulsed Doppler device must be

$$PRF > 2f_{\max}$$

$$\therefore PRF > (4v_{\max}f)/c \tag{5.4}$$

where f_{max} and v_{max} are the maximal Doppler shift frequency and maximal velocity, respectively. To avoid range ambiguity, all echoes must be received before the next burst is transmitted, i.e.,

$$PRP = \frac{1}{PRF} > \frac{2z_{max}}{c} \tag{5.5}$$

where z_{max} is the maximal depth of penetration. Combining Equation (5.4) and Equation (5.5),

$$v_{max} \cdot z_{max} \leq \frac{c^2}{8f} \tag{5.6}$$

The term on the right side of the equation is a constant. This means that the performance of the pulsed Doppler device is limited by the maximal velocity that it can detect or the maximal depth of penetration. To enhance one, the performance of the other must be compromised. Modern high-end ultrasonic imaging machines are equipped with CW and PW capabilities.

5.4 CLINICAL APPLICATIONS AND DOPPLER INDICES

Ultrasonic Doppler devices are inexpensive and are capable of yielding clinically useful information noninvasively. Their primary applications have been in assessing cardiovascular systems, e.g., diagnosing stenosis in blood vessels and cardiac valvular diseases. They have also been used to estimate cardiac valvular stenosis (Feigenbaum, 1986). The velocity measured by the Doppler devices depends upon the Doppler angle, which is difficult to estimate; therefore, a few indices that are not angle dependent have been used frequently in a clinical setting to derive useful diagnostic data.

Figure 5.15 shows the mean velocity waveform from a peripheral artery obtained with a CW Doppler flow meter. The pulsatility index is defined as the ratio of $(S - D)/M$, where S, D, and M are the peak, minimal, and mean velocities, respectively. In this expression, the angle dependence is eliminated. The pulsatility index has been found to be related to the resistance of the vessel downstream from the measurement site. Another useful index is the Purcelot resistance index for the carotid artery, which is defined as $(S - D)/S$.

5.5 POTENTIAL PROBLEMS IN DOPPLER MEASUREMENTS

In Doppler flow measurements, preventive measures must be taken to avoid errors that may result from the following problems:

- Erroneous Doppler angle estimation
- Nonuniform insonification of vessel by the ultrasound beam

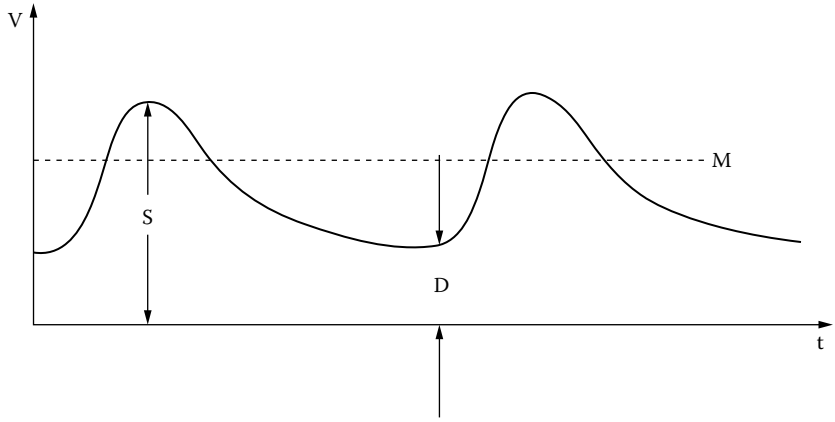

FIGURE 5.15 Mean velocity waveform acquired with a CW flow meter from a peripheral blood vessel can be used to derive indices useful for diagnosing vascular diseases.

- Aliasing of Doppler frequency estimation
- Intrinsic spectral broadening
- Attenuation of intervening tissues between the probe and the region of interest
- Clutter signals generated by show moving moving large anatomical structures

The Doppler angle can be better estimated with the aid of B-mode imaging, although it is still not ideal because of the tortuosity of blood vessels. If the sensitive volume of the ultrasound beam or beams is smaller than the vessel, portions of the blood will not be included in the measurement, resulting in estimated velocity values that may deviate from the true values. Because the attenuation of tissues is linearly proportional to frequency, the Doppler spectrum may be affected if deeper tissues are interrogated. Other problems have been addressed in preceding sections.

5.6 TISSUE DOPPLER AND MULTIGATE DOPPLER

In the Doppler signal processing chain shown in Figure 5.2 and Figure 5.13, if only large amplitude echoes of lower Doppler frequencies from tissues such as myocardium or heart muscle are retained and low amplitude echoes of higher Doppler frequencies are suppressed, the motion of the tissues can be monitored. This will be touched upon again in the next chapter. An amplitude threshold can be set to allow only the larger echoes to pass through. Tissue Doppler has been proven a clinically useful tool for assessing the state of myocardium.

In conventional pulsed Doppler, only one gate is used to measure blood flow within the sampled window or sampling volume confined by the beam width and the gate duration. If blood flow velocities at multiple points along the ultrasound beam need

to be measured, pulsed Doppler flow meters with multiple gates (e.g., 8 or 16 gates) have been developed. These devices allow the measurement of velocities in real time across the lumen and thus have been used frequently to determine the blood flow velocity profile in arteries.

REFERENCES

Evans, D.H. and McDicken, W.N. *Doppler Ultrasound*: *Physics, Instrumentation and Signal Processing*. Wiley: New York, 2000.

Feigenbaum, H. *Echocardiography*, 4th ed. Philadelphia: Lea and Febiger, 1986.

Jensen, J.A. *Estimation of Blood Velocities Using Ultrasound*. Cambridge: Cambridge University Press, 1996.

Mo, L.Y.L. and Cobbold, R.S.C. Theoretical models of ultrasonic scattering in blood. In Shung, K.K. and Thieme, G.A., Eds. *Ultrasonic Scattering in Biological Tissues*, Boca Raton, FL: CRC Press, 1993, 125–170.

Nichols, W.W. and O'Rourke, M.F. *McDonald's Blood Flow in Arteries*. Philadelphia: Lea and Febiger, 1990.

Shung, K.K., Cloutier, G., and Lim, C.C. The effects of hematocrit, shear rate, and turbulence on ultrasonic Doppler spectrum from blood. *IEEE Trans. Biomed. Eng*. 1992, 39:462–469.

6 Flow and Displacement Imaging

Ultrasonic B-mode real-time imaging can be combined with Doppler in a scanner so that the scanner is capable of providing not only anatomical information but also blood flow data. Both sets of information are displayed simultaneously. A cursor line is typically superimposed on the B-mode image to indicate the direction of the Doppler beam. An FFT algorithm is used to compute the Doppler spectrum that is displayed in real time. This type of scanner is called a duplex scanner; a duplex image is shown in Figure 5.6. Alternatively, blood flow data can be displayed in real time and superimposed with the B-mode image if the data acquisition rate and image processing algorithms are sufficiently fast.

6.1 COLOR DOPPLER FLOW IMAGING

Color Doppler flow imaging systems are duplex scanners capable of displaying B-mode and Doppler blood flow data simultaneously in real time (Shung et al., 1992; Routh, 1996; Jensen, 1996; Ferrara and DeAngelis, 1997). The Doppler information is encoded in color. Conventionally, the color red is assigned to indicate flow toward the transducer, and blue is assigned to indicate flow away from the transducer. The magnitude of the velocity is represented by different shades of the color. Typically, the lighter the color, the higher the velocity. The color Doppler image is superimposed on the gray-scale B-mode image. A color Doppler image of a renal transplant is shown in Figure 6.1.

The basic concept of the color Doppler is similar to that of the pulsed Doppler instruments that extract the mean Doppler shift frequency from a sample volume defined by the beam width and the gate width. The only exception is that the color Doppler instruments are capable of estimating the mean Doppler shifts of many sample volumes along a scan line in a very short period of time — on the order of 30 to 50 ms. To be able to do so, fast algorithms must be developed. One such algorithm was based upon the well-known Wiener–Khinchine theorem, which indicates that the autocorrelation function $H(\tau)$ of a function $f(t)$ is the Fourier transform of the power spectrum $P(\omega)$ of $f(t)$ (Kasai et al., 1985). Mathematically, this is given by

$$H(\tau) = \int_{-\infty}^{\infty} f(t) f(t-\tau)\, dt = \int_{-\infty}^{\infty} P(\omega) e^{j\omega\tau}\, d\omega \tag{6.1}$$

Alternatively, $H(\tau)$ can be written in the form of

$$H(\tau) = |H(\tau)|\, e^{j\phi(\tau)} = A(\tau) e^{j\phi(\tau)} \tag{6.2}$$

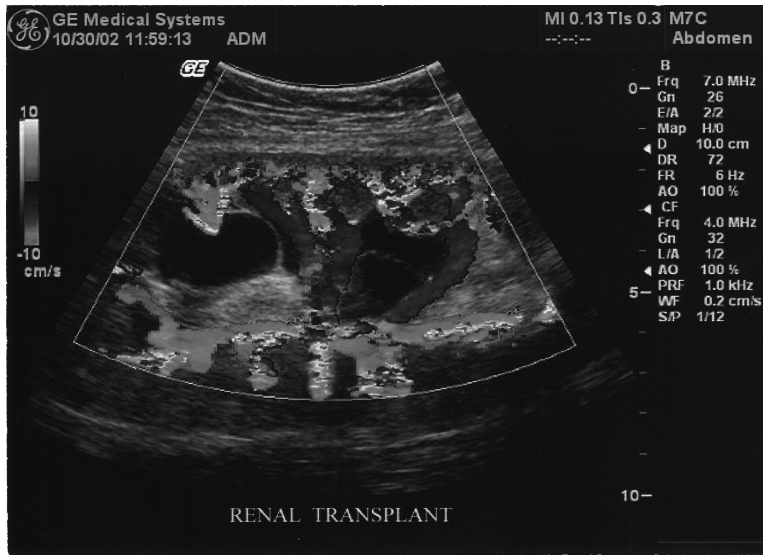

FIGURE 6.1 (See color figure following page 80.) Color Doppler image of a renal transplant obtained with a 7-MHz curved array. The transplant vasculature is represented by the color image and the gray-scale B-mode image delineates the kidney anatomy where large cysts (anechoic regions) are seen. (Courtesy of GE Medical Systems.)

where the magnitude and phase of $H(\tau)$ are an even function and an odd function, respectively. The symbol A is used to represent the magnitude of $H(\tau)$ here.

From Equation (6.1),

$$H(0) = \int_{-\infty}^{\infty} P(\omega)\, d\omega \tag{6.3}$$

$$\dot{H}(0) = j\int_{-\infty}^{\infty} \omega P(\omega)\, d\omega \tag{6.4}$$

where the dot operation represents the first derivative $= \partial H(\tau)/\partial\tau$. Let $<\omega>$ denote the mean of ω and, from the definition of mean angular frequency and Equation (6.3) and Equation (6.4),

$$<\omega> = \frac{\int_{-\infty}^{\infty} \omega P(\omega)\, d\omega}{\int_{-\infty}^{\infty} P(\omega)\, d\omega} = \frac{\dot{H}(0)}{jH(0)} \tag{6.5}$$

This equation can be manipulated to become

$$j<\omega> = \frac{\dot{H}(0)}{H(0)} \tag{6.6}$$

Furthermore, the variance of angular frequency, σ^2, is given by

$$\sigma^2 = <\omega^2> - <\omega>^2 \tag{6.7}$$

$<\omega^2>$ can be calculated from Equation (6.5) and $<\omega^2>$ by definition is

$$<\omega^2> = \frac{\int_{-\infty}^{\infty} \omega^2 P(\omega)\, d\omega}{\int_{-\infty}^{\infty} P(\omega)\, d\omega} = \frac{-\ddot{H}(0)}{H(0)} \tag{6.8}$$

where the double dot operation denotes the second derivative = $\partial^2 H(\tau)/\partial\tau^2$.

Substituting Equation (6.8) into Equation (6.7),

$$\sigma^2 = \left[\frac{\dot{H}(0)}{H(0)}\right]^2 - \frac{\ddot{H}(0)}{H(0)} \tag{6.9}$$

It can be further shown that, for an ultrasonic imaging system transmitting pulses with a pulse repetition frequency, T,

$$<\omega> = \frac{\phi(T)}{T} \tag{6.10}$$

$$\sigma^2 = \frac{1}{T^2}\left[1 - \frac{|H(T)|}{H(0)}\right] \tag{6.11}$$

These are all simple arithmetic operations that require little time for computation if the autocorrelation function, $H(T)$, can be estimated.

Equation (6.10) and Equation (6.11) can be found by considering the fact that, for an even function, the first derivative of the function at the origin = 0 and for an odd function the function = 0 at the origin. That is,

$$\dot{A}(0) = \frac{\partial |H(\tau)|}{\partial\tau}\Big|_{\tau=0} = 0 \quad \text{and} \quad \phi(0) = 0 \tag{6.12}$$

Therefore,

$$\dot{H}(0) = \dot{A}(0)e^{j\phi(0)} + jA(0)e^{j\phi(0)}\dot{\phi}(0) = jA(0)\dot{\phi}(0) \tag{6.13}$$

From Equation (6.6) and Equation (6.13),

$$<\omega> = \dot{\phi}(0) \approx \frac{\phi(T) - \phi(0)}{T} = \frac{\phi(T)}{T}$$

which is Equation (6.10). This expression says that the mean frequency of a spectrum is equal to the slope of the phase of the autocorrelation function at the origin. This can be approximated by the difference in phase at the origin and at one pulse repetition period, T, assuming that the autocorrelation function is sampled at internals of T.

Similarly, it can be shown from differentiating $H(\tau)$ twice that

$$\ddot{H}(0) = \ddot{A}(0) - [\dot{\phi}(0)]^2 A(0) \tag{6.14}$$

Here, $A(\tau)$ can be expanded into a Taylor series, ignoring third-order and higher terms and assuming that τ is small:

$$A(\tau) \approx A(0) + \frac{\tau^2}{2}\ddot{A}(0) \tag{6.15}$$

Rearranging Equation (6.15),

$$\ddot{A}(0) = \frac{2}{\tau^2}[A(\tau) - A(0)] \tag{6.16}$$

$\ddot{H}(0)$ can be found by substituting Equation (6.16) into Equation (6.14). Substituting $\ddot{H}(0)$, $\dot{H}(0)$, and $H(0)$ into Equation (6.9), Equation (6.11) is obtained.

$$\sigma^2 \approx \frac{2}{\tau^2}\left[1 - \frac{A(\tau)}{A(0)}\right] \approx \frac{2}{T^2}\left[1 - \frac{|H(T)|}{H(0)}\right]$$

This expression indicates that the variance of the frequency can be estimated from the magnitude of the autocorrelation function at the origin and at T.

Figure 6.2 shows a version of the autocorrelation method implemented in a commercial scanner a few years ago. Given a real-time function $f(t)$, its quadrature

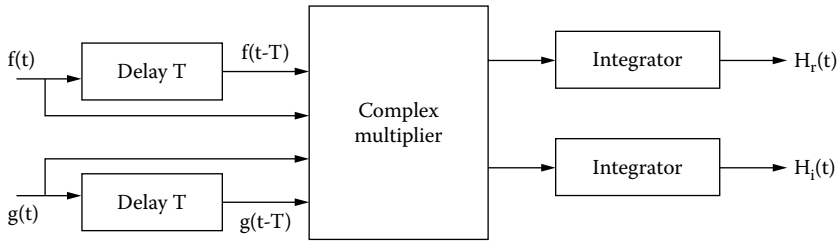

FIGURE 6.2 A hard-wired autocorrelator for estimating the antocorrelation function $H(T)$ from a time signal $f(t)$.

component $g(t)$ can be found by shifting the time function by 90°. A complex function, $z(t) = f(t) + jg(t)$, can be obtained. The complex multiplier performs the operation:

$$[f(t) + jg(t)] \cdot [f(t - T) - jg(t - T)]$$

The autocorrelation function is obtained by integrating the output of the complex multiplier over a period of time, say, nT, where n represents the successive pulses transmitted by a scanner to acquire the autocorrelation function. The three unknowns in Equation (6.10) and Equation (6.11) are readily attainable from the following expressions:

$$|H(T)| = \sqrt{H_r^2(T) + H_i^2(T)} \quad \text{and} \quad \phi(T) = \tan^{-1} \frac{H_i(T)}{H_r(T)}$$

where H_r and H_i are the real and imaginary parts of H, respectively.

It should be noted that $H(T)$ is a function of time or is time dependent. The accuracy of the estimated $H(T)$ is ultimately determined by the time duration in which the estimation is performed. The longer the time duration is, the better the accuracy is. This requirement must be compromised in real-time ultrasonic imaging. The earliest color Doppler scanners had 50 scan lines with a frame rate of 15 per second. The dwelling time of the ultrasound beam at any one direction is

$$t_d = \frac{1}{50 \cdot 15} = 1.33\,\text{ms}$$

If the depth of view is 10 cm, the time needed for a pulse to make a round trip or time of flight is 0.13 ms, assuming an ultrasound speed of 1540 m/s. This means that 1.33/0.13 = 10 ultrasound pulses can be transmitted in this time span and that the autocorrelation function is computed and averaged after ten pulse transmissions. The autocorrelator needs to compute the autocorrelation function for each pixel along a scan line. This is illustrated in Figure 6.3, in which the solid curve and the dotted curve represent, respectively, the pulse–echo waveform after each pulse transmission and the time variation of the echo at a certain pixel for which the autocorrelation function is computed.

In a color Doppler system, the signal received by a probe is divided into three paths: one for constructing the gray-scale B-mode image; one for calculating the flow information from Doppler data using a hard-wired autocorrelator; and one for conventional Doppler measurements. This is delineated in Figure 6.4. Eight or more shades are used in these systems to depict the magnitude of the velocity. The higher the velocity is, the lighter the shade is. Because the basic principle of Doppler flow mapping is similar to pulsed Doppler, the maximal Doppler frequency that can be detected without aliasing is one-half of the pulse repetition frequency. Therefore, a higher pulse repetition frequency is favored for avoiding aliasing and increasing the accuracy of the autocorrelation.

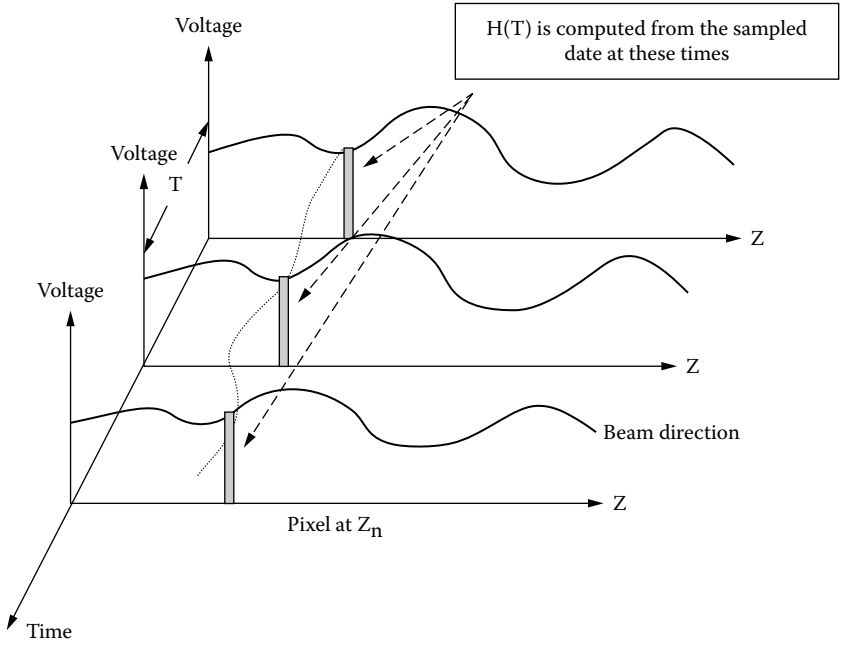

FIGURE 6.3 The autocorrelation function from which the mean and the variance of the Doppler-shifted frequency are estimated is computed for each pixel along a scan line in a color Doppler flow mapping system.

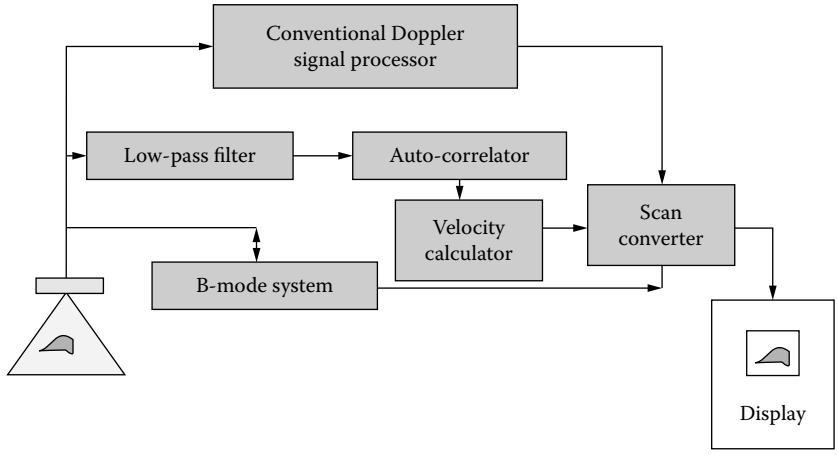

FIGURE 6.4 Block diagram of a color Doppler flow mapping system.

However, limited by the frame rate and field of view, the pulse repetition frequency in most color Doppler systems is between 8 and 16 kHz. As a result, aliasing frequently occurs with color Doppler in cardiac imaging. To overcome these problems, one can reduce the image size or use M-mode color Doppler, in which the beam is fixed in one direction.

In the heart, the myocardium is in motion during a cardiac cycle. Tissue color Doppler images of this motion can be acquired with color Doppler methods previously described as well. The difference lies in that myocardial motion is slower than blood flow and myocardial echoes are stronger than blood. The spurious Doppler signals from blood in this case can be eliminated by thresholding the echoes. A tissue Doppler image of the heart in which the color indicates the velocity of myocardial motion is shown in Figure 6.5.

Many clinical applications have been found for color Doppler flow imaging, including diagnosing tiny shunts in the heart wall and valvular regurgitation and stenosis. It considerably reduces the examination time in many diseases associated with flow disturbance. Problematic regions can be quickly identified first from the flow mapping. More quantitative conventional Doppler measurements are then made on these areas.

Color Doppler has been now widely used in a variety of medical disciplines; however, it has several shortcomings:

- Flow perpendicular to the beam cannot be reliably detected.
- Higher blood flow velocity results in aliasing.
- Its spatial resolution is poorer than B-mode gray-scale imaging.
- The mean velocity estimated is the average velocity within a pixel or voxel.
- Because the color Doppler image is overlaid over the gray-scale B-mode, the overlay process is determined arbitrarily by thresholding, which may result in vessel wall overwrite obscuring the slow blood flow signal near the wall.
- Large echoes due to slow moving tissues can cause the "color flash artifact" because they overlap echoes from flowing blood.

6.2 COLOR DOPPLER POWER IMAGING

A new way of displaying color Doppler information, i.e., "power mode" or "energy mode" imaging, has been introduced to minimize some of the color Doppler problems (Rubin et al., 1994; Zagzebski, 1996) and has been well accepted by the clinical community. All top-of-the-line scanners now have this option. Instead of the mean Doppler shift, the power contained in the Doppler signal is displayed in this approach. There are several advantages to doing so:

- A threshold can be set to minimize the effect of noise.
- The data can be averaged to achieve a better signal-to-noise ratio.
- The images are less dependent upon the Doppler angle.
- Aliasing is no longer a problem because only the power is detected. As a result, signals from blood flowing in much smaller vessels can be detected. The images so produced have an appearance similar to that of x-ray angiography.

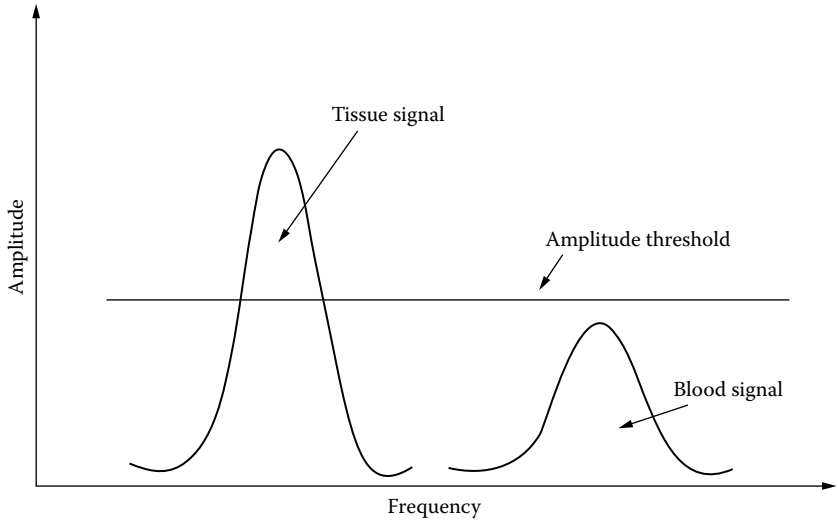

(a)

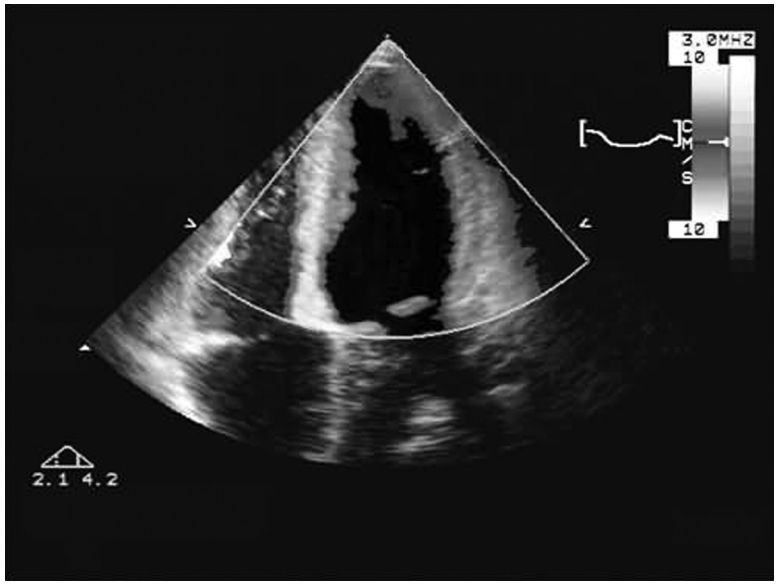

(b)

FIGURE 6.5 (a) Tissue Doppler can be achieved by thresholding the Doppler signals so as to suppress the Doppler signal from blood and retain only the Doppler signals from tissues. (b) Tissue Doppler image of myocardial motion. Colored areas indicate velocity of myocardium motion in the heart walls and anechoic regions indicate intracardiac blood pool. (**See color figure following page 80.**) (Courtesy of Philips ATL.)

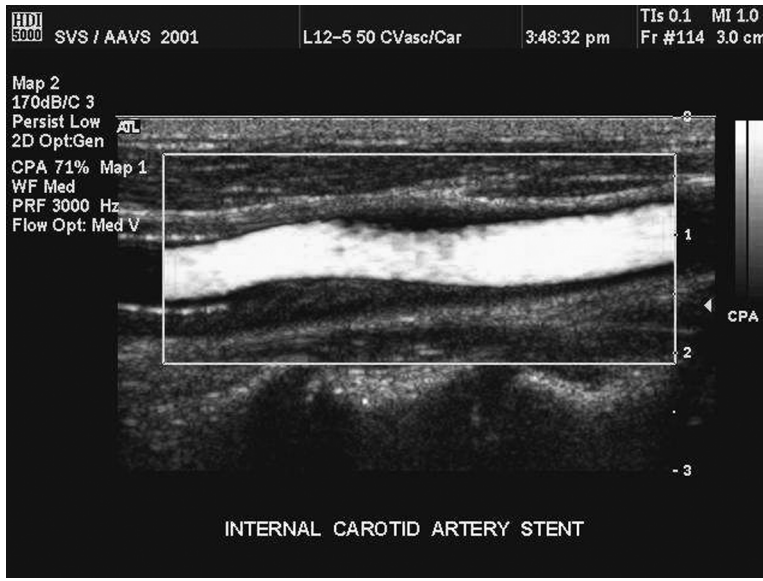

FIGURE 6.6 (See color figure following page 80.) Color Doppler power image of carotid artery acquired with a 12-MHz linear array. The color in this case represents the power contained in the Doppler signal rather than the mean Doppler-shifted frequency. The brightness of the color is proportional to the Doppler power and has nothing to do with the magnitude of velocity. The presence of a color in a pixel merely means that a flow signal is detected in that pixel. (Courtesy of Philips ATL.)

The disadvantages of this approach are that it is more susceptible to motion artifacts because of frame averaging and the image contains no information on flow velocity and direction. A color Doppler "power" Doppler image of a carotid artery is shown in Figure 6.6. The orange-colored region indicates that there is blood flow. The gray-scale B-mode image delineates blood the vessel wall and surrounding tissues.

Power Doppler imaging is in fact easier to implement than conventional color Doppler because Doppler "power" is readily available in conventional color Doppler systems. $H(0)$ in Equation (6.11), which is needed to calculate the variance of Doppler frequencies, is the power contained in the Doppler spectrum. This becomes apparent when setting $\tau = 0$ in Equation (6.1), i.e.,

$$H(\tau = 0) = \int_{-\infty}^{\infty} f^2(t)\,dt = \int_{-\infty}^{\infty} P(\omega)\,d\omega$$

6.3 TIME-DOMAIN FLOW ESTIMATION

Blood flow velocity has been estimated directly from B-mode images, termed speckle tracking, or from radio frequency (RF) echoes. These alternatives accomplish blood flow measurements in the time domain. Frame-to-frame tracking of movement of

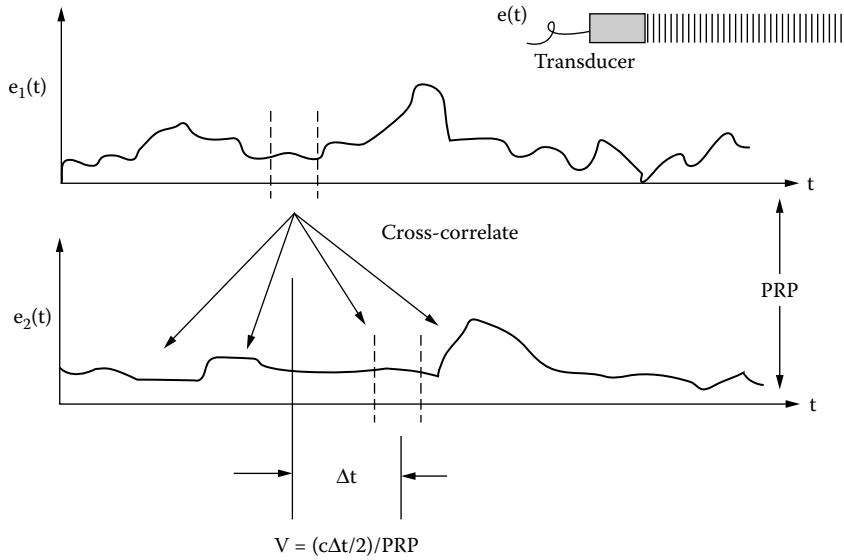

FIGURE 6.7 Cross-correlation can be used to estimate blood flow in time domain.

speckles generated by blood from B-mode images and direct correlation of radio frequency (RF) echoes from blood show great promise.

Suppose that an ultrasonic beam emanating from a transducer is parallel to blood flowing in a vessel and a signal, $e(t)$, is received by the transducer from blood, as shown in Figure 6.7. For frame-to-frame speckle tracking, $e(t)$ denotes the video signal. If RF signals are used, then $e(t)$ denotes the RF signal. Waveforms $e_1(t)$ and $e_2(t)$ are received at time t_1 and t_2, which are separated by the pulse repetition period (PRP). If the distance, d, that the blood has moved within one PRP can be measured, the velocity, V, would be given by $V = d/\text{PRP}$.

A cross-correlation approach has been developed to estimate the distance d (Trahey et al., 1987; Jensen, 1996). A segment of the waveform or the windowed waveform in a pixel, bordered by the dashed lines of $e_1(t)$ in Figure 6.7, is cross-correlated with all segments of similar width of waveform $e_2(t)$ by computing the one-dimensional normalized cross-correlation coefficient, ρ. A match is found when ρ is maximal. If the windowed waveforms are represented by N digitized signals, $E_1 = \{e_1(0), e_1(1), \ldots e_1(i), \ldots e_1(N-1)\}$ and $E_2 = \{e_2(0), e_2(1), \ldots e_2(i), \ldots e_2(N-1)\}$, the normalized coefficient, ρ, can be computed from the following expression as E_1 is correlated with different E_2 segments from waveform $e_2(t)$ by shifting the window from one end of the waveform to the other.

$$\rho = \frac{\sum_{i=0}^{N-1}[e_1(i)-\bar{e}_1][e_2(i)-\bar{e}_2]}{\sqrt{\sum_{i=0}^{N-1}[e_1(i)-\bar{e}_1]^2 \sum_{i=0}^{N-1}[e_2(i)-\bar{e}_2]^2}} \tag{6.17}$$

where $\bar{e}_1$ and $\bar{e}_2$ are the mean values of e_1 and e_2. If maximal ρ occurs when the windowed waveform of $e_2(t)$ is shifted Δt from the windowed segment of $e_1(t)$, it may be assumed that the volume of blood responsible for the windowed $e_1(t)$ has moved a distance $d = c\Delta t/2$, where c is ultrasound velocity. Consequently, blood flow velocity can be estimated from

$$V = \frac{c\Delta t}{2T} \tag{6.18}$$

where T is the pulse repetition period (PRP). If the ultrasound beam makes angle of θ relative to the flow direction, Equation (6.18) should be modified to include the effect of the angle:

$$V = \frac{c\Delta t}{2T\cos\theta} \tag{6.19}$$

Time domain methods differ from Doppler methods in that they track displacements. These methods can be used when there is no motion, but Doppler cannot. They have several advantages over Doppler methods:

- Time domain methods are more immune to noise. This means that they can be used in a noisier environment and need less averaging, yielding a higher frame rate.
- There is no aliasing problem. The search will yield no results if the pulse repetition frequency is not sufficiently high.
- The spatial resolution attainable with these methods is higher than Doppler methods because short pulses are used.
- Two-dimensional flow information can be obtained by matching two-dimensional blocks by computing two-dimensional correlation coefficients.

Frame-to-frame speckle tracking is more desirable in that the flow information can be directly obtained from the B-mode images acquired by the scanner without the need for additional hardware, although it yields poorer spatial resolution than RF correlation. Its drawbacks are that the signal level from blood in the frequency range of 3 to 10 MHz is too weak to obtain a reliable estimation and the frame rate of 30 frames per second is too low to estimate arterial blood flow velocity. The former problem is becoming less of an issue because the performance of recent scanners has been improved and it may be overcome by injecting a contrast agent; a high frame scanner must be used to solve the latter problem. Several echocardiographic scanners now are capable of providing a frame rate as high as 200 frames per second with a smaller field of view.

6.4 ELASTICITY IMAGING

Ultrasound has been widely used to differentiate cysts from solid tumors in tumor imaging because liquid-containing cysts are typically echo poor. However, certain solid tumors that are harder than surrounding tissues are missed sometimes by

ultrasound because their echogenicity is similar to that of surrounding tissues. These tumors or harder tissues are identifiable if their elastic properties can be imaged. At present, two ultrasound approaches have been developed to image tissue elasticity: static and dynamic (Ophir et al., 1991; Lerner et al., 1990).

6.4.1 Elastography

In the static approach dubbed elastography (Ophir et al., 1991), a flat plate, which may be the ultrasonic probe, is used to compress the tissue by a distance Δz. The displacement of the tissue is estimated via cross-correlation from the returned RF echoes, as previously discussed. Under ideal conditions and assuming a one-dimensional case (i.e., the compression is transmitted only in the z-direction), the stress and strain can be estimated from the force applied and area of the plate or transducer and Δz, respectively.

The Young's modulus of the tissue is then given by the ratio of longitudinal stress to longitudinal strain. This idea can be illustrated by the following simple example, which is illustrated in Figure 6.8(a) in which medium I and II are perfectly compressible and incompressible. When a stress, κ, is applied, all points in medium I will be displaced by Δz, whereas in medium II the displacement will be 0. This is plotted in Figure 6.8(b) in which the strain in medium I is given by $-(\Delta z)/L$ and the Young's modulus by $-(L\kappa)/\Delta z$.

This approach has been the focus of attention in breast and prostate imaging for a number of years. An example is shown in Figure 6.9, in which the elastogram and B-mode image of a multiple foci breast lesion are compared. Although elastography may be capable of imaging elastic property of tissues, which cannot be achieved with standard B-mode sonography, it has problems of the same nature as those for

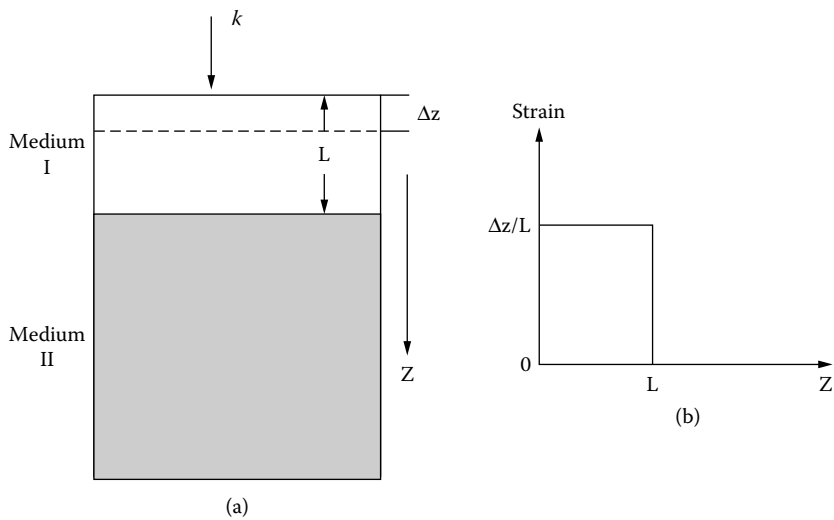

FIGURE 6.8 (a) A stress applied to medium I produces a displacement in medium I. (b) Strain in medium I and II is plotted as a function of depth.

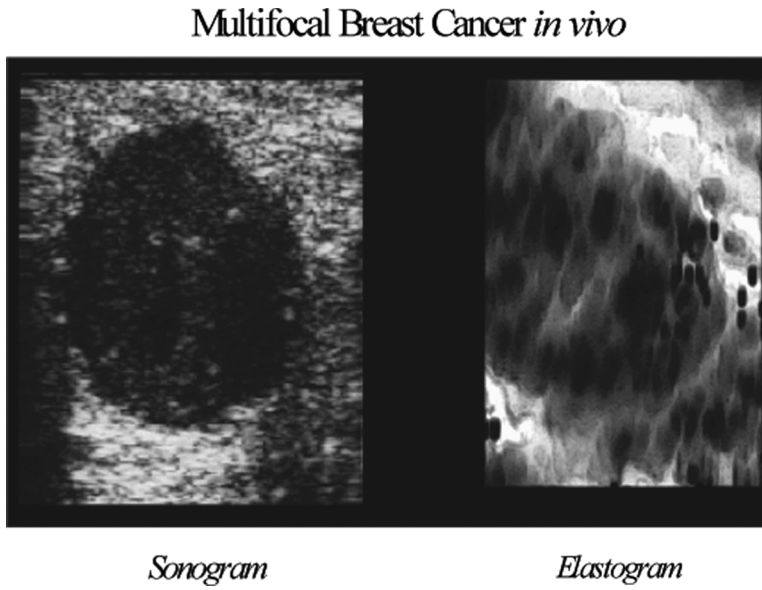

FIGURE 6.9 A comparison of elastogram and B-mode image of a multiple foci breast lesion. (Courtesy of Dr. Jonathan Ophir at University of Texas Medical School at Houston.)

B-mode sonography. The stress propagating into a tissue will be attenuated by tissues, spread into other directions from the primary incident direction, and interact with a boundary between two media of different elastic properties. The effect of boundary on an elastogram can sometimes be distracting.

6.4.2 Sonoelasticity Imaging

Sonoeleasticity imaging (Lerner et al., 1990) is a dynamic approach in which a motion monitoring device, e.g., a color Doppler flow mapping system, is used to measure the motion of tissues produced by the vibration of a source inserted into one of the cavities of the body or placed externally, as illustrated in Figure 6.10. The source typically vibrates at a frequency of a few hundred hertz to a few kilohertz so that a conventional Doppler device can be used to monitor the motion with little modification. This approach has been used to assess prostate cancer with an intrarectal vibrating source. Sonoelasticity imaging suffers from similar problems mentioned previously. The vibration produced by the source is nonuniform and is attenuated by tissues. The energy of the ultrasound generated by the scanner to probe the vibration is also affected by attenuation.

6.5 B-FLOW IMAGING

B-mode blood flow (B-flow) imaging is a new method that improves the resolution, frame rate, and dynamic range of B-mode to image blood flow and tissue simultaneously (Chiao et al., 2000). It combines the coded excitation imaging

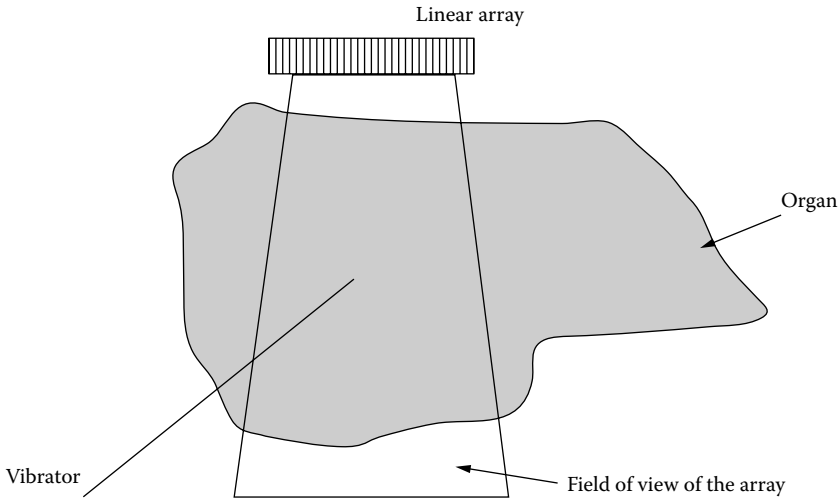

FIGURE 6.10 Sonoelasticity imaging images the motion of tissues induced by a vibrator.

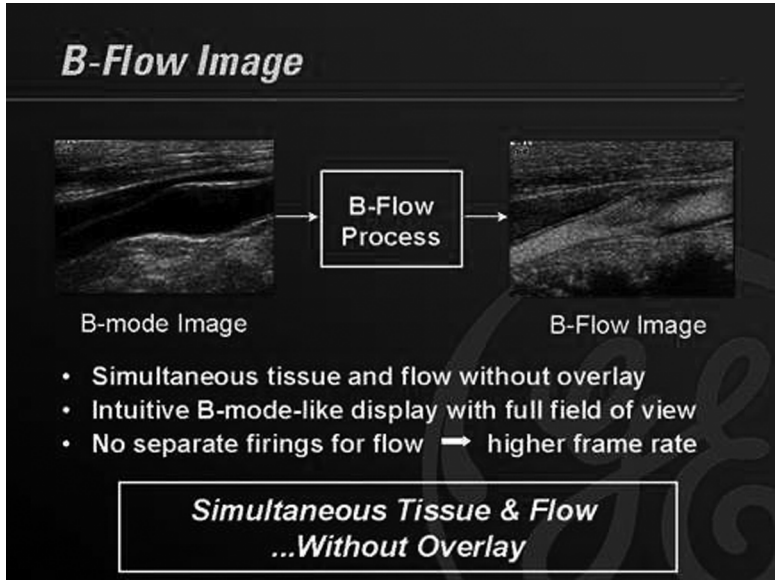

FIGURE 6.11 A comparison of B-mode and B-flow images obtained from a carotid artery. (Courtesy of GE Medical Systems, Milwaukee, WI.)

previously described in Chapter 5 with a scheme to equalize tissue signals, which is necessary because tissue echoes are often much higher than those from blood. The gray scale of an echo is adjusted by correlating the echo waveforms temporally. The correlation function measures the similarity of two echo waveforms and is determined by blood echogenicity, blood flow velocity, and beam width. A filter is designed to suppress large and slow or nonmoving echoes. The result is that the image of blood in an image is enhanced so as to allow the better visualization of blood flow, especially close to the vessel wall. A comparison of the B-mode and B-flow images of a carotid artery is shown in Figure 6.11. It is evident that blood flow is better visualized by B-flow imaging. The vessel lumen where blood flows in the B-mode image is basically anechoic.

REFERENCES

Chiao, R.Y., Mo, L.Y., Hall, A.L., Miller, S.C., and Thomenius, K. B-mode blood flow imaging. In Schneider, S.C., Levy, M., and McAvoy, B.R., Eds. *Proc. 2000 IEEE Ultrason. Symp*. New York, IEEE, 2000, 1469–1472.

Ferrara, K. and DeAngelis, G. Color Doppler mapping. *Ultrasound Med. Biol*. 1997, 23:321–345.

Jensen, J.A. *Estimation of Blood Velocities Using Ultrasound*. Cambridge, U.K.: Cambridge University Press, 1996.

Kasai, C., Namekawa, K., Koyano, A., and Omoto, R. Real-time two-dimensional blood flow imaging using an autocorrelation technique. *IEEE Trans. Sonics Ultrason.* 1985, 32:458–463.

Lerner, R.M., Huang, S.R., and Parker, K. Sonoelasticity images derived from ultrasound signals in mechanically vibrated tissues. *Ultrasound Med. Biol*. 1990, 16:231–239.

Ophir, J., Cespedes, I., Ponnekanti, H., Yazdi, Y., and Li, X. Elastography: a quantitative method for imaging the elasticity of biological tissues. *Ultrasonic Imaging* 1991, 13:111–34.

Routh, H. Doppler ultrasound. *Eng. Med. Biol. Mag*. 1996, 15:31–40.

Rubin, M., Bude, R.O., Carson, P.L., Bree, R.L., and Adler, R.S. Power Doppler US: a potentially useful alternative to mean frequency-based color Doppler US. *Radiology* 1994, 190:853–856.

Shung, K.K., Smith, M.B., and Tsui, B. *Principles of Medical Imaging*. San Diego: Academic Press, 1992.

Trahey, G.E., Allison, J.W., and von Ramm, O.T. Angle independent ultrasonic detection of blood flow. *IEEE Trans. Biomed. Eng*. 1987, 34:965–967.

Zagzebski, J.A. *Essentials of Ultrasound Physics*. St. Louis: Mosby, 1996.

7 Contrast Media and Harmonic Imaging

Contrast media have been used very extensively in radiology, cardiology, and other medical disciplines to enhance certain structures in an image. For instance, iodinated compounds can be injected into the coronary artery to better visualize the coronary vasculature in the heart. Similar ultrasonic agents have been successfully developed (Goldberg et al., 1994; de Jong, 1996) and many applications have been found. Intensive efforts are under way to produce contrast agents for imaging of cardiac chambers, tumor vasculature, and blood flow in various organs, including the kidney and liver. Their ultimate application may well be in quantitating perfusion that is blood supply to a certain region of the organ, which is as yet an unachievable goal for many imaging modalities.

7.1 CONTRAST AGENTS

The primary requirements of an ultrasonic contrast agent are that it is (1) nontoxic; (2) more echogenic than tissues; (3) capable of traversing pulmonary circulation; (4) stable; and (5) uniform in size. The third requirement is dictated by the need for intravenous injection that would minimize the risk of intra-arterial injection. To allow the applications of these agents to imaging left cardiac structures and other parts of the body (e.g., liver and kidney via intravenous injection), they must be smaller than a few microns and stable. They need to persist at least for a duration longer than a few tens of seconds. To satisfy the second requirement, a majority of these agents utilize microscopic air bubbles, which are extremely strong ultrasound scatterers because of the acoustic impedance mismatch.

7.1.1 Gaseous Agents

Echogenic gaseous bubbles are produced by chemical action and/or mechanical agitation. Rigorously stirring a saline solution has been shown to produce air bubbles with a wide distribution of sizes. Typically, however, these bubbles would have a very short lifetime — in the order of a few seconds. Insonication of a saline solution is capable of achieving the same result. Surface agents may be added to stabilize these bubbles. Air bubbles have the advantage of an acoustic impedance mismatch, giving rise to stronger scattering and also resonate when insonified by an ultrasonic wave. The echoes from the bubbles can be further enhanced if the incident wave is tuned to the resonant frequency of the bubbles (Leighten, 1994). The resonant frequency for a free air bubble (a bubble without a shell), f_r, is related to the radius of the bubble, a, by

$$f_r = \frac{1}{2\pi a}\sqrt{\frac{3\gamma P_0}{\rho_w}} \tag{7.1}$$

where

- γ is the ratio of the specific heats at constant pressure and at constant volume of gas and equals 1.4 for air
- P_0 is the hydrostatic ambient pressure and equals $1.013 \cdot 10^5$ Pa or $1.013 \cdot 10^6$ dyn/cm^2 at 1 atm
- ρ_w is the density of the surrounding medium, e.g., water

The scattering cross-section at 2 MHz and resonant frequency of an air bubble of 3-μm radius can be easily calculated from Equation (2.38) and Equation (7.1), assuming that the compressibility and density of air are $6.9 \cdot 10^{-7}$ cm^2/dyn and $1.3 \cdot 10^{-3}$ g/cm^3, respectively. Here, it is assumed that the compressibility term dominates so that the density term can be neglected. Also, G_s in the present case is >> G.

$$\sigma_s = \frac{4}{9}\pi\left(\frac{2\pi}{770 \cdot 10^{-4}}\right)^4 (3 \cdot 10^{-4})^6 \left(\frac{6.9 \cdot 10^{-7}}{4.6 \cdot 10^{-11}}\right)^2$$
$$= 1.04 \cdot 10^{-5} \text{ cm}^2$$

This is much greater than the scattering cross-section of a red cell at 2 MHz. The resonant frequency for an air bubble of 3-μm radius is

$$f_r = \frac{1}{2\pi \cdot 3 \cdot 10^{-4}} \sqrt{\frac{3 \cdot (1.4) \cdot (1.013 \cdot 10^6)}{1.0}}$$
$$= 1.1 \cdot 10^6 \text{ Hz or } 1.1 \text{ MHz}$$

If the bubble radius is decreased to 1.7 μm so as to resonate at 2 MHz, the scattering strength from a bubble may be further increased. The resonant frequency of a bubble as a function of radius is shown in Figure 7.1. Under the conditions that the bubble size is much smaller than the wavelength, the bubble wall displacement is much smaller than its radius, and the surround fluid is incompressible, the scattering cross-section of an oscillating bubble is given by (Medwin, 1977)

$$\sigma_s = \frac{4\pi a^2}{(f_r^2/f^2 - 1)^2 + \chi^2} \tag{7.2}$$

where

- a is the radius of the bubble
- f_r is the resonant frequency
- f is the frequency of the incident wave
- χ is a damping constant consisting of three terms: damping due to reradiation of the ultrasound energy, thermal conductivity (energy loss due to thermal diffusion), and shear viscosity of the surrounding medium (energy loss due to friction)

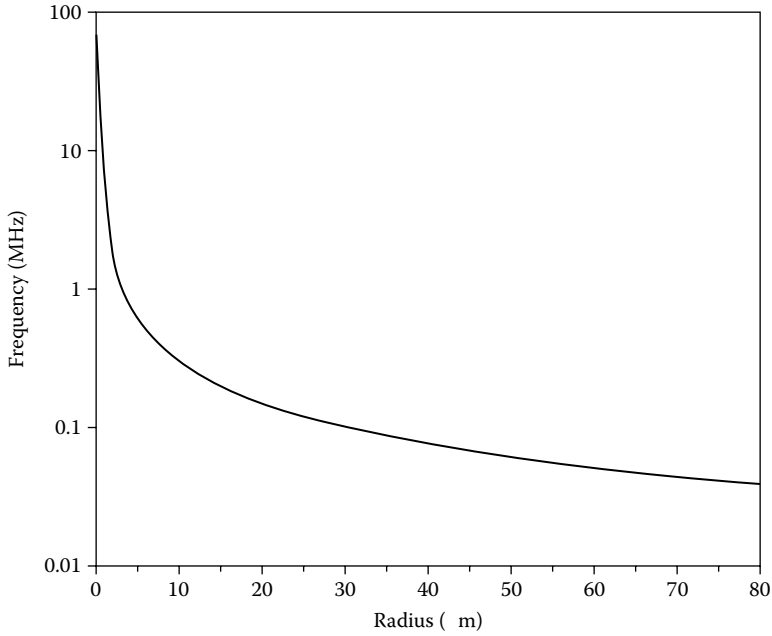

FIGURE 7.1 Calculated resonance frequency vs. radius of a free air bubble.

Equation (7.1) can be rewritten as

$$f_r = \frac{1}{2\pi}\sqrt{\frac{S_a}{m}} \tag{7.3}$$

where S_a is the adiabatic stiffness of the bubble-fluid system defined as (change in force/change in displacement) = $12\pi\gamma P_0 a$ and m effective mass or radiation mass of the system = $4\pi a^3 \rho_w$. Here, an adiabatic equation of state is assumed. However, for bubbles of small radii, surface tension becomes a significant additional restoring force and needs to be considered. Bubble oscillation in this case is better approximated by an isothermal process.

Taking these factors into account, P_0 in Equation (7.1) is replaced by the average interior pressure including surface tension, ςP_0 and γ by the effective ratio of specific heats in the presence of thermal conductivity, $b\gamma$, where b and ς are given by

$$b = (1+B^2)^{-1}\left[1+\frac{3(\gamma-1)}{\xi}\left(\frac{\sinh\xi-\sin\xi}{\cosh\xi-\cos\xi}\right)\right]^{-1} \tag{7.4}$$

$$\varsigma = 1+\frac{2\delta}{P_0 a}\left(1-\frac{1}{3\gamma b}\right) \tag{7.5}$$

In Equation (7.4) and Equation (7.5), δ is surface tension = 75 dyn/cm for an air bubble,

$$B = 3(\gamma + 1)\frac{\xi(\sinh\xi + \sin\xi) - 2(\cosh\xi - \cos\xi)}{\xi^2(\cosh\xi - \cos\xi) + 3(\gamma - 1)\xi(\sinh\xi - \sin\xi)} \tag{7.6}$$

$$\xi = a(2\omega\rho_g C_{pg}/K_g)^{1/2} \tag{7.7}$$

where

K_g is the thermal conductivity of air = $5.6 \cdot 10^{-5}$ cal/cm-sec-°C
ρ_g is the density of air at sea level = $1.3 \cdot 10^{-3}$ g/cm^3
C_{pg} is the specific heat at constant pressure for air = 0.24 cal/g
ω is the angular frequency

Including these parameters, Equation (7.1) should be modified to

$$f_r = \frac{1}{2\pi a}\sqrt{\frac{3b\gamma\varsigma P_0}{\rho_w}} \tag{7.8}$$

The scattering cross-section for a bubble of 1.7-μm radius calculated using Equation (7.2) and Equation (7.8) is shown in Figure 7.2. A scattering peak occurs at approximately 2 MHz, the resonant frequency of the bubble.

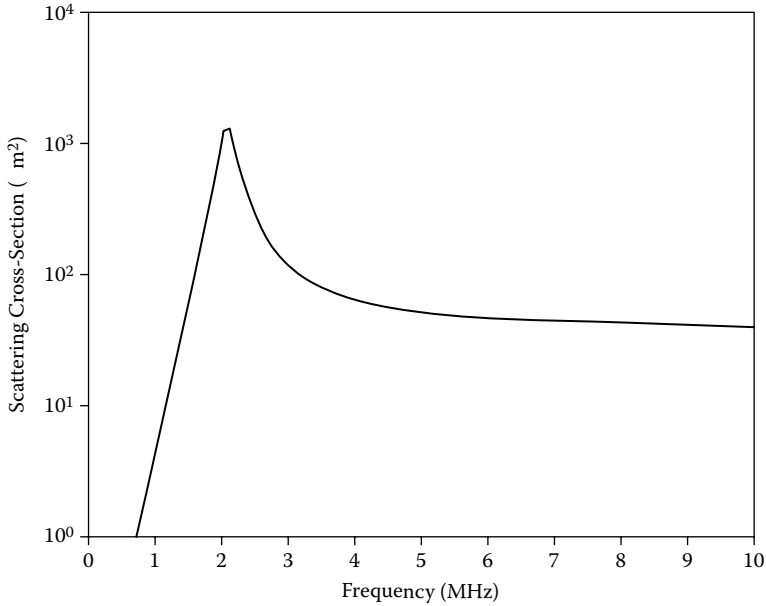

FIGURE 7.2 Calculated scattering cross-section for a free bubble of 1.7-μm radius.

For a beam of ultrasound propagating in a bubbly medium, attenuation will be caused as previously described by scattering and absorption. However, in this case, scattering is more dominant than absorption. For a suspension of bubbles of low concentration where bubble size is smaller than the wavelength, the pressure attenuation coefficient is given by

$$\alpha = \frac{n\sigma_s}{2}$$

where n is the bubble concentration or number of bubbles per unit volume, when the bubble concentration is very low.

7.1.2 Encapsulated Gaseous Agents

Free air bubbles have a very short lifetime, which is not suitable for human applications. This problem can be overcome by encapsulating air with a shell. Two commercial products, Albunex, and Optison (an improved version of Albunex), have the plasma protein, albumin, as the shell material. Albunex contains air and Optison contains a large molecule gas, perfluoropropane, that minimizes the diffusion of the gas out of the shell, thus yielding a much longer bubble lifetime. These types of agents are produced by insonicating human serum albumin solutions.

The effect of a shell on the resonant behavior has been taken into consideration by assuming that the shell causes an additional restoring force to the bubble system, which tends to increase the resonant frequency and decrease the scattering cross-section (de Jong, 1996). The contribution of the shell to the bubble stiffness is given by

$$S_{shell} = 8\pi \frac{El_t}{1-\upsilon} = 8\pi S_p \tag{7.9}$$

where

S_{shell} is the shell stiffness
E is the shell elasticity
l_t is the wall thickness
υ is Poisson's ratio of the shell material
$S_p = El_t/(1 - \upsilon)$, the shell stiffness parameter defined as (change in force/change in displacement) in dynes per centimeter

The resonant frequency of a bubble with a shell can be obtained from Equation (7.3) by including an additional stiffness term:

$$f_r = \frac{1}{2\pi}\sqrt{\frac{b\varsigma S_a + S_{shell}}{m}} \tag{7.10}$$

The parameters given in Equation (7.10) are difficult to estimate. This may be done by fitting experimental data to theoretical models. To better fit the experimental data to theory, an additional damping term accounting for internal friction or viscosity within the shell was introduced by de Jong (1996). The optimal value for the shell stiffness of the Albunex microspheres was estimated to be $8 \cdot 10^3$ dyn/cm.

7.1.3 Dilute Distribution of Bubbles of Varying Size

It is extremely difficult, if not impossible, to produce bubbles of a very narrow range of size distribution. The sonicated solution typically has a larger size distribution than the commercially produced agents. Albunex has a mean diameter of 3 to 5 μm; a large portion of the bubbles have a radius smaller than 10 μm. Figure 7.3 shows the size distribution of Albunex and Optison (FS069). When the volume concentration of the bubbles is lower than 1%, the mean scattering cross-section of the bubbles, $<\sigma_s>$, can be calculated from

$$<\sigma_s> = \frac{\int_0^\infty \sigma_s(a,f)n(a)\,da}{N} \tag{7.11}$$

where

$\sigma_s(a,f)$ is the scattering cross-section of a bubble with a radius at ultrasound frequency f

N is the total number of bubbles

$n(a)da$ is the number of bubbles with a radius between a and $a + da$ (Morse and Ingard, 1968)

In a distribution of bubbles, attenuation is dominated by scattering, so the mean attenuation coefficient can be found in the same way by replacing σ_s with α. The

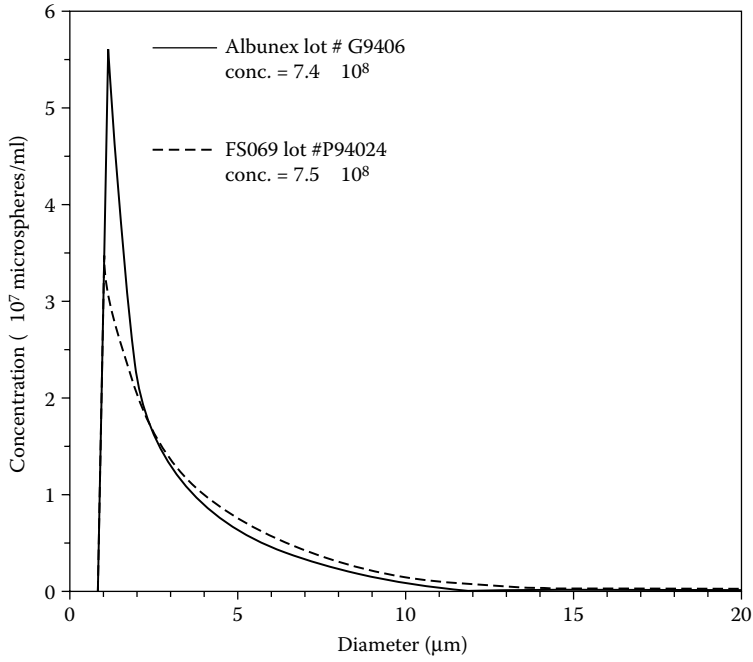

FIGURE 7.3 Size distributions of two commercial contrast agents, Albunex and Optison (FS069).

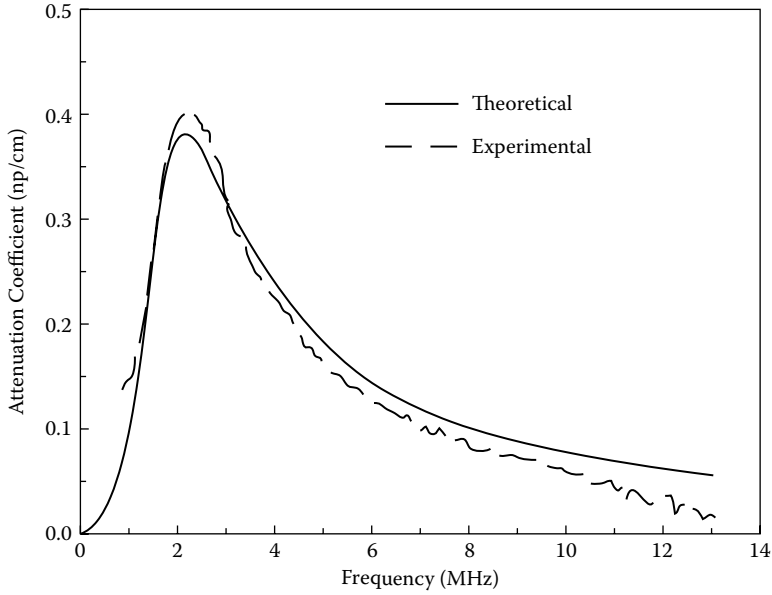

FIGURE 7.4 Experimental data and theoretical curve of attenuation coefficient as a function of frequency for Albunex.

attenuation coefficient of Abunex as a function of frequency is shown in Figure 7.4, in which the maximal attenuation or scattering is seen to occur at approximately 2 MHz.

7.2 NONLINEAR INTERACTIONS BETWEEN ULTRASOUND AND BUBBLES

The nonlinear response of a spherical bubble to a time-varying pressure field in an incompressible fluid has been studied by many investigators, including Rayleigh (1917) and Plesset (1949). It can be obtained by solving the following Rayleigh–Plesset equation under certain assumptions:

- The motion of the bubble is symmetric.
- The wavelength is much greater than the bubble radius.
- The bubble contains vapor and gas.
- There is no rectified diffusion, which means the active pumping of gas initially dissolved in the fluid surrounding the bubble into the bubble by the sound field.
- The bubble oscillates according to the gas law with the polytropic constant, ψ.

The derivation of this equation can be found in Leighton (1994).

$$\rho_w a\ddot{a} + \frac{3}{2}\rho_w \dot{a}^2 = P_g\left(\frac{a_0}{a}\right)^{3\psi} + P_v - P_0 - \frac{2\delta}{a} - \chi\omega\rho_w a\dot{a} - P_a\cos\omega t \qquad (7.12)$$

where

a is the bubble radius
a_0 is the initial bubble radius
ρ_w is the density of surrounding medium
P_g is the initial internal pressure of the bubble = $P_0 - P_v + 2\delta/a_0$
P_0 is the ambient pressure
P_v is the vapor pressure
δ is the surface tension
χ is the damping constant
P_a is the $\cos\omega t$ incident pressure

For an air bubble in water, $P_v = 2.33 \cdot 10^4$ dyn/cm^2 and $P_0 = 1.013 \cdot 10^6$ dyn/cm^2 at 1 atm. The polytropic exponent or constant of gas $\psi = b\gamma$, where b is given by Equation (7.4). For air, $\psi = \gamma$ under adiabatic conditions and = 1 under isothermal conditions. The values for ψ for different gases have been measured (Crum, 1983). Under adiabatic conditions, ψ = 5/3, 7/5, and 4/3 for monoatomic, diatomic, and triatomic gas, respectively.

7.3 MODIFIED RAYLEIGH–PLESSET EQUATION FOR ENCAPSULATED GAS BUBBLES

The Rayleigh–Plesset equation was modified by de Jong et al. (1994) to take the shell into consideration, including from the internal frictional loss and the restoring force caused by shell stiffness:

$$\rho_w a\ddot{a} + \frac{3}{2}\rho_w \dot{a}^2 = P_g\left(\frac{a_0}{a}\right)^{3\psi} + P_v - P_0 - \frac{2\delta}{a} - \frac{S_{shell}}{4\pi}\left(\frac{1}{a_0} - \frac{1}{a}\right) - \chi_t \omega \rho_w a\dot{a} - P_a \cos\omega t \tag{7.13}$$

where

χ_t is the modified damping constant that accounts for the additional damping caused by shell friction
S_{shell} is the shell elasticity parameter, assumed to be a constant = $8 \cdot 10^3$ dyn/cm by de Jong et al. (1994) and de Jong (1996)

7.4 SOLUTIONS TO RAYLEIGH–PLESSET EQUATION

The Rayleigh–Plesset equation can be solved analytically or numerically (de Jong et al., 1994). Figure 7.5 shows the numerical results on the change in radius and velocity of an air bubble of 1.7-μm radius in water at 20°C in the time domain and frequency domain driven by a 30-cycle sinusoidal signal of 40 kPa amplitude at the bubble resonant frequency of 2 MHz. Initially, the bubble is assumed to be resting. Only the results for the last 10 cycles, a time when the system is assumed to have reached steady state, are shown. The bottom panel shows the spectra of the velocity waveforms. As expected, at the maxima or minima of the radius variation of the bubble, the velocity is zero.

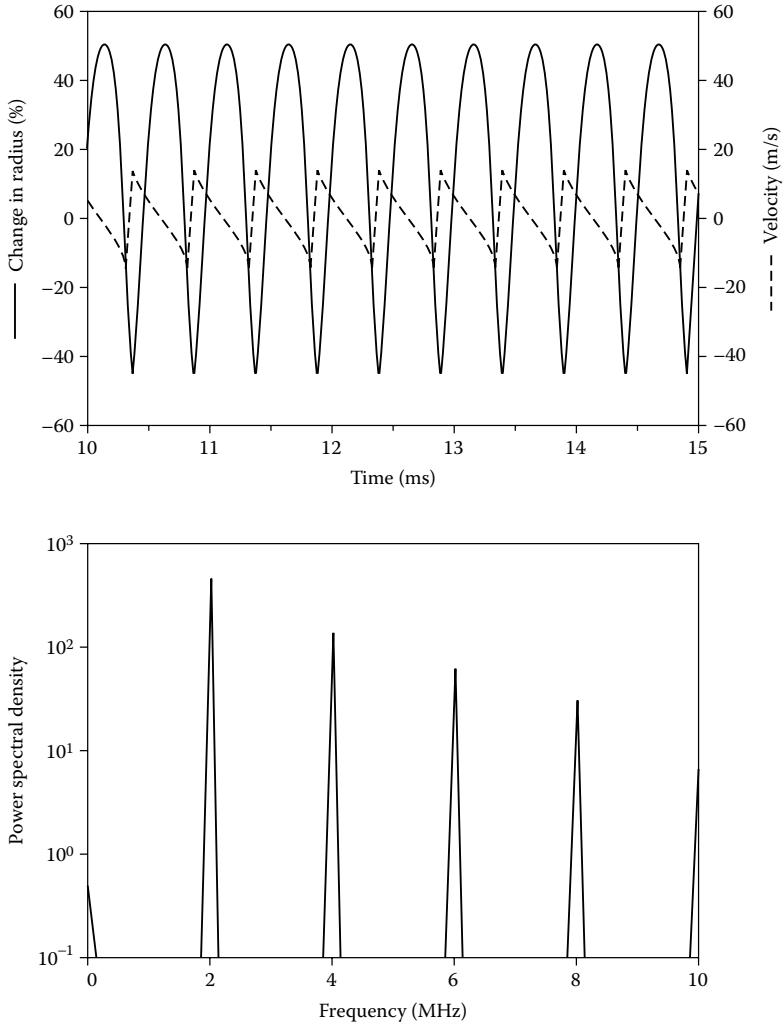

FIGURE 7.5 Response of an air bubble driven at its resonant frequency by an ultrasonic wave of 40 kPa. Top: changes in radius and velocity of bubble wall. Bottom: corresponding power spectra.

Figure 7.6 shows the response for Albunex of 2.4-μm radius driven at 2 MHz, which exhibits a smaller swing in magnitude than a free bubble. Due to its larger stiffness, the radius of Albunex is larger to maintain the resonant frequency at 2 MHz. A value of 8000 dyn/cm was used for the shell elasticity, S_{shell}. The additional damping due to shell friction was also included in the calculation (Chang et al., 1998).

The computed scattering cross-section of an air bubble of 1.7-μm radius and Albunex of 4.7-μm radius at first and second harmonics as a function of the driving frequency is given in Figure 7.7 (de Jong et al., 1994; Chang et al., 1998). The scattering cross-section peaks for first and second harmonics at 2 MHz. Beyond this

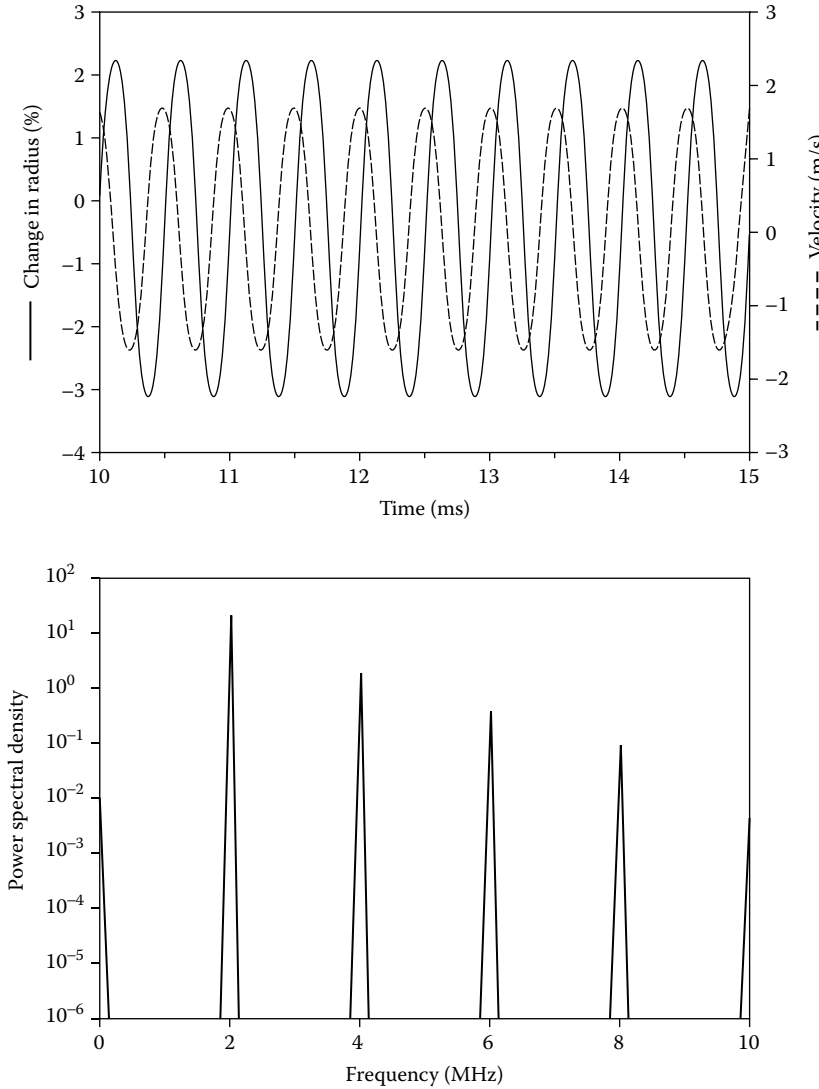

FIGURE 7.6 Response of Albunex driven at its resonant frequency by an ultrasonic wave of 40 kPa. Top: changes in radius and velocity of bubble wall. Bottom: corresponding power spectra.

frequency, it approaches the physical scattering cross-section ($4\pi a^2$). Note that the second harmonic response is only prominent in the vicinity of the resonant frequency. The air bubble also has a secondary maximum at one-half of the resonant frequency, which is a subharmonic frequency (not shown in the figure). The secondary maximum, however, does not exist for Albunex. Figure 7.8 shows the scattered power as a function of the radius from Albunex with a size distribution shown in Figure 7.3 for a transmitted frequency of 2 MHz and an amplitude of 40 kPa. The scattered power peaks at 4.7 μm for the first and second harmonic signals.

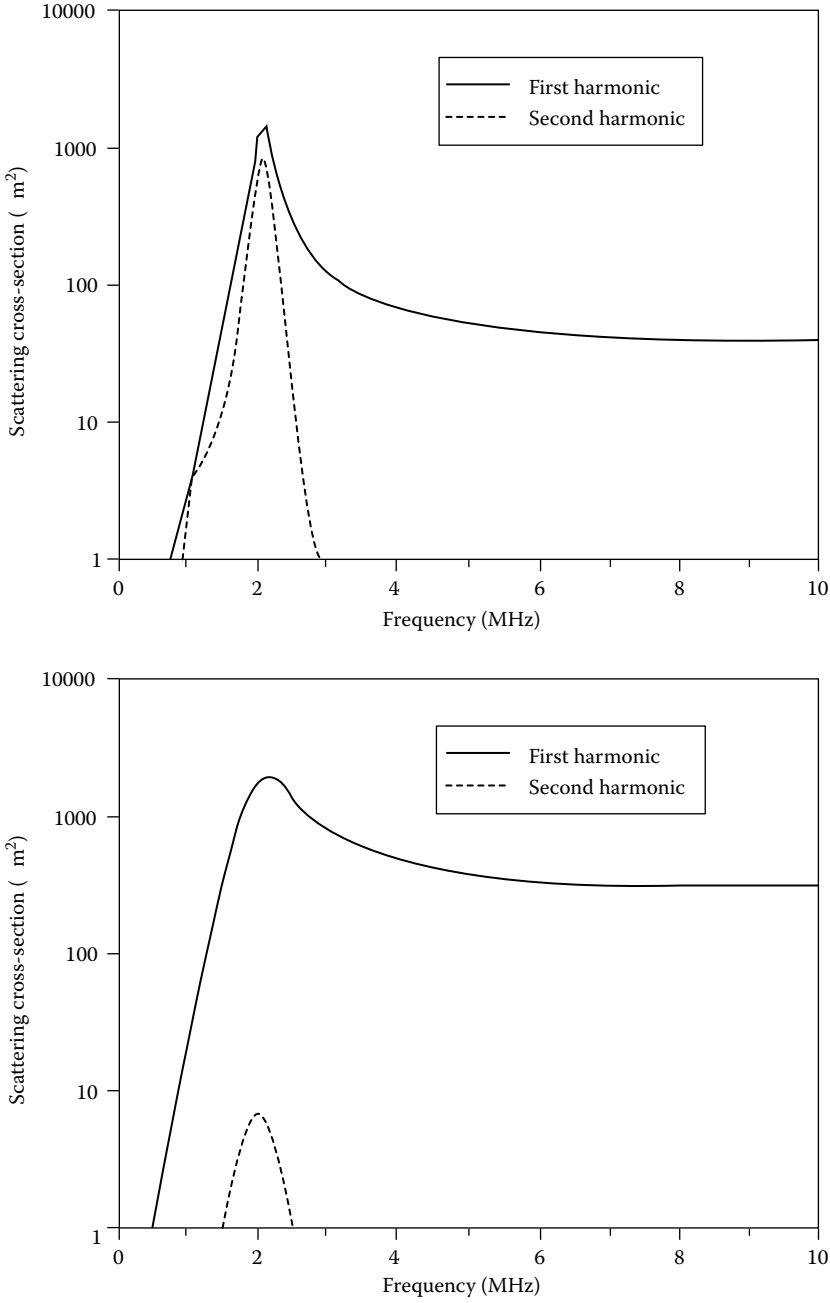

FIGURE 7.7 Calculated scattering cross-section as a function of transmitted frequency at a driving peak pressure of 40 kPa. Top: for a free bubble of 1.7-μm radius. Bottom: for Albunex of 4.8-μm radius.

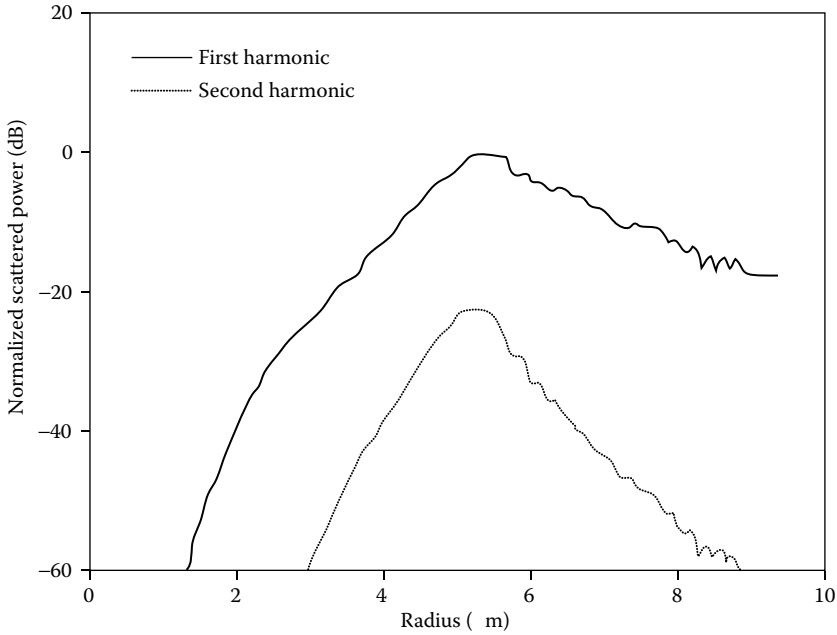

FIGURE 7.8 Normalized scattered power at first and second harmonics as a function of Albunex radius. The size distribution shown in Figure 7.3 is used. The transmitted frequency and peak pressure are 12 MHz and 40 kPa, respectively.

7.5 HARMONIC IMAGING

An exciting new application of the air-containing agents is found in harmonic imaging and Doppler measurements in which the effect of the surrounding stationary structures on the image and results is minimized. Harmonic imaging or Doppler measurements following the injection of a gas-containing contrast agent are possible because only microbubbles resonate when impinged upon by ultrasound and emit ultrasound at harmonic frequencies. Ultrasound at harmonic frequencies will only be produced by anatomic structures that contain these agents. Tissues that do not contain gaseous contrast agents presumably will not produce harmonic signals. A good example is blood flowing in a blood vessel. Blood containing the contrast agent will produce harmonic signals but the blood vessel will not. The contrast between the blood and the blood vessel will therefore be significantly improved in the resultant harmonic image if only the echoes at the harmonic frequency are detected by the transducer.

The simplest approach that may be taken in harmonic imaging is to generate a wide-band signal acoustic signal. Only the harmonic signals are received for image formation, as illustrated in Figure 7.9. The array or transducer is excited with the first harmonic signal or fundamental frequency signal, which can be achieved with a one-cycle sinusoidal signal, indicated by the thin solid line. The echoes received by the transducer are then filtered to collect the data only at the harmonic frequency indicated by the dashed line. The bold line indicates the original spectrum of the transducer. A major problem associated

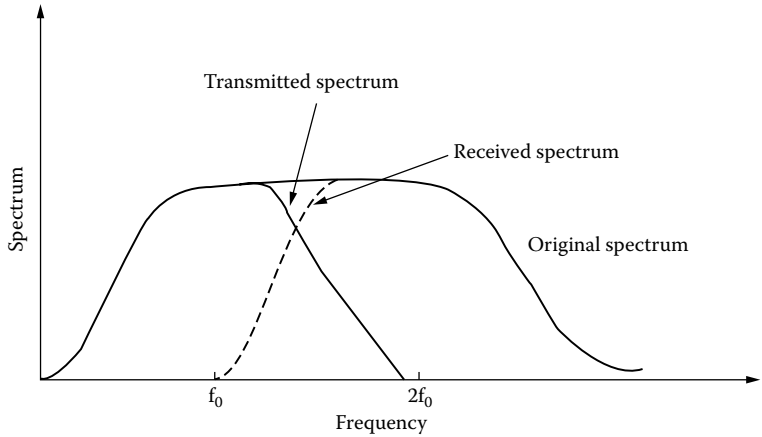

FIGURE 7.9 In harmonic imaging, the spectrum of a pulse within the bandwidth is divided into two bands: one for transmitting the pulse at fundamental frequency and one for receiving the second harmonic signal.

with such an approach is that it is impossible to suppress echoes at fundamental frequency completely due to spectral leakage, i.e., the overlapping area of the two spectra. Thus, they can corrupt the harmonic echoes.

Figure 7.10 and Figure 7.11 illustrate two other types of approaches that have been used to overcome this problem: pulse inversion and amplitude modulation

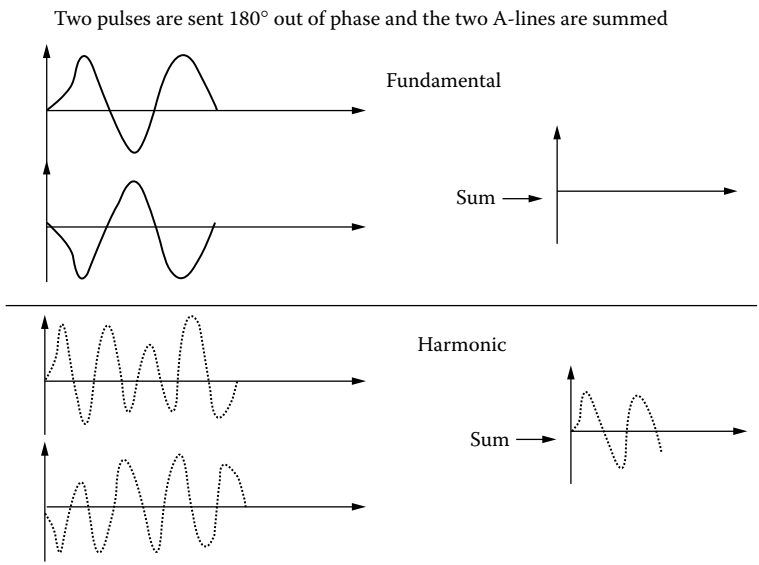

FIGURE 7.10 In pulse inversion harmonic imaging, two pulses 180° out of phase are transmitted. The returned echoes at fundamental frequency will cancel each other out upon summation (top), whereas the echoes at harmonic frequency will not (bottom).

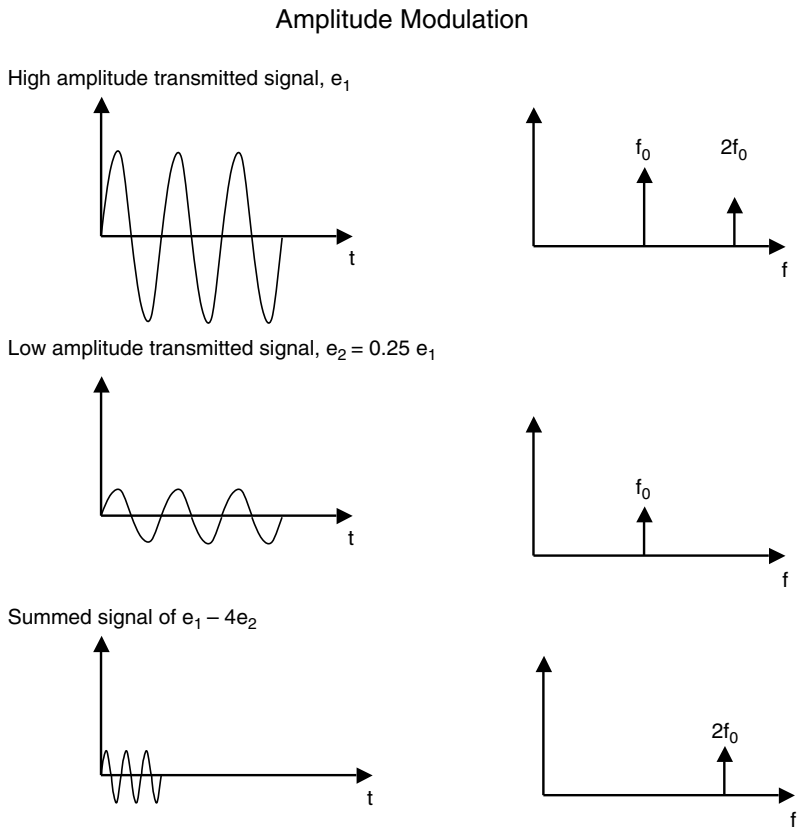

FIGURE 7.11 In amplitude modulation harmonic imaging, two pulses of different amplitudes, e_1 and $e_2 = 0.25\ e_1$, are transmitted. The larger pulse is assumed to produce a second harmonic signal, whereas the smaller one does not. Upon performing the mathematical operation $e_1 - 4e_2$, echoes at the fundamental frequency will be cancelled out and the echoes at harmonic frequency will not.

(Averukiou, 2000). In pulse inversion, two pulses of 180° out of phase are transmitted sequentially. The returned echoes are summed up. The echoes at the fundamental frequency will be cancelled out, but those at the harmonic frequencies will not. In amplitude modulation, two pulses of different amplitudes are transmitted. The larger pulse will produce echoes at harmonic frequencies, but the smaller pulse will not. The signal at fundamental frequency may be subtracted out by adjusting the amplitude of the returned echoes. Only echoes at harmonic frequencies remain. Ideally, these approaches are less affected by spectral leakage.

7.6 NATIVE TISSUE HARMONIC IMAGING

Harmonic imaging can also be performed on tissues without the injection of a contrast agent. Harmonic signals are produced as the ultrasound pulse penetrates into the body because of the nonlinear interaction between the tissues and ultrasound

energy (previously discussed in Section 2.8 in Chapter 2). Energy at the fundamental frequency is partly absorbed, partly scattered, and partly converted into harmonic and subharmonic signals, which increase initially, reach a plateau, and then decrease. Similar approaches described in Section 7.5 can be used to perform native tissue harmonic imaging.

Native tissue harmonic imaging has several advantages over conventional B-mode imaging:

- It can penetrate more deeply into tissues because more harmonic signals are generated until they are offset by the increased attenuation. Consequently, it is frequently observed that harmonic images are better when obese patients are imaged.
- It has better lateral resolution because the beam is narrower due to the higher receiving frequency.
- It is less noisy in the near field because the harmonic signal is small in the near field.
- It has smaller side lobes.

Harmonic imaging also has drawbacks:

- Axial resolution may be compromised as a result of the reduced bandwidth.
- Attenuation is higher, thus shifting the center frequency of the pulse to lower frequencies.

7.7 CLINICAL APPLICATIONS OF CONTRAST AGENTS AND HARMONIC IMAGING

When the contrast agents were first developed, their primary objective was in delineating cardiac structures. For instance, cardiac chamber borders can be better defined with the aid of a contrast agent, as illustrated in Figure 7.12. Since then, many applications have been found, including enhancing color Doppler flow images to better visualize smaller blood vessels (e.g., renal and hepatic arteries). The destruction of contrast agents by insonicating ultrasound has been used to measure blood flow stemming from the observation that the change in echogenicity following destruction is related to blood flow velocity. The most useful application of ultrasonic contrast agents appears to be in quantitating perfusion that is the blood supply to a certain region of an organ; this can seldom be done noninvasively. The wash-in and wash-out times and other parameters that can be estimated form the change in echogenicity of blood following the injection of a bolus of a contrast agent have been investigated as indicators of blood perfusion (Goldberg et al., 1994, de Jong, 1996).

More recently, the interest in ultrasonic contrast agents has focused on their potential in drug delivery and gene therapy. Drugs can be carried by these agents in the interior or in the shell to a targeted organ, where they are released. The releasing of a drug may be achieved by insonicating the agent by ultrasound. The agent may

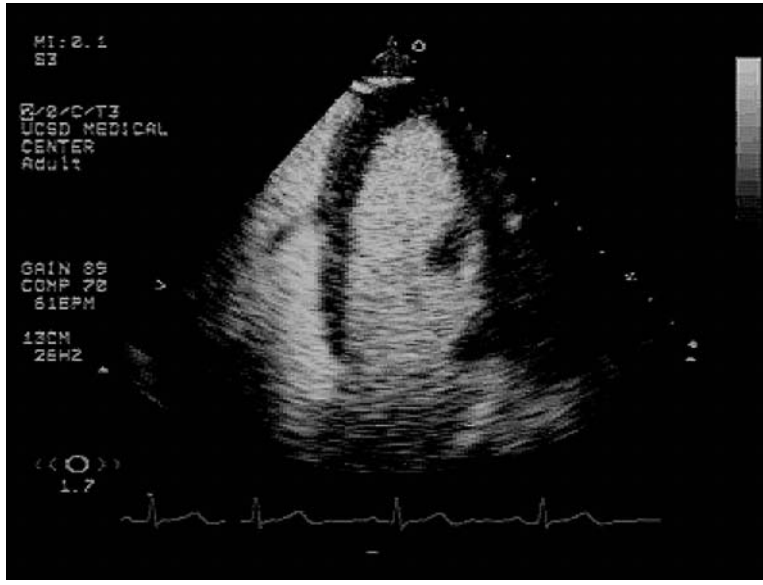

FIGURE 7.12 A four-chamber view of the heart with the interior of the cardiac chamber filled with bright echoes generated by a contrast agent. The borders of the cardiac chamber are better delineated. Echo-poor zones in the cardiac chamber may be due to the presence of thrombi. (Courtesy of Philips Ultrasound.)

be carried by the blood stream passively to an organ of interest or it may actively seek out the targeted tissues by binding them with specific molecules that interact only with a certain group of molecules in a tissue (Lanza et al., 2000).

REFERENCES

Averukiou, M.A. Tissue harmonic imaging. *2000 IEEE Ultrason. Symp. Proc*. 2000, 2:1563–1572.

Chang, P.P. and Shung, K.K. Interaction of ultrasound with contrast agents. In *Trends in Contrast Agents*, Thomsen, H.S., Muller, R.N. and Mattery, R.F., Eds. Berlin: Springer, 1998.

Crum, L.A. and Prosperetti, A. Nonlinear oscillations of gas bubbles in liquids: an interpretation of some experimental results. *J. Acoust. Soc. Am.* 1983, 73:121–127.

De Jong, N., Cornet, R., Lancee, and C.T. High harmonics of vibrating gas-filled microspheres. Part one: simulations. *Ultrasonics* 1994, 32:447–453.

De Jong, N. Improvements in ultrasound contrast agents. *Eng. Med. Biol. Mag*. 1996, 15:72–82.

Goldberg, B.B., Liu, J.B., and Forsberg, F. Ultrasound contrast agents: a review. *Ultrasound Med. Biol*. 1994, 20:319–333.

Lanza, G., Hall, C., Scott, M., Fuhrhop, R., March, J., and Wickline, S. Molecular imaging with targeted ultrasound contrast agent. *2000 IEEE Ultrason. Symp. Proc*. 2000, 2:1917–1926.

Leighton, T.G. *The Acoustic Bubble*. San Diego: Academic Press, 1994.
Medwin, H. Counting bubbles acoustically: a review. *Ultrasonics* 1977, 15:7–13.
Morse, P.M. and Ingard, K.U. *Theoretical Acoustics*. New York: McGraw-Hill, 1968.
Plesset, M.S. The dynamics of cavitation bubbles. *J. Appl. Mech*. 1949, 16:277–282.
Rayleigh, L. On the pressure developed in a liquid during the collapse of a spherical cavity. *Phil. Mag*. 1917, 34:94–98.

8 Intracavity and High-Frequency (HF) Imaging

Conventional ultrasonic imaging systems typically use frequencies from 2 to 15 MHz. Scanners at lower frequencies have the advantage of a larger depth of penetration but suffer from poorer resolution. To improve spatial resolution, one obvious strategy would be to increase the frequency. The axial resolution is determined by the pulse duration or bandwidth of the pulse. For a fixed number of cycles per pulse, an increase in frequency would result in a reduction in wavelength and thus pulse duration.

The relationship between frequency (wavelength) and lateral spatial resolution is given by Equation (3.30). These relationships are graphically illustrated in Figure 8.1 and Figure 8.2. As ultrasound frequency is increased to 50 MHz, an axial resolution and lateral resolution of better than 20 and 100 μm for an f number of 2.9 can be achieved, respectively. The price to be paid is an increase in attenuation. The effect of attenuation coefficient of a few types of tissues of clinical interest is shown in Figure 8.3. At 50 MHz, the depth of penetration for most tissues would be limited to 4 to 5 mm. As was discussed, the depth of penetration may be increased slightly by introducing novel signal processing methods such as coded excitation; however, the range of frequencies that can be applied to a certain organ is limited.

8.1 IMAGING

Intracavity imaging such as transesophageal, transrectal, and transvaginal imaging is a partial solution to achieving improvements in spatial resolution. Imaging organs such as the heart, prostate, and uterus/ovary from the body surface does not usually allow the utilization of frequencies higher than 5 MHz because they are deep-lying organs; however, probes may be modified to be inserted through open cavities of the body. Under these conditions, higher frequencies may be used because the probes are in closer contact with the organ of interest.

8.1.1 Transesophageal Cardiac Imaging

Phased arrays consisting of more than 48 elements at frequencies from 5 to 7.5 MHz can be mounted on the tip of an endoscope with a diameter less than 10 mm for imaging the heart in the esophagus. The endoscope allows the manipulation of the position and direction of the phased array. During scanning, the transesophageal probe is inserted into the esophagus and the tip is positioned against the wall of the

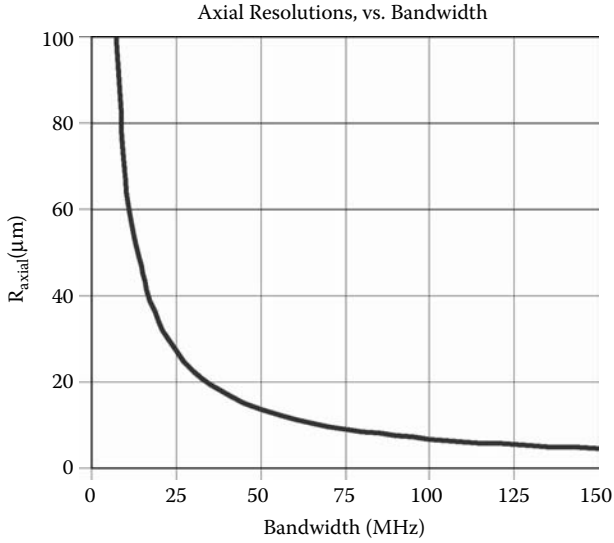

FIGURE 8.1 Calculated axial resolution as a function of bandwidth.

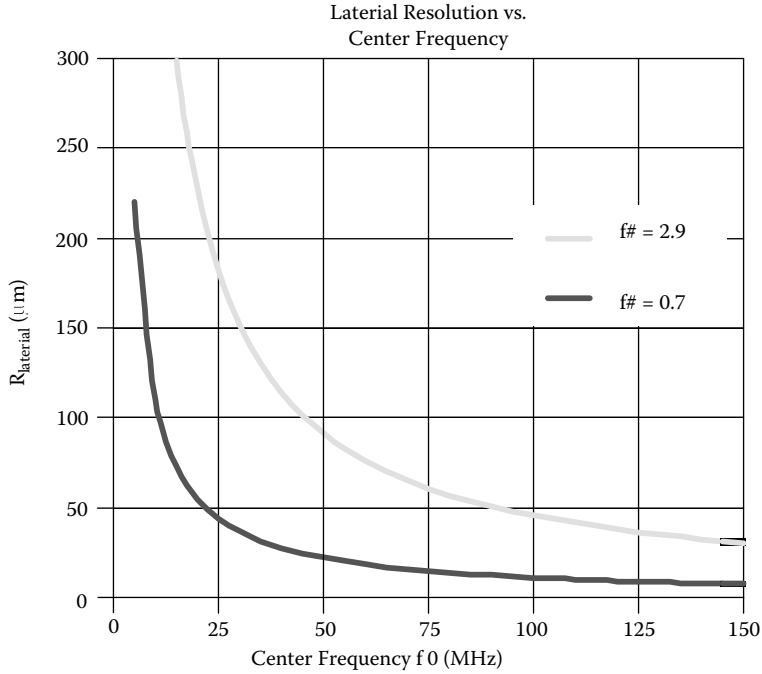

FIGURE 8.2 Calculated lateral resolution as a function of ultrasound center frequency.

At 50 MHz

$\alpha_{blood} \approx 2.5$ dB/mm
$\alpha_{cornea} \approx 1.1$ dB/mm
$\alpha_{iris} \approx 1.7$ dB/mm
$\alpha_{skin} \approx 10$ dB/mm

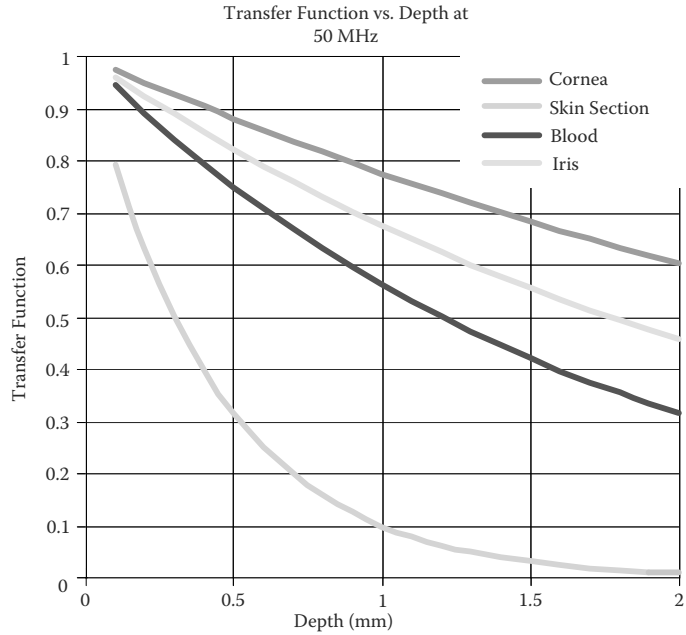

FIGURE 8.3 The effect of ultrasound attenuation of four different types of tissues plotted as a function of depth at 50 MHz. The transfer function is given by $e^{-\alpha z}$ where α is the attenuation coefficient and z is the propagation depth.

esophagus under local anesthesia. A majority of the probes are capable of bi-plane imaging, i.e., two orthogonal images are produced. More advanced versions can produce images in any direction by mechanically rotating the array.

Transesophageal imaging of the heart yields better images of the whole heart because of the higher frequencies as well as of the base of the heart, which cannot be adequately accessed by transthoracic imaging. Additional benefits are that transesophageal imaging allows continuous monitoring of the cardiac functions; this has been proven valuable in anesthesiology during surgery. A photo of such a probe is shown in Figure 8.4. Commercial catheters (10 French units, 1 F = 0.33 mm outer diameter) mounted near the tip is a linear array at a frequency of 8 MHz are also available for intracardiac imaging. The catheter can be guided to the heart by a guide wire via a peripheral artery.

8.1.2 Transrectal and Transvaginal Imaging

Probes at frequencies higher than 5 MHz are available for most of imaging systems for insertion into the rectum or vagina for better imaging of the prostate and uterus/ovary. A linear array or curved linear array is mounted at the side or at the tip of a probe. A full bladder, which used to be recommended for transabdominal

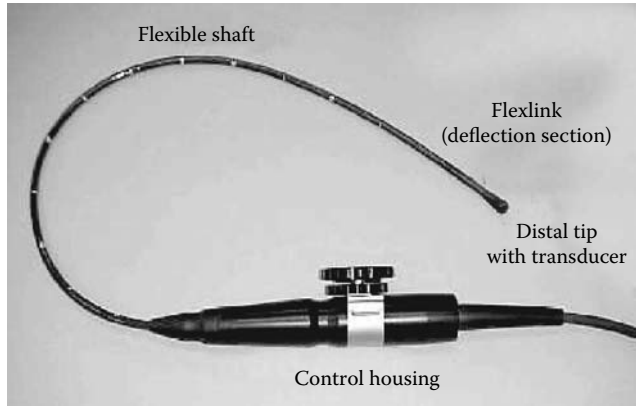

FIGURE 8.4 A photo of a transesophageal probe. (Courtesy of Oldelft B.V., Delft, the Netherlands.)

obstetrical imaging of a fetus, may now be replaced by transvaginal imaging. A photo of several transrectal and transvaginal probes is shown in Figure 8.5.

8.1.3 Endoluminal Imaging

Catheter-based imaging systems have also been used to image the gastrointestinal tract, including colon, esophagus, and stomach (Liu and Goldberg, 1999). A few manufacturers have developed specialized ultrasonic imaging systems to accomplish this by mounting ultrasonic transducers/arrays on the end of an endoscope.

FIGURE 8.5 A photo showing several types of ultrasound probes including linear arrays and linear curved arrays, Doppler probes, and transrectal and transvaginal probes (long and slender ones in the upper half of the photo). (Courtesy of Sound Technology Inc., State College, Pennsylvania.)

8.2 INTRAVASCULAR IMAGING

Imaging of the wall of blood vessels for the purpose of estimation of the degree of stenosis and characterization of atherosclerotic plaques has been pursued for many years with a variety of imaging modalities (Pandian, 1989; Liu and Goldberg, 1999). In the past, x-ray angiography has been the gold standard for assessing stenosis. The drawback is that it is a form of ionizing radiation and the procedure involves the injection of a contrast agent. As a result, its role is being challenged by magnetic resonance imaging and ultrasound (Shung et al., 1992).

Plaque composition characterization is of clinical importance in that it has been hypothesized that vulnerable plaques consisting of a lipid core with a fibrous cap are most likely to rupture, causing the formation of clots and serious clinical consequences such as stroke and heart attack. Imaging options for characterizing plaque composition are quite limited. Fiberoptic angioscopy, in which an optic fiber is introduced via catheterization to the site of interest for the visualization of plaque surface, and transcutaneous ultrasound have been used. The former procedure involves injection of saline for flushing out light opaque blood and only visualizes the lesion surface; the latter suffers from poor resolution. Intravascular ultrasound and optical coherent tomography (OCT) are possible alternatives to alleviating these problems (Liu and Goldberg, 1999; Bouma and Tearney, 2002). Intravascular ultrasound scanners typically are operated in the frequency range from 20 to 60 MHz depending upon the imaging catheter used.

Two different types of imaging catheters are on the market today. In one, a single-element transducer at a frequency from 30 to 60 MHz, of 1.75 mm diameter, and making an angle of 10° relative to the direction normal to the long axis of the catheter, is mounted near the tip of the catheter. The transducer is mechanically rotated at a very high speed (~1800 rpm) by a shaft. These catheters have a size of 3.5 to 6 F. In another, a 64-element array at 20 MHz with a 1.5λ pitch is mounted around the circumference of a 3.5 French catheter (1.2 mm outer diameter). The elevation width of the array is 0.7 mm. Also mounted on the catheter with the array are several integrated circuit chips that perform the functions of low noise broadband preamplification and multiplexing. A synthetic imaging approach in which one element transmits and 14 elements receive is used to form the image.

Figure 8.6 shows a catheter with a mechanically rotated transducer (top) and a catheter with an array wrapped around the circumference (bottom). Although the array catheter has a higher frame rate, it yields an image quality slightly inferior to that of the mechanically rotated type, primarily because of its lower frequency.

In addition to plaque characterization, intravascular ultrasound has been found to be useful in guiding the placement of a stent and monitoring stent restenosis. Figure 8.7 shows a 40-MHz image of an artery and Figure 8.8 shows a 20-MHz image of a stent. At present, all intravascular ultrasonic imaging devices use side-looking catheters, which lack the capability of visualizing anatomic structures in front of the catheter. This capability is important in order not to cause any injury to the blood vessel, such as perforation and dissection, while the catheter is guided to the site of interest. Efforts to develop forward-looking intravascular catheters are now under way.

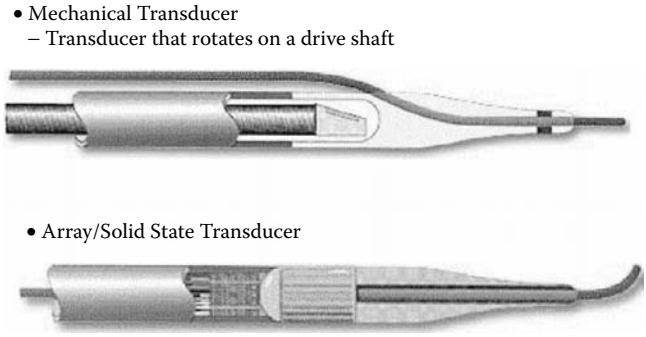

FIGURE 8.6 An intravascular imaging catheter with a mechanically rotated transducer (top) and a catheter with an array wrapped around the circumference (bottom). (Courtesy of Boston Scientific and Volcano Therapeutics.)

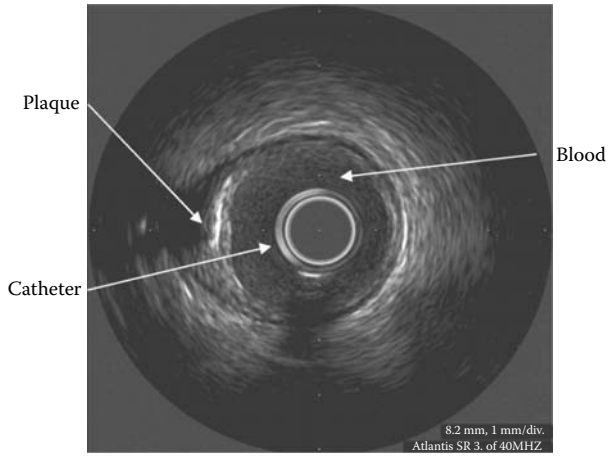

FIGURE 8.7 An image of an artery acquired at 40 MHz by a catheter with a rotating single-element transducer. (Courtesy of Boston Scientific.)

8.3 HIGH-FREQUENCY IMAGING

Scanners operated at frequencies higher than 20 MHz have been developed for applications in ophthalmology, dermatology, and small-animal imaging. These devices, called ultrasonic backscatter microscopes or ultrasonic biomicroscopes (UBMs), typically obtain images by scanning a single-element ultrasonic transducer in a sector format or linearly. The construction of a UBM is identical to that of a static B-mode scanner (Briggs and Arnold, 1994; Pavlin and Foster, 1995).

Scanning can also be achieved by better utilizing the focus of the transducer by incrementally moving the transducer in the axial direction, called B–D (D stands for depth) mode scan. A composite image is formed by combing the focused segments

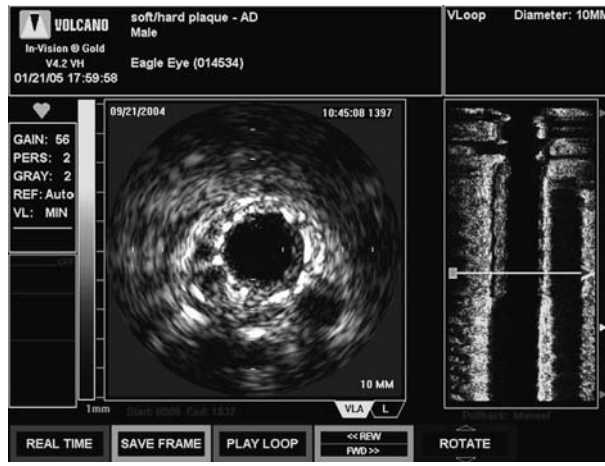

FIGURE 8.8 (See color figure following page 80.) A 20-MHz imaging catheter is placed at the midstent level. The right panel shows a longitudinal view of the stent. The echogenic stent structure is clearly seen. (Courtesy of Volcano Therapeutics.)

of multiple images acquired as the transducer is moved in the axial direction. This mode of scanning improves lateral resolution by sacrificing frame rate. Commercial UBMs can achieve a frame rate of 30/sec because the excursion range of the transducer is extremely small.

High-frequency scanners that utilize linear arrays are not yet commercially available, although extensive investigations to develop HF arrays and associated imaging electronics are under way (Ritter et al., 2002). Conventional dicing technology may be used to fabricate linear arrays up to 50 MHz. For fabricating linear arrays higher than 50 MHz, alternative technology, such as MEMS and laser dicing, may need to be exploited. Other challenges are the high electrical impedance of the small array elements that causes electrical impedance mismatch and the lack of high-speed electronics needed for the development of the HF beam former.

High-frequency ultrasound has many clinical applications. In ophthalmology, scanners at 20 MHz or slightly lower have been used to interrogate the posterior components of the eye, including the retina. Those at 40 MHz and higher are useful for visualizing the anterior segments of the eye, including the cornea, to monitor the state of corneal transplant, and diagnosing tumors and glaucoma. Figure 8.9 shows the anterior segments of the eye obtained by a UBM at 50 MHz *in vitro*. The cornea, including the stroma, iris, and cilliary body, is clearly seen. Figure 8.10 shows an enlarged opening of the pupil when the light is turned off.

Clinical applications of HF ultrasound in dermatology include characterization of tumors and assessing the size of structures in the skin, e.g., the sebaceous gland. An image of the backhand skin obtained by a UBM at 50 MHz is shown in Figure 8.11. In ophthalmology and dermatology, HF ultrasound competes with OCT. The resolution of HF ultrasound is inferior but the depth of penetration is superior.

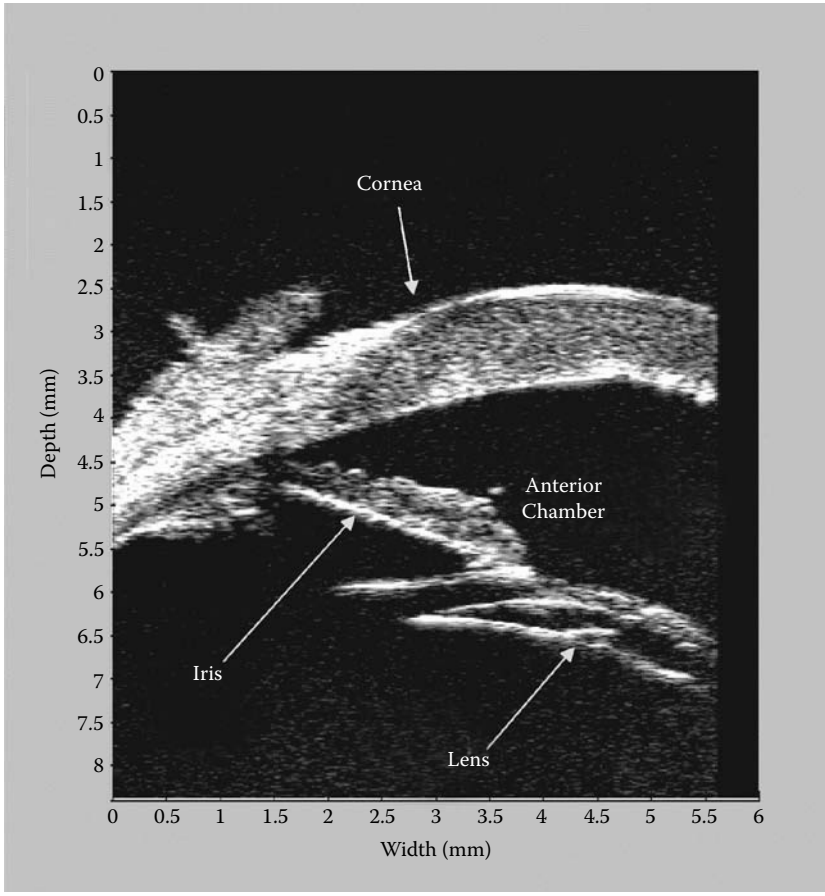

FIGURE 8.9 A UBM image of the anterior segment of the eye obtained *in vitro*.

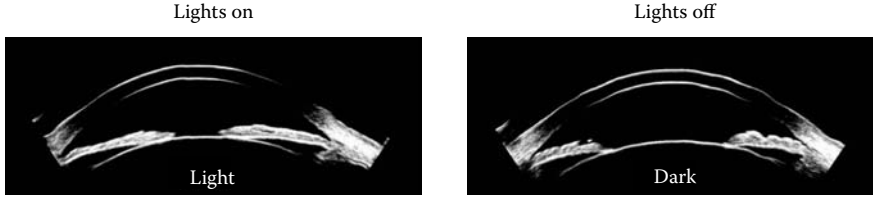

Ultrasound cross-sections of the anterior segment of the eye

FIGURE 8.10 UBM images of the eye before and after turning off the light. (Courtesy of Artemis-2 VHF Arcscan [Ultralink]).

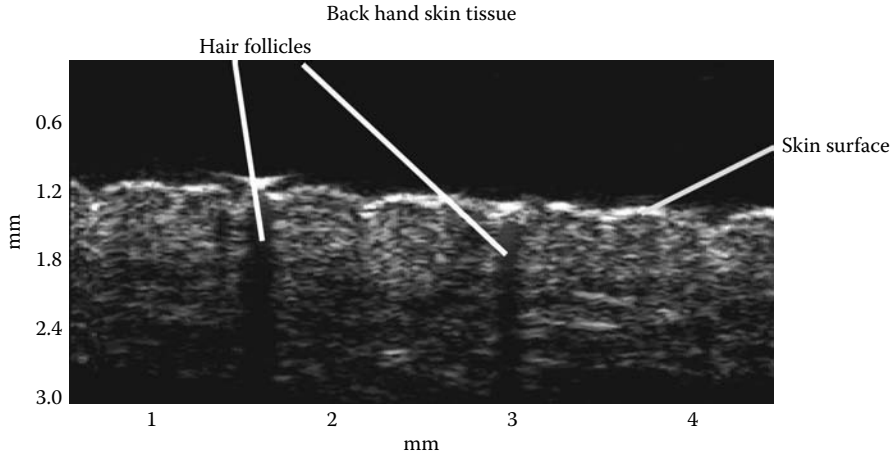

FIGURE 8.11 UBM image of human skin at 50 MHz.

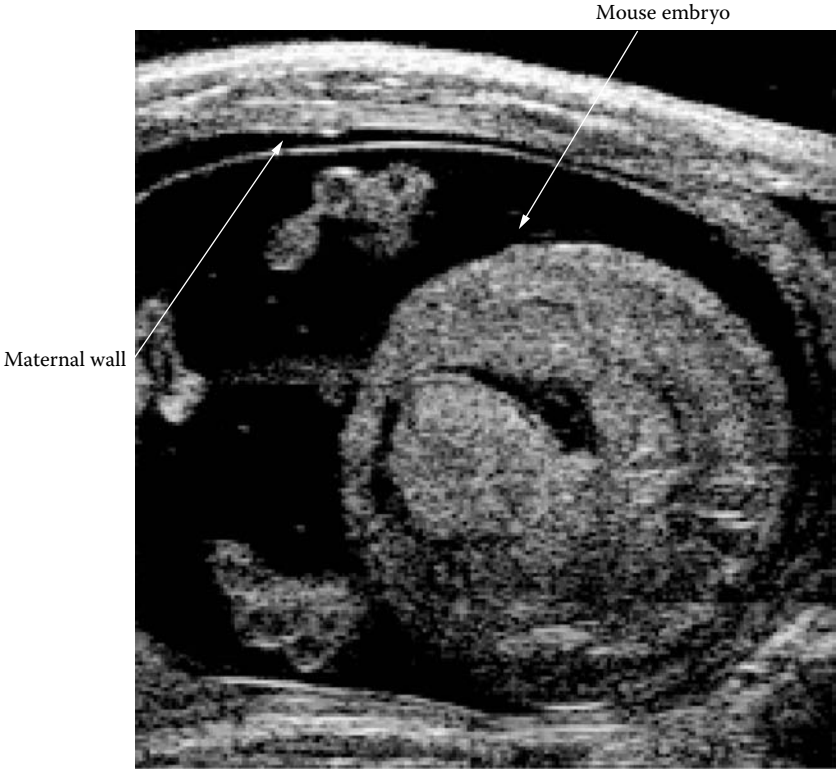

FIGURE 8.12 UBM images of mouse embryo at 40 MHz. (Courtesy of Visualsonics, Toronto, Canada.)

Noninvasive imaging of small animals like mice and rats has recently generated a great deal of interest because, for gene therapy, mice or rats are the preferred animal models. Due to the animals' small size, clinical imaging devices are not capable of yielding sufficient resolution. MicroMR (magnetic resonance), microCT, and microPET (positron emission tomography) designed specifically for small-animal imaging have been developed and are commercially available. UBM has also been used for small-animal imaging. Figure 8.12 shows an example.

8.4 ACOUSTIC MICROSCOPES

At frequencies higher than 100 MHz, UBM-like devices have been developed for imaging cells and material structures. These devices are called scanning acoustic microscopes (SAMs). The construction is similar to that of a UBM except that the transducer design is somewhat different. Typically, a thin layer of zinc oxide is deposited on top of a tightly focused lens made of sapphire in order to minimize the effect of attenuation. At a few gigahertz, SAM has a resolution comparable to that of a light microscope and the advantage of being able to penetrate light-opaque media; however, it has not gained acceptance in the biomedical community because of its limited capability and cost. It has been used mainly for nondestructive evaluation of materials. A variation of SAM is the laser scanning acoustic microscope (SLAM), in which the perturbation of the acoustic field generated by an ultrasonic transducer by an object is mapped by scanning a laser (Kessler and Yuhas, 1979).

REFERENCES

Bouma, B.E. and Tearney, G.J. *Handbook of Optical Coherent Tomography*. New York: Marcel Dekker, 2002.

Briggs, A. and Arnold, W. *Advances in Acosutic Microscopy*. Vol 2. New York: Plenum Press, 1994.

Kessler, L.W. and Yuhas, D.E. Acoustic microscopy. *IEEE Proc.* 1979, 67:526–535.

Liu, J.B. and Goldberg, B.B. 2-D and 3-D endoluminal ultrasound: vascular and nonvascular applications. *Ultras. Med. Biol*. 1999, 25:159–174.

Pandian, P.G. Intravascular and intracardiac imaging: an old concept, now on the road to reality. *Circulation* 1989, 88:1091–1094.

Pavlin, C.J. and Foster, F.S. *Ultrasound Biomicroscopy of the Eye*. New York: Springer-Verlag, 1995.

Ritter, T.A., Shrout, T.R., Tutwiler, R., and Shung, K.K. A 30-MHz piezo-composite ultrasound array for medical imaging applications. *IEEE Trans. Ultras. Ferroelec. Freq. Cont*. 2002, 49:217–230.

Shung, K.K., Smith, M.B., and Tsui, B. *Principles of Medical Imaging*. San Diego: Academic Press, 1992.

9 Multidimensional Imaging

A majority of conventional ultrasonic imaging systems are equipped with a variety of probes, including linear arrays of different frequencies, phased arrays, and Doppler transducers, for performing many imaging functions. Despite numerous improvements that have been made in sharpening the image and eliminating artifacts, problems associated with a lack of focusing on the elevation plane or control of slice thickness remain.

One glaring example is the degradation of image contrast outside elevation focus. Two-dimensional array is the ultimate solution to alleviate this problem (Light et al., 1998; Smith et al., 2002). Unfortunately, for a 128 element × 128 element two-dimensional array, the electronic channel and cable count would be enormously large, expansive, and very difficult if not impossible to manage. As an intermediate step, multidimensional arrays such as 1.25-D, 1.5-D, and 1.75-D arrays have been developed to partially solve the slice thickness problem. One central issue encountered in all multiple dimensional arrays is that more time is needed for data acquisition and signal processing. Current scanners almost exclusively take the approach in which a pulse is transmitted only after all the echoes within the field of view have been received. To gain additional time without sacrificing image quality, the capability of parallel processing is essential.

9.1 PARALLEL PROCESSING

Parallel processing may be achieved by transmitting multiple pulses at the same time. This strategy, however, would make the scanners more expansive and electronics more complicated. Figure 9.1 shows a more reasonable solution, proposed by Shattuck et al. (1984), which uses a linear array. A broader beam than that normally used in a linear array is transmitted and the returned echoes are detected in 4 to 16 directions simultaneously; this is achieved by appropriately adjusting the time delays.

In the initial approach (Shattuck et al., 1984), analog delays were employed. For reception at an angle of $\theta + \Delta\theta_i$, where θ is the angle of the transmitted broad beam and $\Delta\theta_i$ is the angle between θ and the ith received beam ($i = 1 \ldots M$), depending on the design, $M = 4$ to 16, additional delay Δt_i can be applied to the original delay at a steering angle θ

$$\Delta t_i = \Delta t_0(\theta, R_f) + \frac{ng}{c}\sin(\Delta\theta_i) \tag{9.1}$$

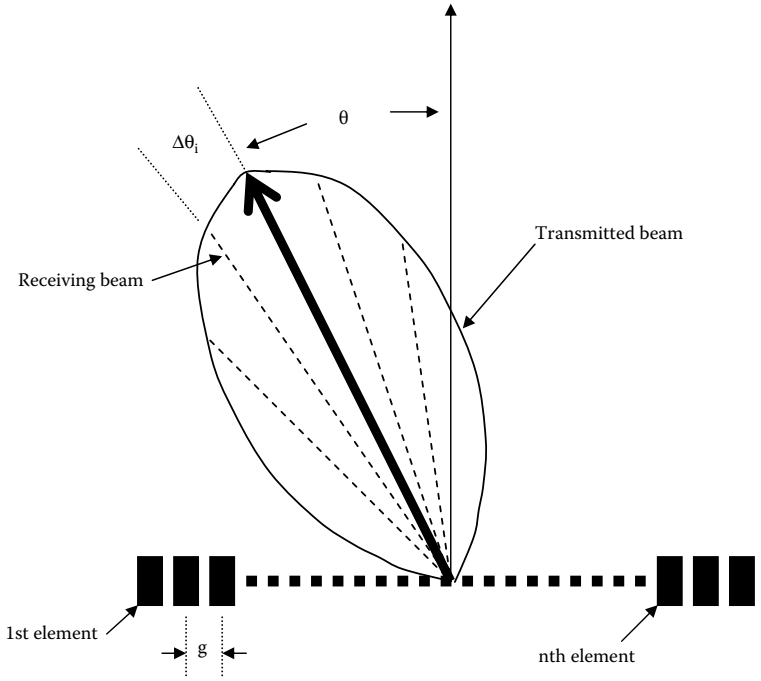

FIGURE 9.1 Parallel processing can be achieved by sending a broader beam and receiving the returned echoes in multiple directions. θ denotes the steering angle. The receiving beams are much narrower than the transmitted beam.

where

R_f is the focal distance of the beam

Δt_0 is the time delay needed to focus the beam at R_f (see Equation 3.33) at an angle θ

n is the number of the element

g is the pitch

c is the sound velocity in the surrounding medium

This expression is valid only if θ and $\Delta\theta_i$ are <26°.

For one transmitted pulse, four lines are received for $M = 4$. This means that the time needed to form one frame is reduced to one-fourth, representing an increase of frame rate by four times. The price to pay for achieving this is a slight degradation of lateral resolution (in that the transmitted beam is broader) and the more complicated electronics.

9.2 MULTIDIMENSIONAL ARRAYS

Multidimensional arrays have been classified into four categories: 1.25-D, 1.5-D, 1.75-D, and two-dimensional arrays (Wildes et al., 1997). These categories are illustrated in Figure 9.2, which shows only the side views of these arrays. A front view of a five-row

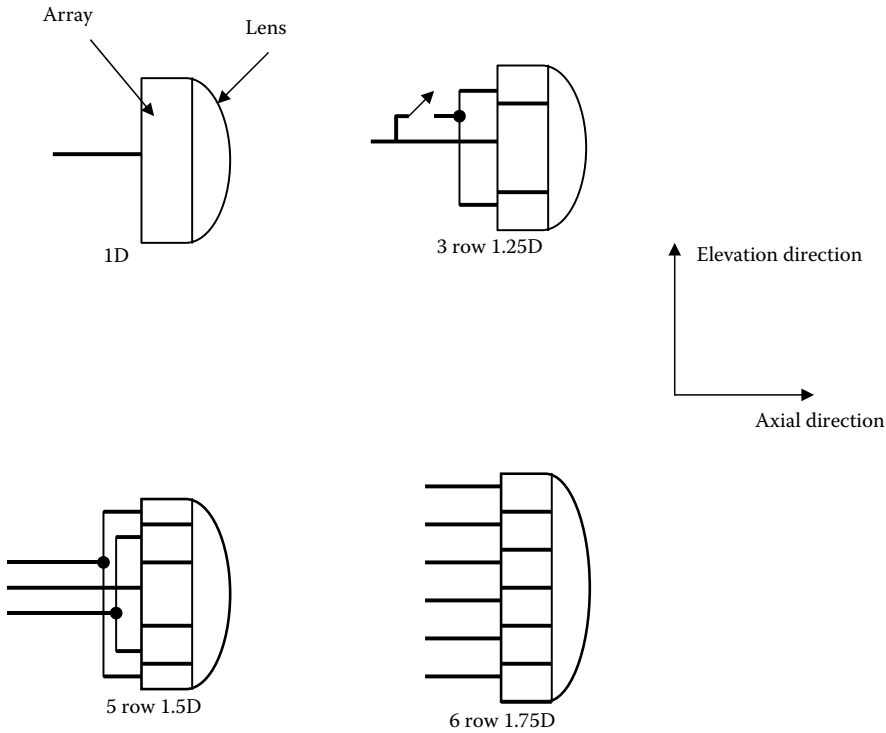

FIGURE 9.2 Side views of multiple dimensional arrays.

1.5-D array can be found in Figure 3.33. For a one-dimensional array, the elevation aperture and focal distance are fixed. For a 1.25-D array, the aperture size is variable, but the focus is fixed. For near-field imaging, the switch is open and only the center row is used. For a 1.5-D array, dynamic focusing is achieved by adjusting the delays of returned echoes and/or transmitted pulses similarly to what can be done on the azimuth plane. Aperture apodization may also be implemented. A 1.75-D array is similar to a 1.5-D array with the exception that there is no symmetry constraint. As in annular arrays, the areas of all rows are typically made equal to ensure equal sensitivity and input electrical impedance. Only a full two-dimensional array can allow dynamic focusing and beam steering in azimuth and elevation directions.

The major advantage that can be gained by going to multidimensional arrays is the better control of slice thickness and an improvement in contrast. The drawbacks are (1) significant grating lobes present in the elevation direction if there are too few rows of elements; (2) an increase in the footprint; and (3) increased complexity in electronics.

A number of scanner manufacturers have developed 1.5-D arrays. More than 1048 electronic channels are used for image acquisition. Significant improvement in image quality has been demonstrated.

9.2.1 Two-Dimensional Arrays

To achieve three-dimensional imaging in real time, a two-dimensional array must be used. A 128 element × 128 element, two-dimensional array would allow the performance achieved by a 128-element, one-dimensional array in the azimuth direction to be extended to the elevation direction. Three-dimensional imaging by a two-dimensional array may be accomplished in two ways: pyramidal scan and rectilinear scan, as illustrated in Figure 9.3 (Smith et al., 2002, Yen and Smith, 2002). In the former, the full two-dimensional aperture is used for beam steering and

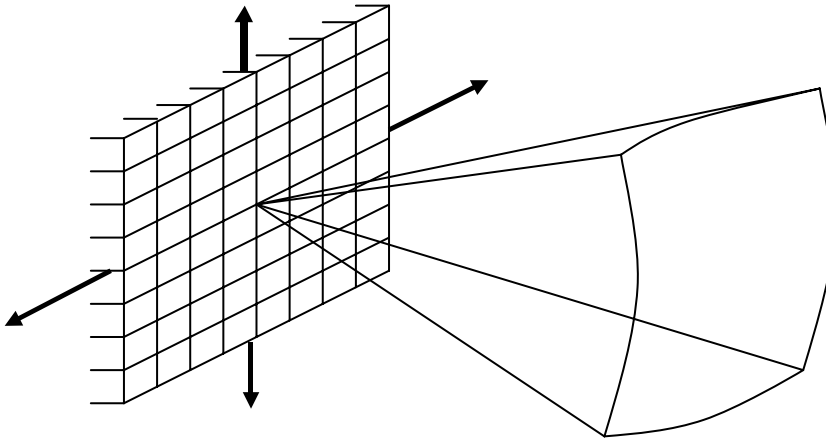

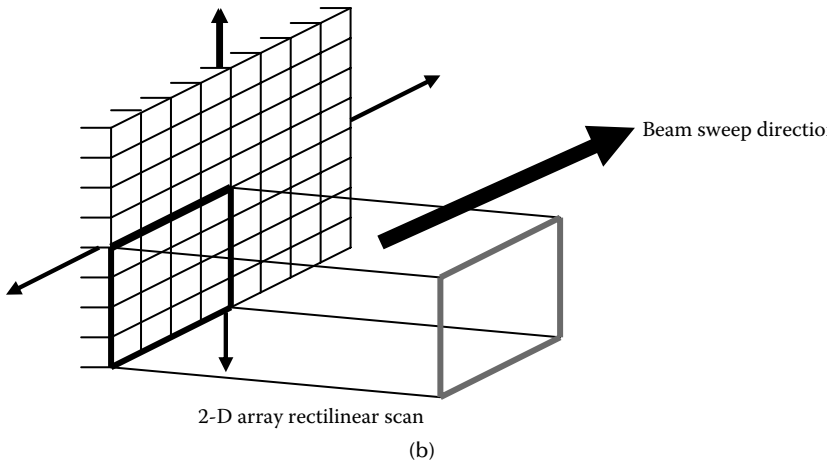

FIGURE 9.3 (a) Pyramidal scan by a two-dimensional array. (b) Rectilinear scan by a two-dimensional array.

focusing in the azimuth and elevation directions. In the latter, only a limited aperture is used and the beam is moved linearly in a raster format to acquire the full image in three dimensions.

Rectilinear scan offers the advantage of reduced complexity and thus cost, but suffers from an inferior resolution due to the smaller aperture size. Fabrication of 128 × 128 two dimensions is not an unsolvable problem and can be done. The difficulty lies in the electrical impedance mismatch due to the small element size, the enormous amount of electronic channels if all elements are connected, and interconnection. Electrical impedance mismatch may be overcome by using piezoelectric materials of high dielectric constant or multilayer piezoelectric materials that are acoustically in series but electrically in parallel (Goldberg and Smith, 1994).

Multilayer piezoelectric materials result in a reduction of $1/N^2$ in output electrical impedance of the array element, where N is the number of layers, recalling that the electrical behavior of a piezoelectric transducer is much like a capacitor near resonance. Multilayer flex circuits could be used to overcome the interconnection problem but the cable size would still be unmanageable. A multilayer flex configuration for a 6 × 39 mm 1.5-D array is shown in Figure 9.4, in which Figure 9.4(a) is a photo of the array assembly and Figure 9.4(b) is an enlarged view of a section. The number of channel counts conceivably may be reduced by multiplexing or by adopting a sparse array approach (Smith et al., 2002; Lockwood et al., 1996).

A full two-dimensional array reported to consist of 60 × 60 elements is now commercially available for three-dimensional, real-time volumetric imaging. In this device, multiplexing and fast electronics are presumably used to reduce the channel

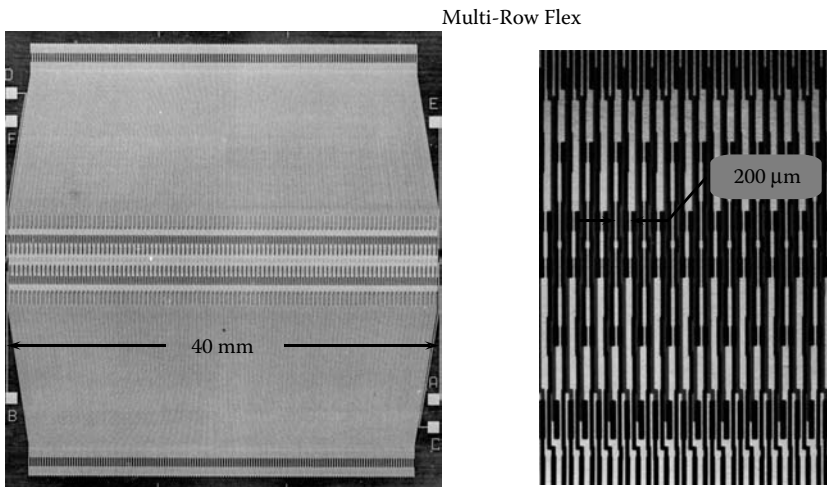

FIGURE 9.4 (**See color figure following page 80.**) (a) A photo of a 1.5-dimensional array with multilayer flex. (b) Enlarged view of a section of the flex. The line width and via hole diameter are 25 and 50 µm, respectively. (Courtesy of D. Wildes, GE.)

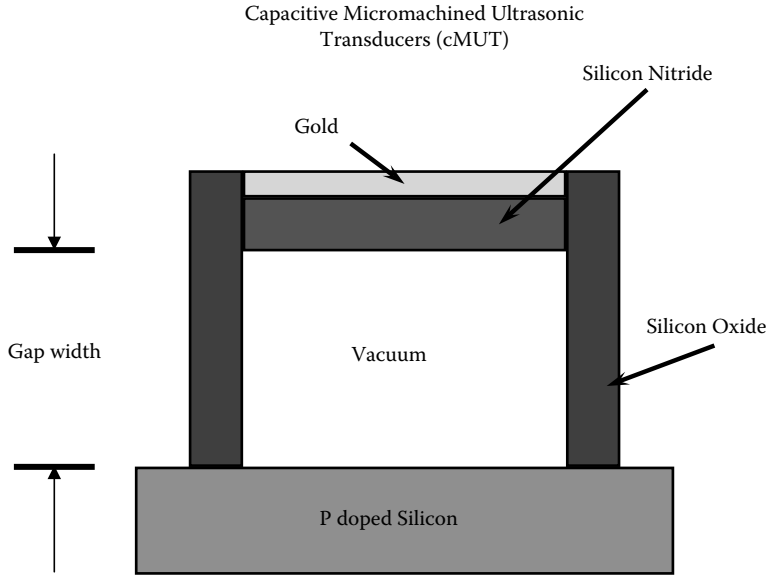

FIGURE 9.5 Construction of one cMUT cell.

count while maintaining a fast frame rate of 30 frames per second. Sparse arrays have been pursued for many years as an alternative to partially circumvent this problem.

A more recent advance in transducer technology, which has a great potential for making the fabrication of two-dimensional array more cost-effective and solving the interconnection problem, is the capacitive micromachined ultrasonic transducer (cMUT) (Ladabaum et al., 1998). This approach differs completely from the traditional transducer design strategy and has the advantage that semiconductor technology, which allows integration of transducers and electronics and miniaturization, is used. Its principle is illustrated in Figure 9.5.

The silicon nitride membrane and the silicon substrate form a capacitor that makes the membrane vibrate upon the application of an AC voltage. The gold layer is an electrode. The sensitivity of the device is inversely proportional to the gap width. The sensitivity increases as the gap width decreases. The thickness of the membrane determines the resonance frequency of the device. At 12 μm, the resonance frequency is approximately 12 MHz. Figure 9.6(a) and Figure 9.6(b) show a photo of several cMUT cells, in which the lighter colored structures are the cell membrane and conductive paths, and an atomic force microscopic image of one cell, respectively.

A 192-element linear array fabricated from this technology is shown in Figure 9.7 and a corresponding image acquired by this array is shown in Figure 9.8 along with an image obtained by a conventional PZT array. An improved axial resolution is clearly seen due to the large bandwidth of cMUT. An additional advantage of cMUT is that it is no longer necessary to match the acoustic impedance between the transducer and the loading medium. However, this technology has a couple of shortcomings: a slight decrease in sensitivity and the need for a bias voltage on the order of 100 V.

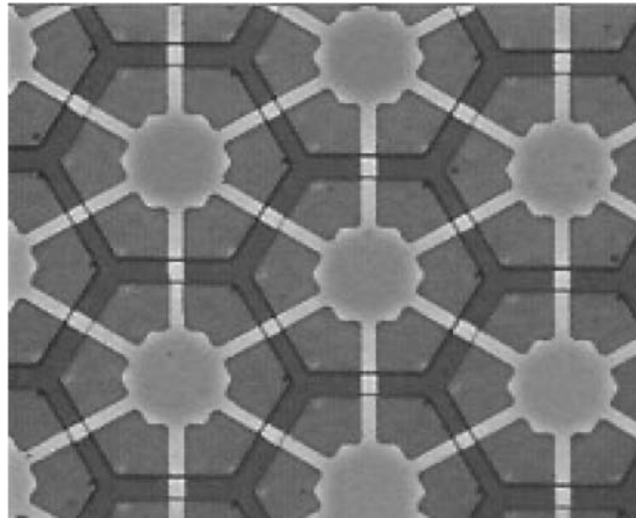

MEMS structures on the surface;
each cell is the width of a human hair

(a)

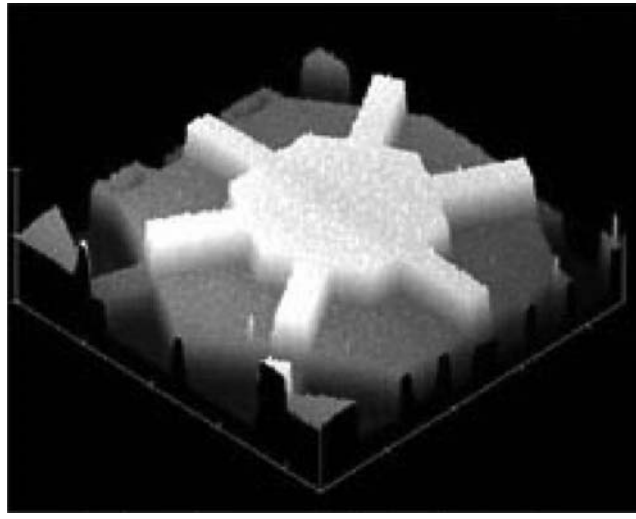

Atomic Force Microscope (AFM) image of one of thousands of cells on the surface of a Silicon Ultrasound transducer

(b)

FIGURE 9.6 (a) Photo showing several cMUT cells. (b) Atomic force microscopic image of one cMUT cell. (Courtesy of Sensant Corp.)

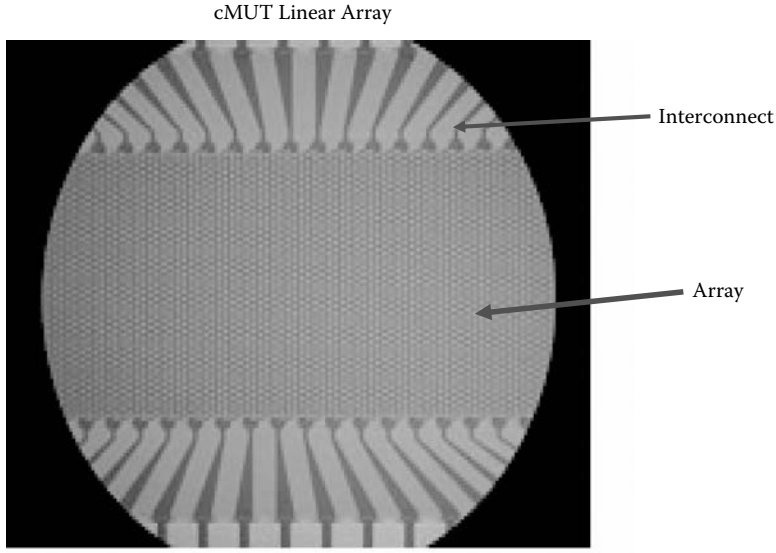

FIGURE 9.7 (See color figure following page 80.) A photo of a cMUT 192-element linear array. (Courtesy of Sensant Corp.)

9.2.2 Sparse Arrays

To reduce the number of elements and channel count, sparse arrays may be used. Piezoelectric elements are randomly placed on a predetermined aperture, as shown in Figure 9.9, where all the elements may be used to transmit and receive or some of the elements used for transmission and some for reception. The advantage of a sparse array is countered by the decrease in sensitivity due to the reduction in aperture size and an increase in the side lobe pedestal or the noise floor outside of the main lobe. This has been shown to be proportional to 1/(number of elements) (Lockwood et al., 1996).

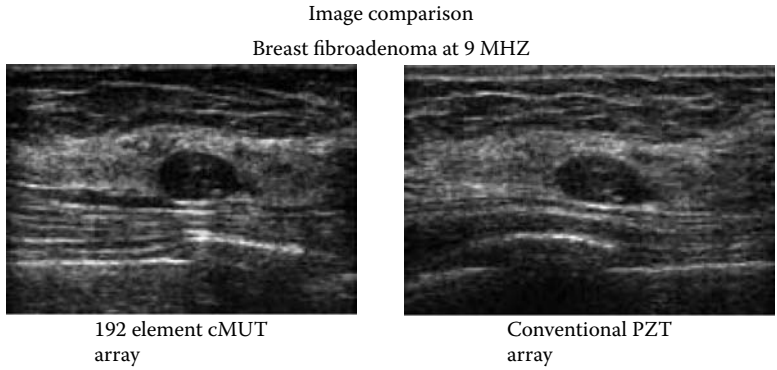

FIGURE 9.8 Images of a breast cancer acquired by the cMUT array (left) and a conventional PZT array (right). (Courtesy of Sensant Corp.)

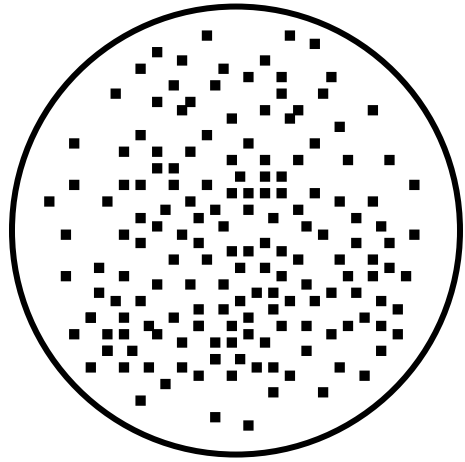

FIGURE 9.9 A random sparse array in which the solid squares represent piezoelectric elements.

To overcome this problem, a periodic sparse array has been suggested by Lockwood et al. (1996). The grating lobes caused by the large pitch in a sparse periodic array may be alleviated by selecting different pitches for transmit and receive arrays. At a direction of ϕ_x, shown in Figure 9.10 at a distance $r >> L$ where L is the width of the array, the transmitted radiation pattern is given by

$$H_T(u) = \int a_T\left(\frac{x}{\lambda}\right) e^{jk\left(\frac{x}{\lambda}\right)u} d\frac{x}{\lambda} \tag{9.2}$$

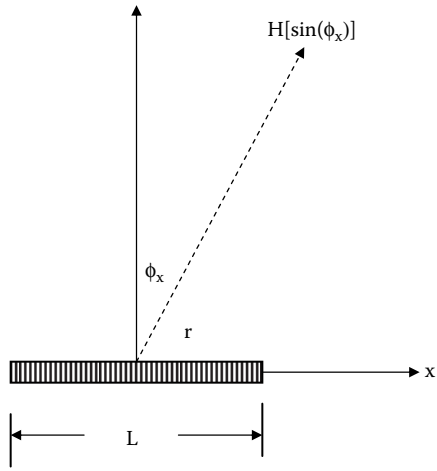

FIGURE 9.10 Radiation geometry for a linear array.

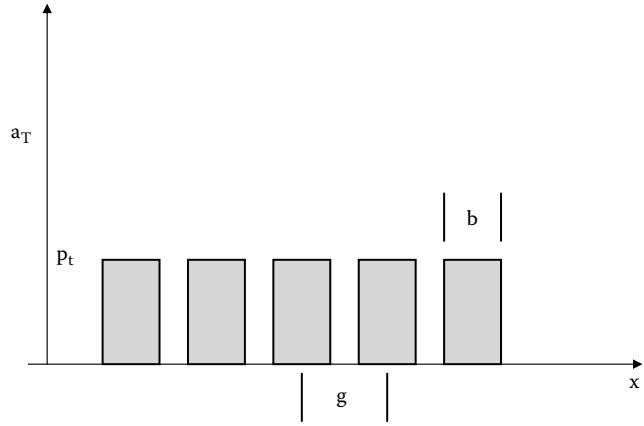

FIGURE 9.11 Transmit aperture function for a linear array of pitch, *g*, and element width, *b*.

where

$\mu = \sin \phi_x$
λ is the wavelength
k is the wave number
a_T is the transmit aperture function

This expression basically states that the radiation pattern of an aperture is the Fourier transform of the aperture function (Steinberg, 1976). For a linear array, the aperture function can be represented by Figure 9.11, where *b* is the element width. If the acoustic independent variable chosen is pressure, $a_t(x/\lambda)$ would be a series of pulses with a pressure amplitude p_t. Here, the distance, *x*, is normalized with respect to λ. If the receive radiation pattern is given by

$$H_R(u) = \int a_R\left(\frac{x}{\lambda}\right) e^{jk\left(\frac{x}{\lambda}\right)u} d\frac{x}{\lambda} \tag{9.3}$$

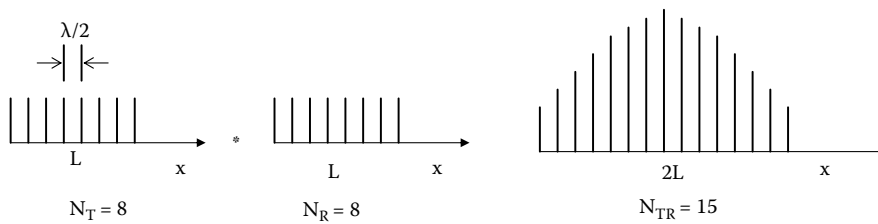

FIGURE 9.12 Desirable effective aperture function can be achieved by convoluting a transmit aperture function with a receive aperture function.

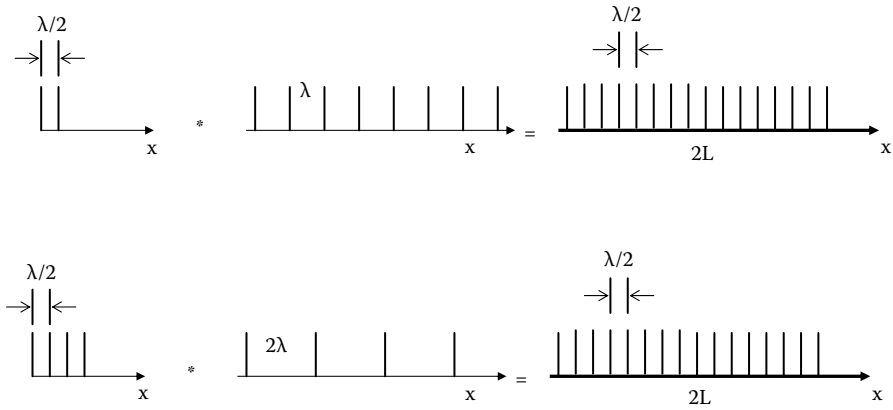

FIGURE 9.13 Two approaches that may be used to obtain a desired effective aperture function.

where a_R is the receive aperture function. The two way pulse–echo radiation pattern would be

$$H_{TR}(u) = H_T(u)H_R(u) = FT[a_T]FT[a_T] = FT[a_T * a_R] \tag{9.4}$$

where * denotes convolution and $E(x/\lambda) = a_T(x/\lambda) * a_R(x/\lambda)$ is frequently called the effective aperture function or co-array function (Steinberg, 1976).

In the far field of the array, i.e., $r >> L$, the rectangular pulses may be represented by impulses, as shown in Figure 9.12. Assuming that N_T and N_R elements are in the transmit and receive apertures, respectively, following the convolution, the number of elements in the effective aperture should be $N_{TR} = N_T + N_R - 1$ with a width of $2L$ and a pitch of one-half λ.

The effective aperture can be reconstructed from the transmit and receive aperture functions in a variety of ways. Figure 9.13 illustrates two of them (Lockwood et al., 1996). This approach is only valid for the far field of a nonfocused array and at the focus of a phased array. In addition, a combination of apodization and addition of extra elements is necessary to make it work successfully.

9.3 THREE-DIMENSIONAL IMAGING

Three-dimensional ultrasound (3DUS) is an important new area of development. It exploits the tomographical capability of ultrasound by acquiring multiple slices of the images. Three-dimensional reconstruction can be accomplished offline or in real time using two-dimensional arrays and parallel processing (Nelson, 2000). If a scanner is capable of displaying the volumetric images in real time, it is often called a four-dimensional scanner.

Offline, three-dimensional imaging is achieved by free-hand scanning with electromagnetic position sensing or by mounting the probe on a mechanical translator whose

FIGURE 9.14 (See color figure following page 80.) Three-dimensional image of a fetus in uterus obtained offline. (Courtesy of GE Medical Systems.)

position is encoded. The data acquired are displayed following image processing by optimized algorithms on a high-resolution monitor. Currently, three-dimensional ultrasound images are displayed in two ways: a series of multiplanar images orthogonal to one another and rendered images that show the three-dimensional structures. Rotation of the images is provided as an option. A three-dimensional image of a fetus obtained offline and a three-dimensional image of a heart obtained in real time or by a four-dimensional scanner are shown in Figure 9.14 and Figure 9.15, respectively.

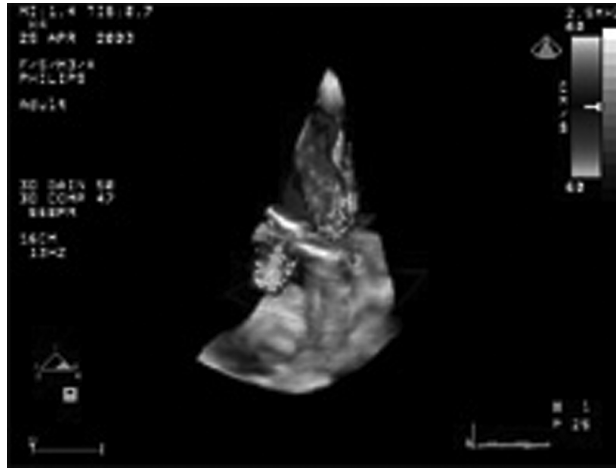

FIGURE 9.15 Three-dimensional image of aortic valve in gray scale and the aortic regurgitant jet in color obtained in real time. (Courtesy of Philips Medical Systems.)

Some examples of clinical applications of three-dimensional ultrasound are visualization of the coronal plane of a fetus, which is not possible with two-dimensional ultrasound; measurement of organ volumes, including the heart; and guidance of interventional procedures, including needle biopsy of prostate. Like several other imaging modalities, the clinical impact of three-dimensional imaging is not yet firmly established and merits further investigation. However, it is clear that, for 3DUS to have a major clinical impact, its performance must match that of two-dimensional ultrasound in terms of image quality and interactivity.

REFERENCES

Goldberg, R.L. and Smith, S.W. Multilayer piezoelectric ceramics for two-dimensional array transducers. *IEEE Trans. Ultrason. Ferroelect. Freq. Contr.* 1994, 41:761–771.

Ladabaum, I., Jin, X., Soh, H.T., Atalar, A., and Khuri–Yakub, B.T. Surface micromachined capacitive ultrasonic transducers. *IEEE Trans. Ultrason. Ferroelec. Freq. Contr.* 1998, 45:678–690.

Light, E.D., Davidson, R.E., Fiering, J.O., Hruschka, P.R., and Smith, S.W. Progress in two-dimensional arrays for real-time volumetric. *Ultrason. Imag*. 1998, 20:1–15.

Lockwood, G.R., Li, P.C., O'Donnell, M., and Foster, F.S. Optimizing the radiation pattern of sparse periodic linear arrays. *IEEE Trans. Ultrason. Ferroelect. Freq. Contr.* 1996, 43:7–14.

Nelson, T.R. Three-dimensional imaging. *Ultras. Med. Biol*. 2000, 26 Suppl. 1:S35–S38.

Shattuck, D.P., Weinshenker, M.D., Smith, S.W., and von Ramm, O.T. Explososcan: a parallel processing technique for high speed ultrasonic imaging with linear phased arrays. *J. Acoust. Soc. Am*. 1984, 75:1273–1282.

Smith, S.W., Lee, W., Light, E.D., Yen, J.T., Wolf, P., and Idriss, S. Two-dimensional array for three-dimensional imaging. *IEEE 2002 Ultras. Symp. Proc*. 2002, 1509–1517.

Steinberg, B.D. *Principles of Aperture and Array Systems*. New York: Wiley, 1976.

Wildes, D.G., Chiao, R.Y., Daft, C.M., Rigby, K.W., Smith, L.S., and Thomenius, K.E. Elevation performance of 1.25-D and 1.5-D transducer arrays. *IEEE Trans. Ultrason. Ferroelect. Freq. Contr.* 1997, 44:1027–1035.

Yen, J.T. and Smith, S.W. Real time rectilinear volumetric imaging. *IEEE Trans. Ultrason. Ferroelect. Freq. Contr.* 2002, 49:114–124.

10 Biological Effects of Ultrasound

In earlier years, for the sake of simplicity, ultrasound propagation in biological tissues was assumed to be a linear phenomenon because it was believed that the power imparted by a diagnostic instrument was so low that nonlinear effects could not occur. As the requirement for better sensitivity (signal-to-noise ratio) and image quality grew, the peak and the average intensity used in diagnostic instruments increased. At sufficiently high ultrasonic pressure levels and intensities, it is inevitable that nonlinear effects appear as well as new acoustic phenomena. Among the most important are heating, wave distortion, cavitation, radiation force, and streaming (NCRP, 1983; Hamilton and Blackstock, 1998). Table 10.1 lists typical acoustic output values for ultrasonic diagnostic instruments (AIUM, 1992a; Patton et al., 1994; Zagzebski, 1996).

10.1 ACOUSTIC PHENOMENA AT HIGH-INTENSITY LEVELS

10.1.1 Wave Distortion

As the power level of the acoustic wave is increased, the sinusoidal pressure wave is distorted. This is because when a medium is compressed, the propagation velocity, which is inversely proportional to the compressibility and the density, increases. Thus, in regions of increased pressure, the propagation velocity is greater, causing the pressure peaks to catch up with the pressure troughs. When this occurs, the sinusoidal waveform begins to look like a sawtooth waveform and significant energy is transferred to higher harmonics of the wave, resulting in a higher absorption, as illustrated in Figure 2.20.

10.1.2 Heating

Ultrasound energy is attenuated as it propagates in a medium. In biological tissues, a major portion of the energy is absorbed and converted into heat. At low ultrasound intensity levels, the heat produced is rapidly diffused out, resulting in little change in local temperature. However, as the intensity is increased, temperature rises. Adverse biological effects may occur if the temperature is elevated to higher than 38.5°C (Barnett et al., 1994).

10.1.3 Cavitation

The term cavitation is used to describe the behavior of gas bubbles in ultrasonic fields. Two different types of cavitation may occur: transient or stable.

TABLE 10.1
Typical Acoustic Outputs of Diagnostic Ultrasonic Instruments

Operating Mode	Peak Pressure (MPa)	I_{SPTA} (mW/cm^2)	I_{SPPA} (W/cm^2)	Power (mW)
B-mode	1.68	18.7	174	18
M-mode	1.68	73	174	3.9
Pulsed Doppler	2.48	1140	288	30.7
Color flow	2.59	234	325	80.5

Transient cavitation describes the phenomenon in which microbubbles suddenly grow and collapse in a liquid medium. The physical process can be described as follows: bubbles in a medium are greatly expanded when pressure decreases rapidly. The pressure increases one-half cycle later, causing bubbles to collapse and disappear. For a very large pressure swing, the radius increases markedly, reaching a peak well past the pressure minimum; as the pressure reaches a peak, the bubble collapses. The internal bubble pressure can become very high, up to 80,000 ATM, with a temperature approaching 10,000K. Such high temperature can cause decomposition of water into chemically active acidic components, causing serious biological effects. A phenomenon called sonoluminescence, in which flashes of light with duration of less than a few picoseconds are generated, may accompany the collapsing of the bubbles (Leighton, 1994).

On the other hand, stable cavitation describes a phenomenon in which the bubbles do not collapse as previously described. Under this circumstance, the behavior of such bubbles is quite stable and is known as stable cavitation, which is more likely to occur at lower ultrasound intensities.

Cavitation can be suppressed by degassing the liquid, increasing the viscosity of the surrounding medium, or by increasing the external pressure applied to the system. It takes a finite amount of time for the gas bubble to respond to the pressure change. Therefore, cavitation is a frequency-dependent phenomenon. If the ultrasound frequency is high enough, it should disappear.

10.1.4 Radiation Force and Streaming

As ultrasound propagates in a fluid, transfer of momentum to the medium via absorption causes acoustic streaming in the direction of the sound beam. If a discrete object is present in the ultrasound beam, a radiation force is exerted on the object, as discussed in Chapter 2. As the object moves, streaming of the fluid near the object may occur. If the object is an air bubble, the oscillation of the bubble can also cause streaming of the fluid. Because acoustic streaming is related to absorption, nonlinear interaction between ultrasound and a medium may increase the acoustic streaming many fold. Acoustic streaming may induce shear stress on interfaces that border the fluid and the object.

10.2 ULTRASOUND BIOEFFECTS

Ultrasound bioeffects have been classified into thermal effects or nonthermal effects such as those caused by cavitation. However, in reality, these effects are usually difficult to separate on animal preparations. A large body of data has been accumulated over the years from water tank studies and animal studies in an effort to establish whether diagnostic ultrasound produces any biological effects.

10.2.1 Thermal Effects

Results that delineate the relationship between temperature elevation and exposure duration needed to cause cell death are similar to those found for hyperthermia-induced fetal abnormalities. They can be generalized to the following equation (Barnett et al., 1994):

$$t_{43} = tR_a^{43-T} \tag{10.1}$$

where

t_{43} is the exposure duration needed to produce bioeffects at 43°C
T is temperature
t is duration of exposure at T
R_a is 0.25 for $T < 43$°C and 0.5 for $T > 43$°C

A review of the literature shows that no lethal effects have been observed for T below 41°C. It can be assumed that exposures that elevate temperature up to 1.5°C will not cause defects in embryonic development.

10.2.2 Thermal Index

A parameter that takes into consideration the attenuation of the tissues, beam profile, and tissue thermal properties was jointly proposed by the American Institute of Ultrasound in Medicine and National Electrical Manufacturers Association to indicate the thermal effect of ultrasound more effectively so that the practitioners can use the ALARA (as low a power level as is reasonably achievable) principle in patient scanning. The manufacturers voluntarily display this index on the scanner (AIUM/NEMA, 1992). For ultrasound propagating in soft tissues during scanning, the thermal index (TI) is given by

$$TI = \frac{W_0}{W_{\text{deg}}} \tag{10.2}$$

where W_0 and W_{deg} are, respectively, the average emitted power of the source in water defined by the beam profile and the estimated power needed to raise the target tissue by 1°C based on tissue thermal models. To take tissue attenuation into account, W_0 in Equation (10.2) should be replaced by the derated power $W_{0.3}(z)$ at a distance

z from the source, assuming a constant attenuation coefficient for all soft tissues of 0.3 dB/cm-MHz, which is 0.035 np/cm-MHz. Therefore,

$$W_{0.3}(z) = W_0 \cdot 10^{-0.03 f_c z} \tag{10.3}$$

where f_c is the ultrasound center frequency.

Equation (10.2) may be used to calculate TI for a scanning transducer with a relatively small aperture size in soft tissues because the power would be the highest at the face of the transducer where $z = 0$:

$$TI = \frac{W_0}{(210/f_c)} \tag{10.4}$$

where W_0 is in milliwatts and f_c in megahertz. For a $W_0 = 100$ mW at 3 MHz, TI = 1.4.

TI for nonscan mode and Doppler mode may be different from that of the scan mode because of differences in transducer aperture and the thermal model. TI for ultrasound propagating in a medium containing bones is also different from that given by Equation (10.3) (AIUM/NEMA, 1992). AIUM/NEMA recommend that, if a device cannot output a power level with a thermal index exceeding 1, it is not necessary to display the TI. However, if it can exceed a TI of 1, the TI should be displayed when it exceeds 0.4 in 0.2 increments.

10.3 MECHANICAL EFFECTS AND INDEX

Cavitation and other nonthermal effects induced by ultrasound have been shown to cause cell lysis, change in cell permeability, and lung damage. Cavitation threshold is found to be related to the rarefactional peak pressure of an acoustic pulse that is the peak of the negative going pressure (see, for instance, Figure 3.12), frequency, pulsing conditions, and properties of the propagating medium including viscosity, gas content, surface tension, and temperature (AIUM/NEMA, 1992). Taking these parameters into consideration, the mechanical index (MI) is defined as

$$MI = \frac{p_{r0.3}(z_{sp})}{\sqrt{f_c}} \tag{10.5}$$

where

$p_{r0.3}$ is the derated peak rarefactional pressure in megapascals by 0.3 dB/cmz-MHz
Z_{sp} is the axial distance where the derated pulse intensity integral $(\text{PII}_{0.3}) = \int I_{0.3}(z)\, dz$ is maximal

PII is illustrated in Figure 10.1. Therefore, I_{SPPA} = PII/pulse duration. The maximal allowable MI is 1.9, which is equivalent to a $I_{\text{SPPA0.3}}$ of 190 W/cm^2.

Although MI has been adopted as a voluntary standard for assessing the mechanical bioeffects of ultrasound, it has several drawbacks. It does not consider (1) the

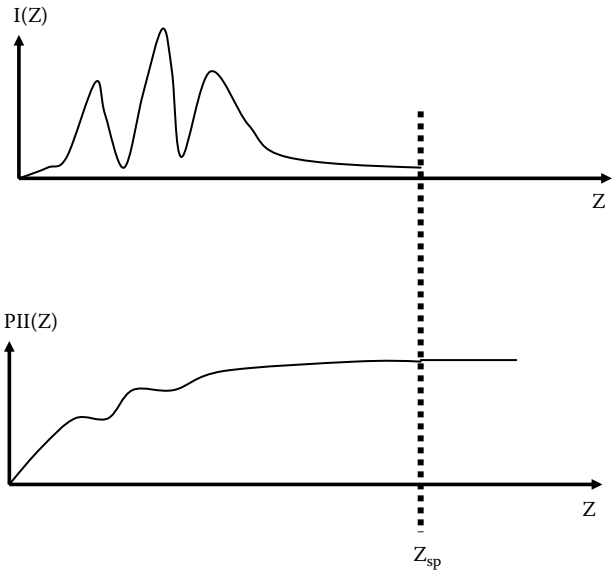

FIGURE 10.1 Definition of PII. The upper panel shows the pulse intensity as a function z. The bottom panel shows the spatial variation of PII.

dwell time, i.e., time involved in patient examination; (2) patient temperature; and (3) the effect of stable cavitation and other nonthermal mechanical effects. Furthermore, MI was developed based on *in vitro* experiments using gas containing polystyrene spheres.

The data collected on bioeffects of ultrasound are frequently inconsistent and controversial. However, at the moment, it is safe to conclude from extensive epidemiological studies and the body of data available in the literature (AIUM, 1992b) that, in the low-megahertz frequency range, no adverse bioeffects have been observed on nonhuman biological tissues exposed *in vivo* under experimental ultrasound conditions if:

- When a thermal mechanism is involved, these conditions are for unfocused beam, I_{SPTA}, below 100 mW/cm^2 and for focused beam, I_{SPTA}, below 1W/cm^2, or thermal index below 2. Furthermore, adverse bioeffects have not been observed for higher values of TI when it is less than

$$6 - \frac{\log_{10} t}{0.6}$$

  where t is the exposure time in minutes.
- When a nonthermal mechanism is involved, these conditions are *in situ* peak rarefactional pressure below approximately 0.3 MPa or MI < approximately 0.3 in tissues that contain well-defined gas bodies. Furthermore, no such adverse effects have been reported for other tissues.

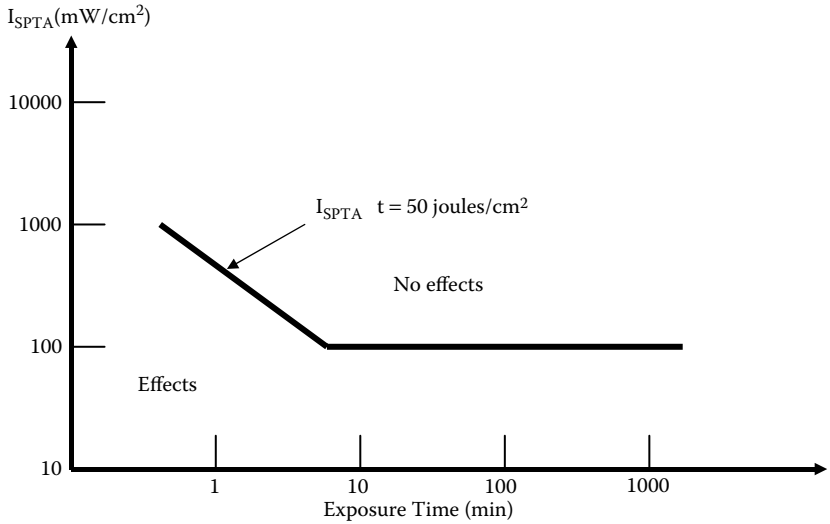

FIGURE 10.2 Summary of the present knowledge of bioeffects of ultrasound.

In summary, the current consensus on possible bioeffects of ultrasound can be best illustrated by Figure 10.2, which shows that, (1) for long exposure time, as long as I_{SPTA} is below 100 mW/cm^2, no adverse bioeffects have been observed; and, (2) for short exposure time, the allowable intensity may be higher. As long as the energy imparted to the tissues is smaller than 50 J/cm^2, no adverse bioeffects have been observed.

The output levels and bioeffect indices of a number of diagnostic ultrasound instruments have been reported by Patton et al. (1994). As a final note, bioeffects produced by ultrasound can also be used to its advantage for therapy — for example, hyperthermia, high-intensity focused surgery (HIFO), drug delivery, and gene transfection (ter Haar, 2000; Miller, 2000).

REFERENCES

AIUM. Acoustical output levels from diagnostic ultrasound equipment. Laurel, MD: American Institute of Ultrasound in Medicine, 1992a.

AIUM. Bioeffects and safety of diagnostic ultrasound. Laurel, MD: American Institute of Ultrasound in Medicine, 1992b.

AIUM/NEMA. Standard for real-time display of thermal and mechanical acoustic outputs indices on diagnostic ultrasound equipment. Laurel, MD: American Institute of Ultrasound in Medicine, 1992.

Barnett, S.B., ter Haar, G.R., Zinskin, M.C., Nyborg, W.L., Maeda, K., and Bang, J. Current status of research on biophysical effects of ultrasound. *Ultrason. Med. Biol*. 1994, 20:205–218.

Hamilton, M.F. and Blackstock, D.T. *Nonlinear Acoustics*. San Diego: Academic Press, 1998.

Leighton, T.G. *The Acoustic Bubble*. London: Academic Press, 1994.
Miller, M.W. Gene transfection and drug delivery. *Ultrason. Med. Biol*. 2000, 26:S59–63.
NCRP. Biological effects of ultrasound: mechanisms and clinical implications. Bethesda, MD: National Council on Radiation Protection Report #74, 1983.
Patton, C.A., Harris, G.R., and Philips, R.A. Output levels and bioeffect indices from diagnostic ultrasound exposure data reported to FDA. *IEEE Trans. Ultrason. Ferroelect. Freq. Contr.* 1994, 41:353–359.
ter Haar, G. Intervention and therapy. *Ultras. Med. Biol*. 2000, 26:S51–54.
Zagzebski, J.A. *Essentials of Ultrasound Physics*. St. Louis: Mosby, 1996.

11 Methods for Measuring Speed, Attenuation, Absorption, and Scattering

For a better interpretation of ultrasound images and an accurate measurement of the structure of a tissue (e.g., size or volume of a tumor), ultrasonic properties of biological tissues such as velocity, absorption, attenuation, and scattering must be known. A variety of methods can be used *in vitro* to measure these properties. Performing these measurements *in vivo*, however, is a totally different matter. A number of methods have been developed for *in vivo* measurements with little success (Greenleaf, 1986; Shung and Thieme, 1993).

11.1 VELOCITY

11.1.1 *In Vitro* Methods

Ultrasound velocity can be measured with a continuous wave excitation or with a pulsed excitation (Schwan, 1969).

11.1.1.1 Interferometric Method

This method, shown in Figure 11.1, uses continuous wave excitation and has been used to measure the velocity in a liquid sample with negligible attenuation to an accuracy of 0.1%. A standing wave is set up between the reflector and the transducer. The wavelength can be determined by adjusting the position of the reflector. If the frequency is known, sound velocity can be easily calculated from Equation (2.2).

11.1.1.2 Pulse–Echo Method

The same arrangement in Figure 11.1 can also be used for pulsed excitation. A measurement of the time of flight $t = 2x/c$ of the pulse, where x is the distance between the reflector and the transducer, would yield c. The accuracy of this method relies on the sharpness of the pulse and is affected by the attenuation of the sample, which can cause a change in the pulse shape. An improvement in accuracy can be made by substituting the sample with a liquid, such as water, with a velocity that is precisely known. From measurements of two time of flights, t_s and t_r, in the sample

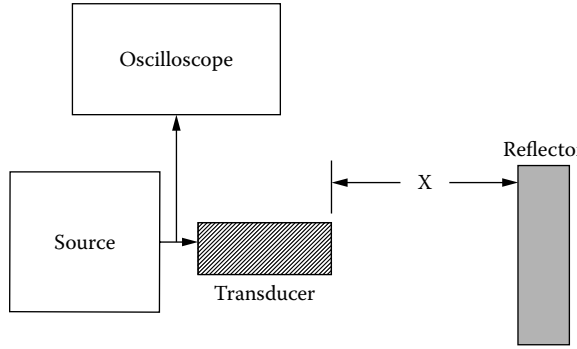

FIGURE 11.1 Experimental block diagram for *in vitro* ultrasound velocity measurements.

and in the reference liquid, and the relationships

$$t_s = \frac{x}{c_s} \tag{11.1}$$

$$t_r = \frac{x}{c_r} \tag{11.2}$$

where c_s and c_r are sound velocity in the sample and in the reference liquid, respectively, c_s can be found from the following equation:

$$\Delta t = t_s - t_r = x\left(\frac{1}{c_s} - \frac{1}{c_r}\right) \tag{11.3}$$

or

$$\frac{t_s}{t_r} = \frac{c_r}{c_s} \tag{11.4}$$

The advantage of using Equation (11.4) is that time-of-flight measurements are much more accurate than distance measurements. Because the distance measurement is eliminated by merely replacing the sample by a liquid of known velocity, this method is called the substitution method.

The pulse–echo approach can also be used to measure sound velocity in tissues. The problem is that it is often difficult to estimate the thickness of the tissue accurately. To maintain parallel interfaces between the transducer and the tissue as well as between the tissue and the reflector, the tissue must be compressed and an undesirable distortion of tissue structure may result. To alleviate this problem, a different approach, in which the need for measuring tissue thickness is eliminated (Kuo et al., 1990), may be used, as illustrated in Figure 11.2. Assume that T_m and T_w are time of flights with and without the sample in the propagation path and t_1 and t_2 are time of flights for the pulse to travel from the transducer to the front and

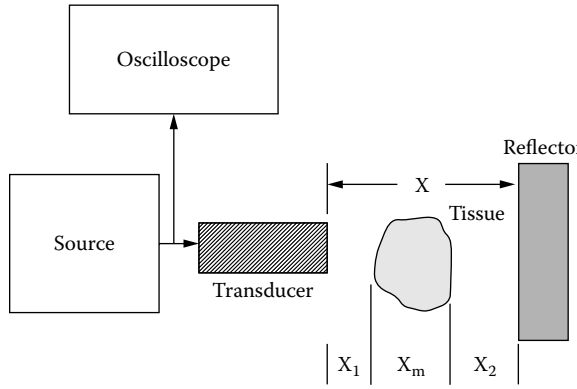

FIGURE 11.2 Experimental block diagram for *in vitro* ultrasound velocity measurements that eliminates the need for tissue thickness measurements by utilizing only time of flights.

rear faces of the sample:

$$x_m = x - x_1 - x_2 = x - \frac{t_1 c_w}{2} - \frac{(T_m - t_2)c_w}{2} \tag{11.5}$$

$$\frac{T_w}{2} = \frac{x_1 + x_m + x_2}{c_w} \tag{11.6}$$

$$\frac{T_m}{2} = \frac{x_1 + x_2}{c_w} + \frac{x_m}{c_m} \tag{11.7}$$

where c_w and c_m are sound velocity in water and in the sample, respectively. Substituting Equation (11.5) into Equation (11.7) and subtracting Equation (11.6) from Equation (11.7), it can be shown that

$$c_m = \left(\frac{T_w - T_m}{t_2 - t_1} + 1 \right) c_w \tag{11.8}$$

This equation shows that the sound velocity in the sample can be determined from a measurement of four times of flight if c_w is known. An alternative to using a reflector to reflect back the transmitted pulse would be to replace the reflector with a hydrophone if the attenuation in the sample is high. In this way, the propagation path is reduced by one-half.

11.1.1.3 Velocity Difference Method

Figure 11.3 shows this extremely accurate (to 0.01%) method for measuring sound velocity in a fluid). A reference liquid and the sample fluid are separated by a thin membrane. If a carriage carrying the transmitting and receiving transducers is moved

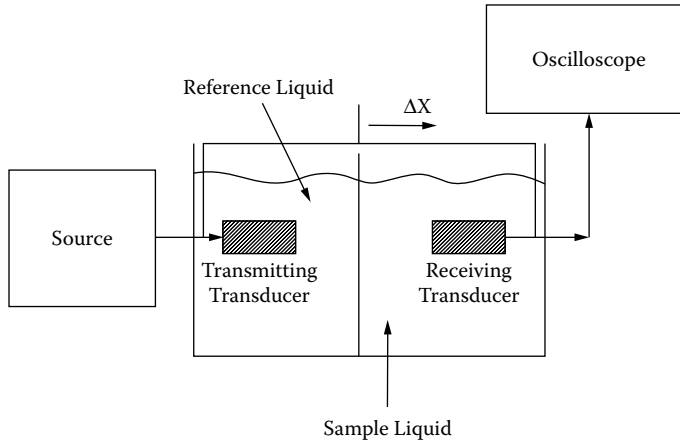

FIGURE 11.3 Experimental block diagram for the fixed-path method for ultrasound velocity measurements.

by a distance Δx, it can be easily shown that the time of flight detected by the receiving transducer, Δt, is given by

$$\Delta t = \frac{\Delta x}{c_m} - \frac{\Delta x}{c_w} \tag{11.9}$$

All parameters in Equation (11.9) are known except for c_m. Continuous excitation can also be used with this method. Instead of measuring time of flight, the change in the phase angle is determined.

11.1.2 *In Vivo* Methods

Very few of the *in vitro* methods can be applied to *in vivo* conditions. As a result, a number of investigations on possible *in vivo* methodologies have been attempted. One of these, called the image registration method (Chen et al., 1987), is shown in Figure 11.4. If a target tissue such as a blood vessel, designated as D, can be found in the body by B-mode imaging, transducer A emits a pulse and target D will show up in the image as B, where $AB = c_0\,\Delta t$ where c_o is the assumed velocity and Δt is the time of flight. Similarly, for transducer A', $A'B' = c_0\,\Delta t'$. For the triangle $AA'D$, it can be shown that

$$\frac{L}{l} = \frac{AD}{AB} = \frac{AD}{AD - AB} = \frac{AD}{AD\left(1 - \frac{c_0}{c_1}\right)} = \frac{1}{1 - \frac{c_0}{c_1}} = \frac{c_1}{c_1 - c_0} \tag{11.10}$$

where c_1 is the true velocity and $AB = (c_0/c_1)AD$. Equation (11.10) can be rearranged to obtain the following equation

$$c_1 = c_0 \frac{L}{L - l} \tag{11.11}$$

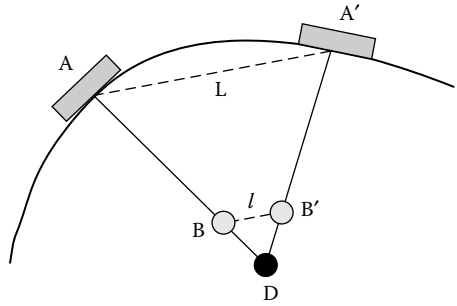

FIGURE 11.4 The image registration method for *in vivo* ultrasound velocity measurements in which a selected target is imaged at two locations.

which indicates that the true velocity can be estimated from the assumed velocity and the distances L and l.

L can be physically measured and l estimated from the image. The true position of the target can be estimated by cross-correlation. Although this method appears to be promising, it has several problems, including the assumption that there is no refraction at tissue boundaries and the ability to find a target tissue. Using this method, Chen et al. (1987) found that *in vivo* sound speed in normal liver was 1.578×10^5 cm/s, whereas it was 1.547×10^5 cm/s in nonfatty cirrhotic liver.

An approach that uses a linear array studied by Kondo et al. (2000) is shown in Figure 11.5. If the distance between two elements, Δy and sin θ_0, is known and the propagation times along paths T_1AR_1, T_1BR_2, and T_2CR_2 represented by t_{11}, t_{12},

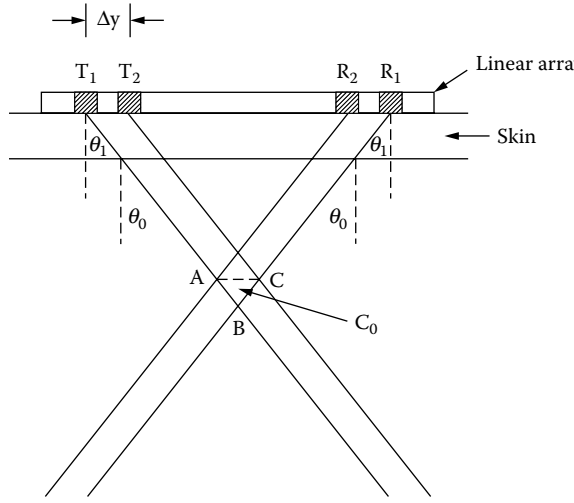

FIGURE 11.5 The cross-beam method for *in vivo* ultrasound velocity measurements in which a selected target is imaged by a linear array.

and t_{21}, respectively, can be measured, c_0, the local sound speed in the volume of tissue defined by *ABC*, is given by

$$c_0 = \frac{\Delta y}{\left(t_{11} - \frac{t_{12} + t_{21}}{2}\right)\sin\theta_0} \tag{11.12}$$

Here it is assumed that $\theta_0 = \theta_1$.

11.2 ATTENUATION

11.2.1 *In Vitro* Methods

Just as with velocity measurements, a variety of methods have been used for measuring attenuation coefficient of biological tissues *in vitro*.

11.2.1.1 Transmission Methods

Narrow-band bursts or broad-band pulses may be used. The former yields better signal-to-noise ratio, but can only be used to obtain the value at one frequency; the latter allows the measurements of the attenuation coefficient over a frequency band, but is susceptible to noise. These methods can be further classified as the fixed-path method and the variable-path method.

As indicated by Equation (2.29), the pressure drops exponentially as the propagation distance increases. If the separation between a transmitting transducer and a receiving transducer is changed, a measurement of the change in the detected pressure should yield the attenuation coefficient if beam diffraction loss can be appropriately compensated. The advantage of the fixed-path method over the variable-path method is that it is not necessary to correct for beam diffraction. The fixed-path method uses the same arrangement shown in Figure 11.3 for measuring ultrasound attenuation in fluids. Assuming that the attenuation coefficients in the reference liquid and the sample liquid are α_0 and α and that p_0 and p_1 are the pressures before and after the carriage movement, it is straightforward to show that

$$\alpha = \alpha_0 + \frac{1}{\Delta x}\ln\left(\frac{p_1}{p_0}\right) \tag{11.13}$$

This approach is not suitable for measurements on biological tissues. A substitution method has been developed to overcome this problem and is still the most reliable and most popular at present. An arrangement similar to that shown in Figure 11.2 is used. Because the detecting device must have a small aperture to minimize the phase cancellation effect or aperture averaging effect (Busse and Miller, 1981), a hydrophone is typically preferred as a receiver in attenuation measurements. This arrangement is depicted in Figure 11.6. Assuming that the scope has the capability of Fourier transform, the signals displayed on the oscilloscope received by the hydrophone without

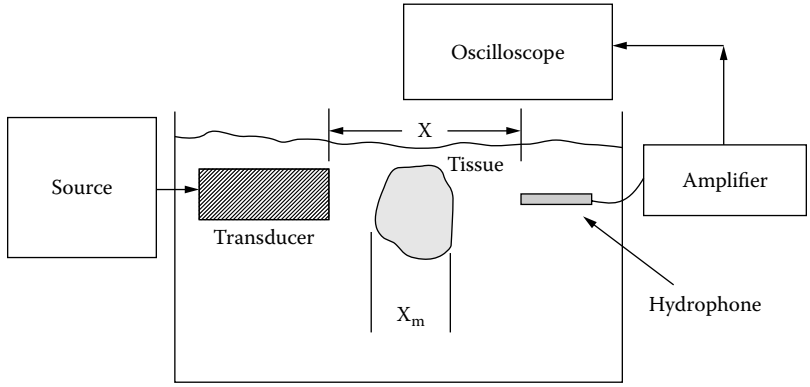

FIGURE 11.6 Experimental block diagram for *in vitro* ultrasound attenuation measurements.

and with a specimen in the path, as a function of frequency, is given by

$$V_a(f) = R_t(f)e^{-\alpha_0 x} \tag{11.14}$$

$$V_b(f) = R_t(f)e^{-\alpha_0 x}e^{-(\alpha-\alpha_0)x_m}T^2 \tag{11.15}$$

where

R_t is the transfer function of the experimental system including the electronic and ultrasonic components

T is the acoustic transmission coefficient at the tissue–water interface

α_0 and α are the attenuation coefficients in the reference liquid and the sample

Dividing Equation (11.14) by Equation (11.15) and taking the log of both sides,

$$\frac{V_a}{V_b} = e^{(\alpha-\alpha_0)x_m}T^2 \tag{11.16}$$

Because the transmission coefficient between a liquid and a soft tissue approaches 1, Equation (11.16) can be simplified to

$$\frac{V_a}{V_b} = e^{(\alpha-\alpha_0)x_m} \tag{11.17}$$

Equation (11.17) shows that the attenuation coefficient of the sample can be determined from a measurement of tissue specimen thickness, x_m, and the ratio of the detected signals if the attenuation coefficient of the reference liquid is known. The advantage of this method is that it is not necessary to know the experimental system transfer function $R_t(f)$. Unlike velocity measurements, the accuracy of thickness measurement is not as

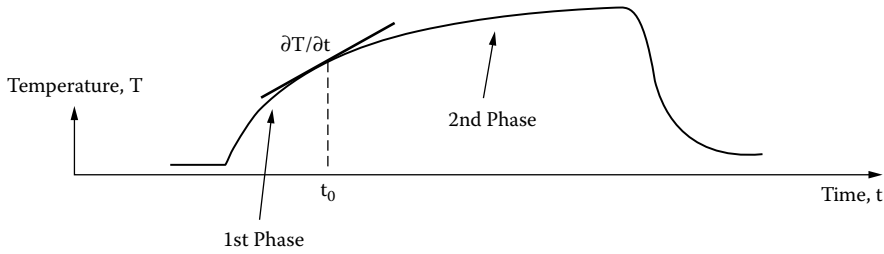

FIGURE 11.7 Temperature increase measured by a thermocouple after exposure to a pulse of ultrasound in a tissue.

critical a factor in attenuation measurements. Specimen thickness, x_m, can be measured manually or with time-of-flight measurements.

11.2.1.2 Transient Thermoelectric Method

As was mentioned in Chapter 2, ultrasonic attenuation in tissues consists of two terms: absorption and scattering. In the medical ultrasound range from 2.5 to 15 MHz, scattering loss is minimal, so the transient thermoelectric method (Schwan, 1969; Parker, 1983) that measures absorption is also useful for measuring attenuation. In this method, a thermocouple is embedded in the volume of tissue of interest exposed by a rectangular acoustic pulse of known intensity. The temperature rise caused by the acoustic pulse measured by the thermocouple is shown in Figure 11.7. If the diameter of the thermocouple wire is sufficiently small, the approximately linear rise in temperature in the second phase is related to the absorption coefficient ~ α by the following equation:

$$\alpha = \frac{C_p J}{2I}\left(\frac{\partial T}{\partial t}\right)_{t_0} \tag{11.18}$$

where C_p, J, and I are the specific heat at constant pressure of the tissue, the mechanical-heat conversion factor = 4.18 J/cal, and acoustic intensity, respectively. $(\frac{\partial T}{\partial t})_{t_0}$ denotes the slope of the temperature rise as a function of time at time = t_0.

The first phase of temperature rise cannot be used because of the heat exchange occurring between the tissue and the wire. For this method to be valid, the wire diameter must be small (<75 μm); the half power beam width greater than 3 mm to minimize the heat loss by conduction to the surrounding regions; and the temperature rise < 1°. These guidelines restrict the application of the technique to high-frequency and tightly focused beams. A pulse decay technique in which the viscous heating artifact is minimized has been developed to overcome these problems (Parker, 1983). In this method, a Gaussian intensity profile is assumed for the ultrasound beam (see Figure 2.8) and the beam is scanned across an embedded thermocouple of 51-μm diameter thermojunction, as shown in Figure 11.8. The

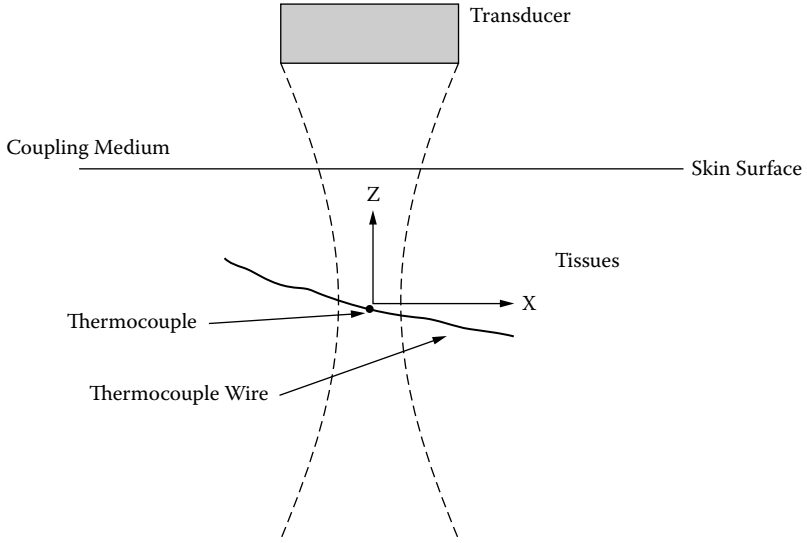

FIGURE 11.8 A transducer is scanned across a thermocouple embedded in a tissue.

intensity profile is assumed to be

$$I(x) = I_m e^{-\frac{x^2}{x_0}} \tag{11.19}$$

where x_0 is a measure of the beam width. After an exposure of duration Δt and assuming no significant heat conduction during the duration, the temperature distribution along x should be

$$T(x) = T_m e^{-\frac{x^2}{x_0}} \tag{11.20}$$

where, from Equation (11.18),

$$T_m = \frac{2\alpha\Delta t}{C_p J} I_m \tag{11.21}$$

The temperature decay at a point x at a function of time following exposure has been found theoretically (Parker, 1983) to be

$$T(x,t) = \frac{T_m}{4k_d t/x_0 + 1} e^{-\frac{x^2}{4k_d t + x_0}} \tag{11.22}$$

At $x = 0$ or on the beam axis,

$$T(0,t) = \frac{T_m}{4k_d t/x_0 + 1} \tag{11.23}$$

where k_d is the thermal diffusitivity of the medium surrounding the heat sensor and equals 1.5×10^{-3} cm^2/s for soft tissues.

Using Equation (11.23), T_m can be estimated from the time history of the temperature decay on the axis given x_0 estimated from Equation (11.19) following a measurement of the beam profile. Here it is assumed that the beam profile measured in a water bath is similar to that in tissues and not affected by attenuation. Then, from Equation (11.21), the absorption coefficient α can be estimated because I_m, Δt, C_p, and J are known. The advantage of this method over the transient thermoelectric method for highly focused beams was clearly demonstrated by Parker (1983).

11.2.2 *In Vivo* Methods

In vitro methods for attenuation measurements are difficult to implement *in vivo*. A few approaches have been studied for *in vivo* estimation of attenuation and can be classified into two categories: loss of amplitude methods and frequency shift methods (Greenleaf, 1986). The central idea for both is to treat the tissue as a uniform distribution of scatterers. If the difference in transducer beam characteristics at different depths in a tissue can be adequately compensated, the difference in echo amplitude from tissues at different depths of the same volume is related to the attenuation coefficient of the tissue and the separation in depth.

11.2.2.1 Loss of Amplitude Method

This method is illustrated in Figure 11.9, in which the amplitude drop as a function of depth of penetration of the ultrasound beam or time of flight of the pulse is shown.

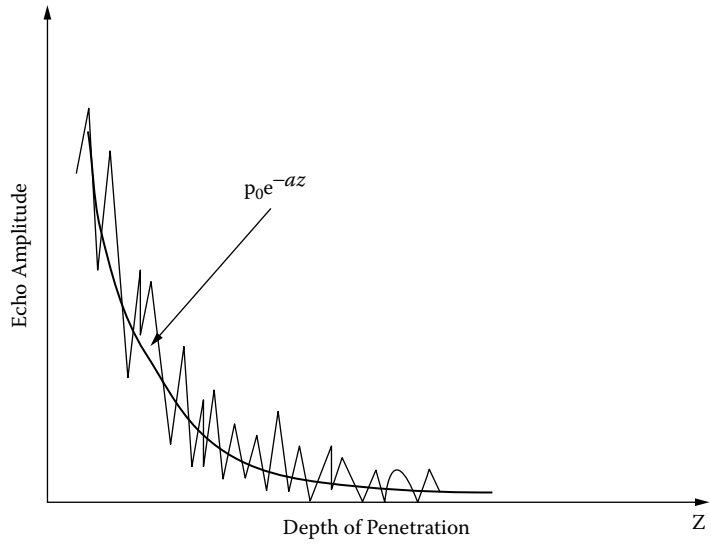

FIGURE 11.9 The echo amplitude scattered from a tissue decreases as a function of depth of penetration. The solid line denotes the fitted curve.

If beam diffraction can be adequately compensated, the drop should be exponential and a curve-fitting algorithm may be used to estimate the attenuation coefficient.

11.2.2.2 Frequency Shift Method

The frequency shift method can be accomplished in the frequency domain by measuring the spectral difference or in the time domain by estimating the zero crossing of the echo waveform (discussed in Chapter 5). This method is illustrated in Figure 11.10. Two regions of an A-line echo waveform, *A* and *B* at different depths, are windowed for Fourier analysis shown in Figure 11.10(a) and (b). Various time window functions, e.g., Hamming, Blackman, and Henning windows, may be used to minimize spectral distortion. The two spectra are then divided to yield the slope of the attenuation curve shown in Figure 11.10(c) if beam diffraction can be adequately compensated.

In logarithmic scale, the difference in the spectra yields the attenuation coefficient as a function of frequency. This process must be repeated many times before any meaningful results can be obtained because biological tissues are far from being homogeneous. The shift in center frequency of the transmitted pulse can also be estimated from determining the zero crossing of the echo waveform. Attenuation coefficients of normal liver and fatty liver with values from 0.45 to 0.5 dB/cm-MHz and from 0.6 to 0.8 dB/cm-MHz, respectively, have been reported from *in vivo* measurements on humans with these methods.

11.3 SCATTERING

The measurement of the scattering properties of tissues is of paramount importance because an ultrasonic image is formed from specularly reflected echoes from tissue boundaries and diffusely scattered echoes from tissue parenchyma.

11.3.1 *In Vitro* Methods

The scattering properties of a medium can only be measured under two extreme cases: scatterer size >> wavelength and scatterer size << wavelength. As was discussed in Chapter 2, for a distribution of scatterers, only if the scatterer concentration, n, is very small, the intensity attenuation coefficient is given by

$$2\alpha = n(\sigma_a + \sigma_s) \tag{11.24}$$

A measurement of the attenuation coefficient would yield σ_s, assuming that $\sigma_s >> \sigma_a$. This condition is satisfied only for large scatterers whose size is >> wavelength. Therefore, only in the case in which the scatter concentration is extremely small and the scatterer size is >> wavelength, can the scattering cross-section be obtained from measuring the attenuation coefficient of the medium. However, several methods have been developed to measure the scattering properties of a medium for a distribution of small scatterers whose size is << wavelength (Shung and

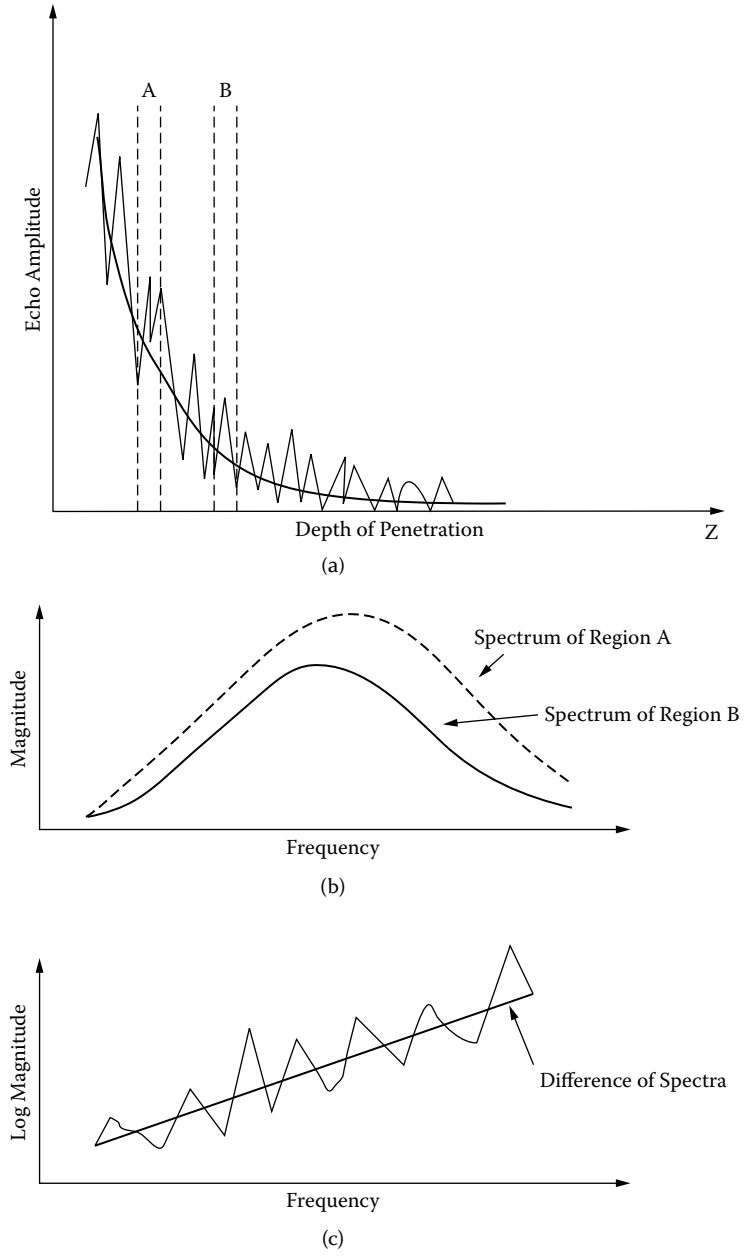

FIGURE 11.10 (a) The scattered echoes from two regions of a tissue, *A* and *B*, can be windowed for spectral or zero crossing analysis. (b) Spectra of echoes from regions *A* and *B*. (c) The difference of the two spectra in log scale can be fitted with a line to estimate the attenuation coefficient.

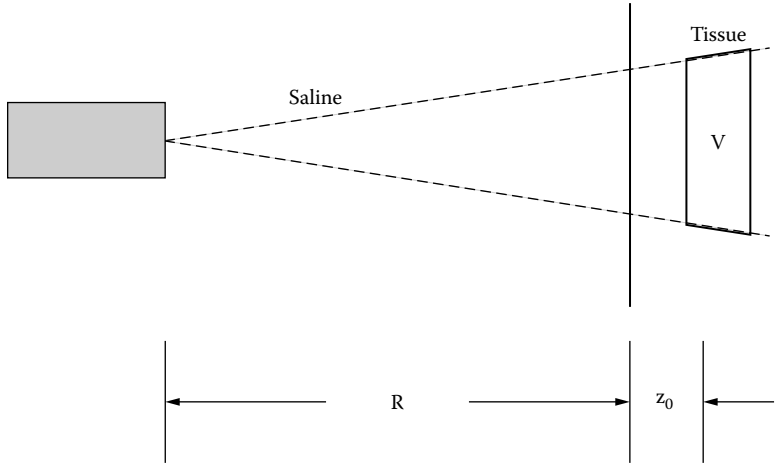

FIGURE 11.11 Experimental block diagram for *in vitro* ultrasound backscattering measurements.

Thieme, 1993). The simplest is the narrow-band substitution method, which was developed by Sigelmann and Reid (1973).

Suppose that a volume of tissue is insonified by an ultrasound beam as illustrated in Figure 11.11. The transducer and the tissue are immersed in saline solution in a water tank. The transducer is located a distance of R from the tissue and saline interface. Saline is preferred over water for a tissue sample to prevent permeation of water into the tissue. Here it is assumed further that R is >> transducer aperture and wavelength so that, at $z > R$, the transducer can be treated as a point source. Under these conditions, the intensity of ultrasound beam at $R + z_0$ is

$$I(z) = \frac{P_0}{(R + z_0)^2} e^{-2\alpha_0 R - 2\alpha z_0} \tag{11.25}$$

where

P_0 denotes the total power emitted by the transducer
$P_0/(R + z_0)^2$ is the spherical spreading of the energy emitted by a point source
α_0 is the attenuation coefficient in saline
α is the attenuation coefficient in the tissue

If the transmitted ultrasound is a series of bursts at a frequency of f with a very narrow bandwidth, the intensity of the scattered wave from a region of tissue can be selected by time gating, which is illustrated in Figure 11.12, for measurement.

$$I_s(0) = \frac{I(z)\eta V}{(R + z_0)^2} e^{-2\alpha_0 R - 2\alpha z_0} \tag{11.26}$$

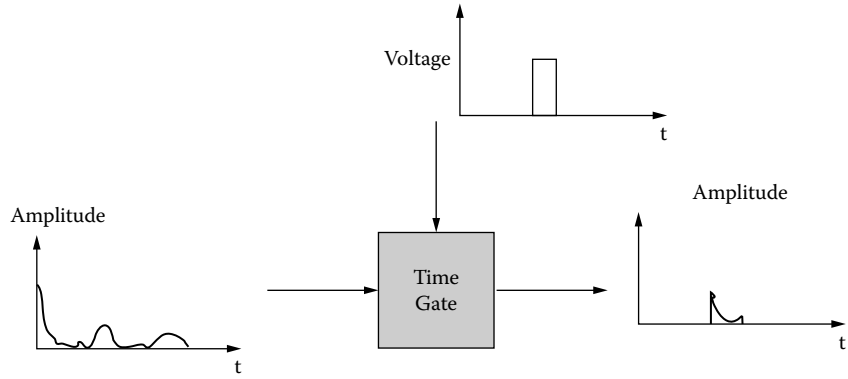

FIGURE 11.12 Time gating allows the selection of a portion of the waveform for signal processing. The gate behaves like a switch that is turned on by a pulse, letting only the waveform pass through within the time window controlled by the pulse duration.

where

V is the scattering volume, bounded by the beam width at $R + z_0$ and duration of the gate, $\tau, = Sc\tau/2$

c is the sound velocity in the tissue

S is the beam cross-section at z_0

η is the backscattering coefficient defined in Chapter 2

It should be noted that $\eta = n\sigma_b$, where σ_b is the backscattering cross-section for very small n.

However, for biological tissues, as was discussed in Chapter 2, σ_b is typically so small that it is impossible to measure. In order to alleviate this problem, the backscattering coefficient, which represents the intensity scattered into one solid angle in the backward direction per unit incident intensity with a unit of 1/cm-sr, is used. For this definition to be valid, the scattering from one unit of volume of scatterers must be so weak that no multiple scattering occurs. Otherwise, Equation (11.26) is not valid. Here it is assumed that individual scattering volumes are independent so as to allow the use of the product ηV to represent the total scattered intensity from a volume of V.

The definition of scattering coefficient may be extended to dense distributions of smaller scatterers (Shung and Thieme, 1993) where scatterers are correlated. Biological tissues may be approximated as dense distributions of small scatterers because, in medical ultrasound frequency range, the wavelength is typically much greater than the sizes of tissue components.

The power received by the transducer of aperture size A can be obtained by substituting Equation (11.25) into Equation (11.26), assuming that $R >> z_0$,

$$P_s = \frac{\eta A S \tau c P_0}{2R^4} e^{-4\alpha_0 R - 4\alpha z_0} \tag{11.27}$$

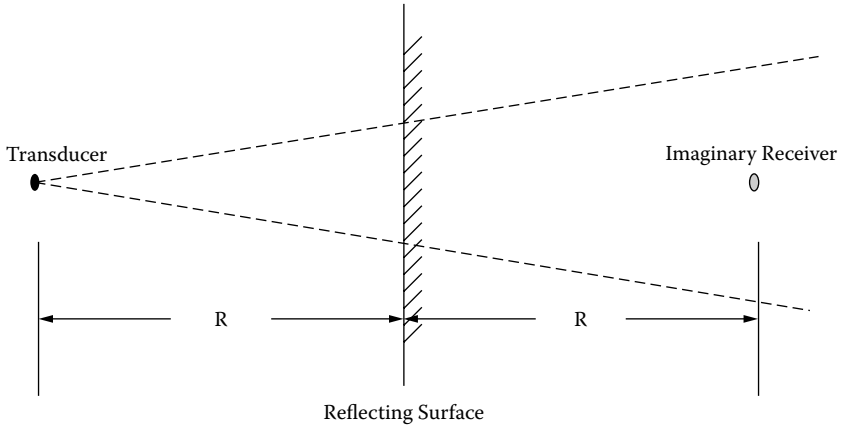

FIGURE 11.13 Diagram illustrating the mirror theory when a wave is impinging on a flat reflecting surface.

The backscattering coefficient can be estimated from Equation (11.27) by measuring S, P_0, α, and α_0 because all other parameters are known. The cross-section of the beam S at the site of measurement may be measured precisely with a hydrophone or simply approximated by its –3-dB contour. The transmitted acoustic power, P_0, is difficult to estimate because the transfer functions of the electronic and acoustic systems must be known. For practical purposes, the need for this knowledge is eliminated by performing an additional procedure — that is, measuring the reflected power from a ideal flat reflector at the position where scattering measurement is made. This is made possible by considering Figure 11.13, which shows that a flat reflector is placed at a distance of R from the transducer, assuming that $R + z_0 \sim R$.

For a nonfocused transducer, it is possible to make the approximation that, in the far field of the transducer, the transducer can be treated as a point source located at the center of the transducer aperture. Applying the mirror theory, the transducer as a receiver would appear as if it were located at a distance $2R$ from the source. The power received from the reflector by the transducer of aperture size A is then

$$P_r = \frac{A\Gamma P_0}{4R^4} e^{-4\alpha_0 R} \tag{11.28}$$

where Γ is the reflectivity of the reflector and approaches 1. Assuming that $\Gamma \sim 1$ and dividing Equation (11.27) by Equation (11.28),

$$\frac{P_s}{P_r} = \frac{2Sc\eta\tau}{R^2} e^{-4\alpha z_0} \tag{11.29}$$

Rearranging this equation, it can be found that

$$\eta = \frac{R^2}{2Sc\tau} \frac{P_s}{P_r} e^{-4\alpha z_0} \tag{11.30}$$

Equation (11.30) can be converted into decibel scale by taking the log of both sides of the equation and multiplying by 10 — that is,

$$10\log\eta = 10\log R^2 - 10\log(2Sc\tau) - (10\log P_s - 10\log P_r) - 10\log(e^{-4\alpha z_0}) \tag{11.31}$$

From this equation, it is easily seen that the backscattering coefficient, η, can be calculated by merely measuring the difference in the scattering power and reflected power in decibels if all other terms are known.

This method has been used to measure the scattering properties of a number of tissues (Shung and Thiem, 1993). Results for several tissues are given in Table 2.1. As indicated earlier, the mirror theory is invoked to calculate the reflected power from a flat reflector. This approach is valid only for nonfocused transducers. When a focused transducer is used, error will result (Yuan and Shung, 1987). The reason for this is illustrated in Figure 11.14, which shows that, for a focused transducer, the imaginary point source is not located at R from the reflector. Not recognizing this crucial assumption in utilizing the substitution method has resulted in a large discrepancy in data reported in the literature for the backscattering coefficient of tissues.

A wideband pulse may be transmitted instead of a burst consisting of several cycles. Following Fourier transform, a backscattering coefficient over a frequency band can be obtained by sacrificing the signal-to-noise ratio. A more accurate

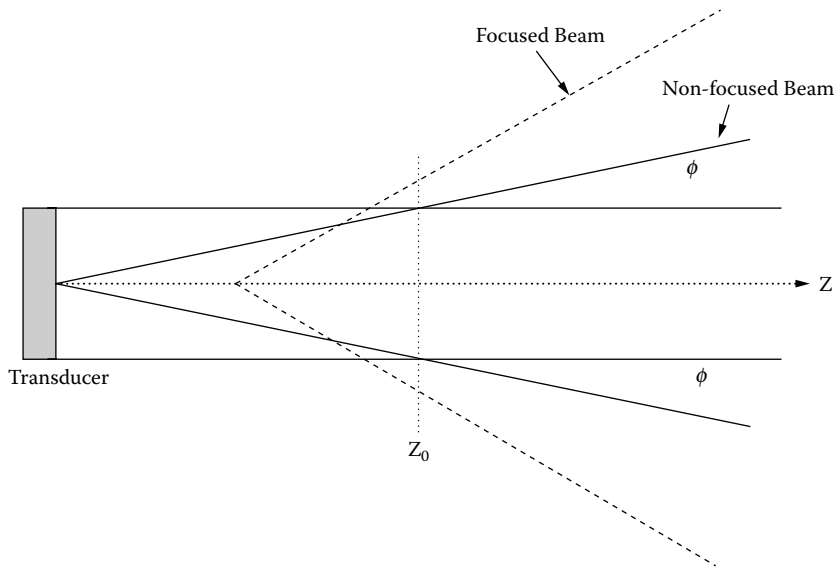

FIGURE 11.14 Only a nonfocused transducer can be approximated as a point source for far-field measurements. This approximation cannot be applied to focused transducers.

substitution method that does not involve any approximation and is therefore much more computing intensive was developed by Madsen et al. (1984).

For scattering measurements in highly absorptive media and at higher frequencies, a particulate reference medium whose scattering properties are well known may be used when the utilization of a focused transducer is necessary to achieve the required signal-to-noise ratio (Chen and Zagzebski, 1996; Wang and Shung, 1997).

11.3.2 *In Vivo* Methods

The gray level of a tissue in an ultrasonic B-mode image obtained by a scanner or the echogenicity of a tissue is related in a nonlinear manner to the ultrasonic backscattering coefficient of a tissue resulting from such signal processing steps as time–gain–compensation, echo amplitude to gray-scale mapping, etc. in a scanner. A one-to-one correspondence occurs between echogenicity and the backscattering coefficient only if these processing schemes can be adequately compensated, although it is extremely difficult to do. By merely quantitating the gray level or echogenicity of a tissue in video images acquired by a scanner *in vivo* following appropriate standardization procedures, a number of studies have shown that it is possible to differentiate diseased tissues from normal tissues in a variety of organs.

More quantitative data can be retrieved by acquiring and analyzing radio frequency (RF) or raw data before signal processing rather than the video data. In fact, a commercial system currently is equipped with an RF output for users who need the RF data. The backscattering coefficient and integrated backscatter (IB) have been measured from a number of tissues *in vivo* (Shung and Thieme, 1993). Most notable achievements have been made in the heart (Miller et al., 1985; Shung and Thieme, 1993) and the eye (Coleman and Lizzi, 1983; Shung and Thieme, 1993) for the purpose of tissue characterization.

REFERENCES

Busse, L.J. and Miller, J.G. Response characteristics of a finite aperture, phase insensitive ultrasonic receiver based upon the acoustoelectric effect. *J. Acoust. Soc. Am*. 1981, 70:1370–1376.

Chen, J.F. and Zagzebski, J.A. Frequency dependence of backscatter coefficient vs. volume fraction. *IEEE Trans. Ultrason. Ferroelect. Freq. Contr.* 1996, 43:345–353.

Chen, C.F., Robinson, D.E., Wilson, L.S., Griffiths, K.A., Manoharan, A., and Doust, B.D. Clinical sound speed measurement in liver and spleen *in vivo*. *Ultras. Imag*. 1987, 9:221–235.

Coleman, D.J. and Lizzi, F.L. Computerized ultrasonic tissue characterization of ocular tumors. *Am. J. Ophthalmol*. 1983, 96:165–175.

Greenleaf, J.A. *Tissue Characterization with Ultrasound*. Boca Raton, FL: CRC Press, 1986.

Kondo, M., Takamizawa, K., Hirama, M., Okazaki, K., Inuma, K., and Takehara, Y. An evaluation of an *in vivo* local sound speed estimation technique by the cross-beam method. *Ultras. Med. Biol*. 1990, 16:65–72.

Kuo, I.Y., Hete, B., and Shung, K.K. A novel method for the measurement of acoustic speed. *J. Acoust. Soc. Am*. 1990, 88:1679–1682.

Madsen, E.L., Insana, M.F., and Zagzebski, J.A. A method for data reduction for accurate determination of acoustic backscatter coefficients. *J. Acoust. Soc. Am.* 1984, 75:913–923.

Miller, J.G., Perez, J.E., and Sobel, B.E. Ultrasonic characterization of myocardium. *Prog. Cardiovasc. Dis*. 1985, 28:85–110.

Parker, K.J. The thermal pulse decay technique for measuring ultrasonic absorption coefficients. *J. Acoust. Soc. Am*. 1983, 74:1356–1361.

Schwan, H.P. *Biological Engineering*. New York: Wiley, 1969.

Shung, K.K. and Thieme, G.A. *Ultrasonic Scattering by Biological Tissues*. Boca Raton, FL: CRC Press, 1993.

Sigelmann, R.A. and Reid, J.M. Analysis and measurement of ultrasound backscattering from an ensemble of scatterers excited by sinewave bursts. *J. Acoust. Soc. Am*. 1973, 53:1351–1355.

Wang, S.H. and Shung, K.K. An approach for measuring ultrasonic backscattering from biological tissues with focused transducers. *IEEE Trans. Biomed. Eng*. 1997, 44:549–554.

Yuan, Y.W. and Shung, K.K. The effect of focusing on ultrasonic backscattering measurements. *Ultras. Imag*. 1986, 8:212–219.